Hole U1415J[1]

K.M. Gillis, J.E. Snow, A. Klaus, G. Guerin, N. Abe, N. Akizawa, G. Ceuleneer, M.J. Cheadle, Á. Adrião, K. Faak, T.J. Falloon, S.A. Friedman, M.M. Godard, Y. Harigane, A.J. Horst, T. Hoshide, B. Ildefonse, M.M. Jean, B.E. John, J.H. Koepke, S. Machi, J. Maeda, N.E. Marks, A.M. McCaig, R. Meyer, A. Morris, T. Nozaka, M. Python, A. Saha, and R.P. Wintsch[2]

Chapter contents

[1]Gillis, K.M., Snow, J.E., Klaus, A., Guerin, G., Abe, N., Akizawa, N., Ceuleneer, G., Cheadle, M.J., Adrião, Á., Faak, K., Falloon, T.J., Friedman, S.A., Godard, M.M., Harigane, Y., Horst, A.J., Hoshide, T., Ildefonse, B., Jean, M.M., John, B.E., Koepke, J.H., Machi, S., Maeda, J., Marks, N.E., McCaig, A.M., Meyer, R., Morris, A., Nozaka, T., Python, M., Saha, A., and Wintsch, R.P., 2014. Hole U1415J. *In* Gillis, K.M., Snow, J.E., Klaus, A., and the Expedition 345 Scientists, *Proc. IODP,* 345: College Station, TX (Integrated Ocean Drilling Program). doi:10.2204/iodp.proc.345.110.2014
[2]**Expedition 345 Scientists' addresses.**

Operations

Integrated Ocean Drilling Program (IODP) Hole U1415J was sited in close proximity to Hole U1415I (see **F8** in the "Expedition 345 summary" chapter [Gillis et al., 2014b]) because of the scientific significance of the layered series recovered at the bottom of Hole U1415I. From the beginning, Hole U1415J was established as a reentry hole in a nested free-fall funnel (FFF) configuration with casing (Fig. **F1**). Hole operations are summarized in Table **T1** and outlined below. All times are ship local time (UTC – 7 h).

Drilling operations

After our last operation in Hole U1415I, a failed attempt to reenter the hole with a 14¾ inch tri-cone bit, we offset the ship 10 m north, verified that the seafloor was free of any boulders, and observed the bit tag the seafloor at 4850.0 meters below rig floor (mbrf). After we recovered the camera system, Hole U1415J was spudded at 1855 h on 31 December 2012 using a 14¾ inch tricone bit. Drilling proceeded at ~1.2 m/h from 0 to 7 meters below seafloor (mbsf) and then slowed to ~0.6 m/h until total depth of 4865 mbrf (15 mbsf).

After three wiper trips to clean the hole, we assembled a FFF around the drill string in the moonpool. The base of the FFF had an opening of 16 inches, and we did not attach a casing stinger below the FFF. We dropped the FFF, and the drill string began taking weight soon after the FFF was deployed. We then spent 11.25 h washing and reaming the bottom 10 m of the hole. After one last wiper trip, the drill string and the 14¾ inch bit were recovered to the rig floor at 1400 h on 2 January 2013.

A 15 m string of 10¾ inch casing was made up and hung off the moonpool doors for free-fall deployment. A new 9⅞ inch rotary core barrel (RCB) bottom-hole assembly (BHA) was made up and lowered through the casing to the seafloor for reentry. The 16 inch FFF was found buried upright in the cuttings pile of Hole U1415J; only the upper parts of the rim and deployment shackles were visible. The FFF was reentered at 0420 h on 3 January and the camera system was retrieved. The drill string began taking weight at 9 mbsf and was easily washed down one more meter to 10 mbsf. The cone of a FFF was assembled around the drill string in the moonpool and connected to the cut-off joint of the 10¾ inch casing that had been previously hung off in the moonpool. The total length of the casing was 15.0 m from the cone base to

doi:10.2204/iodp.proc.345.110.2014

the end of the casing shoe. The assembly was free-fall deployed at 0730 h on 3 January.

The hole was washed and reamed to total depth (15 mbsf) and circulated clean with two 25 bbl mud sweeps. Ghost Core 345-U1415J-2G, containing 0.2 m of rock fragments and two buckets-full of coarse sand interpreted to be drill cuttings was recovered from the cleaned interval at 1045 h on 3 January. We resumed RCB coring and Cores 3R through 5R were retrieved from 15.0 to 34.9 mbsf. Hole problems required washing and reaming at ~32 and 34.9 mbsf, during which ghost Cores 6G and 7G were recovered by 0200 h on 5 January. Another fresh core barrel was dropped, and on this attempt the bit made it easily to total depth (34.9 mbsf), and RCB coring resumed. The hole drilled smoothly, and Core 8R was recovered from 34.9 to 45.2 mbsf at 0805 h. During retrieval, the area between 4878 and 4882 mbrf (28 and 32 mbsf) remained problematic and was once again reamed and conditioned multiple times. RCB coring resumed at 0900 h, and Core 9R was cut from 45.2 to 55.3 mbsf and arrived on deck at 1355 h on 5 January.

Coring continued through Core 13R, which extended the hole to 79.4 mbsf. A wiper trip was conducted, and the bit was raised to 6.5 mbsf without encountering any problems. The bit was then lowered back into the hole and took weight at ~37 mbsf. The driller was able to wash and ream to 45 mbsf. The bit was lowered and encountered weight again at 57 mbsf. The driller washed and reamed the hole to total depth at 79.4 mbsf. The bit was raised off the bottom of the hole and became stuck at 72 mbsf with high circulation pressure, no rotation, and no ability to move the bit up or down. The pipe was worked for 2.5 h before it was pulled free with 100 klb overpull. The bit was pulled up to 6 mbsf inside the 10¾ inch casing. The core barrel that was in place during this wiper trip was recovered (Core 14G), and a new core barrel was dropped.

We decided to use cement to help stabilize the hole. However, we had not yet observed the nested FFFs and therefore did not know how far the 15 m of casing attached to the FFF extended down and into the borehole. We raised the bit back up into the 10¾ inch casing and deployed the camera system to constrain the height of the FFF above seafloor. The top of the second, "upper" funnel appeared to be ~2 m above the rim of the first, leaving the casing shoe at ~13 mbsf. After retrieving the camera system, we wanted to get the bit as deep as possible before cementing. After passing a tight spot at 38 mbsf, we were able to wash and ream to 57 mbsf. However, we could not get past this depth and stopped trying at 0800 h on 7 January. At this time, the core barrel that was in place during this washing and reaming was retrieved (Core 15G). We deployed a new core barrel, washed and reamed back down to 57 mbsf, and pumped 25 bbl of cement that contained 0.25 lb/sack of lost-circulation material. After the cement was in place, we raised the bit up to 15 mbsf and the 10¾ inch casing was flushed to remove any cement from this area. The bit was then pulled out of the hole, and the drill string was flushed to clear out any remaining cement residue. We slipped and cut 115 ft of drill line and then retrieved the drill string. The bit was back on the rig floor at 2315 h on 7 January.

We then assembled a new BHA with a 9 7/8 inch tricone bit for drilling out the cement. This bit does not recover core but has a more robust cutting structure for reaming and clearing operations. The drill string was lowered to the seafloor, and we reentered Hole U1415J at 1130 h on 8 January. After recovering the camera system, the bit was run to 57 mbsf before encountering fill, without any evidence of cement. The hole was reamed once again to 77 mbsf and swept with high-viscosity mud. The bit was pulled up to 14 mbsf for a wiper trip and then lowered back down to 76 mbsf. The bit was then positioned at 63 mbsf, and a second remedial cement job was performed using 35 bbl of cement. During the cement job, the bit was lowered to 71 mbsf. After the cement was pumped, the bit was raised up to the casing shoe, and the 10¾ inch casing was flushed to ensure that no cement remained in this interval. The bit was pulled clear of the seafloor, and the drill string was circulated to flush any remaining cement from the pipe.

Because we wanted to drill out the cement with the same bit, we had to wait for the cement to harden. While waiting for this to happen, we conducted a near-bottom camera and 3.5 kHz pinger survey of two other potential drill sites (see the **"Bench site survey"** chapter [Gillis et al., 2014a]). At the completion of the survey, we reentered Hole U1415J at 2215 h on 9 January. We felt that the cement still needed a little more time to harden, so we kept the bit in the 10¾ inch casing until 0630 h. On lowering the bit into the hole, we encountered the same obstruction at ~35 mbsf, but it was easily passed. This time, the bit encountered cement at 63 mbsf, which we drilled out to 73 mbsf. Several hours were required to drill back down to the total depth of the hole (79.4 mbsf). Little advancement could be made until we significantly reduced the pump strokes to ~30 strokes/min, which allowed the bit to advance to the bottom of the hole. Each time a mud sweep was pumped, clear pump pressure changes were observed, suggesting that the cuttings might now be getting circulated out of the hole. We then drilled 5 m of new hole (to 84.4

mbsf) without coring in an unsuccessful attempt to reach a more competent formation. At this point, we decided to retrieve the drill string to switch back to an RCB coring BHA. The bit was back on the rig floor at 0600 h on 11 January.

We assembled a new BHA with a 9⅞ inch RCB coring bit, lowered it to the seafloor, and reentered Hole U1415J at 1700 h on 11 January. The bit began to take weight at the normal 35 mbsf but was able to pass through quickly. The hole was then washed and reamed, reaching the bottom of the hole (84.4 mbsf) at 0130 h on 12 January. The core barrel used during this reaming (Core 17G) was recovered and on deck at 0230 h on 12 January. We dropped a new core barrel and resumed RCB coring. Core 18R advanced from 84.4 to 89.1 mbsf. All drilling parameters appeared stable and good. Initial indications were that the two remedial cement jobs were successful and that the cuttings were now being expelled from the hole. New fill on bottom between cores appeared to be from the immediate formation being drilled into and not from uphole. Core 19R was advanced from 89.1 to 94.1 mbsf. Coring parameters remained reasonably constant and the penetration rate was initially 2.5 m/h but jumped to 5.0 m/h midway through cutting Core 19R.

After recovering Core 19R, we encountered challenges getting back to the bottom of the hole. Once we did, however, Cores 20R and 21R were cut from 94.1 to 101.8 mbsf and recovered 1.58 m (21%). Hole conditions continued to be problematic, and we conducted a wiper trip up to 74 mbsf that encountered tight spots at 82 and 86 mbsf. Core 22G was recovered from this reamed interval (between 82 and 101.8 mbsf). After eventually getting back to bottom, Core 23R extended 2 m into new formation (101.8–103.8 mbsf). Once again, we had challenges washing and reaming back to the bottom of the hole (103.8 mbsf). In the end, we were unable to get completely back to bottom and our pump pressures remained abnormally high, leading us to suspect that one or more bit nozzles were plugged. We decided to attempt cementing the lower 20 m of the hole (our third cement job in this hole) and then retrieve the drill string to replace the bit while the cement hardened. Before pumping the cement, we retrieved Core 24G. After positioning the bit at 96 mbsf, we pumped 12.5 bbl of cement. The bit was raised to 76 mbsf while pumping the cement. The bit was then pulled to 15 mbsf so that any cement remaining in the casing/FFF could be circulated out. We pulled the bit out of the hole at 1605 h on 13 January. The drill string was then flushed of any remaining cement, and the bit was back on the rig floor at 0135 h on 14 January.

A new RCB (C-7) bit with a mechanical bit release (MBR) was assembled to the bottom of the BHA. We also added a fourth stand of drill collars to the BHA. After tripping to the seafloor, operations were put on hold while a slip and cut of the drill line was completed. We reentered Hole U1415J at 1542 h on 14 January. Once the camera system was back on board, the driller commenced lowering the pipe into the hole. The drill string took weight at 36 mbsf but was able to pass this interval relatively easily. The bit encountered cement at 78 mbsf and was drilled out to 99 mbsf (3 m below the bit depth when cementing). We washed and reamed the rest of the way back down to the bottom of the hole (103.8 mbsf). After we retrieved the core barrel that was in place while washing and reaming from 99.0 to 103.8 mbsf (Core 25G; 0.48 m recovered), we resumed RCB coring. While cutting Core 26R (103.8–111.8 mbsf), the first 4.2 m drilled at a slow 1.3 m/h, but the last 3.8 m was penetrated in <3 min. Core 26R was recovered on deck at 0830 h on 15 January. While retrieving the core, the drill pipe became stuck. We tried to free the drill string for >1 h before deciding to release the bit as the next step in freeing the drill string. When lowering the MBR shifting tool with the sinker bars to release the bit, we attached the core orientation (FlexIT) tool so we could determine the hole inclination. We had to offset the ship ~260 m (~5% of water depth) to lower a tool joint down nearly 8 m to the rig floor so that the core barrels could be removed and the shifting/FlexIT tools deployed. Our attempt to shift the MBR sleeve and release the bit was unsuccessful, so we retrieved the shifting tool. Data from the FlexIT tool indicated the hole was ±3° from vertical. This put to rest one proposed theory that we had been tracking down a high-angle fault and might never drill out of the fractured material. On our second attempt to release the bit, we added a core barrel to the shifting tool and pumped it down to the bit at 70 strokes/min. The sinker bars were then run into the hole to retrieve the shifting tool and release the bit. However, before the sinker bars reached the core barrel, the drill string worked itself free. The sinker bars were recovered, leaving the core barrel and shifting tool in place. If we had recovered the core barrel, the sleeve would have shifted, leaving the bit and MBR in the hole. Once the pipe was free, we were able to pull the drill string, and the bit was back on the rig floor at 0130 h on 16 January. Because of the continually problematic and deteriorating hole conditions and the diminishing return on recovering core samples for science, the decision was made to abandon Hole U1415J and move to a different location.

Igneous petrology

Ninety-one lithologic intervals were identified in the cored sections in Hole U1415J. In addition, 72 lithologic intervals were identified in the ghost cores. Table T2 lists these lithologic intervals and their division into three units and two clusters of ghost cores. The distribution of the principal lithologies within each unit and ghost cluster recovered from Hole U1415J as well as their relative position within the hole are shown in Figure F2. Analyses of cored gabbroic rock of Hole U1415J (excluding cataclasites and chromitites) revealed primitive compositions with Mg# (100 × cationic Mg/[Mg + Fe] with all Fe recalculated as Fe^{2+}) varying between 78.6 and 87.4 (see "Inorganic geochemistry"). The upper three cores (345-U1415J-2G through 4R) are interpreted to represent a surficial zone of rubble, defined as lithologic Unit I.

Two further units were defined based on lithologic and structural constraints. Unit II (Cores 345-U1415J-5R through 9R) is, in general, a layered series dominated by the presence of clinopyroxene oikocrysts in gabbroic rock (Oikocryst-Bearing Layered Gabbro Series in Fig. F2). Unit II consists of oikocrystic-bearing troctolite (36%), gabbro (29%), oikocryst gabbro (12%), olivine gabbro (11%), and gabbronorite (9%), plus minor troctolite (non-oikocryst bearing) and basalt.

Unit III (Cores 345-U1415J-10R through 26R) is characterized by the presence of equigranular troctolites and olivine gabbro and the virtual absence of clinopyroxene oikocrysts (Troctolite Series in Fig. F2). The majority of this unit is troctolite (57%), but it also includes olivine gabbro (39%) plus minor heavily altered chromitite and basalt. Because of the overall low recovery in Hole U1415J (16%), a coherent lithostratigraphic column for this hole is not possible. However, we identified "packages" of probably coherent gabbroic lithologies, which are shown, including short summaries on their petrographic properties in Figure F3.

Based on lithologic and structural constraints and on the position within the hole, ghost cores were grouped into two clusters. Core 345-U1415J-2G was included in the rubble zone of Unit I at the top of the hole. Cores 6G, 7G, and 15G define ghost Cluster 1, which contains mainly rock from the cored interval of Unit II. Cores 14G, 17G, 22G, 24G, and 25G define ghost Cluster 2, which contains mainly rock from the cored interval of Unit III. The distributions of principal lithologies within the two ghost core clusters are also shown in Figure F2. Moreover, based on lithologic constraints, the first four pieces within Section 345-U1415J-23R-1 were interpreted as rubble because the RCB drill bit was used for cleaning the upper part of the hole before the hole advanced to recover Core 345-U1415J-23R.

Below are macroscopic and, where available, microscopic lithologic descriptions for the principal lithologies recovered in Hole U1415J and presented in the distribution graphs of Figure F2. The interval numbers from which these rocks were recovered are given in Table T2. For some thin sections from Hole U1415J, two or three different lithologic domains were defined. Table T3 lists the corresponding thin sections, the number and nature of the individual domains, and the characteristics of the contact between the domains, as well as a link for the corresponding image of the thin section with the domain boundaries marked.

Gabbro

Several intervals containing gabbro as the principal lithology were recovered from all three units of Hole U1415J (Table T2; Fig. F2). Gabbro in Hole U1415J often displays magmatic foliation defined by tabular plagioclase crystals and to a lesser extent by the orientation of prismatic olivine and clinopyroxene (see "Structural geology"). Gabbro in Hole U1415J is generally layered, showing centimeter- to decimeter-scale layering defined by differences in modal mineralogy and sometimes in grain size (for details see "Structural geology," e.g., Fig. F60).

Gabbro

Gabbro (sensu stricto) occurs in Units I and II. The gabbro is fine to medium grained and has equigranular granular texture (Fig. F4). The primary mineralogy of the gabbro is dominated by plagioclase (55%–75%) and clinopyroxene (25%–45%), with trace amounts of olivine, orthopyroxene, and oxide. Plagioclase is euhedral to subhedral with a tabular habit, whereas clinopyroxene is anhedral with a subequant habit.

Olivine-bearing gabbro

Olivine-bearing gabbro occurs in Units I and II and ghost core Clusters 1 and 2. This gabbro ranges from fine to coarse grained and is dominantly equigranular granular in texture (Fig. F5). The primary mineralogy is olivine (1%–5%), plagioclase (48%–73%), and clinopyroxene (25%–50%), with trace amounts of orthopyroxene and oxide. Olivine is euhedral to anhedral with a range of habits (subequant, amoe-

boid, and skeletal). Plagioclase is euhedral to subhedral with tabular habit. Clinopyroxene is anhedral with subequant to poikilitic habit.

Orthopyroxene-bearing gabbro

Orthopyroxene-bearing gabbro occurs as a single interval in Unit II (Interval 17). The gabbro is medium grained and equigranular granular and consists of subhedral to anhedral amoeboid olivine (3%), euhedral to subhedral tabular plagioclase (66%), anhedral subequant to poikilitic clinopyroxene (30%), and subhedral prismatic orthopyroxene (1%), with trace amounts of oxide. Photomicrographs showing details of orthopyroxene-bearing assemblages are presented in **"Descriptions of igneous boundaries."**

Olivine gabbro

Olivine gabbro

Olivine gabbro was recovered from all three units and from the ghost clusters (Table **T2;** Fig. **F2**). Olivine gabbro is dominantly medium grained, displays equigranular granular to granular-poikilitic textures, and consists of olivine (5%–30%), plagioclase (45%–70%), and clinopyroxene (5%–45%), with trace amounts of orthopyroxene (Units I and II) and oxides. Olivine gabbro typically exhibits magmatic foliation defined by the tabular plagioclase crystals and to a lesser extent by aligned olivines and clinopyroxenes (see **"Structural geology"**). Olivine is subhedral to euhedral with amoeboid habit (Fig. **F6**), tabular plagioclase is euhedral to subhedral, and clinopyroxene is anhedral and dominantly subequant, and often poikilitic (Figs. **F6, F7**). One remarkable texture is present in Unit III (Interval 59), where a single, several centimeter–sized clinopyroxene (optically continuous across the entire thin section) is poikilitic in the olivine gabbro but interstitial to the adjacent troctolite of Interval 58 (Figs. **F8, F64A, F64C, F68**).

Orthopyroxene-bearing olivine gabbro

Orthopyroxene-bearing olivine gabbro occurs as two intervals (Intervals 51 and 57) in Unit II. These gabbros are medium grained and equigranular granular and consist of subhedral to anhedral amoeboid olivine (3%), euhedral to subhedral tabular plagioclase (60%–65%), anhedral subequant clinopyroxene (22%–26%), and anhedral subequant to interstitial orthopyroxene (3%–4%).

Olivine-bearing gabbronorite

Olivine-bearing gabbronorite was found only in Unit II in Sections 345-U1415J-5R-1 and 5R-2 (Table **T2;** Fig. **F2**). The olivine-bearing gabbronorite is medium- to coarse-grained rock with equigranular granular texture and displays foliation defined by tabular plagioclase crystals and to a lesser extent by aligned olivine and clinopyroxene (Fig. **F9**) (see **"Structural geology"**). Olivine-bearing gabbronorite typically consists of olivine (2%–5%), plagioclase (60%–65%), clinopyroxene (25%–28%), and orthopyroxene (5%–10%); no oxide is present. Olivine is subhedral to anhedral with amoeboid habit, plagioclase is euhedral to subhedral with tabular habit, clinopyroxene is anhedral with poikilitic habit, and orthopyroxene is subequant with prismatic habit.

Oikocryst-bearing troctolite

Abundant clinopyroxene oikocryst-bearing troctolite and minor troctolite without oikocrysts are distinctive rock types making up lithologic intervals in Units I and II (Table **T2;** Fig. **F2**). Troctolite is medium-grained, seriate poikilitic granular rock with well-developed magmatic modal layering and foliation (see also **"Structural geology"**). In some samples, a strong grain size contrast exists between minerals in the troctolitic matrix and chadacrysts in large clinopyroxene oikocrysts. A spectacular example is shown in Figure **F10** (Unit II, Interval 49). The strong magmatic foliation is formed by the alignment of tabular plagioclase and elongated olivine. Troctolite consists of olivine (10%–42%), plagioclase (45%–70%), and clinopyroxene oikocrysts (3%–35%; 0% in minor troctolite), with trace amounts of oxide (possibly Cr-spinel) and orthopyroxene. Olivine is fine grained and subhedral to anhedral with an elongated, irregular amoeboid habit. Plagioclase is fine grained and subhedral to euhedral with tabular habit. Large clinopyroxene oikocrysts (as large as 15 mm in diameter) are anhedral and poikilitic with a distinctive population of irregularly shaped plagioclase chadacrysts (Fig. **F11**). The plagioclase chadacrysts are randomly oriented within the oikocrysts, in contrast to the surrounding foliated plagioclase fabric. Many of the plagioclase chadacrysts are deformed. Olivine is absent as a chadacryst phase.

Oikocryst gabbro

Oikocryst gabbro (including minor intervals of clinopyroxene oikocryst-bearing olivine gabbro) occurs in Units I and II (Table **T2;** Fig. **F2**). Note that Unit III contains very minor to no oikocrysts. Oikocryst gabbro, together with clinopyroxene oikocryst-bearing troctolite, is a very distinctive lithology recovered in Unit II (Fig. **F12**). Oikocryst gabbro is medium-grained, seriate poikilitic granular rock and consists of olivine (<1%–15%), plagioclase (30%–60%), and clinopyroxene (40%–55%). Olivine is subhedral to anhedral with amoeboid habit. Plagioclase is euhedral to subhedral with tabular habit. Plagioclase

chadacrysts within the clinopyroxene oikocrysts are subhedral to anhedral, tabular, and sometimes show continuous or patchy zoning. Clinopyroxene is anhedral and oikocrystic. For the definition of oikocryst gabbro, as well as an explanation of the differences between oikocrysts and poikilitic clinopyroxene, see **"Igneous petrology"** in the "Methods" chapter (Gillis et al., 2014e).

Troctolite

"Normal" troctolite (without clinopyroxene oikocrysts) occurs in the cores of Unit III as well as in ghost Cluster 2 (Table **T2;** Fig. **F2**). Troctolite in Unit III is easily distinguishable from that in Unit II because of its coarser grain size, weak foliation, lack of clinopyroxene oikocrysts, and distinctive alteration (Fig. **F13**). Troctolite consists of olivine (20%–80%), plagioclase (20%–75%), clinopyroxene (<1%–10%), and trace amounts of oxide (possibly Cr-spinel). Olivine is euhedral to subhedral with subequant to amoeboid habit. Plagioclase is euhedral to anhedral with tabular habit. Clinopyroxene is anhedral with interstitial habit. Troctolite shows only sparse magmatic layering, and most of it exhibits foliation defined by plagioclase and olivine shapes (for details see **"Structural geology"**).

Dolerite

Several doleritic lithologic intervals were recovered from Unit I of Hole U1415J (Table **T2;** Fig. **F2**). Some of the recovered pieces are shown Figure **F14.**

Olivine-bearing dolerite

Olivine-bearing dolerite occurs only in Unit I (Interval 2) and is very fine grained and equigranular with granular texture. Modally, plagioclase and clinopyroxene each comprise ~50% of the rock. Plagioclase forms euhedral to subhedral laths, with interstitial clinopyroxene. Olivine-bearing dolerite in this interval contains ~5% euhedral to subhedral subequant olivine.

Dolerite

Dolerite only occurs in ghost cores in Unit I (Intervals G2 and G3) and as a dike rock in a cataclasite in Unit III (Interval 74) as very fine grained equigranular rock with textures ranging from intergranular to subophitic. Modally, plagioclase and clinopyroxene each comprise ~50% of the rock. Plagioclase forms euhedral to subhedral laths, whereas clinopyroxene is anhedral and interstitial to subophitic (Fig. **F15**).

Doleritic gabbro

Doleritic gabbro only occurs in Unit I (Interval 4) as fine-grained rock with equigranular, doleritic texture. Modally, plagioclase and clinopyroxene each comprise ~50% of the rock. Plagioclase forms euhedral to subhedral laths, whereas interstitial clinopyroxene is anhedral.

Basalt

Several basaltic lithologic intervals were recovered from all three units in Hole U1415J (Table **T2;** Fig. **F2**).

Aphyric basalt

Aphyric basalt occurs in Unit I (Intervals 3, G1, and G4), Unit II (Interval 56), and Unit III (Interval G56) and contains <1% phenocrysts of euhedral to subhedral plagioclase laths and euhedral to subhedral subequant olivine phenocrysts (Figs. **F14, F15**).

Moderately olivine phyric basalt

This lithology interval only occurs in Unit III (Interval 70) and ghost core Interval G59 and contains euhedral to subhedral olivine (6%–7%) and subhedral subequant Cr-spinel as phenocrysts (<1%) (Figs. **F14, F15**).

Completely altered chromitite

Chromitite was recovered from intervals in Unit III (Table **T2;** Fig. **F2**) and is completely altered, making it difficult to establish its primary mineralogy and texture (see **"Chromitite"**).

Detailed description of coherent gabbroic lithologies in Units II and III

Two units have been defined based on lithologic and structural constraints, which are interpreted to represent two lithologically different series of coherent gabbroic rock and are interpreted as variably layered sequences (layering is prominent in Unit II and sparse in Unit III) with boundaries based on changes in mineral mode and/or grain size. The boundaries are described in the next section. Here, we characterize the lithologic features of the rock, which are summarized in Figure **F3.**

The characteristic feature of Unit II is magmatic layering with respect to modal composition and grain size between troctolite and minor gabbro (for details see **"Structural geology"**). Because of the presence of clinopyroxene oikocrysts, this unit was named the Oikocryst-Bearing Layered Gabbro Series (Fig. **F2**).

Typical textural features of this unit are shown in Figure F16. Of all recovered rocks in Unit II, 48% are clinopyroxene oikocryst-bearing rocks. These rocks show centimeter-sized, roundish or elongated clinopyroxene oikocrysts within a troctolitic or olivine gabbroic matrix.

Unit III is characterized by the dominance of equigranular troctolite. An apparent feature of Unit III is the virtual absence of clinopyroxene oikocrysts and the dominance of equigranular, granular troctolite and olivine gabbro which comprise 90% of the recovered rocks. Because troctolite is the most common rock, this is named the Troctolite Series (Fig. F2). The dominant rock type in this unit is homogeneous troctolite, which is characterized by the virtual absence of layering.

Typical textural features of rocks of Units II and III are shown in Figure F16. In Figure F17, the depth log for the modal compositions and mineral grain sizes for both units shows the clinopyroxene-rich nature of Unit II and the general impoverishment of clinopyroxene in Unit III. Because of the overall low recovery of Hole U1415J (16%), a coherent lithostratigraphic column for Units II and III is not possible. However, we identified packages of probably coherent gabbroic lithologies.

Unit II: Oikocryst-Bearing Layered Gabbro Series

Unit II contains six distinct packages of rock that were grouped based on similar lithology or mineralogy (Fig. F3). Typical textural features of the rock recovered in this unit are the presence of magmatic foliation, modal layering, and clinopyroxene oikocrysts. Core 345-U1415J-5R contains two packages: (1) oikocryst-bearing and (2) orthopyroxene-bearing. The oikocryst-bearing package is 0.93 m thick and contains two troctolite intervals (Intervals 19 and 24), two olivine gabbro intervals (Intervals 21 and 22), and a gabbro interval (Interval 20), all of which are oikocryst bearing. The orthopyroxene-bearing package is 0.85 m thick. The majority of this interval is gabbronorite (Intervals 25, 27, 30, and 32) but it also includes troctolite (Intervals 28, 29, and 32), and olivine gabbro (Interval 26). Core 345-U1415J-8R contains three packages: (1) olivine-bearing, (2) olivine-rich, and (3) olivine-bearing gabbro. The olivine-bearing package is 2.53 m thick and consists of four troctolite intervals (Intervals 35, 37, 40, and 41) and three olivine gabbro intervals (Intervals 34, 36, and 39); one gabbro interval (Interval 38) is also included in this package. The olivine-rich package is 0.63 m thick and consists of one olivine gabbro interval (Interval 43), one gabbro interval (Interval 46), and three troctolite intervals (Intervals 44, 45, and 47). The olivine-bearing gabbro package is 1.1 m thick and consists of two intervals that have olivine-bearing gabbro lithologies (Intervals 48 and 50). Core 345-U1415J-9R contains only one package, which is olivine-rich and 0.86 m thick. This package consists of troctolite (Interval 52), olivine gabbro (Interval 54), and olivine-bearing gabbro (Intervals 53 and 55). Figure F3B displays the average modal composition for each of the packages and the size range for dominant mineral assemblage in the packages.

Unit III: Troctolite Series

The Troctolite Series of Unit III consists of three packages: (1) troctolite with olivine gabbro, (2) troctolite, and (3) olivine gabbro (Fig. F3). The majority of the troctolite with olivine gabbro package consists of five troctolite intervals (Intervals 58, 60, 61, 62, and 66), with olivine gabbro also included in this package (Intervals 59, 63, 64, and 65). This is the thickest (20.1 m) package of rock in Hole U1415J. The troctolite package consists only of troctolite and is 9.2 m thick (Intervals 71, 72, 73, and 75). The olivine gabbro package is only olivine gabbro (Interval 78) and is 1.5 m thick. Figure F3B displays the average modal composition for each of the packages and the size range for each mineral in the packages.

Descriptions of igneous boundaries

Within Units II and III, eight different types of igneous boundaries were recovered in Hole U1415J, for which thin sections are available. The thin sections enable microscopic characterization of the boundary, which mostly separates two different igneous lithologies as a consequence of changes in mode and/or grain size, and mostly corresponds to different magmatic layers, as defined macroscopically. Details on each of these boundaries and the corresponding microphotographs are presented as follows (Table T4).

Interval 27/28 (Thin Section 38)

The boundary in Sample 345-U1415J-5R-1, 129–143 cm (Piece 18), is defined as a grain size and modal boundary that is sutured and subparallel to the foliation (Fig. F18). The modal composition is clearly different between the olivine- and orthopyroxene-bearing gabbro domain (Interval 27) and the troctolite (Interval 28) domain. The grain size of the olivine- and orthopyroxene-bearing gabbro is coarser than the troctolite. Minerals are continuous through the boundary.

Interval G20/G21 (Thin Section 40)

The boundary in Sample 345-U1415J-7G-1, 26–34 cm (Piece 5), is defined as a grain size and modal boundary that is sutured and subparallel to the foliation (Fig. F19). The modal composition is clearly different between the clinopyroxene oikocryst-bearing troctolite domain and the gabbronorite domain. The grain size of the gabbronorite (Interval G21) is coarser than the clinopyroxene oikocryst-bearing troctolite (Interval G20), except for clinopyroxene oikocrysts. Minerals are often continuous through the boundary.

Interval G30 (Thin Section 42)

The boundary in Sample 345-U1415J-7G-1, 91–94 cm (Piece 14), is defined as a grain size and modal boundary that is sutured and subparallel to the foliation (Fig. F20). The modal composition is clearly different between the troctolite domain and the clinopyroxene oikocryst-bearing troctolite domain. The grain size of the clinopyroxene oikocryst-bearing troctolite is coarser than the troctolite. Minerals are continuous across the boundary. Both domains are assigned to Interval G30 (clinopyroxene oikocryst-bearing troctolite).

Interval 42/43 (Thin section 52)

The boundary in Sample 345-U1415J-8R-2, 105–122 cm (Piece 9), is defined as a grain size and modal boundary that is sutured and subparallel to the foliation (Fig. F21). The modal composition is clearly different between the olivine gabbro domain (Interval 43) and the olivine-bearing gabbro domain (Interval 42). The grain size of the olivine-bearing gabbro is coarser than the olivine gabbro. Minerals are continuous across the boundary.

Interval 48 (Thin Section 54)

The boundary in Sample 345-U1415J-8R-3, 31–41 cm (Piece 6), is defined as a grain size and modal boundary that is sutured and subparallel to the foliation (Fig. F22). The modal composition is clearly different between the gabbro domain and the olivine gabbro domain. The grain size of the olivine gabbro is coarser than the gabbro. Minerals are continuous across the boundary. Both domains are assigned to Interval 48 (olivine-bearing gabbro).

Interval 58/59 (Thin Section 58)

The boundary in Sample 345-U1415J-10R-1 39–55 cm (Piece 6B), is defined as a grain size and modal boundary that is gradational and subparallel to the foliation (Fig. F23). The clinopyroxene in the olivine gabbro domain (Interval 59) is oikocrystic and continuous through the troctolite domain (Interval 58), but the modal composition is clearly different between the troctolite domain and the olivine gabbro domain. The grain size of the olivine gabbro is coarser than the troctolite, except for the clinopyroxene oikocryst.

Interval 73 (Thin Section 72)

The boundary in Sample 345-U1415J-18R-1, 141–146 cm (Piece 17B), is defined as a grain size and modal boundary that is sutured and subparallel to the foliation (Fig. F24). The modal composition is clearly different between the olivine-rich troctolite domain and the troctolite domain. The grain size of the troctolite is coarser than the olivine-rich troctolite. Minerals are continuous across the boundary. Both domains are assigned to Interval 73 (troctolite).

Interval G69 (Thin Section 85)

The boundary in Sample 345-U1415J-25G-1, 30–38 cm (Piece 5), is defined as a modal boundary that is sutured and subparallel to the foliation (Fig. F25). The modal composition is different between the olivine-bearing gabbro domain and the gabbro domain. Interfingering texture of clinopyroxene grains is observed along the boundary (Fig. F25D). The clinopyroxene of the gabbro intrudes into the clinopyroxene of the olivine-bearing gabbro and contains orthopyroxene blebs. Minerals are continuous across the boundary. Both domains are assigned to Interval G69 (olivine gabbro).

Boundary interpretation

The boundaries recovered in Hole U1415J are mainly sutured or gradational; no sharp boundaries were observed. This description implies that the boundaries were formed at the interface between magmas that were both hypersolidus. Mineral continuity across the boundaries was induced by further crystallization after the magmas were juxtaposed. The lack of chilled margins at the boundaries in Hole U1415J implies that the magmas were near thermal equilibrium.

Significance of orthopyroxene

The presence and abundance of orthopyroxene as a crystallizing phase is similar in Unit II of Holes U1415I and U1415J. Its significance (see the **"Hole U1415I"** chapter [Gillis et al., 2014d]) is related to the widespread perception that orthopyroxene in the ocean crust is limited to the late stages of crystallization. Mohorovicic discontinuity–crossing melts are generally considered to be undersaturated in orthopyroxene because orthopyroxene is almost never

observed as a crystallizing phase in mid-ocean-ridge basalt (MORB), nor is it observed in experiments on dry MORB composition (e.g., Stolper and Walker, 1980; Grove and Bryan 1983). At the same time, the defining literature on the lower crustal sections of the Oman ophiolite, which is regarded as the best example for an ancient fast-spreading oceanic rift system, in those areas not affected by the so-called late-stage magmatism (e.g., Lippard et al., 1986) declare definitively that prismatic orthopyroxene is generally not observed (e.g., Pallister and Hopson, 1981) except in the uppermost evolved gabbro. The discovery of orthopyroxene in mafic lithologies in high quantities in the lower crustal section at Hess Deep is a novel finding, although the presence of orthopyroxene in one primitive gabbro sample from Hess Deep was reported by Coogan et al. (2002).

Three factors are critical to understanding the role of orthopyroxene in this rock. First, orthopyroxene is stabilized relative to clinopyroxene by pressure and oxidizing conditions (Feig et al 2006, 2010). Second, water in the magma destabilizes orthopyroxene in favor of clinopyroxene (Feig et al., 2006, 2010). Third, contrary to the conclusions of Pallister and Hopson (1981), orthopyroxene is found in the Oman lower crustal section (Abily, 2011) in similar abundance and occurrence to that in Holes U1415H–U1415J at Hess Deep. Although this may be related to initiation of subduction, the parallel to the occurrence observed here is striking.

Clinopyroxene textures and the origin of oikocrysts in troctolites in Hole U1415J

The textures of clinopyroxene observed in Hole U1415J gabbro are remarkable for their complexity and diversity. We observed a range of textural habits from interstitial, intergranular, and subophitic to ophitic, sometimes all within the same thin section. Despite this complexity, in a broad sense the observed textures in gabbro vary between two end-members. The first end-member is a relatively medium grained equigranular gabbro containing discrete, relatively equant nonpoikilitic granular clinopyroxene. The second end-member is a relatively coarse grained, strongly seriate gabbro with very large pyroxene oikocrysts, charged with chadacrysts forming what appears to be a continuous interconnecting network of grains (see a definition for oikocryst and poikilitic clinopyroxene in **"Igneous petrology"** in the "Methods" chapter [Gillis et al., 2014e]). For any particular gabbro in Hole U1415J, it is possible to place the observed textures within a continuum between these two end-members. This continuum may reflect an interplay between (1) clinopyroxene resulting from cumulus crystallization at one end and (2) clinopyroxene crystallizing from the rapid cooling of a crystal mush or in melt channels. Imposed on this continuum is magmatic foliation ranging from weak to strong, so it is possible to have both isotropic to foliated equigranular gabbro, for example. Below, we present the features of the end-member textural types and give some intermediate examples.

Clinopyroxene textures in Hole U1415J troctolite

Clinopyroxene oikocrysts in Unit II troctolite are considered separately because of their distinctive nature, reflected in the very large grain size contrast between the relatively fine grained foliated troctolitic matrix and the large clinopyroxene oikocrysts (Figs. **F26, F27**). The oikocrysts appear as isolated large subhedral crystals in a finer grained troctolitic fabric that appears to "swirl"' around the oikocrysts (Fig. **F26A, F26B**). Visually, the comparison to snowball porphyroblasts in some metamorphic rock is inescapable, though their origin is obviously different.

Hole U1415H–U1415J troctolite clinopyroxene oikocrysts show grain boundaries that range from interstitial and optically continuous with the oikocryst (Fig. **F26C**) to sharper boundaries with no interstitial domain. In these oikocrysts, the troctolite fabric wraps around the oikocryst, with olivine and plagioclase in direct contact with clinopyroxene and some of the plagioclase projecting from the troctolite matrix into the interior of the oikocryst (Fig. **F27**).

Another feature of the oikocrysts is the distinctive chadacryst population. Olivine is never a chadacryst despite its presence at oikocryst margins and in the interstitial poikilitic domains of the oikocrysts. The plagioclase chadacryst population is complex, displaying euhedral to irregular shapes with some deformation features (see **"Structural geology"**) (Fig. **F28**). Hence, clinopyroxene crystallized after deformation for it to have captured deformed plagioclase. The chadacrysts are randomly oriented, in marked contrast to the tabular euhedral to subhedral plagioclase in the surrounding strongly foliated troctolitic matrix (Figs. **F26C, F27C, F28**). If the clinopyroxene crystallized late, we would expect it to have captured the surrounding troctolite foliation, and indeed this has occurred in the interstitial margins, yet it is not present in the oikocryst cores. If the oikocryst was the result of late-stage melt-rock reaction, we would also expect to see abundant partly reacted chadacrysts reflecting the original fabric of the troctolite.

In summary, the oikocryst textures suggest that the clinopyroxene

- Crystallized after deformation of the plagioclase chadacrysts (see "Structural geology"),
- Appears to not be in a reaction relationship with olivine and plagioclase of the troctolite matrix, and
- Contains a plagioclase chadacryst population that is difficult to explain as being derived from the surrounding plagioclase population.

Olivine morphology

Skeletal and dendritic olivine textures are preserved in Hole U1415J. Figure F29 shows some examples of skeletal olivine observed in recovered core. Many of these skeletal olivines have a "C" or hook shape associated with them, with plagioclase commonly enclosed in the hook (Fig. F29A, F29C, F29D, F29F). These plagioclases display evidence of resorption in the form of "elbow" joints or 120° grain boundaries. The majority of these skeletal olivines occur in Cores 345-U1415J-3R through 10R.

Other olivine morphologies lack this hook shape but are still classified as skeletal because of their "branching" morphology (Fig. F29B, F29E). This type of morphology has been labeled dendritic. Piece 4 from Section 345-U1415J-11R-1 displays clear macro- and microscopic evidence of this morphology. The red outline in Figure F30A enhances the branches of the dendritic olivine. Clinopyroxene fills the gaps where the branches have broken. The branching nature of the olivine in this sample is further demonstrated in thin section. In Figure F30B, dendritic olivine with pink birefringence is observed next to poikilitic clinopyroxene (tan birefringence). This morphology has been termed "starburst." Another troctolitic sample (345-U1415J-25G-1, 28–30 cm [Piece 4]) also displays signs of dendritic olivine; however, the olivine in this sample is more altered, and the branches are difficult to identify.

Experimental studies suggest that skeletal and branching crystals grow relatively rapidly under conditions of strong supersaturation or magmatic undercooling (e.g., Lofgren and Donaldson, 1975; Donaldson, 1976; Lofgren, 1980). Donaldson (1974, 1977) attributed dendritic development to in situ crystallization under conditions of supersaturation of the magma with respect to olivine. He speculated this might arise from two possible alternative mechanisms: a sudden decrease in the water content of a water-undersaturated feldspathic peridotitic liquid and the transition of a water-saturated peridotitic magma to an unsaturated state by exsolution of volatiles. Hort (1998) also concluded that exsolution of volatiles from magma could induce such an increase in undercooling, giving rise to dendritic and skeletal crystal morphologies. This suggests that replenishment could involve both continual small influxes of magma as well as intermittent large influxes of magma (Butcher et al., 1985; Faithfull, 1985; Renner and Palacz, 1987) and that this periodic influx could be the fundamental cause of much of the layering observed in this section.

Chromitite

Heavily altered chromitite was recovered from two intervals in Unit III (Intervals 70 [Sample 345-U1415J-18R-1, 67–69 cm] and 77 [Sample 21R-1, 5–16 cm]) (Figs. F31, F32, F33) and from one ghost core (Sample 22G-1, 0–3.5 cm [Piece 1]). Chromite grains are also present in the troctolite adjacent to the chromitite, including one small aggregate of chromite grains in one piece of troctolite (Sample 345-U1415J-19R-1, 39–46 cm [Piece 6]). Chromitite is embedded in a series of primitive, olivine-rich, chromite-bearing troctolite and olivine gabbro (between the sequences of troctolite in Sections 345-U1415J-10R-1 through 20R-1 and olivine gabbro in Sections 21R-1 through 26R-1). Two contacts between domains with aggregates of chromitite and heavily altered troctolite within individual pieces are shown in Figures F31 and F33. Although obscured by strong alteration, the primary contacts appear to have a sutured character. One chromite aggregate contains roundish inclusions of now heavily altered material, which is interpreted as former inclusions of olivine (Fig. F31). All these observations imply that these chromitite aggregates represent accumulation of Cr-spinel in an early stage of MORB crystallization.

Because of the severe alteration, estimating the primary lithologies of chromitite is difficult. Several grains in two samples represent relics of the magmatic stage now forming a central core surrounded by "orbicular" aggregates of fine-grained magnetite (Figs. F31, F33; Thin Section 71; Sample 345-U1415J-18R-1 [Piece 9] and Thin Section 76; Sample 21R-1 [Piece 3]). The host rock of the chromitite is troctolite, although it is composed of minerals that are completely altered to chlorite and amphibole. In one sample (21R-1 [Piece 2]), the primary phases are completely replaced by magnetite and/or iron-rich chromite, chlorite, and amphibole with bluish green pleochromism (Fig. F32; see also "Metamorphic petrology"). The texture and mineral assemblage of Sample 21R-1 (Piece 2) is different from other chromitite samples in Hole U1415J (Figs. F31, F33). This rock is interpreted to have formed during chloritization of the surrounding olivine/chromite associations. The chromite grains are surrounded by chlorite, broken apart into elongated magnetite grains, and cut through by chlorite veins (Kelemen, Kikawa,

Miller, et al., 2004; Abe, 2011). These observations imply that the classification of this rock (Sample 345-U1415J-21R-1, 4.5–12 cm [Piece 2]) as "chromitite" is justified, although it is now completely metamorphosed. In order to express the generally high grade of alteration within the chromitites, the term "completely altered chromitite" for the principal rock name was used. Only two reported examples of chromitite recoveries from previous ocean drilling cruises exist. One example is several aggregates of chromite and a chromitite minipod from peridotite cores recovered at Hess Deep from Ocean Drilling Program (ODP) Leg 147 Holes 895C and 895E (Arai and Matsukage, 1996). The other example is from ODP Leg 209 Site 1271 peridotite cores (Shipboard Scientific Party, 2004; Abe, 2011).

Metamorphic petrology

Background alteration

Lithologic Unit I is defined as a gabbroic rubble unit that contains a variety of discontinuous rock samples (Intervals 1–14) as well as a section of drill cuttings (Intervals G2–G4 in Core 345-U1415J-2G). Gabbroic rubble in Unit I is characterized by pervasive background alteration and is typically slightly altered (10%–30%) but locally can be 60%–90% altered (Fig. **F34**). Gabbroic rocks in Unit II exhibit pervasive background alteration and are typically slightly altered (10%–30%) but locally can be 60%–90% altered (Fig. **F35**). Gabbroic rocks in Unit III exhibit pervasive background alteration and are typically moderately altered (30%–60%) but locally can be completely altered (>90%) (Fig. **F36**). More intense alteration is associated with cataclastic zones, olivine-rich zones, intervals with a higher density of microcracks, contacts between igneous layers, and hydrothermal veins. Mineral assemblages defining distinct metamorphic zones are absent, and alteration does not appear to correlate with igneous grain size. Most of the secondary minerals are visible to the naked eye. However, for the identification of some minerals, particularly fine-grained minerals, optical petrography was required. A summary of alteration intensity and secondary modes observed in thin section is presented in Table **T5.** Thin sections with two or more metamorphic domains are listed in Table **T6.** A summary of X-ray diffraction (XRD) results for vein-filling materials and cataclasites is presented in Table **T7.**

Alteration in the three lithologic units in Hole U1415J varies somewhat by unit and is characterized by "normal" pervasive background alteration as well as intense alteration in cataclastic zones. In the Unit I surficial rubble, alteration is characterized by pervasive alteration of olivine to serpentine with poorly developed corona textures. Veins in Unit I are commonly prehnite, with fewer amphibole, chlorite, and clay mineral–bearing veins. Olivine is more pervasively altered with more complete corona development in the Troctolite Series of Unit III than in the Oikocryst-Bearing Layered Gabbro Series of Unit II. Prehnite is the dominant vein-filling mineral throughout Hole U1415J, and chlorite veins occur almost exclusively in the Troctolite Series. Cataclastic zones occur in Units II and III and are characterized by variable alteration of primary plagioclase, pyroxene, and cataclastic cements of prehnite and locally chlorite.

Olivine

Olivine is highly altered (70%–100%) in most samples in Hole U1415J and alteration is slightly more intense in Unit III than in Unit II (Table **T5**). Olivine shows a striking contrast to the freshness of plagioclase, which is commonly <20% altered. Alteration intensity, mineral assemblage, and modal proportion of secondary minerals replacing olivine are variable among pieces and even within individual pieces.

The most common alteration mineral assemblage after olivine is serpentine + magnetite ± sulfides. In samples exhibiting magmatic foliation with shape-preferred orientation (SPO) of plagioclase and olivine, serpentine veins are typically subparallel to foliation (Fig. **F37**). Radial cracks are observed in plagioclase surrounding serpentinized olivine, as in Hole U1415I. Clay mineral replacement occurs in olivine in contact with the dense fracturing related to serpentinization and is especially common adjacent to clinopyroxene oikocrysts in some troctolites (e.g., Samples 345-U1415J-7G-1, 26–34.5 cm [Piece 5], and 8R-3, 22.5–30 cm [Piece 5]). This alteration also seems to be related to fracturing subparallel to the magmatic fabric, as suggested by the propagation of curved fractures subparallel to plagioclase laths surrounding the oikocrysts. A notable observation is serpentine with unusually strong pleochroism from colorless to bluish gray in one sample (Thin Section 72; Sample 345-U1415J-18R-1, 141–143 cm), possibly a submicroscopic mixture of serpentine and clay minerals or tiny opaque minerals.

Corona textures are composed of a concentric zonal aggregate of tremolite and chlorite and characteristically occur as a reaction product between olivine and plagioclase in oceanic gabbroic rocks (e.g., Nozaka and Fryer, 2011) (Fig. **F38A, F38B**). In many samples from Hole U1415J, coronitic tremolite-chlorite is common and locally abundant, particularly near chlorite veins that cut the magmatic foliation at a high intersection angle (Fig.

F38C, F38D). The abundance of coronitic tremolite + chlorite and the completeness of corona formation is highly variable and shows no systematic downhole variation. Completion of the corona-forming reaction (i.e., absence of relict olivine inside a corona) appears more frequently in Unit III than in Unit II (Fig. F39; Table T8). A remarkable observation in Hole U1415J is the occurrence of green spinel associated with coronitic chlorite and amphibole, which is perhaps identified in situ for the first time in oceanic gabbroic rock. The spinel's pale green color suggests enrichment of Al and Mg and deficiency of Cr compared with brown spinel, chromite, and magnetite, which are common spinel-group minerals in mafic or ultramafic rock. The green spinel is sparsely distributed in two samples of troctolite (Thin Section 67; Sample 345-U1415J-13R-1, 53–56 cm, and Thin Section 17; Sample 18R-1, 53–56 cm), showing a close association with coronitic chlorite and amphibole (Fig. F40). The green color and occurrence with chlorite strongly suggest a metamorphic origin for this spinel.

Talc occurs in the assemblage talc ± chlorite ± amphibole ± sulfides. It is not exclusive to the corona-forming reaction, suggesting that talc alteration occurred over a range of temperature conditions. In Thin Section 63 (Sample 345-U1415J-12R-1, 94–96 cm), for example, olivine is completely altered to talc + pyrite with a mesh-like texture similar to that of serpentine + magnetite.

Pyroxene

Clinopyroxene is variably altered to green or colorless amphibole and lesser amounts of chlorite along grain boundaries or cleavage surfaces (Fig. F41). Clinopyroxene is slightly to moderately altered (<10%–60%) in Unit I, slightly to highly altered (10%–90%) in Unit II, and slightly to completely altered (<10% to >90%; mean = 60%–90%) in Unit III. Slightly altered clinopyroxenes have clear cores that grade outward to irregular rims, similar to those in Hole U1415I. Hydrothermal clinopyroxene was not confidently identified in Hole U1415J samples.

Brown amphibole replacing clinopyroxene was only observed in Unit III (Thin Sections 79 and 80; Section 345-U1415J-21R-1 [Pieces 14 and 16, respectively] and Thin Sections 82 and 83; Section 23R-1 [Pieces 7 and 8, respectively]). Brown amphibole is indicative of high-temperature alteration conditions and is commonly intergrown with green amphibole (Fig. F42). Brown amphibole after clinopyroxene represents 5%–30% of the total alteration products in these rock pieces. In Section 345-U1415J-21R-1, replacement of clinopyroxene by brown amphibole occurs as a background alteration product and does not appear to be related to vein halos. In Section 23R-1, brown amphibole is also observed in the cataclastic zone of Piece 7. In Piece 8 of the same section, brown amphibole replacing clinopyroxene occurs only in weakly deformed parts but not in cataclastic zones. The development of brown amphibole does not appear to be related to cataclasis but rather appears to have formed prior to cataclasis.

Orthopyroxene is variably altered to colorless or pale green amphibole, talc, chlorite, serpentine, and clay minerals along fractures or cleavage surfaces and is highly to completely altered (60% to >90%) in Unit I, slightly to highly altered (<10% to >90%) with a mean value of <10% in Unit II, and fresh to slightly altered (<10%–30%) in Unit III. Orthopyroxene is relatively fresh (<10% altered) even in samples containing completely altered olivine (Fig. F43). Most grains of orthopyroxene show no reaction at contacts with plagioclase, in contrast to olivine, which is commonly fringed by coronitic tremolite and chlorite adjacent to plagioclase.

Chromite-magnetite

Although relict chromite is rare in Hole U1415J rock, thin Intervals 71 (Sample 345-U1415J-18R-1, 67–72 cm [Piece 9]), 77 (Sample 21R-1, 5–16 cm [Pieces 2 and 3]), and G57 (Sample 22G-1, 0–3 cm [Piece 1]) are composed primarily of magnetite and chlorite, with minor amphibole. The unusual mineral assemblage of these intervals opens the possibility that they were originally chromite-rich rock (see "Igneous petrology"). In this chromitite or chromite-rich troctolite, amphibole and chlorite show unusual bluish green colors in plane-polarized light, suggesting unusual chemical compositions (perhaps high-temperature ferric-calcic amphibole) (Fig. F44). The geochemistry of this rock shows that it is low in Cr and high in Fe (see "Inorganic geochemistry").

Plagioclase

Plagioclase is variably altered to prehnite, chlorite, and secondary plagioclase and is slightly to moderately altered (<10%–30%) in Unit I, slightly to moderately altered (<10%–60%) in Unit II, and slightly to highly altered (<10%–90%) with a mean value of 60%–90%) in Unit III.

In thin section, magmatic plagioclase is most commonly replaced by chlorite and prehnite in all units. Secondary plagioclase is a common replacement of plagioclase in Units I and II but is less common in Unit III (Table T5). In all units in Hole U1415J, chlorite commonly forms a continuous cryptocrystalline rim in plagioclase adjacent to olivine grains (Fig. F45A). Prehnitization of plagioclase occurs as background alteration in serpentinized olivine-rich rocks

and filling radiating fractures adjacent to serpentinized olivine in all units. Garnet (or hydrogarnet) is rarely developed in association with prehnite and chlorite after plagioclase (Fig. F46). Near cataclastic zones, replacement of plagioclase by prehnite becomes more intense, often with vuggy textures and cores of chlorite or clinozoisite (Fig. F47). In cataclasite samples from Unit III, clinozoisite and epidote are intergrown with and may replace prehnite after plagioclase and may also rarely replace plagioclase directly. Irregular replacement of plagioclase by zeolite occurs uncommonly in vein margins, sometimes accompanied by clay minerals.

Sulfide minerals

Sulfide minerals occur as secondary phases in all of the gabbroic lithologies recovered in Hole U1415J. These minerals occur in mineral replacement pseudomorphs and are commonly associated with alteration products after clinopyroxene and olivine. Pyrite is common in all units and is widely disseminated as a trace phase in nearly all of the lithologic intervals. Fine-grained, isolated pyrite grains commonly occur in serpentine microveins after olivine. Clusters of pyrite and pentlandite ± chalcopyrite rarely form sulfide mineral assemblages near magnetite stringers associated with olivine alteration. Chalcopyrite forms irregular grains associated with magnetite stringers within serpentine mesh and also in the chlorite replacements of plagioclase. Pyrite and perhaps pentlandite are also observed in some thin sections, intergrown with or entirely surrounded by magnetite (e.g., Thin Section 36; Sample 345-U1415J-5R-1, 62–64 cm [Piece 12]). Detailed observations of sulfide mineralization are recorded in the visual core descriptions (see **"Core descriptions"**).

Veins

Thin (1–2 mm), massive prehnite veins are the most common vein type in Hole U1415J (Fig. F48). The dominant vein types in lithologic Unit I are prehnite ± chlorite ± zeolite and are typically 1–2 mm thick and 2–4 cm long with massive texture. A smaller number of dominantly chlorite, dominantly amphibole, and dominantly clay mineral veins also occur in thin vein networks in Unit I. The dominant vein types in Unit II are (1) prehnite ± chlorite ~1 mm thick and 2–3 cm long with a massive or radiating texture (Fig. F49D) and (2) thin and relatively short veins of chlorite <1 mm thick and a few millimeters to a few centimeters long (Fig. F49B). Prehnite-bearing veins (Type 1) are observed throughout Unit II (Fig. F86). Halos of enhanced alteration adjacent to the veins are 0.5–2 cm thick and commonly surround prehnite veins, especially in Sections 345-U1415J-8R-1 through 8R-3 (Fig. F49A). Chlorite veins (Type 2) start to appear at the top of Section 8R-1 in Unit II. Chlorite veins typically follow grain boundaries and open out into irregular chlorite patches, often containing amphibole needles and late calcite (Fig. F45B). In some cases, tiny needles of amphibole were observed in corona rims at the contact with unaltered plagioclase adjacent to olivine and orthopyroxene. Networks of massive clay mineral veins are present in Sections 345-U1415J-8R-1 and 8R-2 but become rare in Section 8R-3 and deeper cores.

Chlorite and prehnite veins are also the dominant vein types in Unit III (including ghost Cluster 2). Chlorite veins are commonly monomineralic but also include mixtures of chlorite-amphibole (Samples 345-U1415J-18R-1 [Pieces 1, 7, and 8], 21R-1 [Piece 2], 23R-1 [Piece 7], and 26R-1 [Piece 4]). Less commonly, chlorite veins may also include magnetite stringers (Sample 345-U1415J-18R-1 [Piece 7]). Many chlorite veins show cross-fiber texture with chlorite growing from vein rims to centers and typically lack alteration halos (Fig. F50A). Chlorite veins typically form relatively dense vein networks in the cataclastic intervals in Sections 345-U1415J-21R-1 through 26R-1 and increase in abundance with depth (Fig. F86).

Throughout Hole U1415J, prehnite veins are commonly crosscut by chlorite veins but also crosscut chlorite veins. Prehnite veins are typically thin, polycrystalline, and monomineralic. In five thin sections (Thin Sections 25, 47, 54, 69, and 73; Samples 345-U1415J-2G-1, 10–13 cm; 8R-1, 73–76 cm; 8R-3, 35–38 cm; 14G-1 [Piece 1]; and 19R-1, 18–19 cm; respectively), composite veins filled with chlorite and lesser amounts of prehnite are partially replaced by carbonates (Fig. F50). In these veins, prehnite occurs between the crossing fibers of chlorite and radiating prehnite clusters are distributed along the veins (Fig. F50E, F50F).

Rare epidote veins appear in Unit III (Figs. F49D, F51G, F51H), along with rare massive clinozoisite veins (mineralogy confirmed by XRD). Epidote veins occur in the dolerite dikes cutting cataclastic gabbro in Sections 345-U1415J-24G-1 and 25G-1 and are brecciated in cataclastic zones. In intervals containing clinozoisite veins, plagioclase is almost entirely replaced by prehnite or clinozoisite (i.e., Sample 345-U1415J-4R-1 [Piece 4]). Clay mineral veins are rare in Unit III and appear in only four pieces (Samples 345-U1415J-10R-1 [Piece 3], 21R-1 [Pieces 3 and 7], and 23R-1 [Piece 1]). Zeolite veins are also rare and observed in only five pieces (Samples 345-U1415J-11R-1 [Piece 2], 12R-1 [Pieces 1 and 6], 18R-1 [Piece 16], and 23R-1 [Piece 6]) (Figs. F50C, F50D, F51C, F51D).

Within cataclastic intervals, polycrystalline prehnite veins crosscut cataclastic zones in which prehnite ± chlorite replace the comminuted matrix minerals (Sections 345-U1415J-12R-1 and 12R-2; intervals 20R-1, 9–19 cm, and 21R-1, 16–131 cm; Section 21R-2; and interval 23R-1, 19–54 cm) (Fig. F49). These crosscutting polycrystalline prehnite veins are commonly brecciated by subsequent cataclasis.

The density of veins increases with the deformation degree of the rock. Undeformed cores contain only a few veins per 10 cm of core, whereas strongly deformed cores contain >20 veins per 10 cm. For downhole variations of vein density and vein mineralogy, see "Structural geology" and Figure F86.

Alteration in and associated with cataclasite

A wide range of cataclastic textures exist in Hole U1415J, from narrowly spaced networks of fractures a few micrometers wide to intensely comminuted zones millimeters to centimeters wide to variably brecciated core measured in decimeters and finally to foliated mylonitic cataclasites (Fig. F71). Alteration associated with the cataclasite zones is commonly intense and fracture controlled and generally appears to be superimposed on the background alteration documented in previous sections.

In intervals affected by cataclasis, chlorite appears to form complete pseudomorphs with relict serpentine mesh textures after olivine (Fig. F52). These pseudomorphs often appear to be deformed in the cataclasite zones, forming chlorite foliae. Epidote occurs as brecciated vein material within chlorite in the cataclastic matrix of some highly altered samples. Turbid and fluid inclusion-rich, possibly secondary, plagioclase is locally associated with chlorite and is fairly common as a clast in the cataclasite.

Comminuted plagioclase within cataclasite zones is commonly replaced by prehnite and rarely by carbonate (Fig. F47), whereas clinopyroxene is relatively fresh and occurs as fragments dispersed within the prehnite (Fig. F53A). Replacement of plagioclase by prehnite is variable, with some cataclastic zones being essentially prehnite-free. In other intervals, relatively coarse grained prehnite replaces the matrix (primarily plagioclase) in the relatively fine grained cataclastic intervals in Units II and III. Relatively coarse grained prehnite is commonly brecciated and included as clasts in successive cataclasite. Epidote may occur within prehnite, and prehnite + chlorite + epidote may be a stable assemblage in some samples (Fig. F53).

Drill cuttings

Core 345-U1415J-2G consists mainly of coarse sand–size (0.5–1 mm) drill cuttings. Two grain-mount sections from this interval were point-counted to establish primary and secondary mineralogy (Table T9). Clasts in the grain mounts were highly altered compared to the average recovered core, containing significant amphibole, prehnite, secondary plagioclase, zeolite, chlorite, and clay minerals and broken coronitic aggregates of amphibole and chlorite after olivine. The clasts also contain cataclasite (12%–20%) with local overprints of prehnite.

Although the reconstructed primary mode of the grain mounts is similar to the typical olivine gabbro in Hole U1415J (Table T9), alteration and deformation are as intense as the most deformed and altered intervals in the Unit II gabbroic lithologies. These observations suggest that the drilling sand was collected mainly from a fault zone or that unrecovered parts of each section consisted of such rocks. In either case, it is clear that the recovered core is not fully representative of the extent of alteration and cataclastic deformation in the hole.

Metamorphic conditions and deformation processes

Background alteration

The mineral assemblages of the rocks recovered in Hole U1415J suggest a range of temperature conditions from upper amphibolite to subgreenschist facies. Plagioclase alteration is variable in mineral association and spatial distribution, suggesting a wide range of temperature conditions and localized fluid infiltration along microcracks, grain boundaries, fractures, and cataclastic zones. Coronitic textures (olivine + plagioclase = tremolite + chlorite ± talc) are variably developed, indicating middle to lower amphibolite facies hydration (Blackman et al., 2011; Nozaka and Fryer, 2011). A significant difference of Hole U1415J from the other Expedition 345 holes is the localized occurrence of brown amphibole and green spinel, suggesting upper amphibolite facies. Green spinel has been reported from metagabbro of the Oman ophiolite and is interpreted there as the product of high-temperature (700°–800°C) hydrothermal alteration (Abily et al., 2011). Low-temperature alteration of olivine to serpentinite and clay

minerals appears to result from fracturing controlled by the physical properties and/or magmatic fabrics of the original rock. Veins are mostly thin and isolated and are dominated by prehnite, zeolite, and clay minerals, implying relatively low temperature alteration conditions.

The background alteration of gabbroic rock in Hole U1415J is similar to alteration in the Site 894 gabbroic rock, although far less secondary clinopyroxene and green amphibole along plagioclase grain boundaries and filling microfractures were observed in the rock of Hole U1415J (Shipboard Scientific Party, 1993; Früh-Green et al., 1996).

Cataclastic zones

The replacement of magmatic minerals by metamorphic alteration products requires introduction of aqueous fluids, and cataclastic zones are obvious potential pathways for their introduction. A wide range of cataclastic zones exist in Hole U1415J, from narrowly spaced networks of 1 mm wide fractures to foliated mylonitic cataclasite with potentially large displacements (see **"Structural geology"**). It is possible that the presence of poorly cemented fault rock was responsible for the many meters of core that were not recovered and for the meters of sand containing fragments of cataclasite that were recovered (see **"Drill cuttings"**).

Chlorite and prehnite are the dominant secondary minerals in the cataclastic zones. These minerals primarily cement broken and angular shards of plagioclase and pyroxene (e.g., Fig. **F54**). Not all cataclastic zones are associated with new mineral growth, however. Figure **F55** shows an incipient cataclastic zone in which crystallization of hydrous minerals is limited to the narrow chlorite-filled shear zones and extensional "pull apart" structure where calcite, chlorite, and prehnite precipitated. Fibrous chlorite veins are commonly truncated by the cataclasite and demonstrate that fluids infiltrated into this rock prior to the cataclastic event.

Chlorite is locally a significant alteration product after plagioclase; however, prehnite is the more common replacement mineral in the cataclastic zones (e.g., line CC-CC, Figs. **F56, F57**). In a typical cataclasite (Sample 345-U1415J-21R-1, 103–107 cm [Piece 14]), chlorite embays the plagioclase clasts in the cataclasite, suggesting substantial replacement (Fig. **F58**). The prehnite vein cuts plagioclase with smooth boundaries (yellow arrows), whereas chlorite embays plagioclase clasts in the phyllonitic matrix and widens the walls of the adjacent fractured grains; this feature is most conspicuous in reflected light that highlights the two-dimensional interface (white arrows). In this case, these sutured boundaries suggest that plagioclase was dissolved and replaced by the adjacent chlorite.

Where slip subsequent to chlorite formation occurs, fibrous chlorite veins appear to have developed (Figs. **F55, F56**), and the slip seems to establish a preferred orientation of the chlorite flakes. The chlorite content of some cataclasites may be high enough and the preferred orientation strong enough that the rock becomes a foliated cataclasite; in some cases multiple deformation events are evident (Fig. **F59**). In spite of the relatively strong cleavage developed in this rock, it was still cut by fractures that were later filled with prehnite.

Multiple cycles of deformation are apparent in some samples, and crosscutting relationships help to establish the order of brecciation. Figure **F54** shows an example of a cataclasite in which five or more separate bands of breccia are visible. Each band is composed primarily of prehnite in interlocking crystals <50 µm in diameter. This matrix contains many inclusions of coarser grained prehnite with angular outlines, suggesting that they were relatively coarse grained veins broken up by cataclastic events. Band C5 also contains fragments of relatively fine grained prehnite with a texture similar to that in Band C2. Most bands contain a few small fragments of plagioclase and clinopyroxene, especially Band C1. Band C5 may be the youngest because it truncates layering (arrows in Fig. **F54**) in adjacent bands (C2, C3, and C4) in the cataclasite veins. In turn, Band C3 truncates layering in both Bands C2 and C1, suggesting the order of brecciation. Band C1 also contains more relict clinopyroxene and less coarse-grained prehnite, implying that this band may have been one of the earlier generations of cataclasite. Figure **F54** identifies one domain (C3A) that might exist as either a separate cataclastic event or a large individual clast. The small size of the sample does not allow discrimination between these possibilities.

Rare brittle-plastic deformation occurs in two samples (Thin Section 77; Sample 345-U1415J-21R-1, 17–19 cm [Piece 4] and Thin Section 79; Sample 21R-1, 107–108.5 cm [Piece 14]). In Sample 21R-1, 103–107 cm (Piece 14), two contrasting cataclasites are juxtaposed across a chlorite vein (Fig. **F57**). The lower part of the figure is dominated by relatively coarse and fine-grained prehnite microbreccia, whereas the cataclasite in the upper part of the image contains more abundant plagioclase than prehnite. Some plagioclase is cloudy because of abundant tiny inclusions, suggesting that it is secondary plagioclase. Much of the chlorite between the two domains is in random orientation, but chlorite adjacent to the walls of the vein has a strong preferred orientation (white arrows in the figure) and phyllonitic bands

have developed. Apparently, the randomly oriented chlorite acquired its preferred orientation by brittle-plastic deformation along the walls of the vein. The same relationships are evident in Sample 345-U1415J-21R1, 17–19 cm (Piece 4) (Fig. F59), where chlorite in the cataclastic matrix defines a strong preferred orientation, suggesting that slip along these grains postdated the cataclasis. Apparently, the fractures that allowed the precipitation of chlorite were reactivated in a ductile fashion to create phyllonite ("Ph" in Fig. F59). Nevertheless, renewed deformation involved brittle fracturing, as evident from the crosscutting prehnite-filled fractures.

From shipboard observations and interpretations, we conclude that the cataclastic zones were formed by brittle deformation in close association with repeated prehnite and chlorite formation under subgreenschist facies conditions.

Structural geology

Magmatic structures

Macroscopic observations: lithologic Unit I

The uppermost cores (345-U1415J-1R, 2G, 3R, and 4R) comprise a surficial rubble unit (Unit I; see "Igneous petrology") with 11 cobbles and 6 cored pieces of gabbro, olivine gabbro, and troctolite. All pieces from these four cores are relatively small (13 cm maximum length), and weak modal layering was only recognized in one piece (Sample 345-U1415J-3R1, 49–55 cm [Piece 11]). Of the plutonic pieces, 82% (by length) exhibit planar magmatic foliation defined by weak to strong plagioclase and olivine SPO. The dip of the magmatic foliation in the five oriented pieces recovered ranges from 15° to 47° (mean = 32.4°; standard deviation = 13°), which is consistent with dip values seen in the higher recovery cores of Unit II. Distinct clinopyroxene lineation was observed in interval 345-U1415J-3R-1, 17.5–28.5 cm (Pieces 5 and 6).

Macroscopic observations: lithologic Unit II

Drilling in Unit II (Cores 345-U1415J-5R, 6G, 7G, 8R, 9R, 14G, and 15G) recovered a layered sequence of troctolite, olivine gabbro, gabbro, and gabbronorite showing centimeter- to decimeter-scale layering (Fig. F60) defined by differences in modal mineralogy and sometimes by grain size. Figures F61A and F61B show examples of the layering observed in Unit II. The most conspicuous layering is indicated by the boundaries between gabbro and the more olivine-rich rock types (olivine gabbro and troctolite) and is therefore primarily defined by variations in modal olivine accompanied by changes in modal pyroxene and, to a lesser degree, plagioclase. Some of the boundaries show grain size variation caused by the appearance of large (2–5 mm) pyroxene crystals and other variations caused by increases in olivine grain size from 1–2 to >5 mm. Plagioclase grain size changes less dramatically across these boundaries, with small increases in mean grain size from 1–2 to 3–4 mm. The layers have planar boundaries with sharp contacts at the centimeter scale but are gradational and sutured at the 1–5 mm (grain size) scale (see "Igneous petrology" for more details). Of the recovered pieces, 23% exhibit layering, but this must be regarded as a minimum because layering thicker than piece length will only be recognized if boundaries are preserved. The dip of the layers in all cores in the unit, except for Core 345-U1415J-7G, is consistently between 30° and 49° (mean dip = 36.5°; standard deviation = 6°) (Fig. F60). Boundaries between layers that were observed in both core pieces and in thin sections are parallel or near parallel to the magmatic foliation. No abrupt intrusive contacts were observed, which is consistent with the interpretation that the layering formed under hypersolidus conditions.

Ghost Core 345-U1415J-7G comprises gabbro, olivine gabbro, and troctolite very similar to that found in Cores 5R and 8R (see "Igneous petrology"); however, layering of the entire Core 7G has a mean dip of 59° (standard deviation = 21°). If the lower two pieces are excluded, the mean dip of the upper part of the core is 76° (standard deviation = 5°). Given this core is a ghost core recovered after redrilling through the same depth interval as Core 8R, the simplest interpretation of the data is that Core 7G was recovered from a block that had rotated >40° into a large cavity at 34–40 mbsf during drilling.

Of the Unit II core pieces, 97% (by length) exhibit foliation defined by plagioclase, olivine, and rarely pyroxene SPO (Fig. F61A–F61C), compared to ~75% for the entire hole. These estimates should be regarded as minima because weak fabrics are hard to recognize in pieces that have also undergone cataclasis, are small, or are coarse grained. Estimates of foliation strength in core pieces were validated by examination of the foliation in thin section, where possible. Figure F62 illustrates that >60% of the core from Unit II has moderate to strong foliation strength compared to 48% for the whole core and only 30% for Unit III. Therefore, Unit II generally exhibits a stronger foliation compared to the rest of the core.

Magmatic foliation intensity appears to increase in strength with increasing olivine content (Fig. F63), although it should be noted that the color contrast between olivine and plagioclase crystals on the outer

surface of the core means that magmatic foliation is more easily recognized in olivine-rich rock. Gabbro tends to have weak magmatic foliation and olivine gabbro shows moderate foliation, whereas troctolite, the dominant rock type in this unit (see **"Igneous petrology"**), exhibits moderate to strong foliation (Fig. **F63**). Too few pieces of gabbronorite were recovered from this hole to allow for meaningful analysis of its characteristic fabric strength.

Foliation is predominantly planar, although it can be seen to anastomose around large (1–2 cm diameter) clinopyroxene oikocrysts (Fig. **F61C**), a feature that is also seen around smaller (<1 cm diameter) oikocrysts in thin section. Very rarely, foliation can vary in dip by as much as 15° on a core piece scale. Dip of magmatic foliation for Unit II (excluding the ghost cores) ranges from 10° to 57° (mean = 35°; standard deviation = 9°) (Fig. **F60**). A weak olivine lineation was observed within the plane of foliation in a few intervals of troctolite and olivine gabbro.

Similar depth of recovery, lithology, and dip of magmatic layering and foliation seen in Core 345-U1415J-5R to that seen in Core 345-U1415I-4R recovered in Hole U1415I (see **"Structural geology"** in the "Hole U1415I" chapter [Gillis et al., 2014d]) suggests that these units can be correlated (Fig. **F60**). Therefore, this unit has a subsurface horizontal extent of at least 10 m and a vertical thickness of ~30 m.

Macroscopic observations: lithologic Unit III

Drilling in Unit III (Cores 345-U1415J-10R through 26R and ghost Cores 17G, 22G, 24G, and 25G) recovered a sequence of coarse-grained, troctolite, olivine gabbro, and gabbro that show only sparse magmatic layering (3% of the piece length). Again, this must be regarded as a minimum because layering thicker than piece length will only be recognized if boundaries are preserved and because of the large proportion of cataclastic rock in this unit. The best two of four recovered pieces exhibiting layering are shown in Figure **F64.** All recognized boundaries are planar at the >1 cm length scale and parallel to magmatic foliation based on both core and thin section observation. Boundaries are defined by variations in modal proportions of olivine accompanied by changes in proportions of plagioclase and pyroxene but additionally may be defined by grain size (Fig. **F64;** see **"Igneous petrology"** for more details). Boundaries may be sharp or gradational; the two oriented examples from RCB (nonghost) cores have a steeply dipping orientation (66° and 90°). No abrupt intrusive contacts were observed, which is consistent with the interpretation that the layering formed under hypersolidus conditions.

Of the core pieces from Unit III, 55% (by length) exhibit foliation defined by plagioclase, olivine, and rarely pyroxene SPO (Fig. **F64**) compared to ~75% for the entire hole. This estimate should be regarded as minima because the core has a large proportion of cataclasites that make recognition of primary magmatic foliation impossible. However, no strong magmatic foliations were recognized in this unit (Fig. **F66**), suggesting that Unit III has generally weaker fabric strength than Unit II. Figure **F63** shows that troctolite, the dominant rock type, has mostly moderate foliation strength. Too few pieces of the other rock types were recovered from this hole to allow for meaningful analysis of their characteristic fabric strength.

Magmatic foliation recorded in Unit III is planar (Fig. **F64A, F64B**), with dips ranging from 57° to 90° (mean dip = 78°; standard deviation = 11°) (Fig. **F60**). One piece (Sample 345-U1415J-13R-1, 37.5–51.5 cm [Piece 6]) exhibits an anomalously shallow dip of 17°. We suggest that this piece is likely from a small, <1 m scale rotated block within a fault zone cutting this unit. The mean dip of Unit III is significantly steeper than the mean dip recorded in Unit II (35°). This difference considered with the different compositions of Units II and III, the freshness of the rock, lack of recovery and poor drilling conditions at the depth of the boundary between Units II and III, and the character of the seafloor bathymetry typical of submarine mass wasting suggests that Unit II is a tens of meters–scale slump block lying on top of Unit III. The vertical dip of magmatic foliation in Unit III together with the difficult drilling conditions raises the possibility that it, too, might be a tens of meters thick slump block (see **"Paleomagnetism"**).

Microscopic observations

The similarity of the core recovered from lithologic Units I and II in Hole U1415J to that found in Hole U1415I means that the Hole U1415J Unit I and II core shows many of the microstructural features associated with the magmatic foliation discussed in the **"Hole U1415I"** chapter (Gillis et al., 2014d). Many of the common features are therefore only briefly discussed here. Significant differences are shown in Unit III and include larger olivine and plagioclase mean grain size in troctolites, weaker magmatic foliation, and a relative paucity of equant clinopyroxene oikocrysts.

Magmatic foliation in all units is defined by plagioclase crystals but may also be defined by olivine and, to a lesser extent, orthopyroxene and clinopyroxene when the crystals have suitable habits. In all cases, the foliation is controlled by both the preferred ori-

entation and shape anisotropy of the crystals. Plagioclase crystals are commonly tabular and as long as 8 mm but normally 1–2 mm in length, with aspect ratios as high as 8:1. The [010] albite twin planes typically run parallel to the long axes of the crystals. Olivine crystals defining the foliation are often tabular or weakly skeletal and 1–5 mm in length, with aspect ratios as high as 6:1 and [010] olivine axes likely perpendicular to foliation. Less commonly, orthopyroxene and clinopyroxene crystals (3–8 mm in length) also exhibit elongation of up to 10:1 parallel to foliation (Fig. F65A, F65B). However, in many cases clinopyroxene appears as relatively large (0.5–2 cm in diameter) equant to subequant oikocrysts, around which the plagioclase-defined foliation may be deflected.

Lithologic Unit I

Unit I consists of troctolite and olivine gabbro with magmatic foliation similar to that observed in Unit II and in Hole U1415I (discussed below). This unit also contains gabbro with distinctive magmatic fabrics that are relatively rare in the core. Interval 345-U1415J-3R-1, 17.5–28.5 cm (Pieces 5 and 6), contains large (as long as 8 mm), high aspect ratio (10:1) twinned clinopyroxenes that define a very strong lineation within weak plagioclase foliation and more numerous smaller, equant clinopyroxene crystals (Fig. F65A). The elongate pyroxenes are largely undeformed, show only rare undulose extinction and seriate grain boundaries with adjacent plagioclase crystals (Fig. F65B), and have a few plagioclase chadocrysts compared to the more equant clinopyroxene crystals. Plagioclase crystals are commonly annealed with 120° triple junctions and gently curved grain boundaries and are therefore typical in this respect in comparison with much of the core.

Figures F65C and F65D illustrate an interval of gabbro (interval 345-U1415J-3R-1, 78.5–85.5 cm [Piece 16]) with relatively coarse plagioclase grain size (2–5 mm) and moderate plagioclase foliation. The plagioclase crystals show significant deformation twinning and bending but show less well developed grain-boundary annealing than elsewhere in the core. This piece supports the assertion that plagioclase grain-boundary annealing is less well developed in the coarser grained rocks.

Lithologic Unit II

As discussed above, Unit II correlates with Unit II of Hole U1415I, and therefore only selected examples of magmatic foliation are presented here. Figure F66 shows examples of the typical tabular olivine- and plagioclase-defined magmatic foliation developed within and around equant clinopyroxene oikocrysts in (Fig. F66A) and at the margin of (Fig. F66B) the troctolite. In both cases, magmatic foliation within the relatively fine grained (1–3 mm) troctolitic portion of the rock is strong and wraps around parts of the oikocrysts. Note that the most distinctive wrapping of foliation is around the right side and bottom of the oikocrysts in Figure F66A; it is not solely confined to the bottom of the oikocrysts. Locally, the undeformed oikocrysts include bent plagioclase crystals (Fig. F66B), indicating that crystal-plastic deformation associated with mush development was occurring above the solidus. Magmatic foliation outside of the oikocrysts also contains large, bent plagioclase crystals with deformation twins and subgrains (Fig. F66D–F66F), which likely also records crystal-plastic deformation within the mush. Figure F66F additionally shows typical, small (<1 mm) plagioclase crystals immediately adjacent to and within the margins of a large, bent plagioclase crystal, illustrating how parts of the plagioclase network of crystals are commonly annealed and strain-free. Figure F66D shows a relatively unstrained, large (2–3 mm) plagioclase crystal oriented almost perpendicular to magmatic foliation. The survival of this crystal within the strong foliation perhaps suggests that foliation was not formed solely by recrystallization.

Figure F67 shows examples of textural features relevant to the origin of magmatic foliation not seen in thin sections of rock recovered in Hole U1415I. Figure F67A shows an olivine gabbro with large (up to 2 cm), elongate (and twinned) clinopyroxene oikocrysts aligned with the olivine and plagioclase foliation. These oikocrysts partially enclose relatively large (2–3 mm) plagioclase crystals aligned with the dominant foliation, indicating that the pyroxene margins continued to grow after/during foliation development (Fig. F67B). Conversely, just above these large plagioclase crystals and elsewhere in the thin section, moderate plagioclase foliation shown by smaller (<1 mm) plagioclase crystals appears to wrap around the oikocrysts, suggesting that some compaction of foliation occurred against clinopyroxene oikocrysts formed earlier. The larger, perhaps earlier formed, plagioclase crystals commonly show deformation twins in this thin section, again suggesting hypersolidus deformation within a crystal mush.

Figure F67D shows a clinopyroxene oikocryst-bearing troctolite with strong magmatic foliation defined by annealed plagioclase and tabular olivine crystals (Fig. F67E). The foliation wraps around the uppermost oikocryst in Figure F67D. Interestingly, that oikocryst is deformed and exhibits subgrain development (Fig. F67F), suggesting that oikocrysts can be deformed under near-solidus conditions, likely to-

ward the end of foliation development. Figures F67B and F67C show an example of northeast–southwest imbricated or tiled plagioclase crystals within magmatic foliation that runs approximately horizontally in the figure. Imbrication suggests that a shear component was involved during foliation development.

Lithologic Unit III

Unit III is dominated by coarse-grained (≥5 mm) troctolite not seen in Unit II or Hole U1415I. Unfortunately, this troctolite is generally more altered than the finer grained troctolite seen elsewhere and mostly contains only serpentinized olivine and pseudomorphed plagioclase crystals. Plagioclase crystals appear to be tabular, and olivine varies from tabular to highly skeletal morphologies (Fig. F68E). The moderate foliation of these rocks is mostly defined by the SPO of plagioclase and, to a lesser extent, by tabular olivine crystals when present. Figures F64A and F64C show that the olivine gabbro on the right side of Sample 345-U1415J-10R-1, 43–51 cm (Piece 6), contains large (0.5 cm), altered, skeletal olivine crystals that do not define SPO. However, the plagioclase crystals between the skeletal olivine crystals do define moderate magmatic foliation (Figs. F64C, F68A). The observation that there is plagioclase foliation between larger, apparently only weakly deformed olivine crystals again supports the suggestion that foliation started to form at high melt fractions early in the history of the formation of these cumulates, perhaps as a deposit of crystals from a magmatic current. The finer grained (0.5–1.0 mm) troctolitic portion of Piece 6 shows features that are typical of those found in other units. Strong magmatic foliation is defined by tabular plagioclase and olivine crystals (Figs. F65C, F68B). Olivine crystals also exhibit skeletal morphologies with limited deformation (subgrains but no kinking), but likely with some annealing, to form smooth grain boundaries (Fig. F68B, F68C). Small plagioclase crystals (<0.5 mm) are typically annealed, with gently curved grain boundaries and 120° triple junctions (Fig. F68D). Interesting in this sample is a large clinopyroxene oikocryst extending across the boundary between olivine gabbro and troctolite, suggesting the boundary formed under hypersolidus conditions and was subsequently overgrown by late crystallizing clinopyroxene (Fig. F64C).

Sample 345-U1415J-11R-1, 22–24 cm (Piece 4), is a relatively weakly altered troctolite with isotropic magmatic foliation (Fig. F68E). Large (as wide as 1 cm) skeletal olivine shows some undulose extinction and subgrain development but no kinking. Tabular plagioclase crystals have a bimodal grain size distribution, with the larger grains (3–5 mm) showing deformation twins, bent grains, undulose extinction, and subgrain formation and the smaller grains (<2 mm) showing greater grain-boundary annealing and less deformation. The presence of this isotropic troctolite within a sequence of foliated troctolite argues against large-scale, melt-poor shearing of Unit III. The existence of small annealed plagioclase crystals within this sample suggests that annealing is not a consequence of foliation development or strain-induced recrystallization and may simply develop passively during near-solidus cooling of the units in Hole U1415J.

Figure F69 shows photomicrographs of an olivine gabbro (Sample 345-U1415J-25G-1, 11–15 cm [Piece 2]) that, although from a ghost core, exhibits high-temperature, near-solidus deformation within and between clinopyroxene oikocrysts. The piece also exhibits a dramatic range in grain size, with large (1–3 cm) clinopyroxene oikocrysts, 0.5–1.0 cm skeletal olivine crystals, and 0.5–5.0 mm long plagioclase crystals (Fig. F69A). Similar to other samples, larger (1–5 mm) plagioclase crystals commonly show deformation twinning, whereas finer grained (<1 mm) plagioclase crystals are commonly annealed (Fig. F69B, F69C). The piece shows no magmatic foliation, but the smaller plagioclase crystals within the clinopyroxene oikocrysts often occur in chain-like clusters resembling relict grain boundaries within the oikocrysts (Fig. F69A, F69E). We speculatively suggest that these clusters may represent the boundaries of former 0.5 cm diameter olivine crystals (similar to those found outside of the oikocryst) that have since been replaced by clinopyroxene. Figure F69D shows a narrow zone (0.5–2 mm wide) of submillimeter plagioclase and clinopyroxene crystals between two large clinopyroxene oikocrysts. Here the grain boundaries are not annealed, and the tiny (<0.5 mm) fragments of clinopyroxene suggest that this zone might be a recrystallized, high-temperature, near-solidus deformation zone between two clinopyroxene oikocrysts. The presence of subgrains within the oikocrysts elsewhere in the thin section (Fig. F69A) indicates that the sample did undergo near-solidus strain/deformation.

Crystal-plastic deformation

Very little significant, structurally continuous, subsolidus crystal-plastic deformation was observed in the recovered section, barring narrow (1–2 mm thick) zones of incipient crystal-plastic deformation (undulose extinction and subgrain formation in plagioclase and olivine and bent grains of clinopyroxene) associated locally with margins of zones of intense cataclasis/ultracataclasis. In addition, four thin (≤5 cm) intervals of deformation likely associated

with alteration minerals and reaction weakening (see also "Cataclastic deformation") were recovered in Hole U1415J. These zones are 2–40 mm thick and include intervals at 65.440 mbsf (Sample 345-U1415J-11R-1, 44–49.5 cm [Piece 7]), 69.805 mbsf (Sample 12R-1, 11–13 cm [Piece 3A]), 98.965 mbsf (Sample 21R-1, 16–23 cm [Piece 4]), and 101.895 mbsf (Sample 23R-1, 10–12 cm [Piece 3]). Each zone and the associated foliation is defined by anastomosing ultrafine-grained dark to light brown layers (chlorite and clay?) separated by lenses hosting porphyroclasts of plagioclase, prehnite, epidote, clinozoisite/zoisite, and carbonate that have themselves undergone subgrain formation and/or twinning and locally significant grain size reduction (Fig. F70). Macroscopic observations show rotation of foliations into the fine-grained zones, microfaulting, and asymmetric porphyroclasts or "fish" (Passchier and Trouw, 2005). Although sense-of-shear indicators are recognized in thin section, none of the recovered pieces hosting these microstructures are oriented; therefore, no shear sense was determined.

Cataclastic deformation

Brittle structures are locally well developed in Hole U1415J and comprise roughly 37% of recovered pieces (Fig. F71). Although nondisplacive microfracturing and veining are by far the most dominant brittle deformation processes recorded in Hole U1415J, distinct zones of cataclastic deformation were recovered. Cores from lithologic Units I and II (Cores 345-U1415J-2G through 9R) record only minor brittle deformation, whereas cores from Unit III reveal thicker zones of variable fracture intensity and cataclasite/ultracataclasite, especially Cores 12R (69.70–71.25 mbsf) and 21R (98.80–100.42 mbsf) (Figs. F71, F72). Cataclastic deformation intensity rankings in Hole U1415J range from 0 (>60% recovered core length) to 5 (~3% recovered core length). Figures F73 and F74 show the macroscopic character of three examples of brittle deformation displaying the range of cataclastic fabric strength observed in the core (see "Structural geology" in the "Methods" chapter [Gillis et al., 2014e]):

1. Dense-anastomosing fractures (Rank 3),
2. Well-developed brecciation (Rank 4), and
3. Cataclasite (Rank 5).

Macroscopic estimates of cataclastic fabric intensity in core pieces were validated by examination of the fabric in thin section, where possible.

The dip of zones of cataclastic deformation measured in core from Hole U1415J varies from gentle to subvertical (mean = 59°; n = 19) (Fig. F75), with no clear relationship between downhole depth and dip.

Macroscopic observations show that the cataclastic deformation zones exhibit heterogeneous grain sizes and degrees of alteration and reflect the variable intensity of cataclasis over a centimeter scale. The majority of pieces in Core 345-U1415J-12R are characterized by brittle fabrics of intensity Ranks 3–5 (Fig. F73A–F73C) and host several types of veins. Most pieces show little preferred orientation, whereas a few pieces show strong preferred orientation and development of cataclastic foliation (Fig. F73C). Unfortunately, because of the small size of recovered pieces, none have measurable dips (Fig. F75).

Microscopically, zones of cataclastic deformation in Core 345-U1415J-12R show very heterogeneous grain sizes and degrees of alteration. Cataclastic fabrics are characterized by grain size reduction by microcracking and rotation of the primary igneous and metamorphic minerals, producing angular to subrounded porphyroclasts of variably altered plagioclase, pyroxene, prehnite/chlorite, and/or compound gabbroic clasts in a fine-grained clast-clay(?) matrix (Fig. F73). This microstructure is commonly cut by prehnite and minor chlorite veins in turn cut by another period of cataclastic deformation (Fig. F73F). Crosscutting relations indicate a complex succession of vein formation and brittle deformation.

As with Core 345-U1415J-12R, most pieces from Core 21R host brittle structures ranging from dense anastomosing fractures to cataclasite (Fig. F74A–F74C). Pieces recovered in Core 21R also contain deformed/fractured prehnite and chlorite veins. The subvertical orientation in these pieces (Fig. F76) is likely related to veining and associated cataclastic deformation. One piece shows very well developed cataclastic foliation (Figs. F70, F74C). The microstructure locally hosts both angular and rounded clasts of plagioclase, clinopyroxene, and prehnite in a fine-grained matrix (Fig. F74E). Narrow zones of ultracataclasite locally cut the less-fractured host, with chlorite veins both cutting and deformed by zones of fracture and/or cataclasis (Fig. F74D, F74F). Crosscutting relationships in Core 21R therefore record a complex succession of vein formation and cataclastic deformation and suggest that vein formation is at least locally synchronous with cataclastic deformation.

In Hole U1415J, unique brittle structures were recovered in several pieces from Cores 345-U1415J-13R, 19R, and 26R. Section 345-U1415J-13R-1 contains a cream-colored string of fractured anorthosite (Sample 345-U1415J-13R-1, 18.5–32.0 cm [Piece 4]) (Fig. F76A) indicating a subvertical zone of localized, relatively "dry" (associated with little alteration) brittle strain. Microscopic observation illustrates an almost "shattered" texture characterized by angular plagio-

clase clasts locally hosted in a chlorite and/or prehnite matrix (Fig. F76B–F76D).

Several pieces of fractured dolerite adjacent to altered cataclasite were recovered (e.g. Sample 345-U1415J-19R-1, 63.5–70 cm [Piece 10]) (Fig. F77A). Microstructural observations suggest that the dolerite hosts a chilled/undercooled margin that was likely emplaced into cohesive cataclastic gabbro hosting variable intensity prehnite/chlorite alteration. Although subsequently fractured/sheared, grain size in the dolerite decreases toward the contact between the two rocks types (Fig. F77B).

The cataclasite zone (interval 345-U1415J-19R-1, 63.5–70 cm [Piece 10]) shows both angular and rounded clasts of plagioclase, prehnite aggregates, and clinopyroxene within a partially chlorite filled matrix (Fig. F77C). Away from the contact with the cataclastic gabbro, dolerite shows an intersertal texture characterized by tabular laths of plagioclase hosting anhedral grains of clinopyroxene (Fig. F77D) cut locally by branching chlorite-filled zones of cataclasis. The contact zone between the cataclasite zone and dolerite zone shows two distinct ultracataclasites (Fig. F77E). These ultracataclasites contain minerals from each rock type, indicating that it could be derived from both dolerite and cataclasite (Fig. F77F). Although both epidote and chlorite veins cut the dolerite, contact zone, and cataclastic gabbro, these veins were deformed by later cataclasis (Fig. F77B, F77E, F77F), implying deformation and fluid flow likely were repeated events under medium- and low-grade metamorphic conditions (≤400°C; see "Metamorphic petrology").

A thin interval of dolerite cataclasite was recovered in Core 23R (Sample 345-U1415J-23R-1, 9.5–13 cm [Piece 3]) with widely developed epidote and prehnite veins (Fig. F78A). This zone of intense cataclasis comprises clasts of epidote, prehnite, and altered minerals in a fine-grained matrix of prehnite (Fig. F78B, F78C). Clasts of epidote, prehnite, and other fine-grained alteration minerals form aggregates that locally include chlorite. The dolerite hosts epidote, clinozoisite, and prehnite veins that show mutually crosscutting relations (Fig. F78D). Between veins, dolerite locally shows ultracataclastic texture. Furthermore, dolerite contains a chilled margin, again cut by a zone of cataclasis, with a sharp boundary between the two (Fig. F78A, F78E). Crosscutting relationships indicate a complex succession of dolerite and vein intrusion and cataclasis, suggesting that the successive cataclastic deformation and fluid flow events occurred after dolerite intrusion under relatively medium and low grade metamorphic conditions.

In the deepest core recovered, Core 345-U1415J-26R, cataclastic rock appears less altered with angular and rounded plagioclase clasts in a fine-grained matrix derived from plagioclase, clinopyroxene, and prehnite, within which a narrow ultracataclasite zone has developed (Fig. F79). Prehnite only partially replaces plagioclase, with fractured plagioclase locally filled by chlorite (Fig. F79C). Crosscutting relationships suggest that cataclasis of the gabbro occurred prior to infiltration by prehnite and chlorite, similar to relations seen above in other sections.

Alteration veins

Alteration veins represent a ubiquitous, although volumetrically insignificant, component of the rock types recovered in Hole U1415J and reflect the cracking and fluid circulation experienced by the gabbroic rocks exposed at the Hess Deep Rift. Alteration veins are filled with various types of "secondary" minerals or mineral assemblages, including talc, amphibole, epidote, chlorite, serpentine, prehnite, carbonate, zoisite, zeolite, and clay minerals (see "Metamorphic petrology").

Vein shape and structure of the vein-filling material

Alteration veins recovered in Hole U1415J are all very thin; their maximum thickness rarely exceeds 5 mm. Veins thicker than 1 mm are not frequent, with the large majority being only a few hundred micrometers across. The thinnest veins identified with the naked eye, and thus systematically logged, are ~100 µm thick, but thin section observation reveals a population of much thinner alteration veins. A continuum exists between "macroscopic" and "microscopic" veins and what is described as pervasive alteration.

Vein length generally exceeds the width of the core (~6 cm), but vein tips are quite common. Therefore, we inferred that veins are rather short features, likely not much longer than a few decimeters. Most veins have irregular geometry (lightning-bolt shapes; Fig. F80A), with many veins curved, and form intricate networks with complex branching and crosscutting relationships. Networks with regularly spaced parallel veins are less common; they were only observed in lithologic Unit III (Fig. F80B). En echelon vein networks, diagnostic of crack-opening in a shear-stress regime, are virtually absent.

Texture of the vein-filling material depends on mineralogy; some minerals preferentially develop a fibrous texture, whereas others are more blocky. Most veins show evidence of progressive filling from their

walls and are termed crack-seal veins. This type of vein is best illustrated by chlorite veins that commonly show two sets of fibers that grew from each vein wall and join in the center of the vein (Fig. F81A). This relationship shows that veins were previously open cracks where hydrothermal fluids circulated and eventually sealed with alteration minerals. Some veins show evidence of multiple filling with different minerals. In some rare examples, the filling was not completed and geode-like microcavities are preserved.

Many veins show evidence of weak to moderate shearing parallel to their walls (Fig. F81B–F81E). This shearing may be locally intense in intervals affected by postvein emplacement cataclasis. Filled tension gashes were observed in some cataclasites (Fig. F81F), potentially affording an estimate of paleostress orientation in oriented blocks.

Alteration vein density

Alteration veins are found in ~75% of the cored length, with an average density of a few veins per decimeter and average vein thickness of <1 mm. Accordingly, veins represent <<1% of the volume of the recovered cores. A sampling bias likely exists because of the brittle nature of the veins. In fact, some pieces are limited at both ends by thick alteration halos, allowing us to infer that intervals of intensely altered veins (thick veins or intervals with high vein density) were not recovered.

A semiquantitative scale ranging from 0 (no veins) to 5 (>20 intercepts with veins per 10 cm) was used to describe downhole variations in vein density (see **"Structural geology"** in the "Methods" chapter [Gillis et al., 2014e]). When considering the entire hole, the different density ranks occur at approximately equal frequency (Fig. F82). However, veins are not evenly distributed throughout Hole U1415J; vein density presents a marked and rather progressive increase downhole (Fig. F83). In summary, the upper two units of the hole (above 55.3 mbsf; Cores 345-U1415J-3R–5R, 8R, and 9R) have overall low vein density. Almost 40% of the recovered core length in these units has no veins, and <10% of the recovered length has high vein density (Classes 4 and 5). In contrast, Unit III (55.30–104.55 mbsf) is characterized by ~50% of the cored length exhibiting a high to very high alteration vein density.

Alteration vein dip

Many pieces recovered from Hole U1415J are long enough to allow measurement of vein dip. The entire range of dips, from shallow to vertical, is observed over the length of the hole (Fig. F84). At the scale of single pieces, we observed that the scatter in vein azimuth is also quite high. Accordingly, the orientation of alteration veins can be described as globally random; they form a network with no preferred orientation, consistent with hydraulic fracturing.

When comparing vein dips from the upper two units (I and II) with those from Unit III, dips preserve random orientation in the upper half of the hole and show two maxima, one at intermediate dips and a second subvertical maximum in Unit III (Fig. F85). This tendency is confirmed by observations at the scale of some larger pieces of core showing two preferred vein orientations (Fig. F80A).

No relationship between vein dip and vein mineralogy is recognized (Fig. F86). Chlorite and prehnite veins are present throughout the entire hole, whereas epidote and talc veins have a more restricted distribution primarily correlated with one of the zones of cataclasis in Core 345-U1415J-12R. Low-temperature zeolite veins are most common in Units I and II, with rare zeolite veins recognized as deep as 85 mbsf (Core 18R).

Crosscutting relationships and apparent vein chronology

Alteration veins are observed both in rock where the background alteration is poorly developed (Fig. F81B) and in highly altered core (Fig. F81A). Emplacement of alteration veins may therefore both predate and postdate an early stage of pervasive alteration. The mineralogy of the vein-filling material may change according to the nature of the crosscut mineral (e.g., the same vein may be filled with prehnite through plagioclase and serpentine when through olivine).

Apparent crosscutting relationships were frequently observed, but in detail it is hard to distinguish between actual crosscutting and branching relationships. Very few measurable offsets were identified. A systematic hierarchy in crosscutting relationships between veins with different fillings is hard to establish. Epidote, amphibole, and talc veins are generally early and predate the cataclastic deformation (if present). Chlorite veins are also generally affected by late deformation events but can be contemporaneous with cataclasis, as attested by tension gashes filled with chlorite. Prehnite veins can be deformed but most cut previous structures, although chlorite veins crosscutting prehnite veins were observed in some thin sections. Zeolite veins are clearly late, as they crosscut all other features.

Temporal evolution

Temporal evolution of structures recovered in Hole U1415J is, from oldest to youngest,

- Intrusion of moderately high MgO MORB magmas;
- Crystallization of olivine-rich cumulates and formation of magmatic layering;
- Development of magmatic foliation initially at high-melt fractions (>40%);
- Shearing/viscous compaction–accentuated foliation intensity in troctolitic intervals, accompanied by some hypersolidus crystal-plastic deformation in the mush;
- Likely static, near (above and below)-solidus annealing of plagioclase grain boundaries;
- A complex history of cataclastic faulting preserved in Unit III associated with either East Pacific Rise or Nazca-Cocos faulting including
  - Localized extensional cataclasis and fluid flow associated with faulting and low-temperature (<400°C) vein formation,
  - Vein intrusion,
  - Cataclasis,
  - Emplacement of dolerite dikes, and
  - Cataclasis
- Open fractures possibly associated with mass wasting; and
- Accumulation of 10–100 m thick slump blocks in a mass wasting deposit.

Paleomagnetism

Remanence data

Continuous measurements

Remanence measurements were made at 2 cm intervals on all archive-half core pieces longer than ~9 cm. All archive-half cores were subjected to stepwise alternating field (AF) demagnetization at 5 mT steps up to maximum peak fields of 80 mT. Remanence data and corresponding archive-half core point magnetic susceptibility data were filtered to preserve only data corresponding to the intervals where remanence measurements were made and to discard data obtained within 4.5 cm of piece ends.

For the purpose of characterization based on bulk magnetic parameters, the lithologies recovered from Hole U1415J are grouped into two categories. Group 1 consists of gabbroic rock (olivine-bearing gabbro, olivine gabbro, orthopyroxene-bearing olivine gabbro, gabbronorite, olivine-bearing gabbronorite, and oikocrystic gabbro) with a geometric mean natural remanent magnetization (NRM) intensity of 22.6 mA/m (range = 0.9–893 mA/m; n = 66) (Fig. F87). These values are considerably lower than geometric mean values for gabbroic samples (~1 A/m) reported by Gee and Kent (2007), who compiled NRM intensities (reduced to equatorial latitudes) from a range of sites where generally more evolved gabbros were encountered than during Expedition 345 (Varga et al., 2004; Gee et al., 1992, 1997; Kikawa and Pariso, 1991; Dick, Natland, and Miller, 1999; Kelemen, Kikawa, Miller, et al., 2004; Cannat, Karson, and Miller, 1995; Pariso et al., 1996; Blackman, Ildefonse, John, Ohara, Miller, MacLeod, and the Expedition 304/305 Scientists, 2006). Group 2 consists of troctolitic rock (troctolite, troctolitic olivine gabbro, and clinopyroxene oikocryst-bearing troctolite) with a geometric mean NRM intensity of 1.00 A/m (range = 109 mA/m to 8.140 A/m; n = 36) (Fig. F87). The geometric mean magnetic susceptibilities of Group 1 and 2 samples are 77.6×10^{-5} and 471.4×10^{-5} SI, respectively. Higher mean intensities and susceptibilities in the troctolitic rock most likely reflect variable degrees of serpentinization of these more olivine-rich lithologies leading to the production of secondary magnetite (see "Metamorphic petrology").

Remanent magnetization directions were calculated by principal component analysis (PCA; Kirschvink, 1980) at all measurement points along the core pieces where linear components could be identified on orthogonal vector plots of demagnetization data. Only principal components with a maximum angular deviation <10° were considered acceptable. Figure F88 shows representative examples of AF demagnetization behavior, and Figure F89 shows downhole variations in NRM and PCA pick inclinations, NRM and PCA pick intensities of magnetization, and low-field magnetic susceptibility measured using the Section Half Multisensor Logger (SHMSL). The majority of samples have an initially downward directed remanence, with evidence of inclination steepening caused by acquisition of a drilling-induced magnetization that is at least partially removed by low-field treatments (<15 mT). This is followed by removal of a moderately inclined, downward-directed component, typically by fields of 25–30 mT (Fig. F88). The mean inclination of this component is 37.5° (k = 20.7; α_{95} = 3.9°; n = 69), calculated using the Arason and Levi (2010) maximum likelihood method. During removal of this component, remanences typically migrate to the upper hemisphere, but no linear components with negative inclination are present. Instead, at demagnetization fields >30 mT remanence directions migrate back to the lower hemisphere and intensities of magnetization increase continuously up to the peak applied field of 80 mT (Fig. F88D, F88F). This behavior is due to acquisition of spurious, laboratory-imparted, anhysteretic remanent magnetization (ARM) along the z-axis of the superconducting rock magnetometer (SRM) system, which has been a characteristic problem of the SRM system observed during several IODP expeditions

(e.g., Teagle, Ildefonse, Blum, and the Expedition 335 Scientists, 2012). In rare examples, linear components decaying toward the origin without significant ARM acquisition are successfully isolated (Fig. F88G, F88H), although in some cases this final component is directed along the *z*-axis of the SRM (Fig. F88I) and must be treated with caution as a potential ARM. Unfortunately, clear examples of demagnetization unaffected by ARM acquisition are limited in number. In the majority of cases, anomalous ARMs in archive-half core samples prevent isolation of sufficient high-coercivity components to allow geological interpretation. The significance of the moderately inclined, downward-directed component with medium coercivity is discussed in **"Reliability of linear remanence components in superconducting rock magnetometer data."**

Discrete samples

Shipboard experiments were conducted on 27 discrete minicube samples from Hole U1415J. Two samples were AF demagnetized, one sample was thermally demagnetized, and the remaining 24 samples were subjected to two cycles of low-temperature demagnetization (LTD) followed by thermal demagnetization. In all cases, remanent magnetization directions were calculated by PCA for all demagnetization intervals where linear components could be identified on orthogonal vector plots of demagnetization data. Only principal components with a maximum angular deviation <10° were considered acceptable (Table T10). Two samples displayed erratic demagnetization data. One of these (Sample 345-U1415J-13R-1, 28 cm) came from a piece of white, highly altered troctolite with an exceptionally low NRM intensity (0.5 mA/m) in which intense alteration may have resulted in destruction of remanence-carrying phases. These samples are not discussed further. The remaining samples are divided into three categories according to demagnetization behavior and reliability:

1. Samples with large oikocrysts,
2. Samples with high unblocking temperature single components of magnetization, and
3. Samples with multicomponent remanences.

Samples with large oikocrysts

Five discrete samples were collected in gabbro and troctolite containing large pyroxene oikocrysts. Figure F90 shows orthogonal vector plots and stereographic projections of demagnetization data from two adjacent samples collected from Section 345-U1415J-8R-1. These discrete samples include large oikocrysts in the 8 cm^3 minicubes. Sample 8R-1, 80 cm, unblocks across the full range of temperatures (see inset normalized intensity decay curve in Fig. F90) and then displays a high unblocking temperature component that decays to the origin with a declination of 023.2° and inclination of –41.7°. In contrast, Sample 8R-1, 84 cm, has a significant drilling-induced magnetization that is removed by low-temperature demagnetization to leave a steeply inclined component that unblocks close to the magnetite Curie temperature (585°C), with a declination of 206.3° and an inclination of –79.5°. Hence, these two adjacent samples record significantly different magnetization directions, with a solid angle of 59° between PCA components. This is beyond the variability that may be attributed to unresolved secular variation, especially in samples that must have experienced nearly the same cooling history. The source of this variability in this heterogeneous, coarse-grained, oikocryst-bearing rock is uncertain. As a precaution, these data and those from the remaining three oikocrystic discrete samples are excluded from subsequent geological interpretation.

Samples with high unblocking temperature single components of magnetization

Samples from a wide range of lithologies (gabbroic and troctolitic) display well-defined linear remanence components following removal of variably developed drilling-induced magnetizations by low-temperature demagnetization or treatment by fields of <20 mT. A selection of typical examples is shown in the orthogonal vector plots of Figure F91. Some samples display a bend in the thermal demagnetization path (e.g., Samples 345-U1415J-5R-1, 130 cm, and 13R-1, 42 cm) at ~550°C before decaying linearly toward the origin. In such cases, the highest unblocking temperature segment has been picked as the characteristic remanence component.

Unblocking temperature spectra for these samples are remarkably similar to each other (Fig. F92), with ~70% of remanence lost within 40°C of the magnetite Curie temperature. Such discrete unblocking at high temperatures is characteristic of thermoremanent magnetizations carried by fine-grained (single domain and pseudosingle domain) grains of magnetite, and such remanences are unlikely to have been thermally overprinted after thermoremanent magnetization acquisition. Hence, we interpret these components as the primary magnetization in this rock, suitable for subsequent geological interpretation below.

Samples with multicomponent remanences

Three discrete samples in Hole U1415J display complex demagnetization paths that include multiple linear remanence components within each sample and are illustrated in Figure F93. Each exhibits a

high-temperature remanence component that unblocks above 500°/520°C (red labels) and an intermediate temperature component of nearly antipodal direction that unblocks between 425°/450°C and 500°/520°C (green labels). In addition, Sample 345-U1415J-23R-1, 22 cm, displays a third component that unblocks between 100° and 350°C (blue label) that is nearly parallel to the highest unblocking temperature component in this sample. These multiple, nearly antipodal components strongly suggest that remanence in these samples was acquired in different geomagnetic polarity periods. However, without independent reorientation of the core piece and recovery of original declinations it is impossible to define the original polarity of each component.

Similar multicomponent, multipolarity remanences have been seen previously in lower crustal rock recovered by drilling in slow-spreading crust along the Mid-Atlantic Ridge. Meurer and Gee (2002) reported three components of different polarities in gabbro from the Mid-Atlantic Ridge Kane Fracture Zone area sampled during ODP Leg 153 and interpreted these as components acquired across the Jaramillo Subchron and Matuyama and Brunhes Chrons during protracted construction of the lower crust by intrusion of thin sills. Morris et al. (2009) reported three component remanences from gabbro recovered from the footwall of Atlantis Massif sampled during IODP Expedition 304/305 and showed that the multicomponent remanences resulted from prolonged cooling of the section across the polarity reversals on either side of the Jaramillo Subchron. In both cases, the data provide constraints on the thermal history of the sampled sections. Alternatively, such remanences might result from successive phases of alteration and acquisition of thermoviscous magnetizations. Clearly, further sampling and detailed thermal demagnetization and rock magnetic experiments are now required in order to understand the distribution, origin, and geological significance of multicomponent remanences within gabbro recovered from Hole U1415J.

Reliability of linear remanence components in superconducting rock magnetometer data

As noted previously, archive-half core data from the SRM show a characteristic, moderately inclined, linear remanence component at AF steps below ~30 mT. This occurs after apparent removal of the drilling-induced remanence and prior to the acquisition of significant anhysteretic remanence at higher fields. In Hole U1415J, this component has a well-defined mean inclination of 37.5° (k = 20.7; α_{95} = 3.9°; n = 69). It is important, therefore, to determine whether this linear component is a distinct natural component of potential geological significance or whether it represents an artifact of spurious origin.

Figures F94 and F95 provide a comparison of LTD/thermal demagnetization data from discrete samples (measured using the JR6A spinner magnetometer) and the equivalent archive-half core demagnetization data measured using the SRM (within 2 cm of the discrete sample). Only one sample (345-U1415J-8R-3, 112–113 cm; Fig. F94A) shows a good correlation between these data types and is a sample with no significant drilling-induced magnetization or ARM. Such behavior in the archive-half core data is rare (seen at 14 out of 102 measuring points). The remaining samples show a variety of mismatches between archive-half core and discrete sample data. Sample 8R-3, 84 cm, has a single, well-defined remanence component with an upward-directed inclination (Fig. F94B). Equivalent archive-half core data display the common, moderately inclined, downward-directed component, but demagnetization data follow a great circle connecting the NRM direction to the final ARM direction that passes through the discrete sample direction without reaching a stable endpoint. Samples 5R-2, 61 cm (Fig. F94C), and 13R-1, 42 cm (Fig. F94A), have high unblocking temperature components with southeast declinations that are distinctly different from all parts of the equivalent archive-half core demagnetization paths. Sample 18R-1, 144 cm, displays two well-defined components with upward-directed inclinations and northeast declinations (Fig. F95B). The equivalent archive-half core data define a curved path on the lower hemisphere that connects the NRM and ARM directions without passing onto the upper hemisphere. Finally, archive-half core data corresponding to the clearest sample carrying a multicomponent remanence (Sample 23R-1, 22 cm) define a box-shaped demagnetization path on an orthogonal vector plot with no convincing linear segments between the drilling-related and ARM components (Fig. F95C). Hence, in the majority of cases, poor to no correlation exists between well-defined discrete sample magnetization directions and equivalent archive-half core data, which must therefore be treated with extreme caution.

Figure F96A shows a stereographic equal-area projection of the downward-directed linear component (present in the majority of archive-half core demagnetization data) from measurement points in the immediate vicinity of discrete samples. These data come from a range of core pieces that are azimuthally unconstrained in the core reference frame yet show significant clustering toward northwest–northeast declinations. Equivalent discrete sample high unblocking temperature components (Fig. F96B) are

widely scattered in declination, which is expected for data from core pieces that are free to rotate in the core barrel with both upward- and downward-directed inclinations. These data further confirm that the downward-directed linear component in the archive-half core samples has no geological significance.

Detailed previous studies of the geometry of drilling-induced remanences in ODP core sections have documented a pronounced radial drilling-induced magnetization component in addition to the dominant subvertical component. In particular, experiments conducted during ODP Leg 206 (Shipboard Scientific Party, 2003) on a suite of subsamples cut from a whole-round basaltic core piece in Hole 1256D demonstrated that drilling-related overprints result in a bias of archive-half core remanences toward northerly declinations in the core reference frame (i.e., toward the center of the core section). The preferred clustering of directions seen in Figure **F96A** may therefore result from the effects of this drilling-related bias.

Geological interpretation of inclination data from discrete samples

Inclinations of the highest unblocking temperature components in discrete samples from Hole U1415J are illustrated in Figure **F97.** Samples are presented sequentially rather than by depth scale to allow comparison of data from widely spaced sampling points. Data from oikocrystic rock are excluded. Both upward- and downward-directed inclinations were observed, with inclinations ranging from +55° to –73° (compared to an expected geocentric axial dipole field inclination of ±4.7°). Therefore, these data indicate substantial rotation of the cored section. A clear distinction exists between downward-directed magnetizations in the upper part of Hole U1415J (Cores 345-U1415J-3R through 8R) and upward-directed magnetizations in the lower part (Cores 9R through 23R), although data are insufficient to determine statistically robust mean inclinations. Within these groups, variation in inclination between samples may be due to incomplete averaging of geomagnetic secular variation at the sample level or to the effects of strong anisotropy in sampled lithologies. Sample 345-U1415J-13R-1, 42 cm, is inferred to be anomalous, as structural observations in this section suggest sampling of a block that has fallen in the hole.

With a subhorizontal expected direction of magnetization at Hess Deep, the magnetic polarity of this rock cannot be uniquely determined in the absence of reoriented core samples. However, U-Pb dating of zircons from samples collected in the immediate vicinity of Site U1415 during the JC21 site survey cruise yielded ages of 1.42–1.27 Ma (Rioux et al., 2012). These dates lie in the middle of reversed polarity Chron C1R (Cande and Kent, 1995), suggesting that any primary magnetizations preserved in the sampled rock should be of single, reversed polarity. Hence, coherent tectonic rotation of the sampled section is incompatible with observed upward- and downward-directed remanences. These data strongly suggest, therefore, that at least two displaced blocks with independent rotation histories have been sampled in Hole U1415J. The interval from the top of the hole to ~40 mbsf (Sample 345-U1415J-8R-3, 113 cm) should therefore be treated separately from the interval below 40 mbsf in lithologic and structural syntheses. This grouping is equivalent to lithologic Units II and III. In addition, the anomalously high inclination of Sample 9R-1, 47 cm, and the presence of shallowly inclined, high unblocking temperature components in multicomponent-bearing Samples 23R-1, 22 and 51 cm, potentially indicate that these data also come from blocks that have experienced differential rotation during emplacement to their present orientation (although data are too restricted to confirm this).

Magnetic susceptibility, natural remanence intensity, and Königsberger ratio

In mafic igneous rock, low-field magnetic susceptibility (k) is principally controlled by the volume concentration of magnetite. NRM variability is also controlled by variations in magnetite content but may also be influenced by variability in the magnitude of drilling-induced remanent magnetizations. The relation of NRM intensity and susceptibility is expressed by the Königsberger ratio (Q), which is defined as the ratio of remanent to induced magnetization in a rock (where induced magnetization equals the product of k (SI) and the geomagnetic field strength (A/m). Values of $Q > 1$ indicate that remanence dominates the magnetization of a rock unit.

Figure **F98** shows a log-log plot of NRM intensity against k for archive-half core and discrete samples from Hole U1415J, together with lines of equal Q calculated for a field of 25 A/m. The majority of samples plot above $Q = 1$ and close to $Q = 10$. This suggests that parts of the sampled section with higher NRM intensities may contribute a significant fraction to marine magnetic anomalies when in situ. However, caution is required in the interpretation of Q ratios calculated for these samples, as NRM intensities may be artificially increased by drilling-induced magnetization.

Anisotropy of magnetic susceptibility

Anisotropy of magnetic susceptibility (AMS) was measured from 27 discrete samples in Hole U1415J. Each sample was measured three times to check consistency and maintain quality control on any shipboard noise. These three measurements were averaged using a bootstrap approach to determine the average AMS eigenparameters for each discrete sample (Table **T11**). Eigenvectors and their associated bootstrapped uncertainties are illustrated on the equal-area stereographic projections in Figure **F99.** Susceptibility tensors are weakly to moderately anisotropic (corrected anisotropy degree [P'] < 1.40; mean = 1.13) (Jelinek, 1981). A majority of ellipsoid shapes are oblate, although all three shapes (triaxial, oblate, and prolate) are also represented in these samples (Fig. **F99C**). Bulk susceptibilities range from 1.26×10^{-4} to 5.87×10^{-2} SI, with an average of 7.35×10^{-3} SI that indicates predominance of ferromagnetic mineral contributions to the AMS signal in most samples.

Five samples have large (>25°) bootstrapped confidence ellipses around their eigenvectors, suggesting weak signals and inconsistent repeated measurements from the same sample. These five samples (345-U1415J-3R-1, 26 cm; 8R-3, 68 cm; 12R-1, 109 cm; 21R-1, 57 cm; and 21R-1, 120 cm) have an average bulk susceptibility of 2.40×10^{-4} SI, suggesting that some paramagnetic minerals may contribute to the signal. These samples are not shown in Figures **F99A** and **F99B,** and they are also disregarded from further geological interpretation until the AMS source can be better determined.

Structural measurements of magmatic foliation in the upper portion of Hole U1415J show close agreement with the AMS fabrics (minimum eigenvector [k_{min}] near the magmatic foliation pole) and indicate well-developed fabrics that consistently dip eastward within the core reference frame (Fig. **F99A**). However, intersample fabric consistency is not evident deeper in Hole U1415J (below ~45.66 mbsf), and a wider range of eigenvector directions is illustrated in Figure **F99B.** Overall, AMS magnetic foliation is nearly parallel to the magmatic foliation (average solid angle between k_{min} and magmatic foliation pole <30°), with only one sample (345-U1415J-18R-1, 144 cm) showing poor agreement with the structural fabric (solid angle = 66°).

Inorganic geochemistry

Chemical analyses were performed on 1 aphyric basalt and 24 plutonic rocks (including 14 orthopyroxene- and olivine-bearing gabbroic rocks), 8 samples from troctolite-dominated intervals, and 2 samples of drill cuttings. Sample selection was based on discussion among representatives from all expertise groups within the shipboard scientific party. Inductively coupled plasma–atomic emission spectroscopy (ICP-AES) was used for determining major and trace element concentrations, and gas chromatography was used for S, H_2O, and CO_2 quantification. Selected data are shown in Figures **F100, F101, F102,** and **F103** and fully reported in Table **T1** in the "Geochemistry summary" chapter (Gillis et al., 2014c). Major and trace elements are reported on a volatile-free basis.

Aphyric basalt

One aphyric basalt was sampled from the rubble unit in ghost Core 345-U1415J-2G (Sample 345-U1415J-2G-1, 0–13 cm). The basalt is strongly altered (~30%; see **"Metamorphic petrology"** and thin section descriptions in **"Core descriptions"**), with a loss on ignition (LOI) of 1.86 wt% and 1.8 wt% H_2O, and is characterized by a relatively high Mg# of 69, high Cr (520 ppm) and Ni (210 ppm) contents, and low incompatible trace element contents (e.g., Y = 24 ppm). Major element geochemistry defines this rock as a tholeiitic basalt, similar in composition to the primitive MORB previously sampled in the Hess Deep area at Site 894 (Shipboard Scientific Party, 1993) and at the more primitive end of the East Pacific Rise basalt recovered along the Northern Escarpment of the Hess Deep Rift (Mg# = 44–66; Stewart et al., 2002).

Gabbroic rock

Olivine gabbro, clinopyroxene oikocryst-bearing gabbro, and gabbro

The analyzed gabbroic samples comprise three gabbro samples, one clinopyroxene oikocryst-bearing olivine gabbro sample, and nine olivine-bearing and olivine gabbro samples (>5% olivine); minor orthopyroxene (0.1%–4%) is reported in the gabbroic rock sampled in Intervals 5, 11, 32, 38, and 42 in lithologic Unit II (see **"Igneous petrology"** and thin section descriptions in **"Core descriptions"**). All samples are altered to various degrees, with LOIs ranging from 1.1 to 5.9 wt%. The water content (1.2–5.3 wt%) correlates with the LOI (Fig. **F100**). CO_2 content is low (0.01–0.4 wt%) and does not appear to correlate with any of the other analyzed elements or with any igneous and alteration features reported in the thin section descriptions. Sulfur is highly variable (160–1740 ppm) in the analyzed gabbro. Minor pyrite, pentlandite, and chalcopyrite were observed in Hole U1415J (see **"Metamorphic**

petrology"). The observed variations in sulfur compositions are probably related to the amount of sulfide in the analyzed samples.

Hole U1415J gabbro has primitive compositions, with Mg# 81–87 and 130–490 ppm Ni (Fig. F101). The gabbro overlaps in composition of major and trace elements (Figs. F102, F103) with the gabbroic rocks sampled in Hole U1415I, with 45–50 wt% SiO_2, 0.1–0.3 wt% TiO_2, and 1.6–6.5 ppm Y. No systematic compositional variations were observed downhole (Fig. F101) or between the oikocryst-bearing gabbro, olivine gabbro, and gabbro samples (see Table T1 in the "Geochemistry summary" chapter [Gillis et al., 2014c]). Compared to the relative minor changes in Mg#, strong variations in CaO, Al_2O_3, and Na_2O as well as in trace element compositions, in particular Sc, were observed (e.g., Al_2O_3 = 13–25 wt%) (Fig. F102). These variations mainly reflect local changes in the primary plagioclase- and clinopyroxene-dominated modal composition of the samples, with variable amounts of olivine. Na_2O and Al_2O_3 are concentrated mainly in plagioclase, CaO and Sc are mainly concentrated in clinopyroxene (the former is abundant in plagioclase also), and olivine is depleted in all of these elements.

The gabbroic rocks sampled in Hole U1415J have Cr compositions ranging from 200 to 850 ppm, which is typical of primitive gabbroic series (e.g., Cannat, Karson, Miller, et al., 1995; Godard et al., 2009), except for three samples characterized by low Cr concentrations (<100 ppm). These low concentrations may reflect a change in the mobility of Cr during alteration; the Cr-depleted samples were recovered between 99 and 104 mbsf, where cataclasites and high-temperature alteration (500°–600°C) are reported (see "Metamorphic petrology"). Three samples are distinguished by their high Cr content (2100–2500 ppm) (Fig. F101). These variations could not be correlated with any igneous and alteration features observed in thin sections (see thin section descriptions in "Core descriptions") or with other analyzed elements. These high Cr concentrations may reflect the occurrence of Cr-rich clinopyroxene and/or of a Cr-rich minor phase (e.g., chromite) in the samples. The origin of the high Cr contents of these olivine gabbro samples will be further investigated using onshore technical facilities (e.g., by electron probe microanalyzer).

Troctolitic intervals

Eight samples were collected from the troctolite-dominated intervals from lithologic Units II and III: three clinopyroxene oikocryst-bearing troctolite samples (Intervals 24, 38, and 47) in Unit II and two troctolite samples (Intervals 58 and 73), one clinopyroxene-bearing troctolite sample (Interval 66), one olivine-bearing anorthosite sample, and one chromitite sample (345-U1415J-18R-1, 67–72 cm; see "Igneous petrology") in Unit III. The LOI (2.7–9.1 wt%) and H_2O content (2.2–7.9 wt%) of the troctolitic samples are correlated (Fig. F100); on average, they are higher than that of Hole U1415J gabbro. The highest water contents were observed in samples having the highest olivine content in their primary assemblage (45%–50% olivine in Samples 345-U1415J-13R-1, 38–44 cm, and 19R-1, 15–19 cm). These samples reflect the water-rich composition of the alteration minerals replacing olivine, such as serpentine (~13 wt% H_2O) (see "Metamorphic petrology" and thin section descriptions in "Core descriptions"). CO_2 (0.01–0.3 wt%) and sulfur (310–1160 ppm) contents are highly variable and similar to those of Hole U1415J gabbro.

Olivine-bearing anorthosite, troctolite, and clinopyroxene oikocryst-bearing troctolite overlap in composition with Hole U1415J gabbro for most major elements (Figs. F101, F102). Similar to gabbro, they display highly variable CaO, Na_2O, and Al_2O_3 contents that mainly reflect the variable plagioclase/clinopyroxene ratios in the analyzed samples. For example, olivine-bearing anorthosite is distinguished by its high Al_2O_3 content (26.8 wt%) compared to Hole U1415J troctolitic samples (Al_2O_3 = 12.0–21.4 wt%). Olivine-bearing anorthosite, troctolite, and clinopyroxene oikocryst-bearing troctolite also overlap in composition with gabbro for Cr (365–680 ppm), Zn (18–48 ppm), and Cu (11–110 ppm), although plagioclase-rich olivine-bearing samples from the cataclasite interval at the bottom of Unit II (~38 mbsf) have low Cr contents (<35 ppm) (Fig. F101). In contrast to the Cr-depleted gabbros sampled at the bottom of Hole U1415J, no indication is apparent of a change in the conditions of alteration in these samples compared to neighboring samples; only the presence of talc could indicate a different alteration pathway that may have affected Cr mobility (see "Metamorphic petrology" and thin section descriptions in "Core descriptions"). It must be noted also that gabbro (Sample 345-U1415J-8R-3, 35–38 cm) sampled next to the most Cr-depleted troctolite (Sample 8R-3, 26–29 cm) has a composition typical of the gabbro sampled in Hole U1415J (590 ppm), indicating that the Cr composition in this rock is controlled by highly localized processes.

Troctolite has Mg# ranging from 81 to 89 and high Ni contents (260–1490 ppm) (see Table T1 in the "Geochemistry summary" chapter [Gillis et al., 2014c]). Ni is highly concentrated in olivine, and the most Ni rich samples are also the ones that have the

highest fraction of olivine in their primary assemblage (e.g., Samples 345-U1415J-13R-1, 39–41 cm, and 19R-1, 18–19 cm; see thin section descriptions in "Core descriptions" and Table T1 in the "Geochemistry summary" chapter [Gillis, et al., 2014c]). Troctolite has low TiO_2 (<0.1 wt%); Sc (<13 ppm); and V, Y, and Zr (<20 ppm) compared to Hole U1415J gabbro (Fig. F103; see Table T1 in the "Geochemistry summary" chapter [Gillis, et al., 2014c]). These low concentrations, together with their refractory composition, suggest that the troctolite probably precipitated from less evolved melts than the neighboring gabbro.

Chromitite (Sample 345-U1415J-18R-1, 67–72 cm) is distinguished by its enrichment in Fe_2O_3 (30.5 wt%) and MgO (22.8 wt%) and depletion in SiO_2 (31 wt%) and TiO_2 (0.02 wt%) compared to other rock sampled in the troctolitic intervals in Hole U1415J. These compositions are consistent with its modal composition (60% olivine and 40% oxide). This sample was interpreted as a chromitite whose composition was modified during late hydrothermal alteration (see "Igneous petrology" and "Metamorphic petrology"). Chemical data indicate that the oxides present in the sample are Fe rich and Ti poor, probably magnetite. The sample's trace element composition is similar to that of Hole U1415J troctolite, including its Cr content (640 ppm).

Drill cuttings

Two samples of sandy material were selected from ghost Core 345-U1415J-2G in Unit I (see "Metamorphic petrology"). The samples comprise abundant altered rock material and have high LOI (2.7–3.3 wt%) and H_2O (3.4–3.9 wt%) and CO_2 (0.07–0.14 wt%) contents, even when compared to the altered drilling-induced disaggregated gabbro sampled in Hole U1415I. The samples of drill cuttings have lower Mg# (76), lower Ni (150 ppm) content, and higher TiO_2 (0.6–0.7 wt%) and incompatible trace element (e.g., Y = ~12–13 ppm) contents compared to plutonic rock sampled in Hole U1415J, which suggests that they comprise more evolved gabbroic material. Compared to all of the plutonic rock sampled at Site U1415, these drill cuttings are characterized by enrichment in Na_2O (2.6–3 wt%) and Ba (70–100 ppm), indicative of the presence of higher fractions of altered minerals (Na-rich albitized plagioclase and chlorite) and, probably, contamination by the Ba- and clay-rich drilling muds mixed with seawater used during coring operations. Therefore, these results should be treated with caution for petrogenetic interpretations.

Physical properties

Physical properties of the gabbroic rock recovered in Hole U1415J were characterized through a series of measurements on whole-core sections, half-core sections, half-core pieces, and discrete samples as described in "Physical properties" in the "Methods" chapter (Gillis et al., 2014e). We measured gamma ray attenuation (GRA) density and magnetic susceptibility on the Whole-Round Multisensor Logger (WRMSL); natural gamma radiation (NGR) on the Natural Gamma Ray Logger (NGRL); point magnetic susceptibility, reflectance spectroscopy, and colorimetry on the SHMSL; and thermal conductivity, *P*-wave velocity (V_P), density, and porosity on discrete samples. Rock names reported in data tables correspond to the primary lithologies assigned by the igneous group (Tables T12, T13). Data are summarized as a function of depth in Figure F104; data from ghost cores (i.e., WRMSL, SHMSL, and only one discrete sample from Core 345-U1415J-7G) are not shown in this figure.

Raw GRA density, magnetic susceptibility, reflectance spectrometry, and colorimetry data were uploaded to the Laboratory Information Management System database and subsequently filtered following the procedures described in "Physical properties" in the "Methods" chapter (Gillis et al., 2014e) to remove spurious points that correspond to empty intervals in the liner, broken pieces, and pieces that were too small. Both raw and filtered data are provided in PHYSPROP in "Supplementary material."

Multisensor core logger data

Natural gamma radiation

In Hole U1415J, 16 of the 30 core sections were measured on the NGRL; other sections contained pieces too small to provide reliable data with this instrument. NGR is, overall, very low (0–1.53 cps), which is significantly lower than background level (~5 cps). NGR values in ghost cores are in the same range as those in routine RCB cores.

Gamma ray attenuation density

In Hole U1415J, 18 of the 30 core sections were measured in the WRMSL. GRA density measurements are volume dependent, and filtered GRA data range between 1.27 and 2.85 g/cm^3, with an average of 2.35 g/cm^3 (85% of the values are <2.5 g/cm^3 and are not shown in Fig. F104). These values are generally significantly lower than bulk density measured on discrete samples in the same cores.

Magnetic susceptibility

Magnetic susceptibility was measured on both the WRMSL (16 core sections) and SHMSL (26 core sections). The whole-round core measurements are volume measurements that give an average apparent susceptibility value over an 8 cm long interval, whereas SHMSL values are given by point measurements (see **"Physical properties"** in the "Methods" chapter [Gillis et al., 2014e]). When measured on whole-round cores, magnetic susceptibility is generally underestimated, with values significantly lower than point magnetic susceptibility (Fig. **F104**). The mean magnetic susceptibility of rock recovered in Hole U1415J is very low (~750 × 10^{-5} ± 1450 × 10^{-5} SI for point magnetic susceptibility), reflecting the absence of magmatic Fe-Ti oxides. The only exceptions to this are two intervals (345-U1415J-18R-1, 67–71 cm, and 21R-1, 4–16 cm) that contain Fe oxide–rich material (presumably altered chromitite; see **"Igneous petrology"**), in which WRMSL magnetic susceptibility has been corrected (see Fig. **F20** in the "Methods" chapter [Gillis et al., 2014e]) and is as high as ~14,400 × 10^{-5} SI in Section 345-U1415J-18R-1 (Piece 9) and ~25,000 × 10^{-5} SI in Section 21R-1 (Piece 2).

Reflectance spectroscopy and colorimetry

Reflectance spectroscopy and colorimetry data were systematically acquired, together with point magnetic susceptibility data, using the SHMSL with a measurement interval of 1 cm. As described in **"Physical properties"** in the "Hole U1415I" chapter (Gillis et al., 2014d), absolute values of chromaticity parameters a* and b* are not reliable. The mean value of the lightness (L*) is ~43 ± 8.

Discrete sample measurements

Moisture and density

Bulk density, grain density, and porosity were calculated from measurements on 25 cubic samples (2 cm × 2 cm × 2 cm) taken from the working-half sections (Table **T12;** Fig. **F104**). These samples comprise four rock types: gabbronorite, gabbro, olivine gabbro, and troctolite. Average bulk density and grain density are 2.83 ± 0.08 and 2.86 ± 0.07 g/cm^3, respectively, and are similar to the densities measured at Hess Deep (Site 894) (Fig. **F105**). Olivine-rich lithologies (olivine gabbro and troctolite) have average grain densities (2.92 ± 0.04 g/cm^3) that are ~0.1 g/cm^3 lower than gabbro and gabbronorite (2.81 ± 0.06 g/cm^3). This difference reflects the average differences in background alteration for these lithologies, which is primarily related to olivine contents because olivine is generally more strongly altered than plagioclase and clinopyroxene (Fig. **F106;** see also **"Metamorphic petrology"**). Porosity is generally low, ranging from 1.7% to 4.1%, and generally increases downhole (Fig. **F104**).

P-wave velocity

The same 25 cubic samples used for moisture and density analyses were measured for V_P along the three principal directions (*x*, *y*, and *z*) in the core reference frame (see Fig. **F2** in the "Methods" chapter [Gillis et al., 2014e]). Results are listed in Table **T12** and plotted in Figures **F104** and **F105.** Average V_P is 6.12 ± 0.38 km/s, and the apparent anisotropy varies from 0.8% to 5.5%. As detailed in ***"P*-wave velocity"** in the "Hole U1415I" chapter (Gillis et al., 2014d) the precision of our V_P measurements is ~2%. Hence, the relatively low measured apparent anisotropies should be treated with caution.

Results for all samples from Site U1415 measured so far (Holes U1415I and U1415J) are compared in Fig. **F105,** with V_P and grain density measurements made during previous ODP legs and IODP expeditions on gabbroic samples from fast-spreading and slow-spreading oceanic crust. V_P values are consistent with measurements made at Hess Deep (Site 894). V_P measurements made on board over time show a large dispersion, which probably cannot be solely explained by petrophysical variations (note that, for example, the ~1 to 1.5 km/s difference in velocity between Hole 735B data and data from other slow-spreading crust locations even though they have similar composition, porosity, and alteration). These data should therefore be treated with caution.

As expected, measured V_P at room pressure depends primarily on porosity (Fig. **F107**). Because we avoided taking discrete samples with metamorphic or alteration veins, the progressive increase of porosity downhole (Fig. **F104**) primarily reflects increasing fracturing in the sample groundmass, as is also suggested by the general correlation between V_P/porosity and the macroscopically estimated intensity of cataclastic deformation (Fig. **F108**).

Thermal conductivity

Thermal conductivity was measured in 11 gabbroic rock samples (≥8 cm long and representative of the various recovered lithologies) taken at irregularly spaced intervals in Hole U1415J (Table **T13;** Fig. **F104**). Measured values range from 2.1 to 4.1 W/(m·K) and are averages of 6–20 measurements for each piece, with a standard deviation <2.8% (average = 0.9%). The relatively high thermal conductivity values measured in two troctolite samples from the

bottom of the hole (3.4 and 4.1 W/[m·K]) might be explained by the presence of relatively abundant magnetite (~5.3 W/[m·K]) in altered olivine.

We attempted to measure anisotropy in a foliated olivine-bearing gabbronorite and a foliated troctolite (Sections 345-U1415J-5R-2A [Piece 2] and 18R-1A [Piece 14]) by using the shorter probe (see **"Physical properties"** in the "Methods" chapter (Gillis et al., 2014e), collecting two series of measurements with the probe needle aligned parallel and perpendicular to the foliation. The apparent anisotropies are 3.6% in the olivine-bearing gabbronorite and 0.1% in the troctolite. These values are lower than or close to the measurement standard deviations (Table **T13**) and are probably not meaningful. The small probe tends to return less stable values than the large probe, which makes the exercise of estimating the anisotropy of thermal conductivity difficult in this type of lithology.

References

Abe, N., 2011. Petrology of podiform chromitite from the ocean floor at the 15°20′N FZ in the MAR, Site 1271, ODP Leg 209. *J. Mineral. Petrol. Sci.,* 106(2):97–102. **doi:10.2465/jmps.101022**

Abily, B., 2011. Caractéristiques pétrographique, géochimique et structurale de la section crustale profonde de l'ophiolite d'Oman: implications pour la genèse des magmas et le fonctionnement des chambres magmatiques à l'aplomb d'un centre d'expansion océanique [Ph.D. thesis]. Univ. Toulouse, France. **http://tel.archives-ouvertes.fr/docs/00/62/75/53/PDF/Manuscrit_de_these_Abily_Benedicte_16_Mars_2011.pdf**

Abily, B., Ceuleneer, G., and Launeau, P., 2011. Synmagmatic normal faulting in the lower oceanic crust: evidence from the Oman ophiolite. *Geology,* 39(4):391–394. **doi:10.1130/G31652.1**

Arai, S., and Matsukage, K., 1996. Petrology of the gabbro-troctolite-peridotite complex from Hess Deep, equatorial Pacific: implications for mantle–melt interaction within the oceanic lithosphere. *In* Mével, C., Gillis, K.M., Allan, J.F., and Meyer, P.S. (Eds.), *Proc. ODP, Sci. Results,* 147: College Station, TX (Ocean Drilling Program), 135–155. **doi:10.2973/odp.proc.sr.147.008.1996**

Arason, P., and Levi, S., 2010. Maximum likelihood solution for inclination-only data in paleomagnetism. *Geophys. J. Int.,* 182(2):753–771. **doi:10.1111/j.1365-246X.2010.04671.x**

Blackman, D.K., Ildefonse, B., John, B.E., Ohara, Y., Miller, D.J., Abe, N., Abratis, M., Andal, E.S., Andreani, M., Awaji, S., Beard, J.S., Brunelli, D., Charney, A.B., Christie, D.M., Collins, J., Delacour, A.G., Delius, H., Drouin, M., Einaudi, F., Escartín, J. Frost, B.R., Früh-Green, G., Fryer, P.B., Gee, J.S., Godard, M., Grimes, C.B., Halfpenny, A., Hansen, H.-E., Harris, A.C., Tamura, A., Hayman, N.W., Hellebranc, E., Hirose, T., Hirth, J.G., Ishimaru, S., Johnson, K.T.M., Karner, G.D., Linek, M., MacLeod, C.J., Maeda, J., Mason, O.U., McCaig, A.M., Michibayashi, K., Morris, A., Nakagawa, T., Nozaka, T., Rosner, M., Searle, R.C., Suhr, G., Tominaga, M., von der Handt, A., Yamasaki, T., and Zhao, X., 2011. Drilling constraints on lithospheric accretion and evolution at Atlantis Massif, Mid-Atlantic Ridge, 30°N. *J. Geophys. Res.: Solid Earth,* 116(B7):B07103. **doi:10.1029/2010JB007931**

Blackman, D.K., Ildefonse, B., John, B.E., Ohara, Y., Miller, D.J., MacLeod, C.J., and the Expedition 304/305 Scientists, 2006. *Proc IODP,* 304/305: College Station, TX (Integrated Ocean Drilling Program Management International, Inc.). **doi:10.2204/iodp.proc.304305.2006**

Butcher, A.R., Young, I.M., and Faithfull, J.W., 1985. Finger structures in the Rhum complex. *Geol. Mag.,* 122(5):491–502. **doi:10.1017/S001675680003541X**

Cande, S.C., and Kent, D.V., 1995. Revised calibration of the geomagnetic polarity timescale for the Late Cretaceous and Cenozoic. *J. Geophys. Res.: Solid Earth,* 100(B4):6093–6095. **doi:10.1029/94JB03098**

Cannat, M., Karson, J.A., Miller, D.J., et al., 1995. *Proc. ODP, Init. Repts.,* 153: College Station, TX (Ocean Drilling Program). **doi:10.2973/odp.proc.ir.153.1995**

Coogan, L.A., Gillis, K.M., MacLeod, C.J., Thompson, G.M., and Hékinian, R., 2002. Petrology and geochemistry of the lower ocean crust formed at the East Pacific Rise and exposed at Hess Deep: a synthesis and new results. *Geochem., Geophys., Geosyst.,* 3(11):8604. **doi:10.1029/2001GC000230**

Dick, H.J.B., Natland, J.H., Miller, D.J., et al., 1999. *Proc. ODP, Init. Repts.,* 176: College Station, TX (Ocean Drilling Program). **doi:10.2973/odp.proc.ir.176.1999**

Donaldson, C.H., 1974. Olivine crystal types in harrisitic rocks of the Rhum pluton and in Archean spinifex rocks. *Geol. Soc. Am. Bull.,* 85(11):1721–1726. **doi:10.1130/0016-7606(1974)85<1721:OCTIHR>2.0.CO;2**

Donaldson, C.H., 1976. An experimental investigation of olivine morphology. *Contrib. Mineral. Petrol.,* 57(2):187–213. **doi:10.1007/BF00405225**

Donaldson, C.H., 1977. Laboratory duplication of comb layering in the Rhum pluton. *Mineral. Mag.,* 41(319):323–336. **doi:10.1180/minmag.1977.041.319.03**

Expedition 304/305 Scientists, 2006. Site U1309. *In* Blackman, D.K., Ildefonse, B., John, B.E., Ohara, Y., Miller, D.J., MacLeod, C.J., and the Expedition 304/305 Scientists, *Proc. IODP,* 304/305: College Station, TX (Integrated Ocean Drilling Program Management International, Inc.). **doi:10.2204/iodp.proc.304305.103.2006**

Faithfull, J.W., 1985. The lower eastern layered series of Rhum. *Geol. Mag.,* 122(5):459–468. **doi:10.1017/S001675680003538X**

Feig, S.T., Koepke, J., and Snow, J.E., 2006. Effect of water on tholeiitic basalt phase equilibria: an experimental study under oxidizing conditions. *Contrib. Mineral. Petrol.,* 152(5):611–638. **doi:10.1007/s00410-006-0123-2**

Feig, S.T., Koepke, J., and Snow, J.E., 2010. Effect of oxygen fugacity and water on phase equilibria of a hydrous tholeiitic basalt. *Contrib. Mineral. Petrol.,* 160(4):551–568. **doi:10.1007/s00410-010-0493-3**

Früh-Green, G.L., Plas, A., and Dell'Angelo, L.N., 1996. Mineralogic and stable isotope record of polyphase alteration of upper crustal gabbros of the East Pacific Rise (Hess Deep, Site 894). *In* Mével, C., Gillis, K.M., Allan, J.F., and Meyer, P.S. (Eds.), *Proc. ODP, Sci. Results,* 147: College Station, TX (Ocean Drilling Program), 235–254. **doi:10.2973/odp.proc.sr.147.015.1996**

Gee, J., Natland, J.H., Hurst, S.D., and Nilsson, K., 1992. Magnetic properties of ocean crust samples from Hess Deep: implications for marine magnetic anomalies. *Eos, Trans. Am. Geophys. Union,* 73:490.

Gee, J.S., and Kent, D.V., 2007. Source of oceanic magnetic anomalies and the geomagnetic polarity timescale. *In* Kono, M. (Ed.), *Treatise on Geophysics: Geomagnetism* (Vol. 5): Amsterdam (Elsevier), 455–507.

Gee, J.S., Lawrence, R.M., and Hurst, S.D., 1997. Remanence characteristics of gabbros from the MARK area: implications for crustal magnetization. *In* Karson, J.A., Cannat, M., Miller, D.J., and Elthon, D. (Eds.), *Proc. ODP, Sci. Results,* 153: College Station, TX (Ocean Drilling Program), 429–436. **doi:10.2973/odp.proc.sr.153.042.1997**

Gillis, K.M., Snow, J.E., Klaus, A., Guerin, G., Abe, N., Akizawa, N., Ceuleneer, G., Cheadle, M.J., Adrião, Á., Faak, K., Falloon, T.J., Friedman, S.A., Godard, M.M., Harigane, Y., Horst, A.J., Hoshide, T., Ildefonse, B., Jean, M.M., John, B.E., Koepke, J.H., Machi, S., Maeda, J., Marks, N.E., McCaig, A.M., Meyer, R., Morris, A., Nozaka, T., Python, M., Saha, A., and Wintsch, R.P., 2014a. Geochemistry summary. *In* Gillis, K.M., Snow, J.E., Klaus, A., and the Expedition 345 Scientists, *Proc. IODP,* 345: College Station, TX (Integrated Ocean Drilling Program). **doi:10.2204/iodp.proc.345.114.2014**

Gillis, K.M., Snow, J.E., Klaus, A., Guerin, G., Abe, N., Akizawa, N., Ceuleneer, G., Cheadle, M.J., Adrião, Á., Faak, K., Falloon, T.J., Friedman, S.A., Godard, M.M., Harigane, Y., Horst, A.J., Hoshide, T., Ildefonse, B., Jean, M.M., John, B.E., Koepke, J.H., Machi, S., Maeda, J., Marks, N.E., McCaig, A.M., Meyer, R., Morris, A., Nozaka, T., Python, M., Saha, A., and Wintsch, R.P., 2014. Methods. *In* Gillis, K.M., Snow, J.E., Klaus, A., and the Expedition 345 Scientists, *Proc. IODP,* 345: College Station, TX (Integrated Ocean Drilling Program). **doi:10.2204/iodp.proc.345.102.2014**

Gillis, K., Mével, C., Allan, J., et al., 1993. *Proc. ODP, Init. Repts.,* 147: College Station, TX (Ocean Drilling Program). **doi:10.2973/odp.proc.ir.147.1993**

Godard, M., Awaji, S., Hansen, H., Hellebrand, E., Brunelli, D., Johnson, K., Yamasaki, T., Maeda, J., Abratis, M., Christie, D., Kato, Y., Mariet, C., and Rosner, M., 2009. Geochemistry of a long in-situ section of intrusive slow-spread oceanic lithosphere: results from IODP Site U1309 (Atlantis Massif, 30°N Mid-Atlantic-Ridge). *Earth Planet. Sci. Lett.,* 279(1–2):110–122. **doi:10.1016/j.epsl.2008.12.034**

Grove, T.L., and Bryan, W.B., 1983. Fractionation of pyroxene-phyric MORB at low pressure: an experimental study. *Contrib. Mineral. Petrol.,* 84(4):293–309. **doi:10.1007/BF01160283**

Hanna, H.D., 2004. Geochemical variations in basaltic glasses from an incipient rift and upper level gabbros from Hess Deep, eastern equatorial Pacific [M.Sc. thesis]. Duke Univ., Durham.

Hékinian, R., Bideau, D., Francheteau, J., Cheminee, J.L., Armijo, R., Lonsdale, P., and Blum, N., 1993. Petrology of the East Pacific Rise crust and upper mantle exposed in Hess Deep (eastern equatorial Pacific). *J. Geophys. Res.: Solid Earth,* 98(B5):8069–8094. **doi:10.1029/92JB02072**

Hort, M., 1998. Abrupt change in magma liquidus temperature because of volatile loss or magma mixing: effects on nucleation, crystal growth and thermal history of the magma. *J. Petrol.,* 39(5):1063–1076. **doi:10.1093/petroj/39.5.1063**

Jelinek, V., 1981. Characterization of the magnetic fabric of rocks. *Tectonophysics,* 79(3–4):T63–T67. **doi:10.1016/0040-1951(81)90110-4**

Kelemen, P.B., Kikawa, E., Miller, D.J., et al., 2004. *Proc. ODP, Init. Repts.,* 209: College Station, TX (Ocean Drilling Program). **doi:10.2973/odp.proc.ir.209.2004**

Kikawa, E., and Pariso, J.E., 1991. Magnetic properties of gabbros from Hole 735B, Southwest Indian Ridge. *In* Von Herzen, R.P., Robinson, P.T., et al., *Proc. ODP, Sci. Results,* 118: College Station, TX (Ocean Drilling Program), 285–307. **doi:10.2973/odp.proc.sr.118.148.1991**

Kirchner, T.M., and Gillis, K.M., 2012. Mineralogical and strontium isotopic record of hydrothermal processes in the lower ocean crust at and near the East Pacific Rise. *Contrib. Mineral. Petrol.,* 164(1):123–141 **doi:10.1007/s00410-012-0729-5**

Kirschvink, J.L., 1980. The least-squares line and plane and the analysis of palaeomagnetic data. *Geophys. J. R. Astron. Soc.,* 62(3):699–718. **doi:10.1111/j.1365-246X.1980.tb02601.x**

Lippard, S.J., Shelton, A.W., and Gass, I.G., 1986. *The Ophiolite of Northern Oman.* Mem.—Geol. Soc. London, 11.

Lofgren, G., 1980. Experimental studies on the dynamic crystallization of silicate melts. *In* Hargraves, R.B. (Ed.), *Physics of Magmatic Processes:* Princeton (Princeton Univ. Press), 487–565.

Lofgren, G.E., and Donaldson, C.H., 1975. Curved branching crystals and differentiation in comb-layered rocks. *Contrib. Mineral. Petrol.,* 49(4):309–319. **doi:10.1007/BF00376183**

Meurer, W.P., and Gee, J., 2002. Evidence for the protracted construction of slow-spread oceanic crust by small magmatic injections. *Earth Planet. Sci. Lett.,* 201(1):45–55. **doi:10.1016/S0012-821X(02)00660-X**

Miller, D.J., Iturrino, G.J., and Christensen, N.I., 1996. Geochemical and petrological constraints on velocity behavior of lower crustal and upper mantle rocks from the fast-spreading ridge at Hess Deep. *In* Mével, C., Gillis, K.M., Allan, J.F., and Meyer, P.S. (Eds.), *Proc. ODP, Sci.*

Results, 147: College Station, TX (Ocean Drilling Program), 477–490. doi:10.2973/odp.proc.sr.147.028.1996

Morris, A., Gee, J.S., Pressling, N., John, B.E., MacLeod, C.J., Grimes, C.B., and Searle, R.C., 2009. Footwall rotation in an oceanic core complex quantified using reoriented Integrated Ocean Drilling Program core samples. *Earth Planet. Sci. Lett.,* 287(1–2):217–228. doi:10.1016/j.epsl.2009.08.007

Natland, J.H., and Dick, H.J.B., 2009. Paired melt lenses at the East Pacific Rise and the pattern of melt flow through the gabbroic layer at a fast-spreading ridge. *Lithos,* 112(1–2):73–86. doi:10.1016/j.lithos.2009.06.017

Nozaka, T., and Fryer, P., 2011. Alteration of the oceanic lower crust at a slow-spreading axis: insight from vein-related zoned halos in olivine gabbro from Atlantis Massif, Mid-Atlantic Ridge. *J. Petrol.,* 52(4):643–664. doi:10.1093/petrology/egq098

Pallister, J.S., and Hopson, C.A., 1981. Samail ophiolite plutonic suite: field relations, phase variation, cryptic variation and layering, and a model of a spreading ridge magma chamber. *J. Geophys. Res.: Solid Earth,* 86(B4):2593–2644. doi:10.1029/JB086iB04p02593

Pariso, J.E., Kelso, P., and Richter, C., 1996. Paleomagnetism and rock magnetic properties of gabbro from Hole 894G, Hess Deep. *In* Mével, C., Gillis, K.M., Allan, J.F., and Meyer, P.S. (Eds.), *Proc. ODP, Sci. Results,* 147: College Station, TX (Ocean Drilling Program), 373–381. doi:10.2973/odp.proc.sr.147.023.1996

Passchier, C.W., and Trouw, R.A.J., 2005. *Microtectonics* (2nd ed.): Berlin (Springer).

Pedersen, R.B., Malpas, J., and Falloon, T., 1996. Petrology and geochemistry of gabbroic and related rocks from Site 894, Hess Deep. *In* Mével, C., Gillis, K.M., Allan, J.F., and Meyer, P.S. (Eds.), *Proc. ODP, Sci. Results,* 147: College Station, TX (Ocean Drilling Program), 3–19. doi:10.2973/odp.proc.sr.147.001.1996

Perk, N.W., Coogan, L.A., Karson, J.A., Klein, E.M., and Hanna, H.D., 2007. Petrology and geochemistry of primitive lower oceanic crust from Pito Deep: implications for the accretion of the lower crust at the southern East Pacific Rise. *Contrib. Mineral. Petrol.,* 154(5):575–590. doi:10.1007/s00410-007-0210-z

Renner, R., and Palacz, Z., 1987. Basaltic replenishment of the Rhum magma chamber: evidence from Unit 14. *J. Geol. Soc. (London, U. K.),* 144(6):961–970. doi:10.1144/gsjgs.144.6.0961

Rioux, M., Lissenberg, C.J., McLean, N.M., Bowring, S.A., MacLeod, C.J., Hellebrand, E., and Shimizu, N., 2012. Protracted timescales of lower crustal growth at the fast-spreading East Pacific Rise. *Nat. Geosci.,* 5(4):275–278. doi:10.1038/ngeo1378

Saunders, A.D., Fornari, D.J., Joron, J.-L., Tarney, J., and Treuil, M., 1982. Geochemistry of basic igneous rocks, Gulf of California, Deep Sea Drilling Project Leg 64. *In* Curray, J.R., Moore, D.G., et al. (Eds.), *Init. Repts. DSDP,* 64: Washington, DC (U.S. Govt. Printing Office), 595–642. doi:10.2973/dsdp.proc.64.112.1982

Shipboard Scientific Party, 1989. Site 735. *In* Robinson, P.T., Von Herzen, R., et al., *Proc. ODP, Init. Repts.,* 118: College Station, TX (Ocean Drilling Program), 89–222. doi:10.2973/odp.proc.ir.118.107.1989

Shipboard Scientific Party, 1993. Site 894. *In* Gillis, K., Mével, C, Allan, J., et al., *Proc. ODP, Init. Repts.,* 147: College Station, TX (Ocean Drilling Program), 45–108. doi:10.2973/odp.proc.ir.147.103.1993

Shipboard Scientific Party, 1999. Site 735. *In* Dick, H.J.B., Natland, J.H., Miller, D.J., et al., *Proc. ODP, Init. Repts.,* 176: College Station, TX (Ocean Drilling Program), 1–314. doi:10.2973/odp.proc.ir.176.103.1999

Shipboard Scientific Party, 2003. Site 1256. *In* Wilson, D.S., Teagle, D.A.H., Acton, G.D., *Proc. ODP, Init. Repts.,* 206: College Station, TX (Ocean Drilling Program), 1–396. doi:10.2973/odp.proc.ir.206.103.2003

Shipboard Scientific Party, 2004. Site 1271. *In* Kelemen, P.B., Kikawa, E., Miller, D.J., et al., *Proc. ODP, Init. Repts.,* 209: College Station, TX (Ocean Drilling Program), 1–129. doi:10.2973/odp.proc.ir.209.106.2004

Stewart, M.A., Klein, E.M., and Karson, J.A., 2002. Geochemistry of dikes and lavas from the north wall of the Hess Deep Rift: insights into the four-dimensional character of crustal construction at fast-spreading mid-ocean ridges. *J. Geophys. Res.: Solid Earth,* 107(B10):2238. doi:10.1029/2001JB000545

Stolper, E., and Walker, D., 1980. Melt density and the average composition of basalt. *Contrib. Mineral. Petrol.,* 74(1):7–12. doi:10.1007/BF00375484

Teagle, D.A.H., Ildefonse, B., Blum, P., and the Expedition 335 Scientists, 2012. *Proc. IODP,* 335: Tokyo (Integrated Ocean Drilling Program Management International, Inc.). doi:10.2204/iodp.proc.335.2012

Varga, R.J., Karson, J.A., and Gee, J.S., 2004. Paleomagnetic constraints on deformation models for uppermost oceanic crust exposed at the Hess Deep Rift: implications for axial processes at the East Pacific Rise. *J. Geophys. Res.: Solid Earth,* 109(B2):B02104. doi:10.1029/2003JB002486

Publication: 12 February 2014
MS 345-110

Figure F1. Reentry hardware deployed in Hole U1415J with driller's interpretation of subseafloor conditions. FFF = free-fall funnel, CSG = casing, TC = total depth.

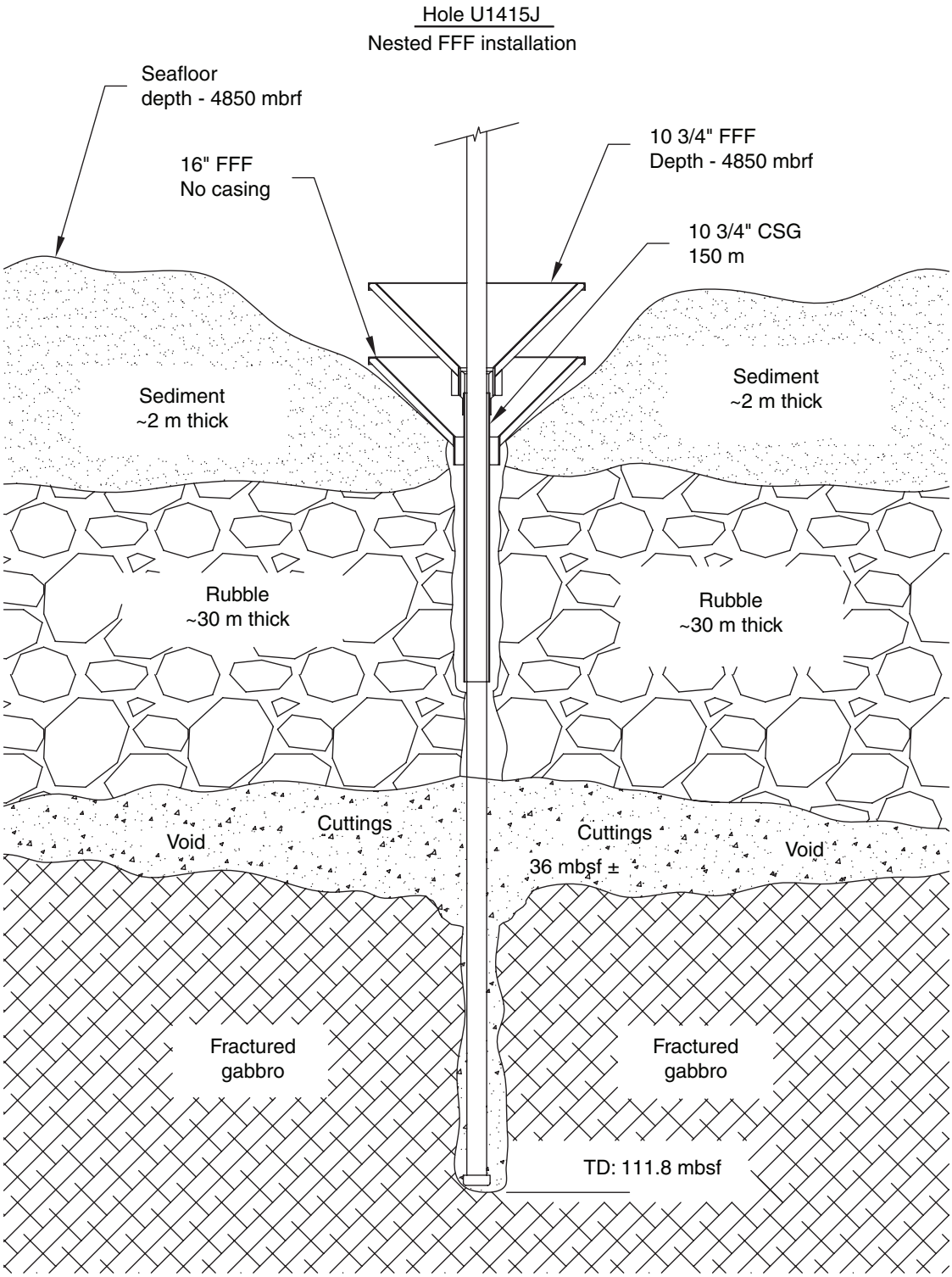

Figure F2. A. Core recovery and principal lithologies, Hole U1415J. **B–H.** Proportions of recovered rock types. Ol = olivine.

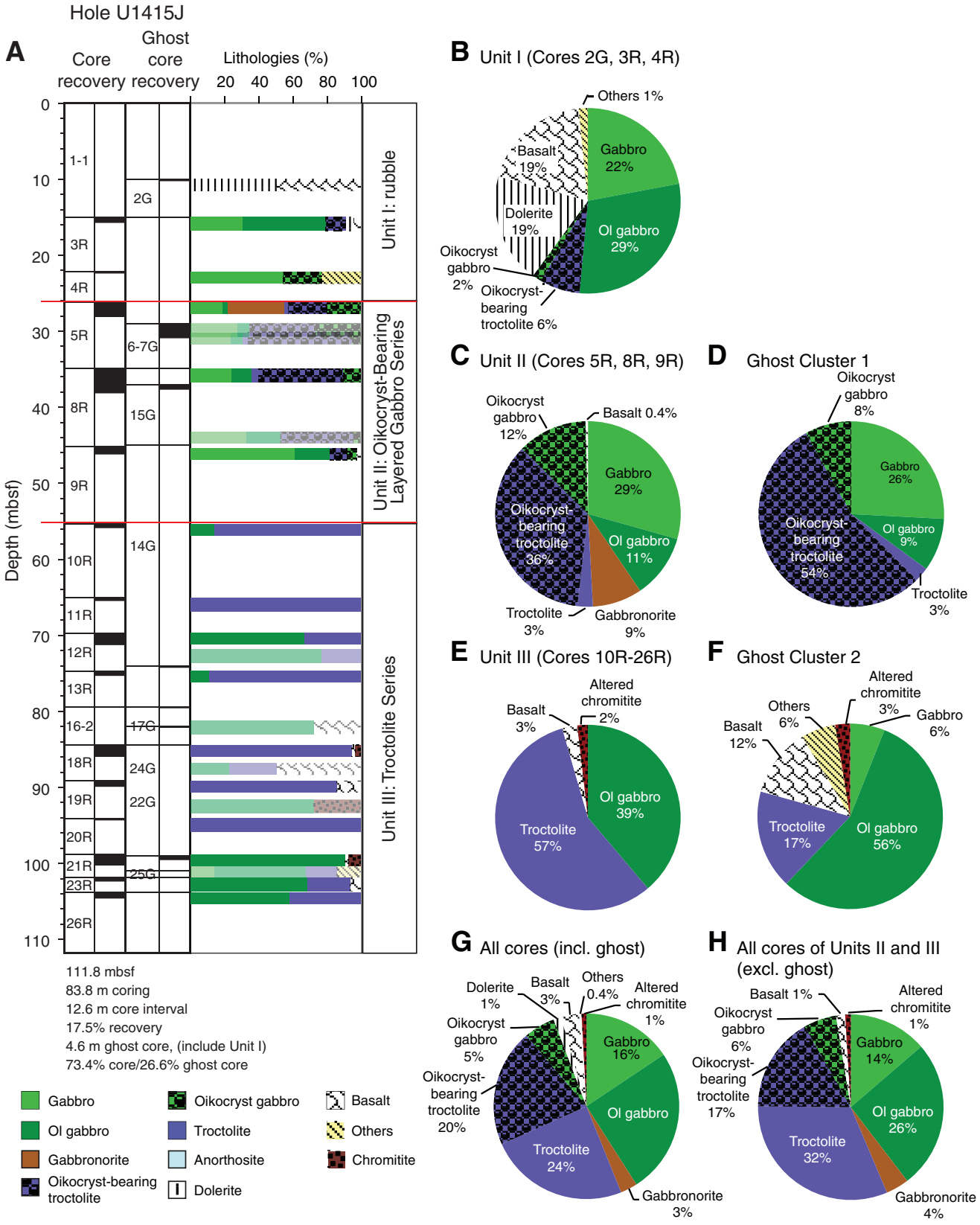

Figure F3. A. Distribution of coherent packages of lithologies within Units II and III, Hole U1415J. Unit II = Oikocryst-Bearing Layered Gabbro Series (abundance of clinopyroxene oikocrysts), Unit III = Troctolite Series (multiple recovered sections of troctolite). See text for further discussion). **B.** Average modal abundance and grain size range for each of the packages in A. Note that the total of the average may not equal 100%.

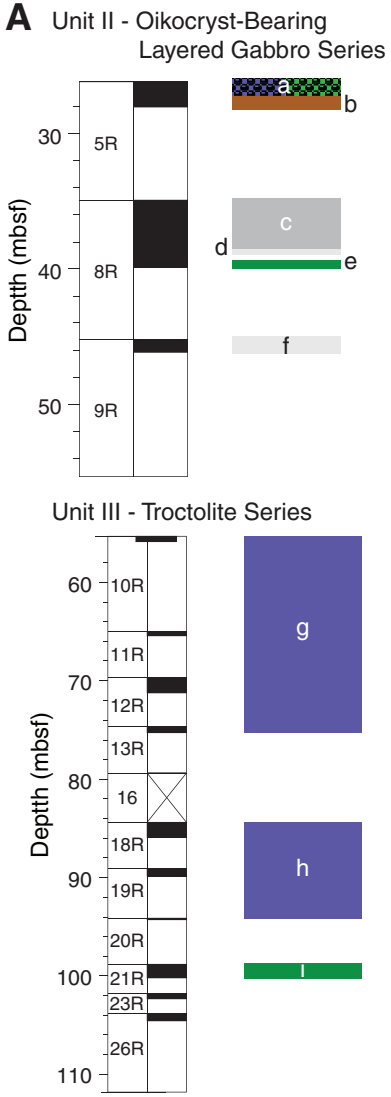

a: **Oikocryst bearing** (0.9 3 m)
5 oikocryst bearing intervals (troctolite [19, 24], 1 gabbro [20], and 2 olivine gabbro [21, 22]); rocks range from medium grained (19-23) to coarse grained (24), with granular (23) to poikilitic-granular (19, 20, 21, 22, 24) texture.

b: **Orthopyroxene bearing** (0.85 m)
4 olivine-bearing gabbronorite intervals (25, 27, 30, 32), 3 troctolite intervals (28 [also oikocryst bearing], 29, 32), and 1 olivine-bearing gabbro interval (26); intervals 25-28 are coarse grained, whereas intervals 29-32 are medium grained; all intervals except 28 are granular, interval 28 is pokilitic-granular; intervals 29-32 are also foliated.

c: **Olivine bearing** (2.53 m)
5 oikocryst-bearing lithologies (troctolite [35, 37, 40, 41], gabbro [38]), and 3 olivine-gabbro intervals (34, 36, 39); intervals 34, 35, 36, 38, 40, 41 are medium grained and intervals 37 and 39 are fined grained; intervals 34, 36, 39 have a granular texture and intervals 35, 37, 38, 40, 41 have a poikilitic-granular texture.

d: **Olivine rich** (0.63 m)
1 olivine gabbro interval (43), 2 troctolite intervals (44, 45), and 2 oikocryst-bearing intervals (gabbro [46] and troctolite [47]); intervals 44, 45 are fine grained and intervals 43, 46, 47 are medium grained; intervals 43, 44, 45 have granular textures and intervals 46, 47 have poikilitic-granular textures.

e: **Olivine-bearing gabbro** (1.1 m)
2 intervals (48, 50) contain solely olivine-bearing gabbro, which is both medium grained and granular.

f: **Olivine rich** (0.86 m)
2 oikocryst-bearing intervals (troctolite [52], olivine gabbro [54]), and 2 olivine-bearing gabbro intervals (53, 55); intervals 52-54 are medium grained and interval 55 is coarse grained; intervals 52 and 54 are poikilitic-granular and intervals 53 and 55 have granular textures

g: **Troctolite with olivine gabbro** (20.1 m)
5 troctolite intervals (58,60,61,62,66) with 4 olivine gabbro intervals (59,63,64,65); package as a whole is medium grained with a granular texture. From 45-55 cm within Section 10R-1, there is a subvertical contact between troctolite and olivine gabbro.

h: **Troctolite** (9.2 m)
4 troctolite intervals (71, 72, 73, 75); rocks are medium (71, 72, 73) to coarse (75) grained with a granular texture.
From 129-150 cm in Section 18R-1, there is subvertical modal contact between troctolite and olivine-richer troctolite.

i: **Olivine gabbro** (1.5 m)
1 olivine gabbro interval (78); rocks are medium grained with a granular texture.

Legend:
- Gabbro
- Olivine gabbro
- Gabbronorite
- Oikocryst-bearing troctolite
- Oikocryst gabbro
- Troctolite
- Anorthosite
- Dolerite
- Basalt
- Cataclasite (or altered)
- Chromitite

B

Package	Olivine	Plagioclase	Clinopyroxene	Orthopyroxene
a	Average = 12.0% Size range = 1-5 mm	Average = 62.2% Size range = 3-5 mm	Average = 25.8% Size range = 4-10 mm	
b	Average = 12.8% Size range = 3-5 mm	Average = 62.5% Size range = 3-6 mm	Average = 20.4% Size range = 3-5 mm	Average = 8.8% Size range = 3-10 mm
c	Average = 18.8% Size range = 2.5-8 mm	Average = 50.0% Size range = 2-7 mm	Average = 31.3% Size range = 4-20 mm	
d	Average = 23.0% Size range = 10-30 mm	Average = 58.0% Size range = 2-5 mm	Average = 31.7% Size range = 5-20 mm	
e	Average = 5.0% Size range = 11-12 mm	Average = 50.0% Size range = 5-10 mm	Average = 45.0% Size range = 3-10 mm	
f	Average = 11.8% Size range = 2-25 mm	Average = 53.8% Size range = 4-10 mm	Average = 34.5% Size range = 3-15 mm	
g	Average = 27.2% Size range = 2-10 mm	Average = 57.2% Size range = 2-6 mm	Average = 17.8% Size range = 5-12 mm	
h	Average = 47.0% Size range = 5 mm	Average = 52.4% Size range = 9-10 mm	Average = 0.8% Size range = 1.5-3 mm	
i	Average = 30.5%	Average = 65.5.3%	Average = 5.0% Size range = 4 mm	

Figure F4. Equigranular granular textures in gabbro, Unit I (Thin Section 63; Sample 345-U1415J-3R-1, 79–85.5 cm [Piece 16]; Interval 11). **A.** Core close-up. **B.** Plane-polarized light. Cpx = clinopyroxene, Pl = plagioclase. **C.** Under crossed polars.

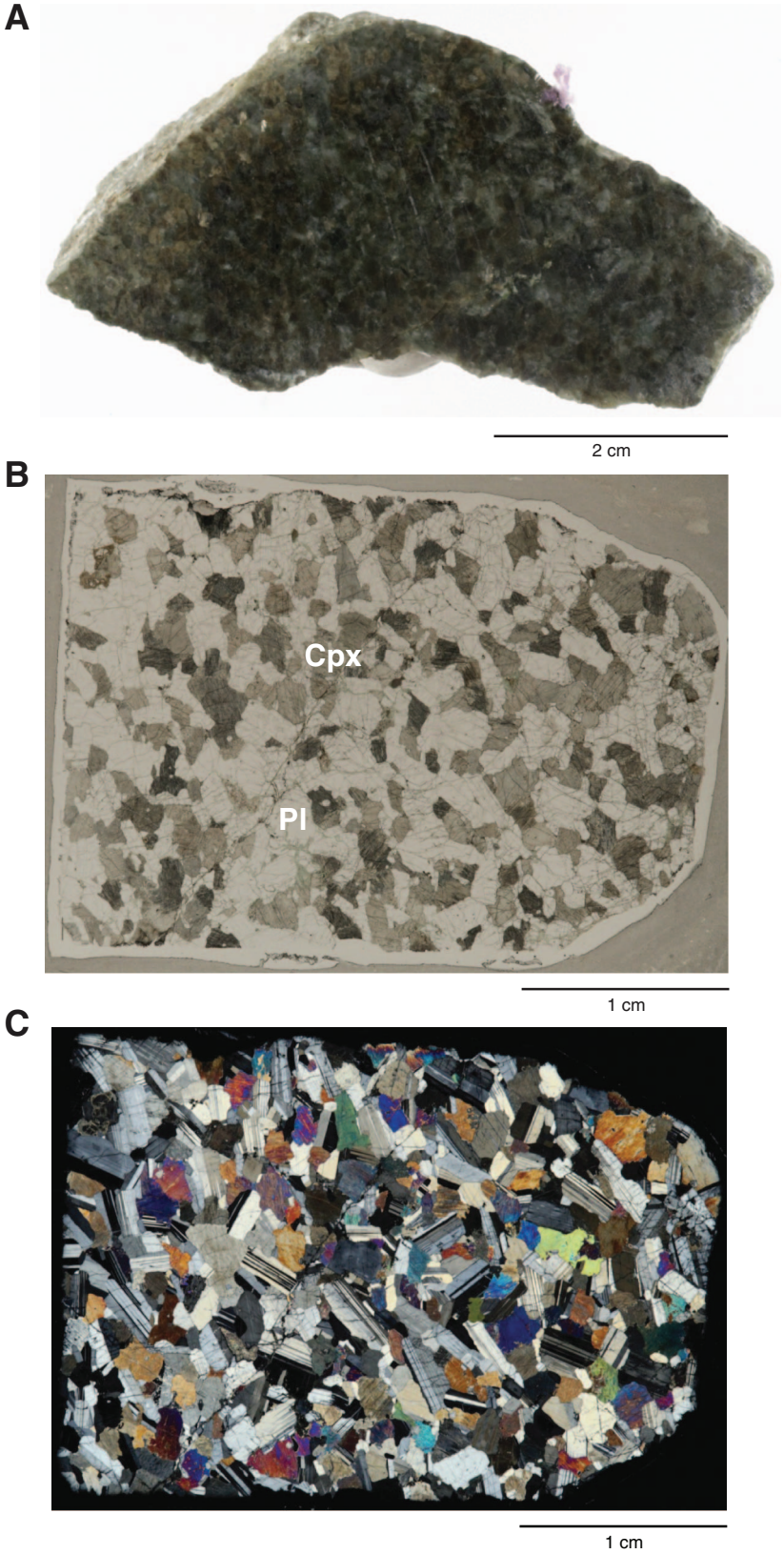

Figure F5. Equigranular granular texture and strong foliation defined by both plagioclase (Pl) and clinopyroxene (Cpx) in olivine (Ol)-bearing gabbro, Unit I (Sample 345-U1415J-3R-1, 22–24 cm [Piece 6]; Interval 6). Note the presence of twinning in clinopyroxene. **A.** Core close-up. **B.** Plane-polarized light. **C.** Under crossed polars.

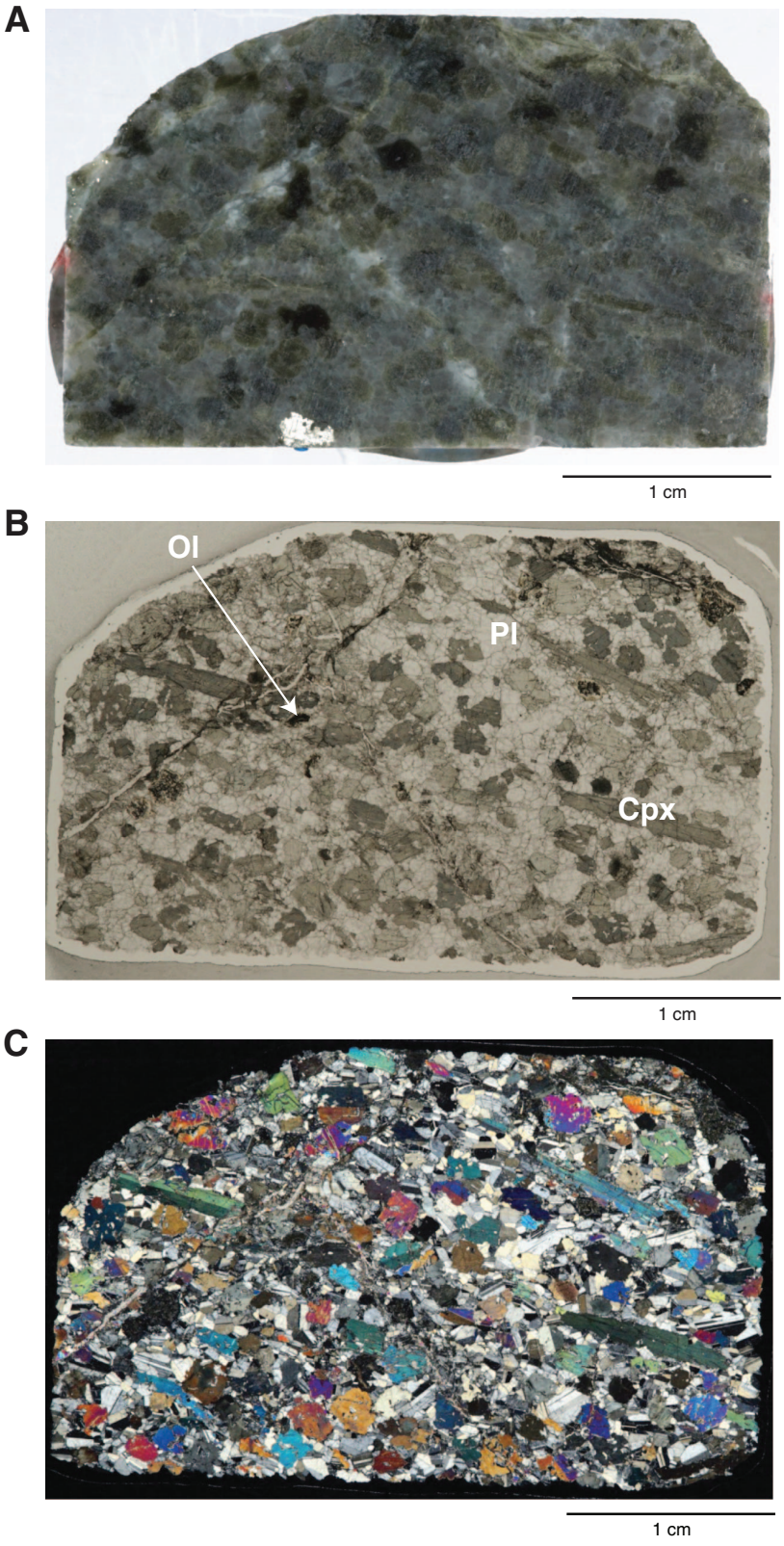

Figure F6. Equigranular granular to poikilitic texture in olivine (Ol) gabbro, Unit I (Thin Section 31; Sample 345-U1415J-3R-1, 45–48 cm [Piece 10]; Interval 10). **A.** Core close-up. **B.** Plane-polarized light. Cpx = clinopyroxene, Pl = plagioclase. **C.** Under crossed polars.

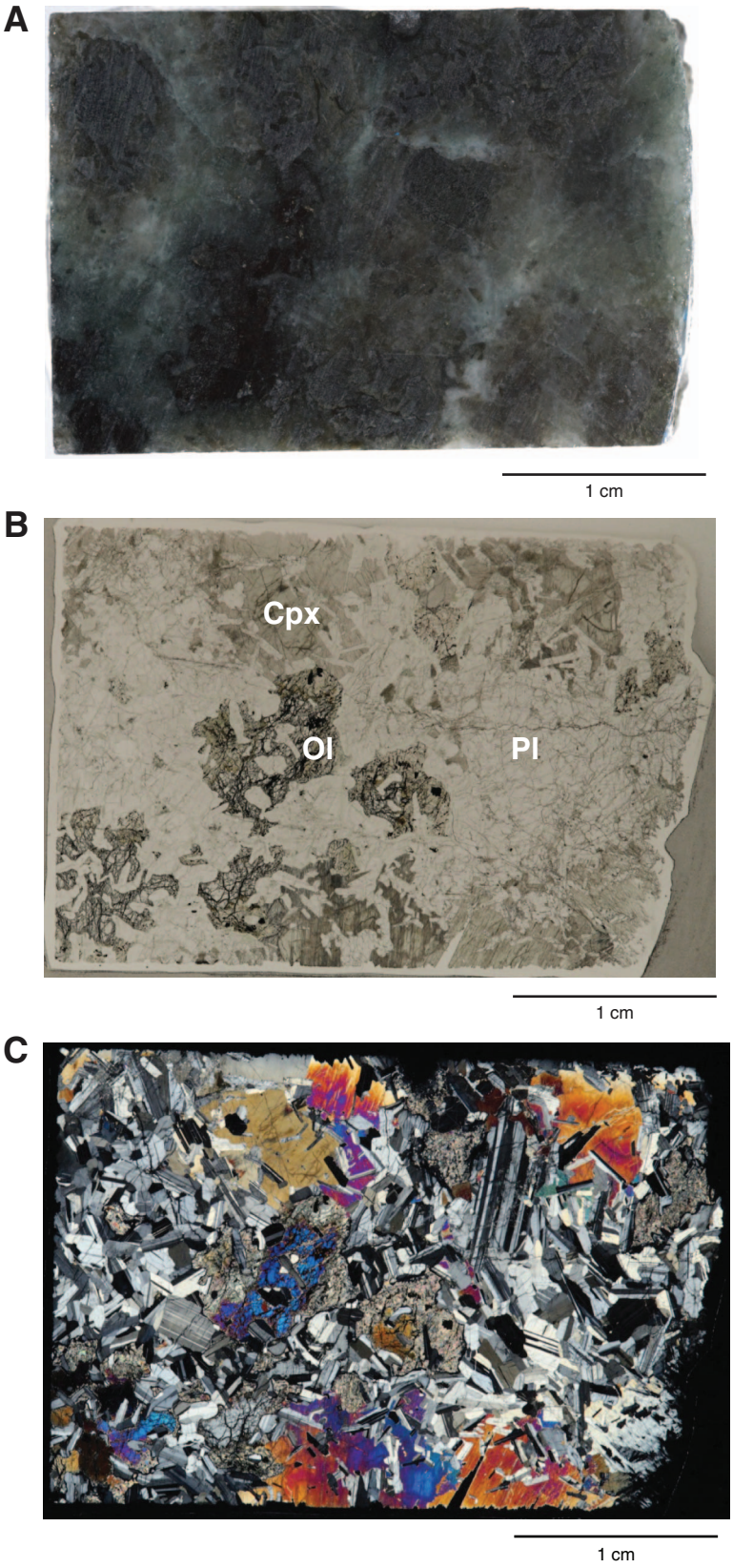

Figure F7. Equigranular granular texture in olivine (Ol) gabbro, Unit III (Thin Section 63; Sample 345-U1415J-12R-1, 95–104 cm [Piece 13]; Interval 13). **A.** Core close-up. **B.** Plane-polarized light. Cpx = clinopyroxene, Pl = plagioclase. **C.** Under crossed polars.

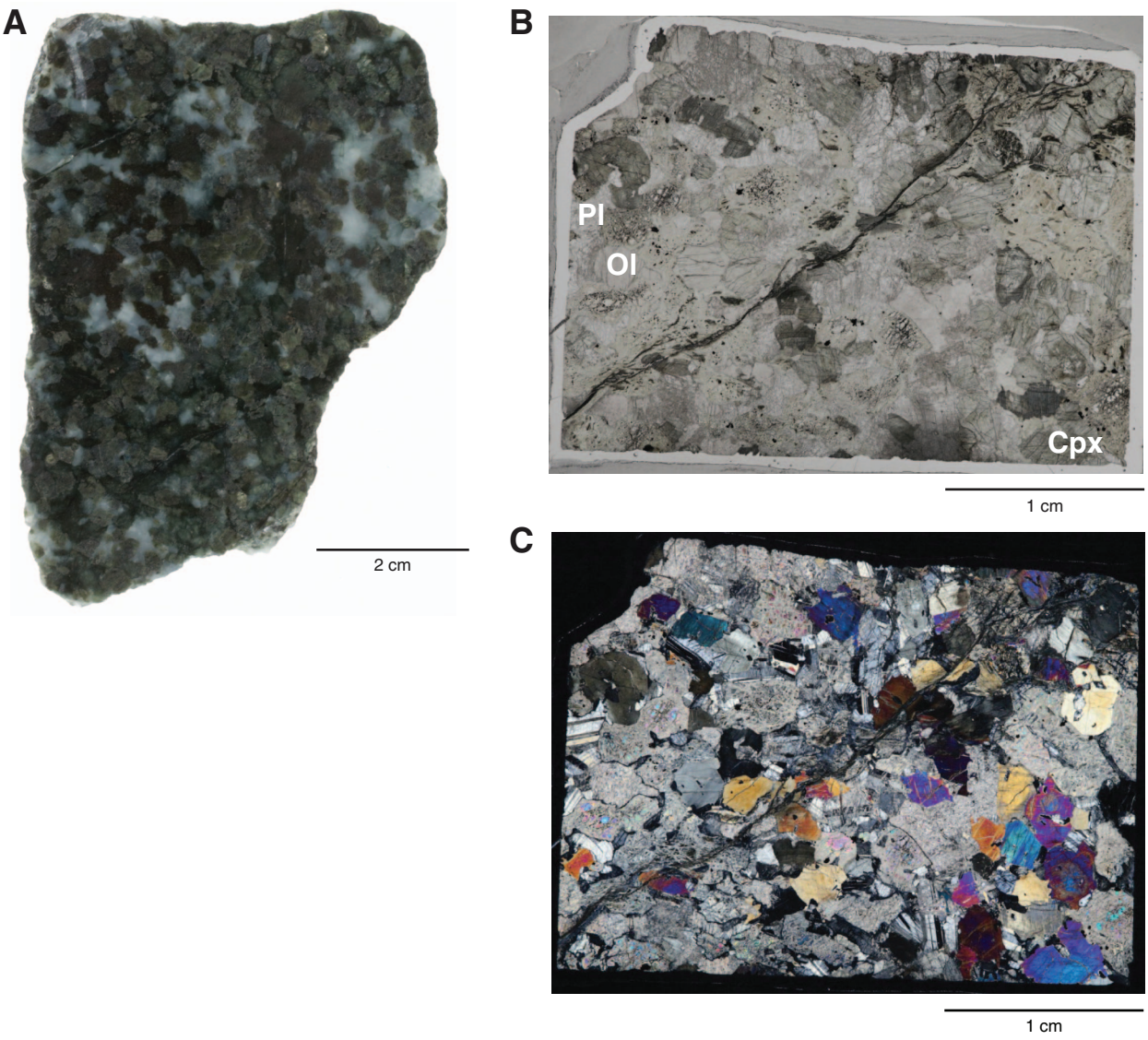

Figure F8. A. Boundary between olivine (Ol) gabbro (Interval 59) and troctolite (Interval 58), Unit II (Sample 345-U1415J-10R-1, 39–55 cm [Piece 6B]). **B, C.** Large poikilitic clinopyroxene (Cpx) that is larger than the width of the thin section and optically continuous throughout, forming the interstitial clinopyroxene in the troctolite of Interval 58 (dashed pink line marks the boundary of this oikocryst). Dashed red line in C marks the boundary between lithologies (Thin Section 58). B is under plane-polarized light and C is under crossed polars. (Ol) = altered olivine, Pl = plagioclase. See also Figure F10.

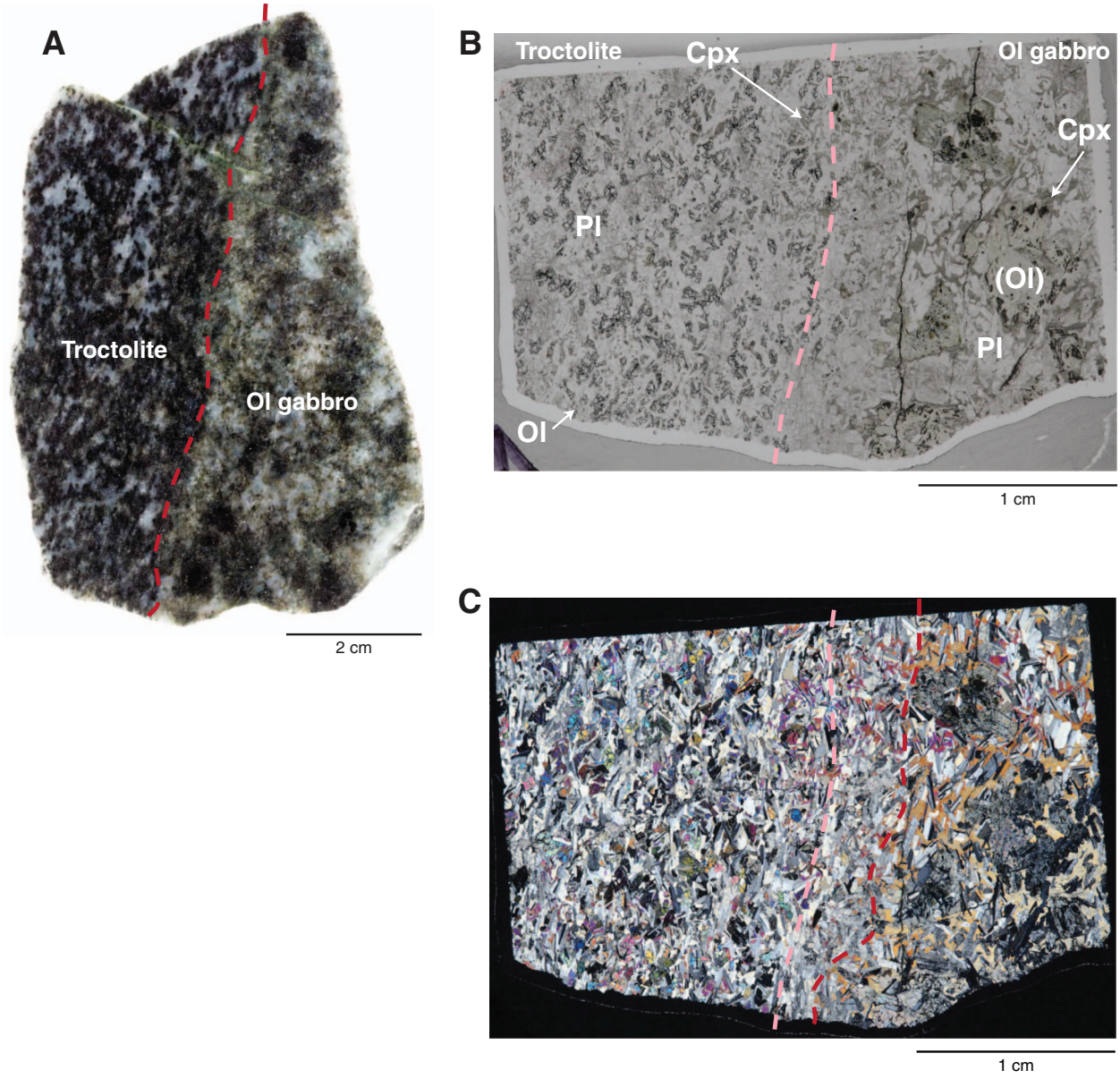

Figure F9. Olivine-bearing gabbronorite, Unit II (Sample 345-U1415J-5R-2, 41–65 cm [Piece 3]; Interval 32). **A.** Dry image. **B.** Wet image.

Figure F10. Clinopyroxene oikocryst-bearing troctolite, Unit II (Sample 345-U1415J-8R-3, 79–91 cm [Piece 9]; Interval 49). Note the strong grain size contrast between the oikocrysts and the surrounding troctolitic matrix. **A.** Dry image. **B.** Wet image.

Figure F11. Clinopyroxene (Cpx) oikocryst-bearing troctolite. The strongly foliated troctolite shows a single large clinopyroxene oikocryst with abundant randomly orientated subhedral to resorbed deformed to undeformed plagioclase (Pl) chadacrysts (Thin Section 53; Sample 345-U1415J-8R-3, 23–29 cm [Piece 5]; Interval 47). **A.** Core close-up. **B.** Plane-polarized light. Ol = olivine. **C.** Under crossed polars.

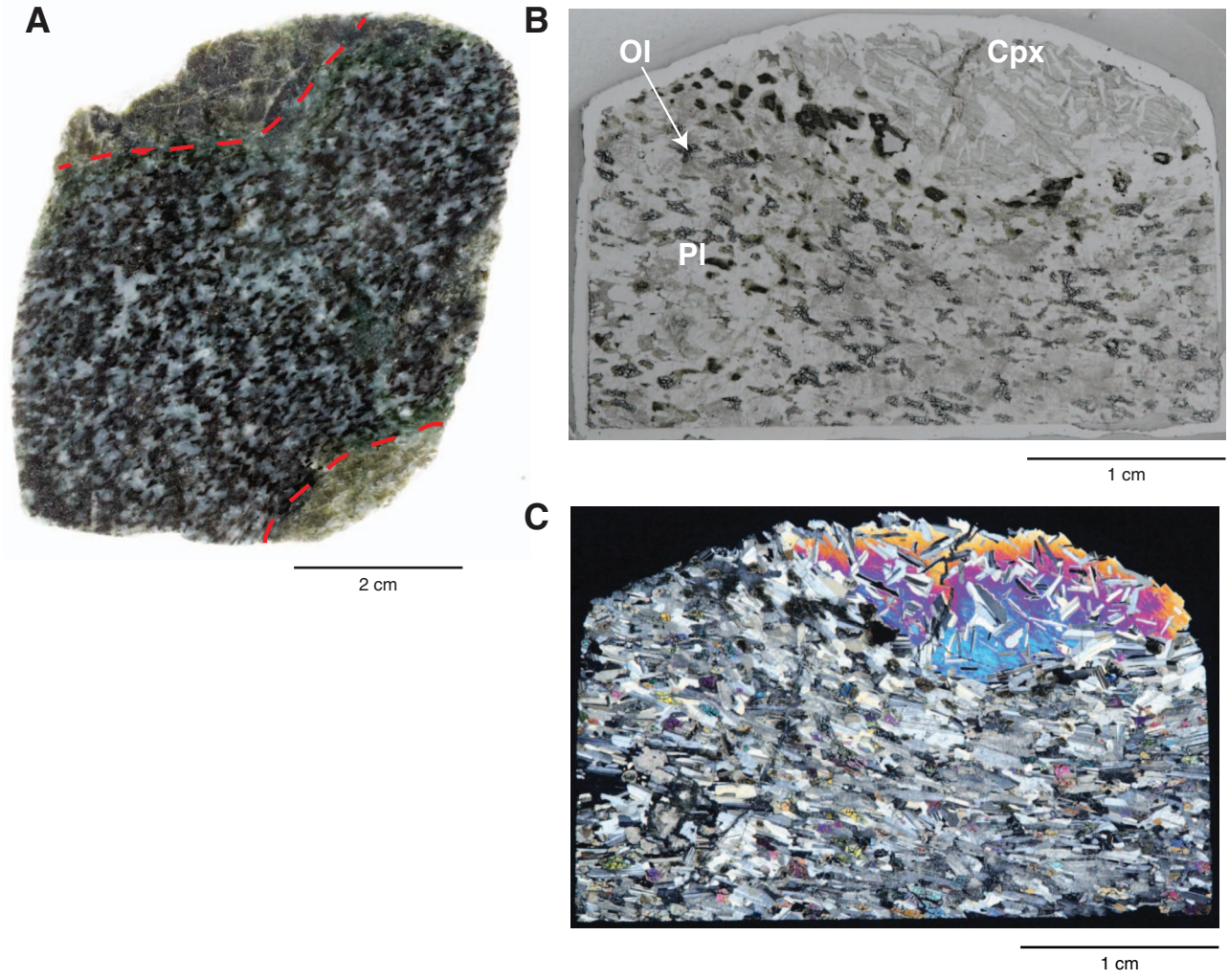

Figure F12. Oikocryst gabbro, Unit II (Sample 345-U1415J-8R-1, 89–107 cm [Piece 14]; Interval 36). **A.** Dry image. **B.** Wet image.

Figure F13. Troctolite, Unit III (Thin Section 66; Sample 345-U1415J-13R-1, 45–52 cm [Piece 6]; Interval 66). **A.** Core close-up. **B.** Plane-polarized light. Ol = olivine, Pl = plagioclase. **C.** Under crossed polars.

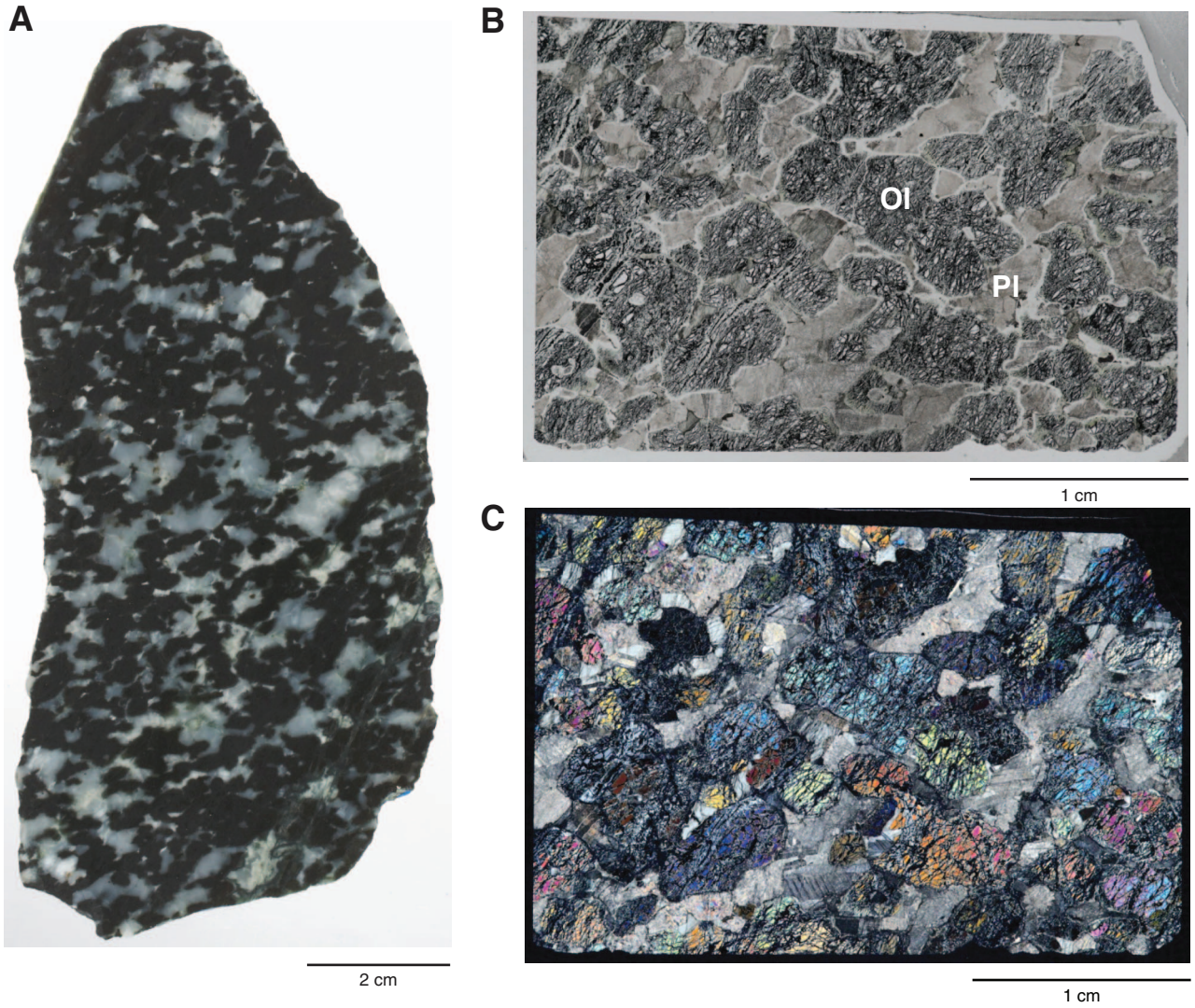

Figure F14. Basaltic intervals recovered from cored intervals. **A.** Intervals 2–4 showing (1) aphyric basalt, (2) doleritic gabbro, and (3) olivine-bearing dolerite (Sample 345-U1415J-3R-1, 7–10 cm [Piece 3]). **B.** Aphyric basalt (Sample 345-U1415J-9R-1, 97–100 cm [Piece 14]; Interval 56). **C.** Moderately olivine-phyric basalt (Sample 345-U1415J-18R-1, 26–29 cm [Piece 4]; Interval 68).

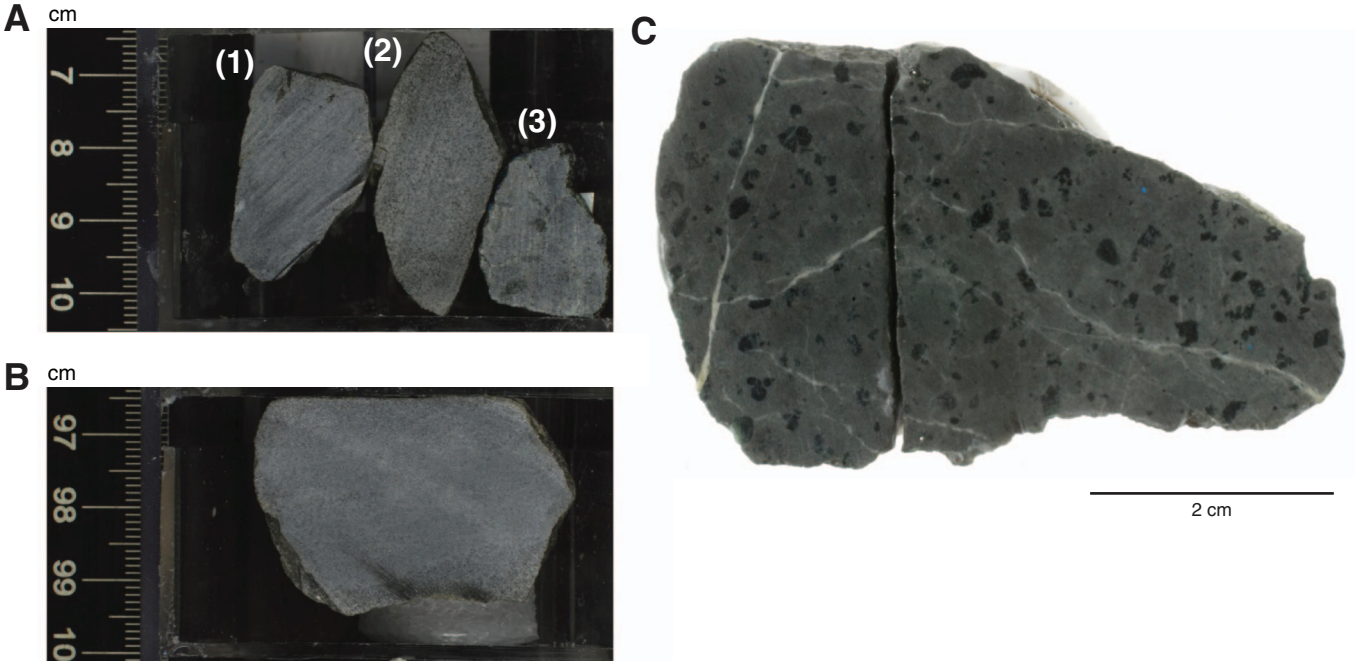

Figure F15. Basaltic intervals recovered from ghost cores (photomicrographs under crossed polars). **A.** Aphyric basalt (Thin Section 25; Sample 345-U1415J-2G-1, 0–4 cm [Piece 1]; Interval G1). **B.** Dolerite (Thin Section 26; Sample 345-U1415J-2G-1, 4–8 cm [Piece 1]; Interval G2). **C.** Aphyric basalt with euhedral olivine phenocrysts (Sample 345-U1415J-17G-1, 8–12 cm [Piece 2]; Interval G56). **D.** Moderately olivine-phyric basalt (Sample 345-U1415J-24G-1, 0–6 cm [Piece 1]; Interval G59).

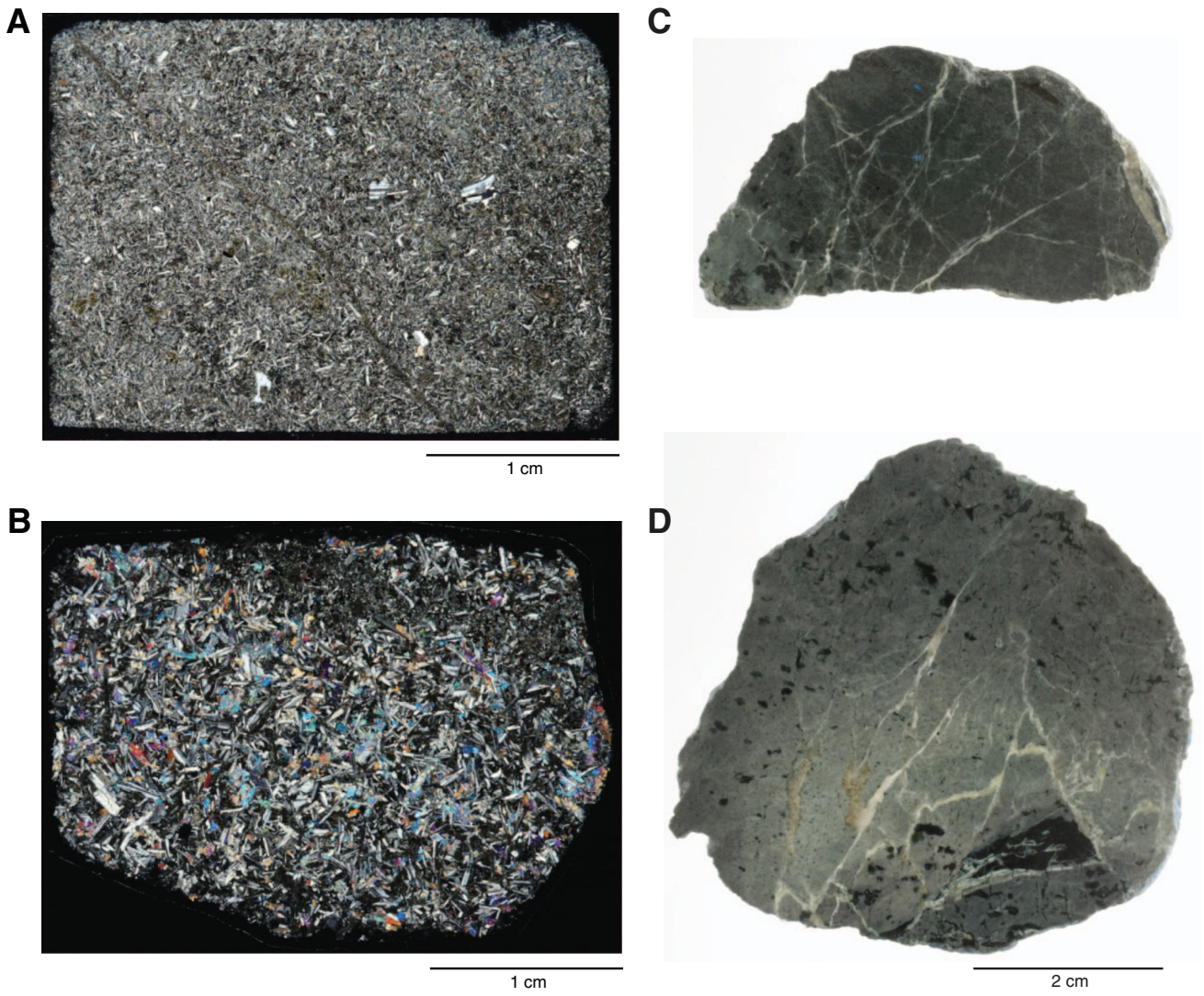

Figure F16. Typical pieces of rock recovered from Hole U1415J showing characteristic textural and modal differences between Unit II and III lithologies. **A–C.** Modal and grain size layering in Unit II (Oikocryst-Bearing Layered Gabbro Series) is parallel to foliation. **D, E.** In contrast, layering is very rare in Unit III (Troctolite Series), but foliation is still common although weaker compared to Unit II. Core image in E shows one of the rare examples of modal and grain size variation observed in the lower part of Unit III. Note the change of foliation dip between the different units (subvertical for the troctolites of Unit III). (A) Troctolite (Sample 345-U1415J-5R-2, 0–21.5 cm [Piece 1]; Interval 29; wet image). (B) Olivine-bearing gabbro (Sample 345-U1415J-8R-3, 30–42 cm [Piece 6]; Interval 48; wet image). (C) Clinopyroxene oikocryst-bearing troctolite. Note the centimeter-sized clinopyroxene oikocrysts wrapped by much finer grained, strongly foliated troctolitic matrix (Sample 345-U1415J-8R-3, 76–91 cm [Piece 9]; Interval 49; dry image). (D) Troctolite (Sample 345-U1415J-18R-1, 96–106 cm [Piece 14]; Interval 71; dry image). (E) Troctolite with modal boundary (Sample 345-U1415J-18R-1, 128–130 cm [Piece 17A]; Interval 72; dry image).

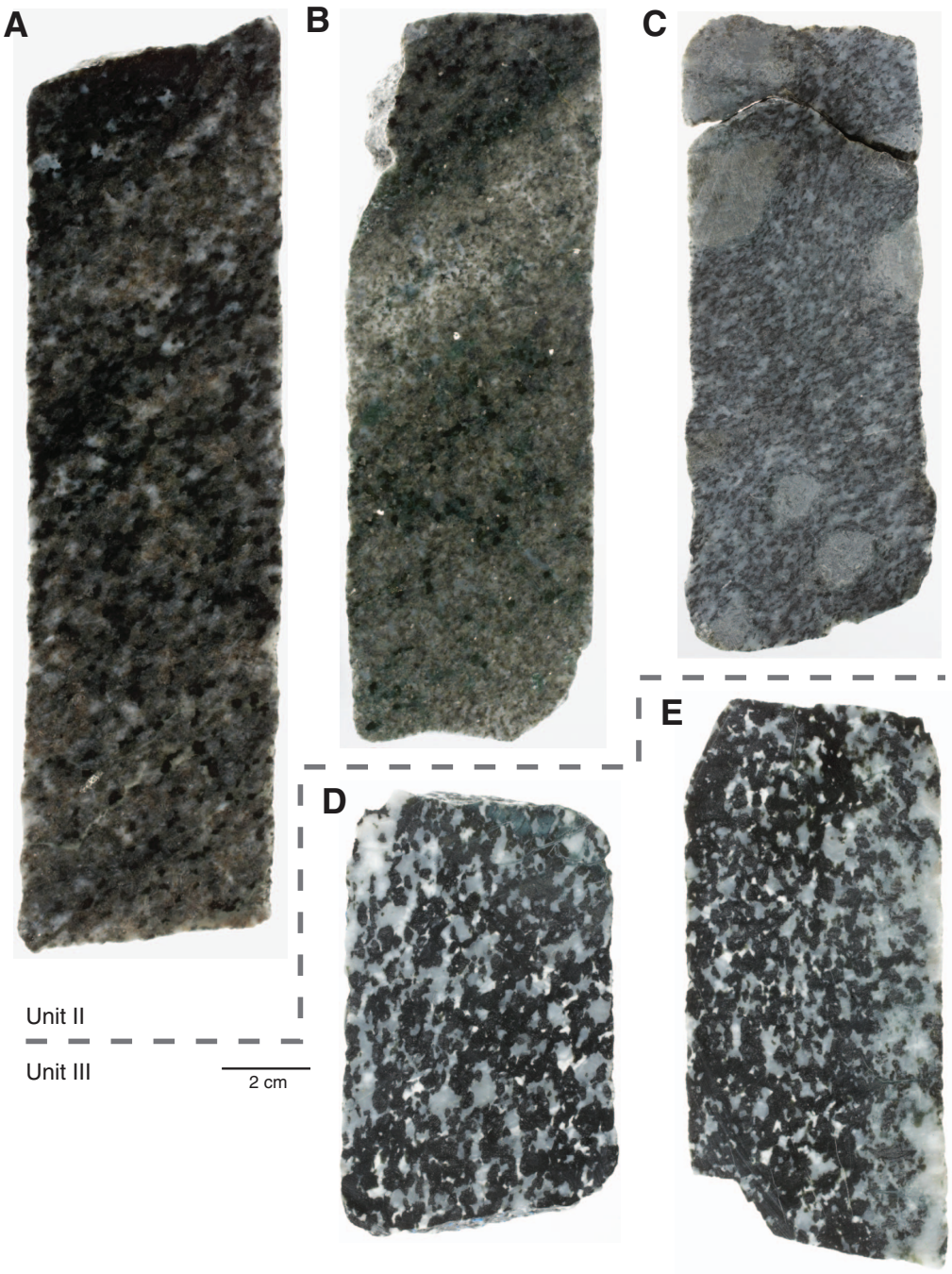

Figure F17. Stratigraphic variations of modal composition and grain size of minerals in Cores 345-U1415J-5R through 26R (ghost cores not included) based on core description. a–i = packages in Figure F3. Red stars = horizons where Cr-spinel crystals were found. Black lines and blue diamonds represent mode and maximum of grain size, respectively. Ol = olivine, Plg = plagioclase, Cpx = clinopyroxene, Opx = orthopyroxene, OXs = oxides.

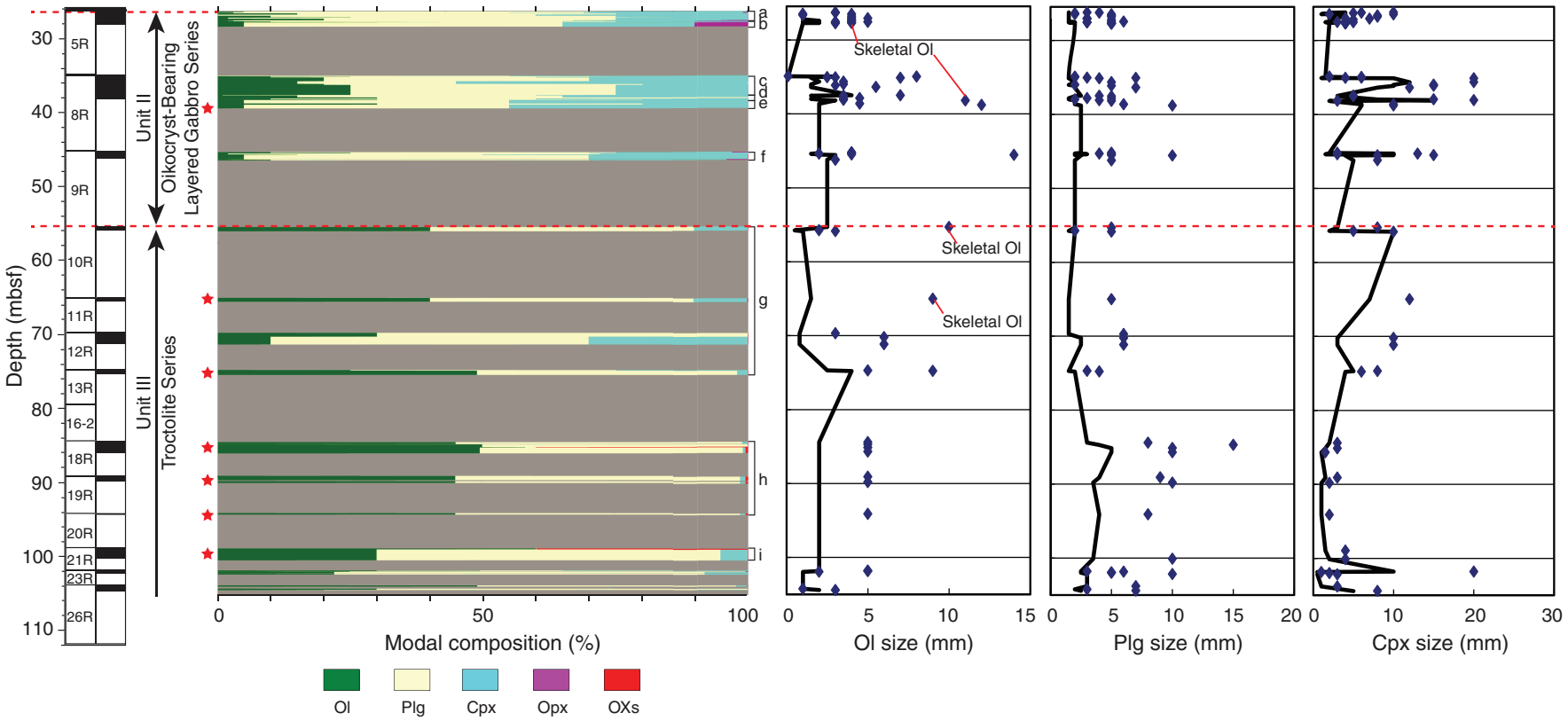

Figure F18. Boundary between olivine (Ol)- and orthopyroxene (Opx)-bearing gabbro and troctolite (red dashed line) (Thin Section 38; Sample 345-U1415J-5R-1, 129–143 cm [Piece 18]). Cpx = clinopyroxene, Pl = plagioclase. Boundary type = grain size and modal and boundary definition = sutured. **A.** Core close-up. **B.** Plane-polarized light. **C.** Under crossed polars.

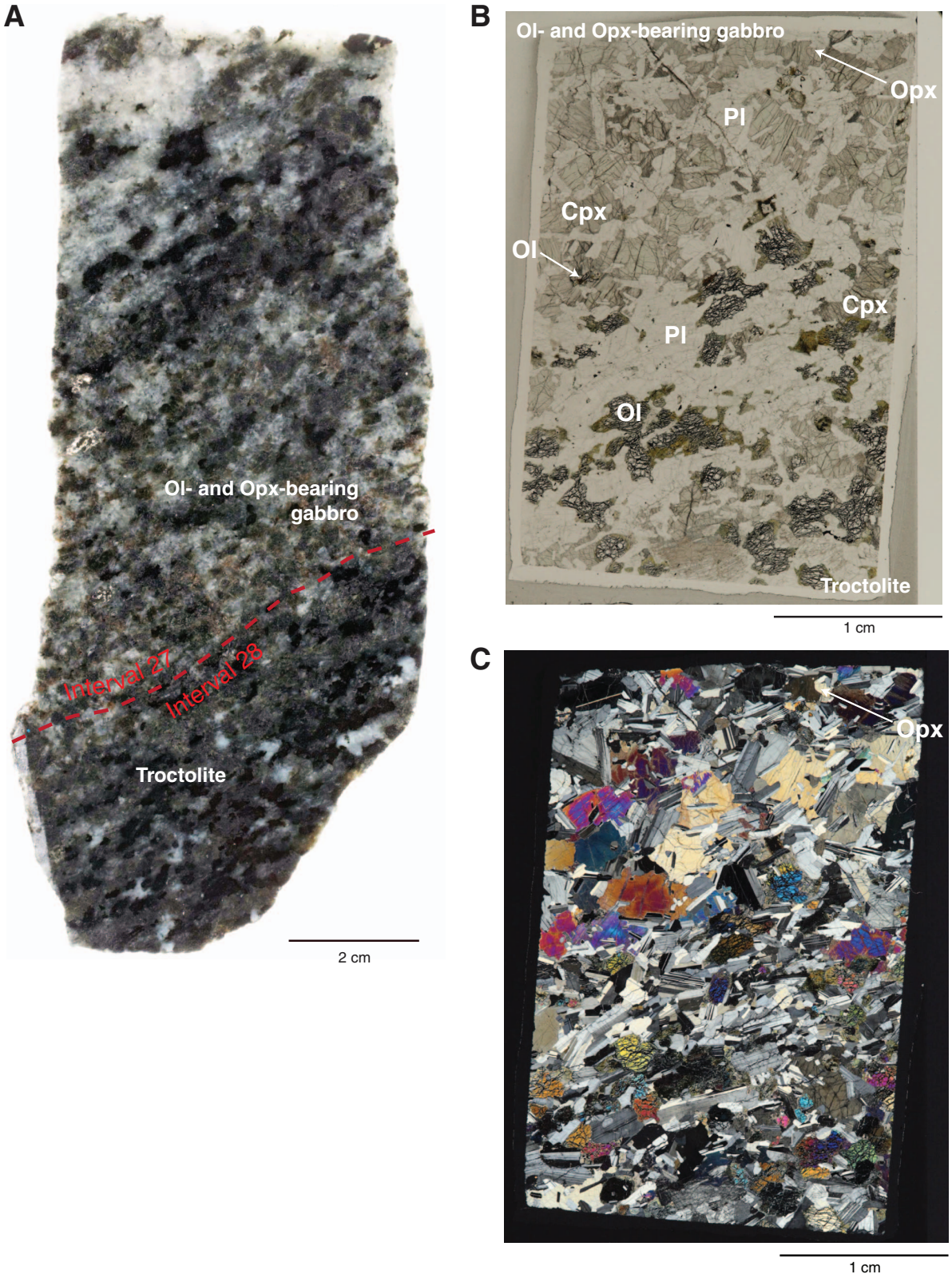

Figure F19. Boundary between gabbronorite and clinopyroxene (Cpx) oikocryst-bearing troctolite (red dashed lines) (Thin Section 40; Sample 345-U1415J-7G-1, 26–34 cm [Piece 5]). Boundary type = grain size and modal; boundary definition = sutured. **A.** Core close-up. **B.** Plane-polarized light. Ol = olivine, Opx = orthopyroxene, Pl = plagioclase. **C.** Under crossed polars.

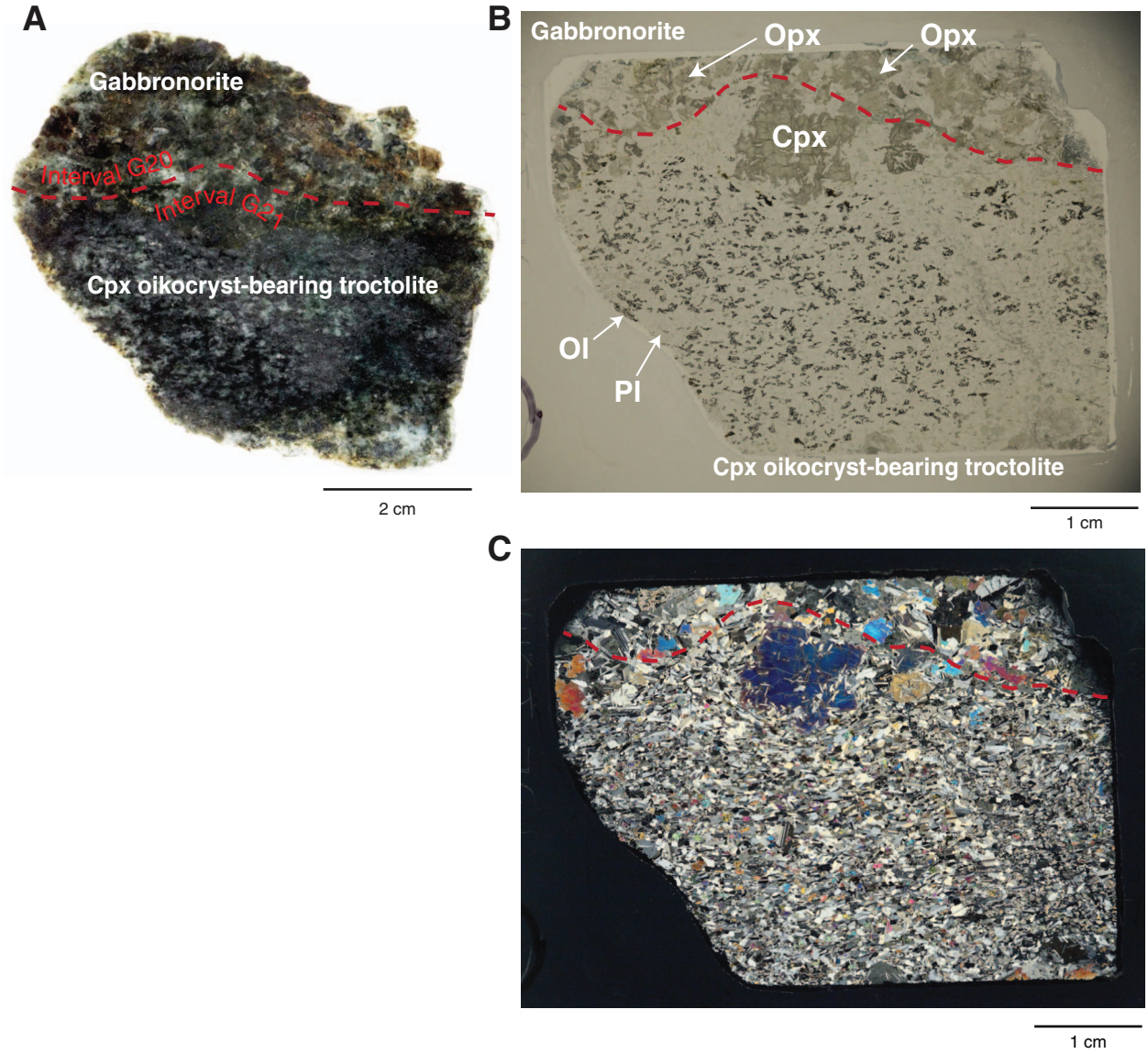

Figure F20. Boundary between oikocryst-bearing troctolite and troctolite (red dashed lines) (Thin Section 42; Sample 345-U1415J-7G-1, 91–94 cm [Piece 14]). Boundary type = grain size and modal; boundary definition = sutured. **A.** Core close-up. **B.** Plane-polarized light. Ol = olivine, Cpx = clinopyroxene, Pl = plagioclase. **C.** Under crossed polars.

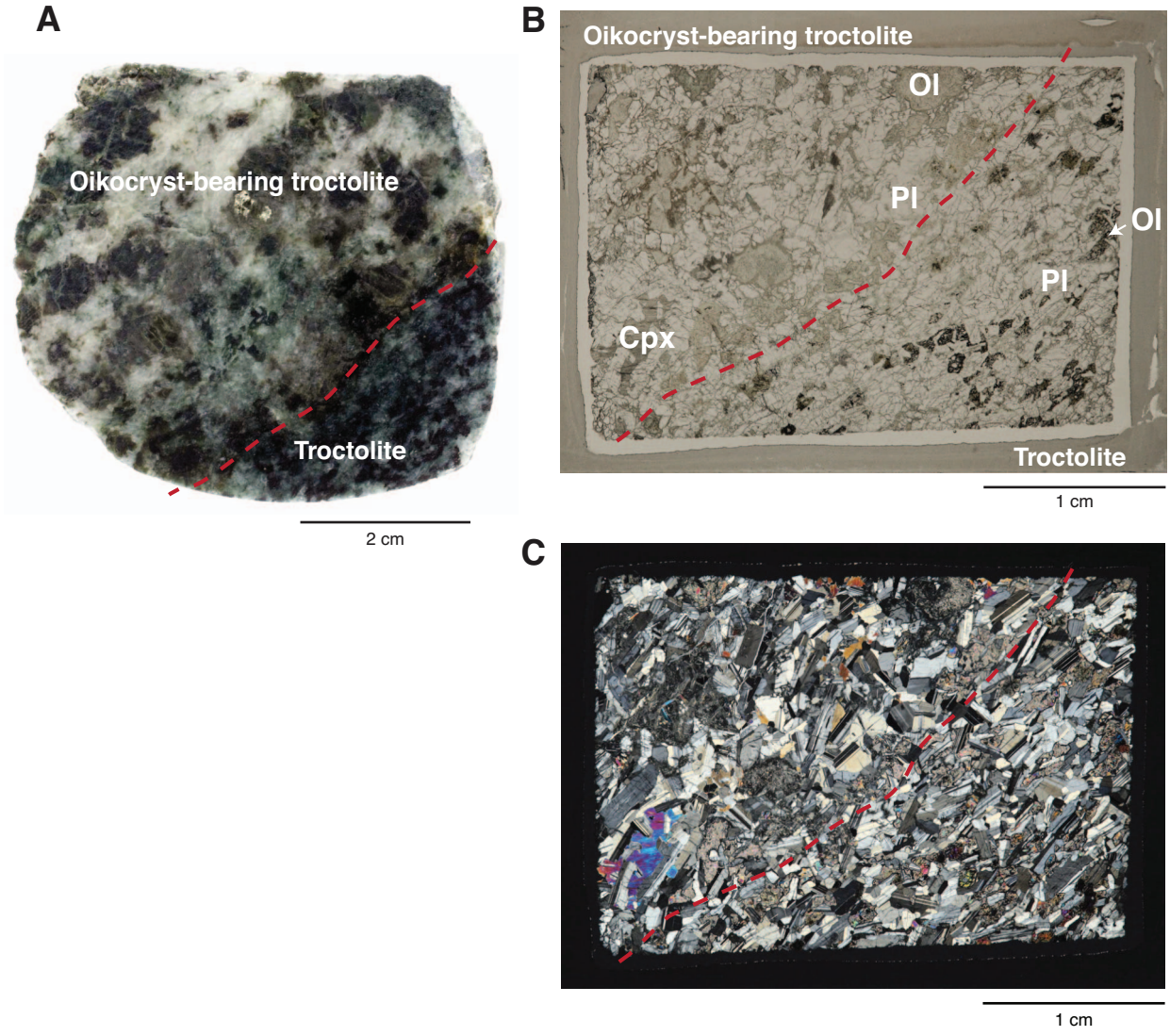

Figure F21. Boundary between olivine (Ol) gabbro and olivine-bearing gabbro (red dashed lines) (Thin Section 52; Sample 345-U1415J-8R-2, 105–122 cm [Piece 9]). Boundary type = grain size and modal; boundary definition = sutured. **A.** Core close-up. **B.** Plane-polarized light. Cpx = clinopyroxene, Pl = plagioclase. **C.** Under crossed polars.

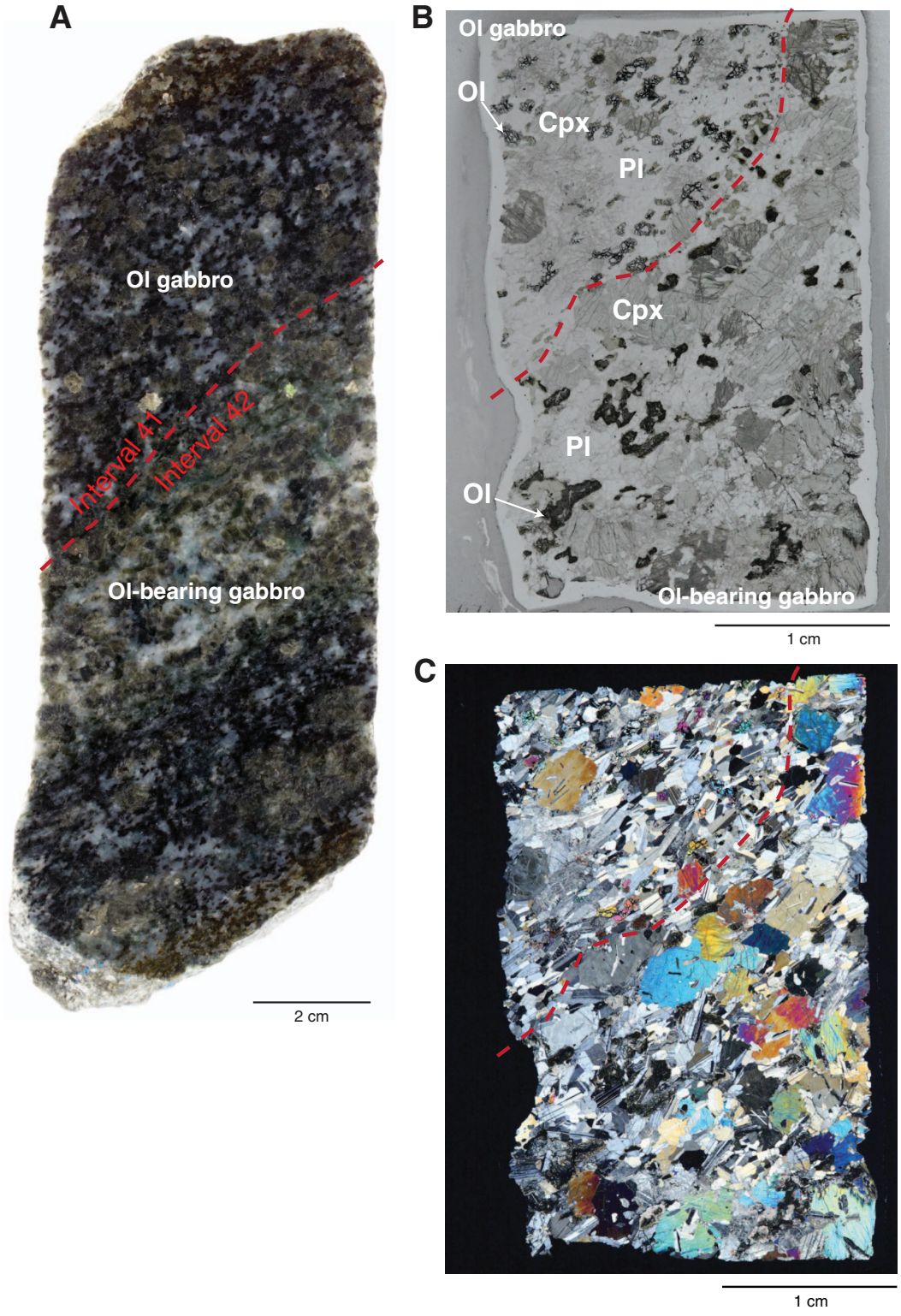

Figure F22. Boundary between gabbro and olivine (Ol) gabbro (red dashed lines) (Thin Section 54; Sample 345-U1415J-8R-3, 31–41 cm [Piece 6]). Boundary type = grain size and modal; boundary definition = sutured. **A.** Core close-up. **B.** Plane-polarized light. Cpx = clinopyroxene, Pl = plagioclase. **C.** Under crossed polars.

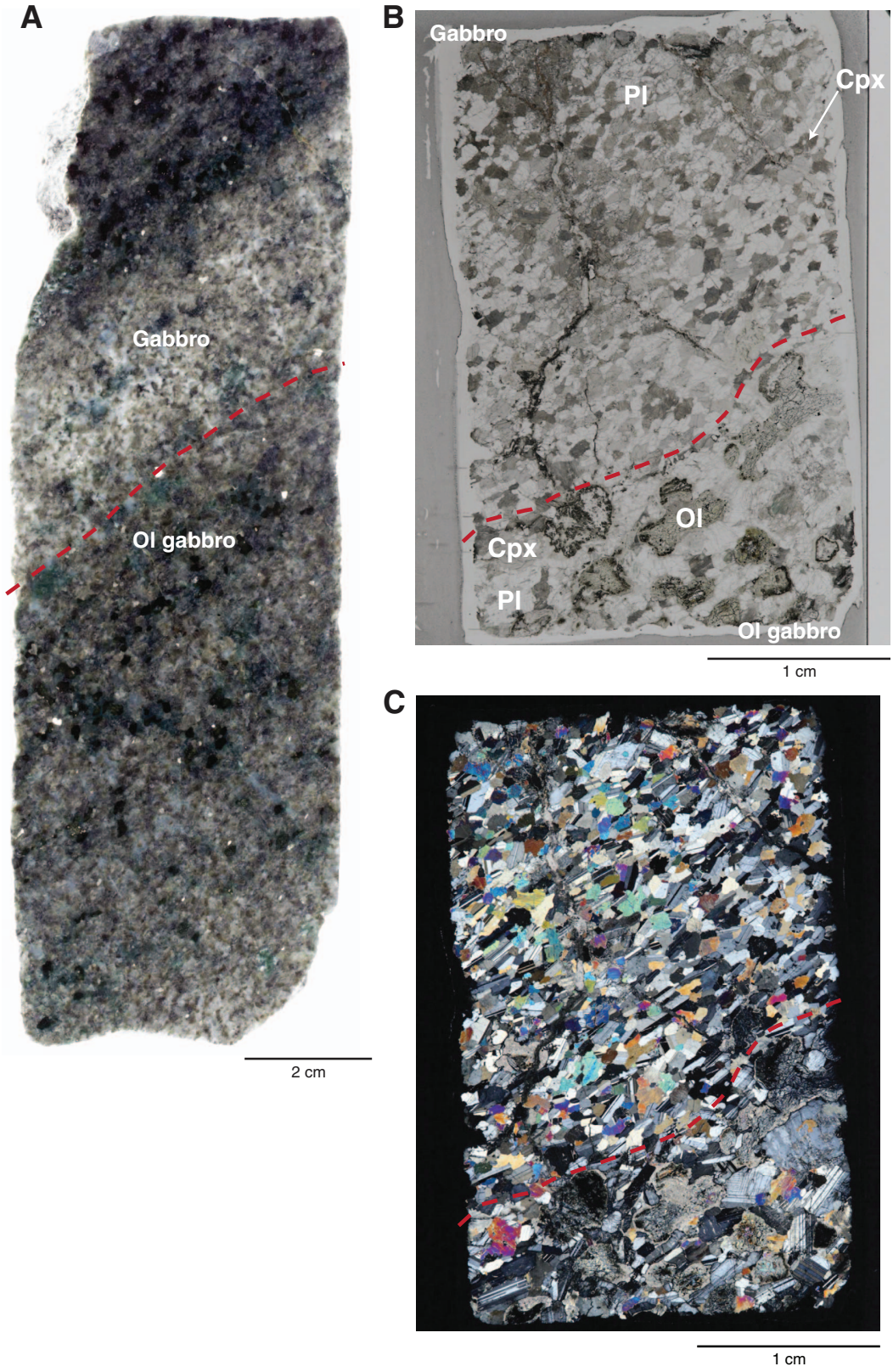

Figure F23. Boundary between troctolite and olivine (Ol) gabbro (red dashed lines) (Thin Section 58; Sample 345-U1415J-10R-1, 39–55 cm [Piece 6B]). Boundary type = grain size and modal; boundary definition = gradational. **A.** Core close-up. **B.** Plane-polarized light. (Ol) = altered olivine, Cpx = clinopyroxene, Pl = plagioclase. **C.** Under crossed polars.

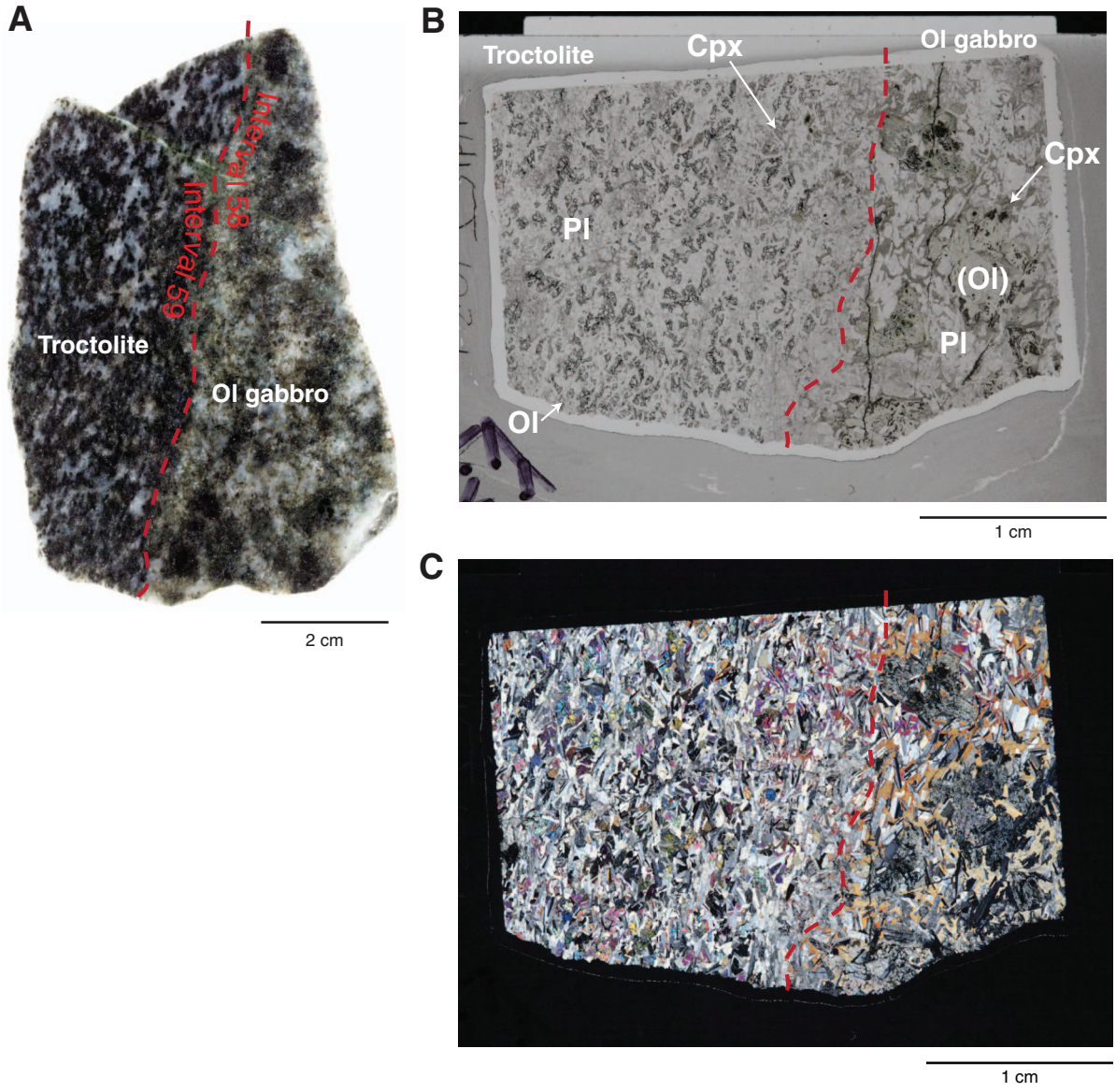

Figure F24. Boundary between olivine (Ol)-rich troctolite and troctolite (red dashed lines) (Thin Section 72; Sample 345-U1415J-18R-1, 141–146 cm [Piece 17B]). Boundary type = grain size and modal; boundary definition = sutured. **A.** Close-up image. **B.** Plane-polarized light. Ol-rich troctolite = olivine-rich gabbro, (Ol) = altered olivine, Pl = plagioclase. **C.** Under crossed polars.

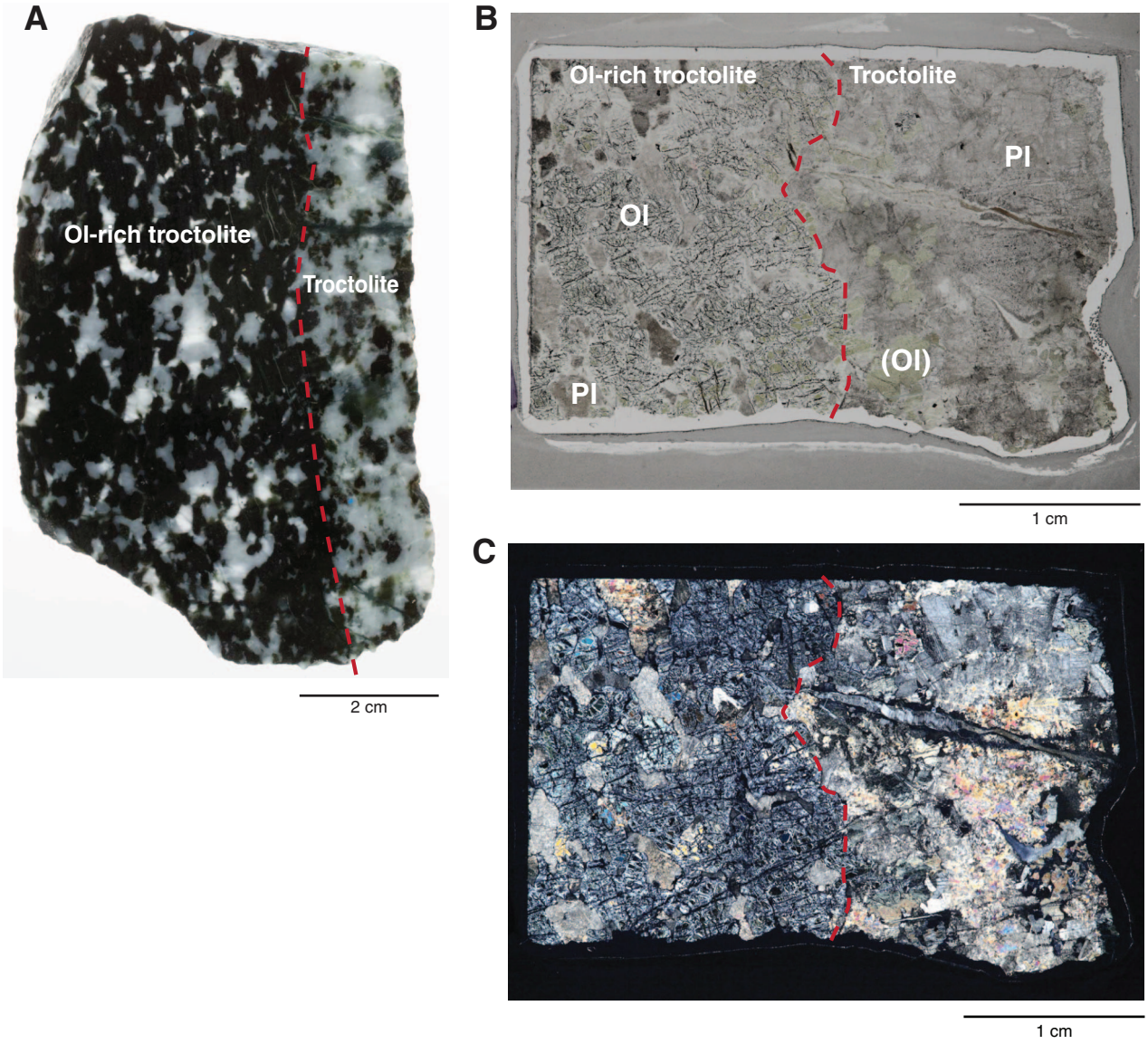

Figure F25. Boundary between olivine (Ol)-bearing gabbro and gabbro (red dashed lines) (Thin Section 85; Sample 345-U1415J-25G-1, 30–38 cm [Piece 5]). Boundary type = modal; boundary definition = sutured. **A.** Close-up image. **B.** Plane-polarized light. Pl = plagioclase, Cpx = clinopyroxene. **C.** Under crossed polars. **D.** Clinopyroxenes with interfingering texture. Opx = orthopyroxene.

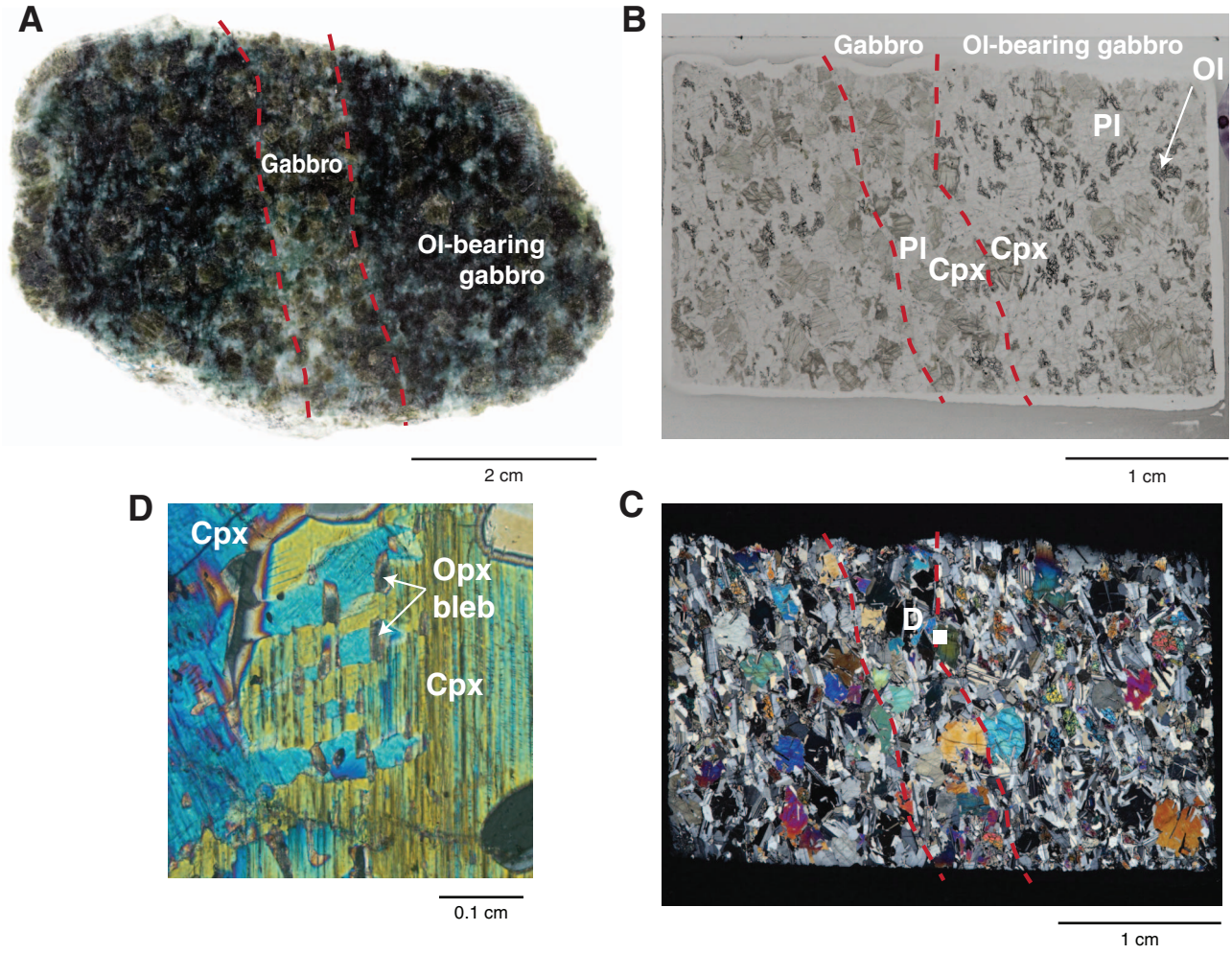

Figure F26. Clinopyroxene oikocryst-bearing troctolite, Unit II. **A.** Sample 345-U1415J-8R-3A, 79–91 cm (Piece 9); Interval 49. **B.** Sketch of core section. Note the tails of clinopyroxene oikocrysts. **C.** Thin section image (length of section = 3.2 cm) (Thin Section 55; Sample 345-U1415J-8R-3, 83–86 cm [Piece 9]; under crossed polars). Note that interstitial clinopyroxene crystals (red arrows) share the same extinction angles with a large clinopyroxene oikocryst.

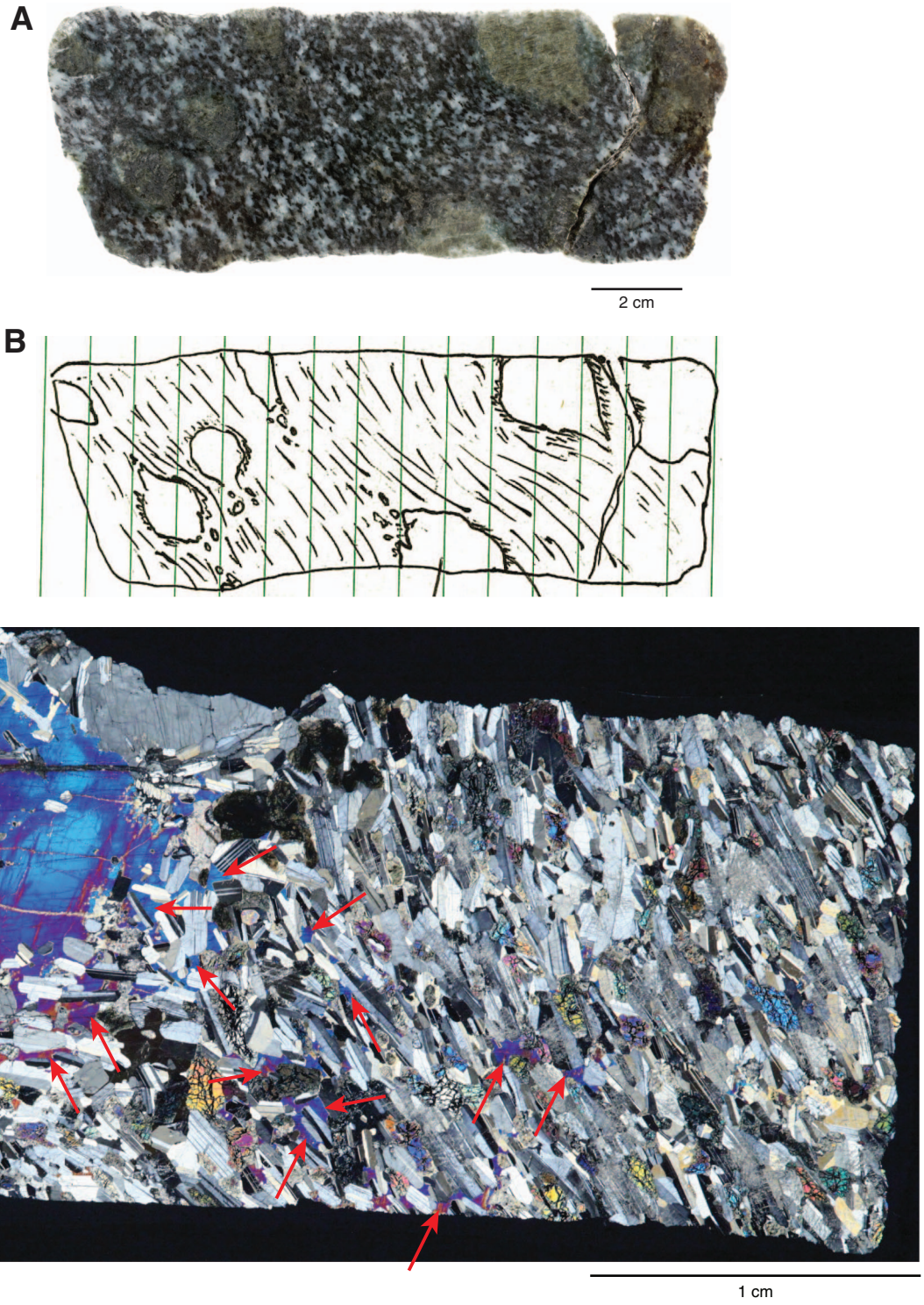

Figure F27. Clinopyroxene (Cpx) oikocryst-bearing troctolite, Unit II (Thin Section 53; Sample 345-U1415J-8R-3, 26–29 cm [Piece 5]; Interval 47; under crossed polars). **A.** Thin section image (length of section = 3.1 cm). **B.** A film of clinopyroxene occurs between olivine (Ol) and plagioclase (Pl) grains in the troctolitic matrix. **C.** Boundary between a clinopyroxene oikocryst and the troctolitic matrix. Some plagioclase crystals that are partly included in the oikocryst develop their facet.

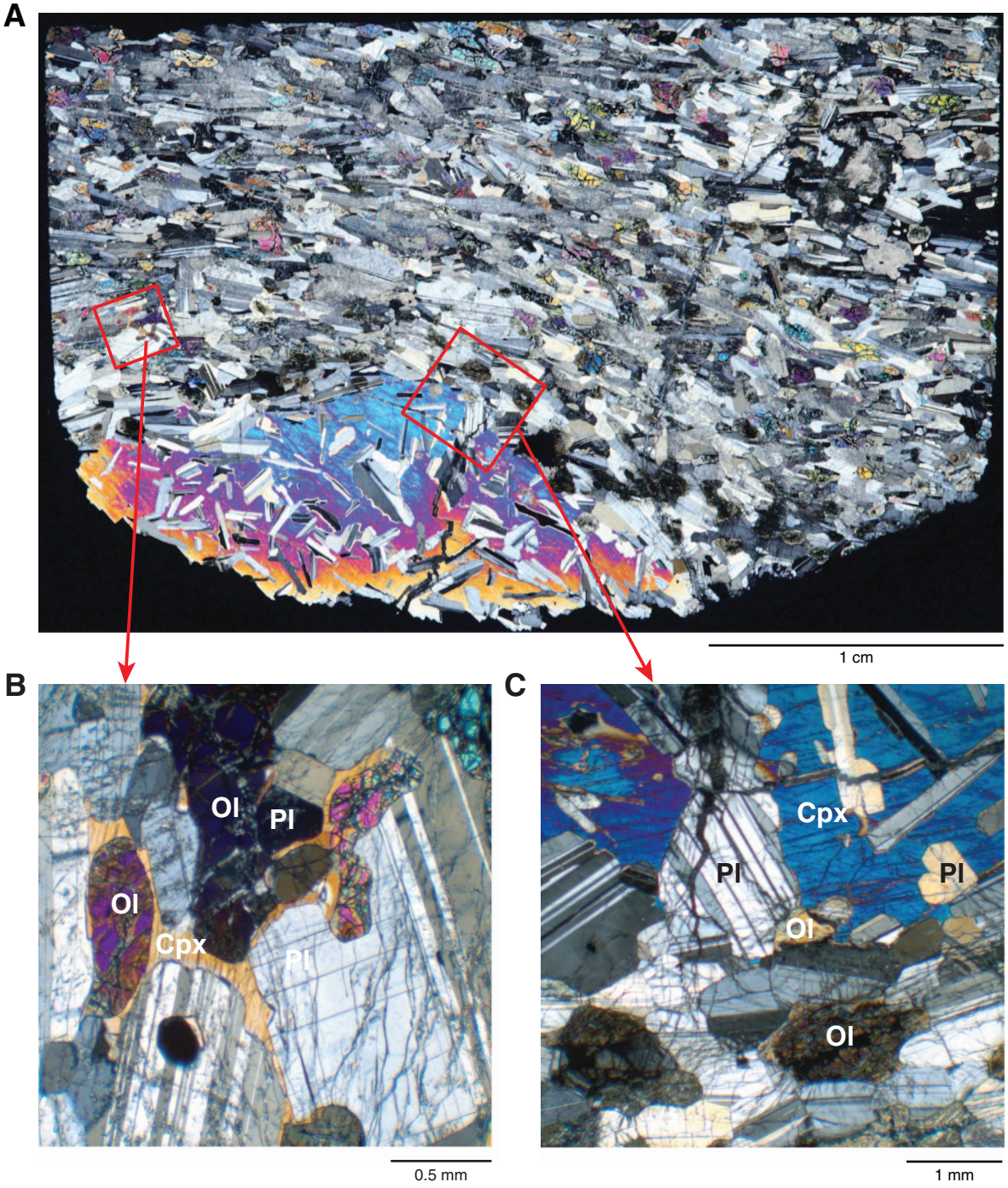

Figure F28. Plagioclase (Pl) chadacrysts included in clinopyroxene (Cpx) oikocrysts in clinopyroxene oikocryst-bearing troctolite, Unit II (under crossed polars). Red arrows = deformation twins. **A, B.** Thin Section 53; Sample 345-U1415J-8R-3, 26–29 cm; Interval 47. **C, D.** Thin Section 55; Sample 345-U1415J-8R-3, 83–86 cm; Interval 49.

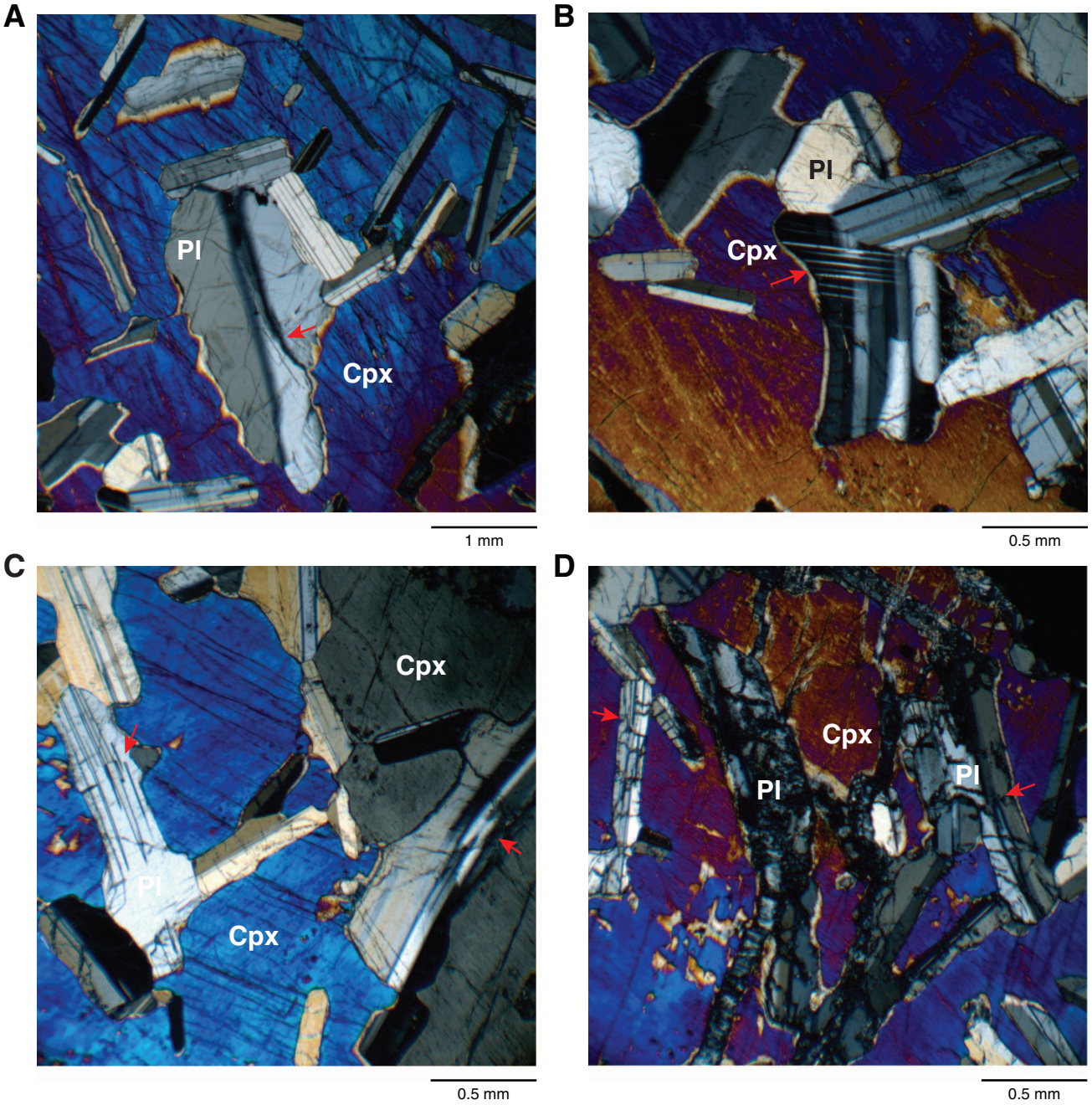

Figure F29. Skeletal olivine (Ol) morphology (under crossed polars). See text for details. Cpx = clinopyroxene, Pl = plagioclase. **A.** Thin Section 21; Sample 345-U1415J-4R-1, 35–38 cm (Piece 6). **B.** Thin Section 31; Sample 345-U1415J-3R-1, 45–48 cm (Piece 10). **C.** Thin Section 32; Sample 345-U1415J-3R-1, 73–75 cm (Piece 14). **D.** Thin Section 36; Sample 345-U1415J-5R-1, 62–64 cm (Piece 12). **E.** Thin Section 58; Sample 345-U1415J-10R-1, 53–55 cm (Piece 6B). **F.** Thin Section 85; Sample 345-U1415J-25G-1, 32–35 cm (Piece 5).

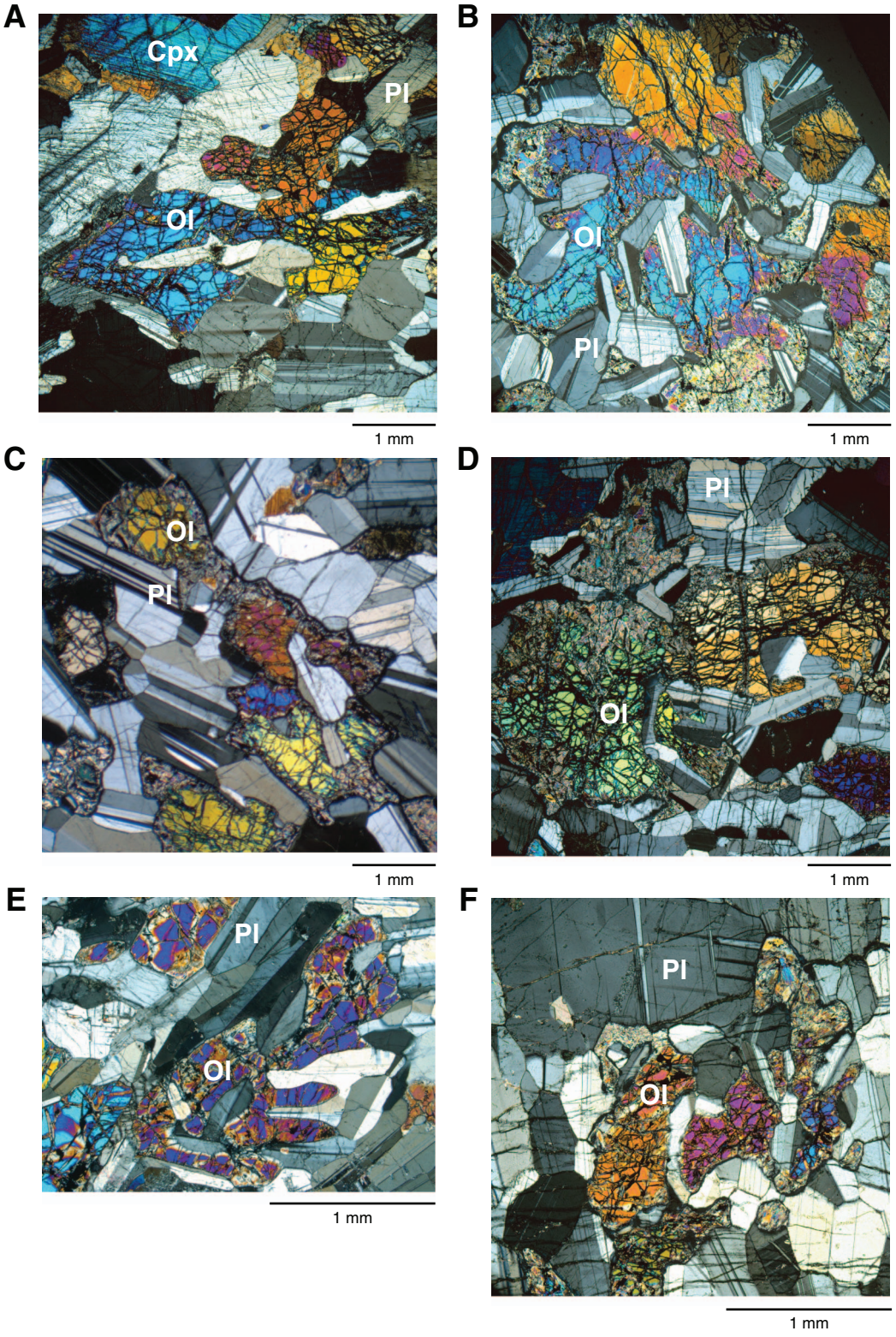

Figure F30. Skeletal olivine (Ol) (Sample 345-U1415J-11R-1, 23–28 cm [Piece 4]). **A.** Core close-up. Red dashed lines define the skeletal growth of olivine branches. **B.** Dendritic or star burst growth of olivine (Thin Section 59; under crossed polars). See text for details. Cpx = clinopyroxene, Pl = plagioclase.

Figure F31. Chromitite (Thin Section 71; Sample 345-U1415J-18R-1, 67–73 cm [Piece 9]). **A.** Core close-up. "Chr" = altered chromitite, Tro = troctolite. **B.** Plane-polarized light. **C.** Under crossed polars. **D.** Chromite pseudomorph with globular inclusions. Mgt = magnetite.

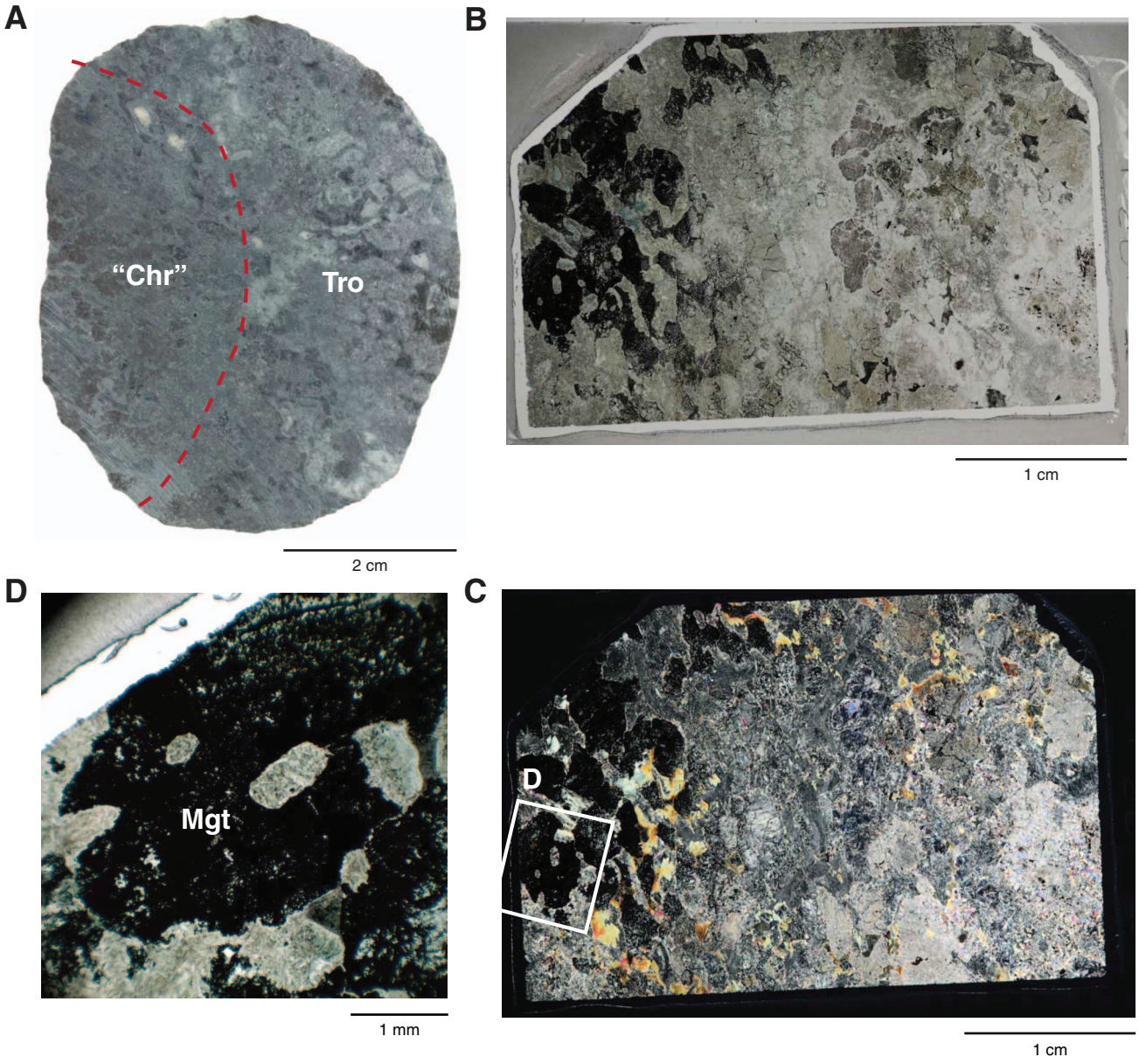

Figure F32. Chromitite (Thin Section 75; Sample 345-U1415J-21R-1, 4–12 cm [Piece 2]). **A.** Core close-up. **B.** Plane-polarized light. **C.** Under crossed polars. **D.** Typical appearance of ferrite chromites (Ferr chr), which are tabular in shape. Chl = chlorite. **E.** Assembly of tabular-shaped ferrite chromites.

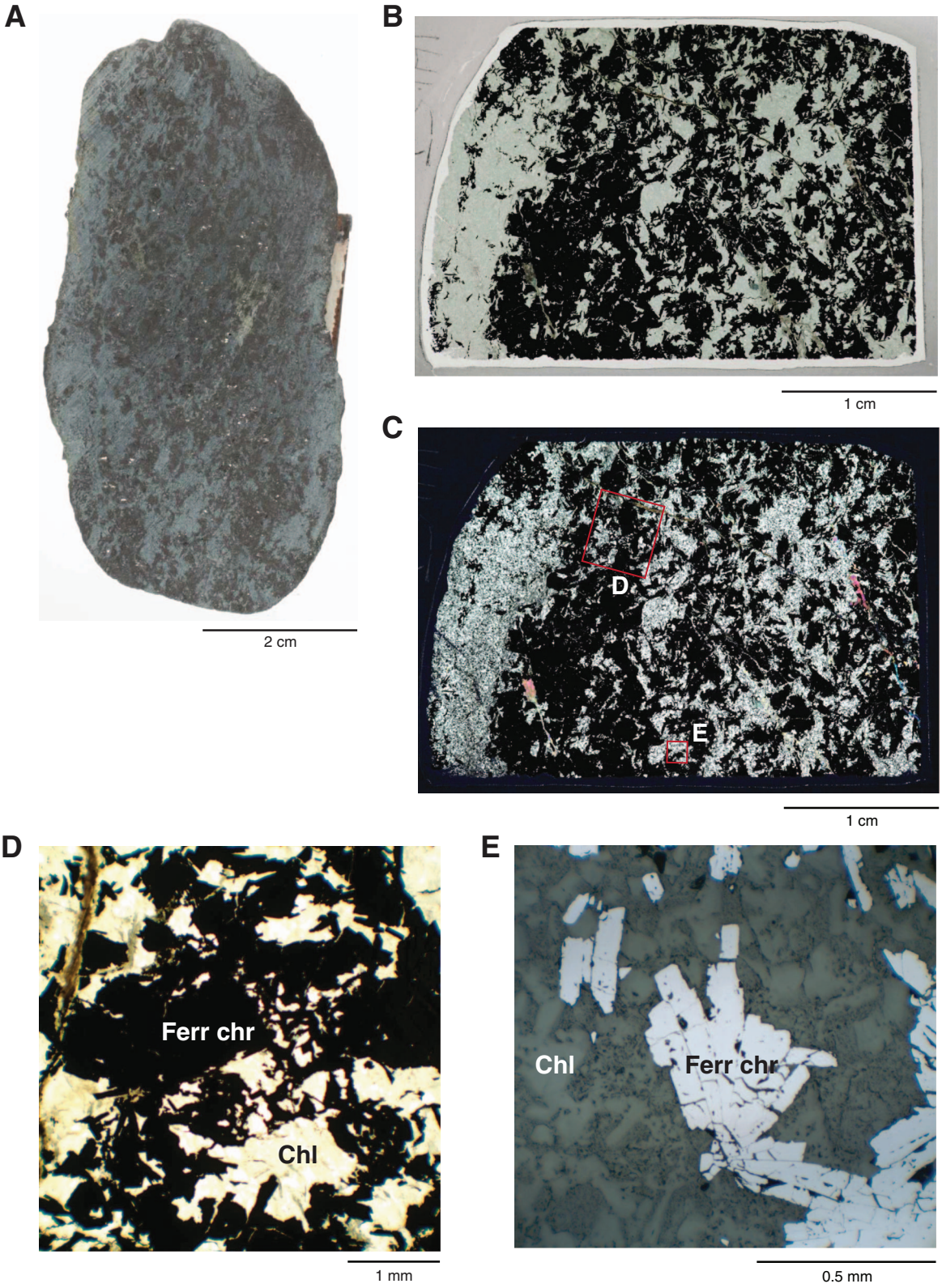

Figure F33. Chromitite (Thin Section 76; Sample 345-U1415J-21R-1, 12–16 cm [Piece 3]). **A.** Core close-up. **B.** Plane-polarized light. **C.** Under crossed polars. **D.** Chromite (Chr) with magnetite (Mgt) aureole.

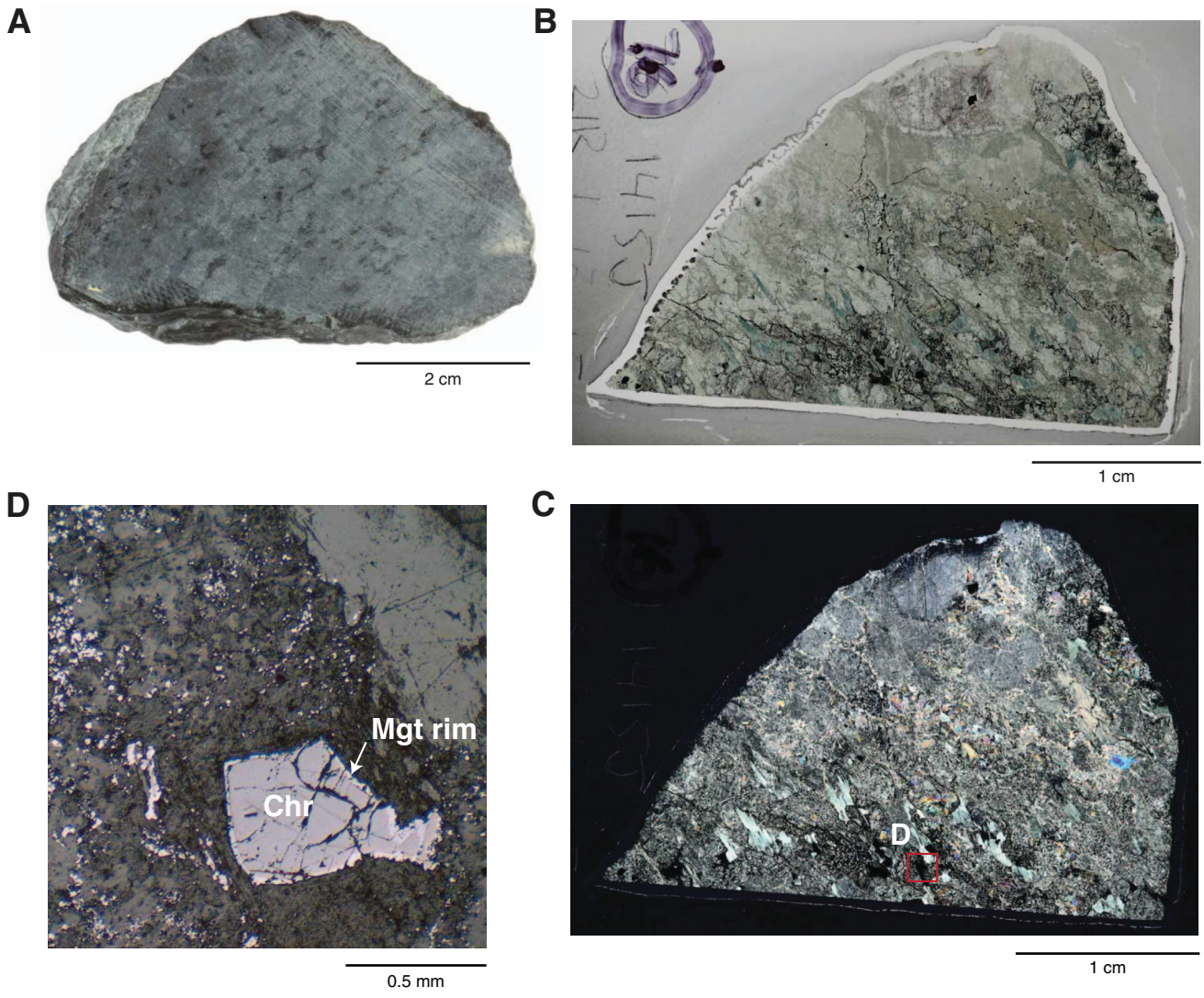

Figure F34. Downhole variation in alteration intensity of igneous minerals, Unit I. Cpx = clinopyroxene, Ol = olivine.

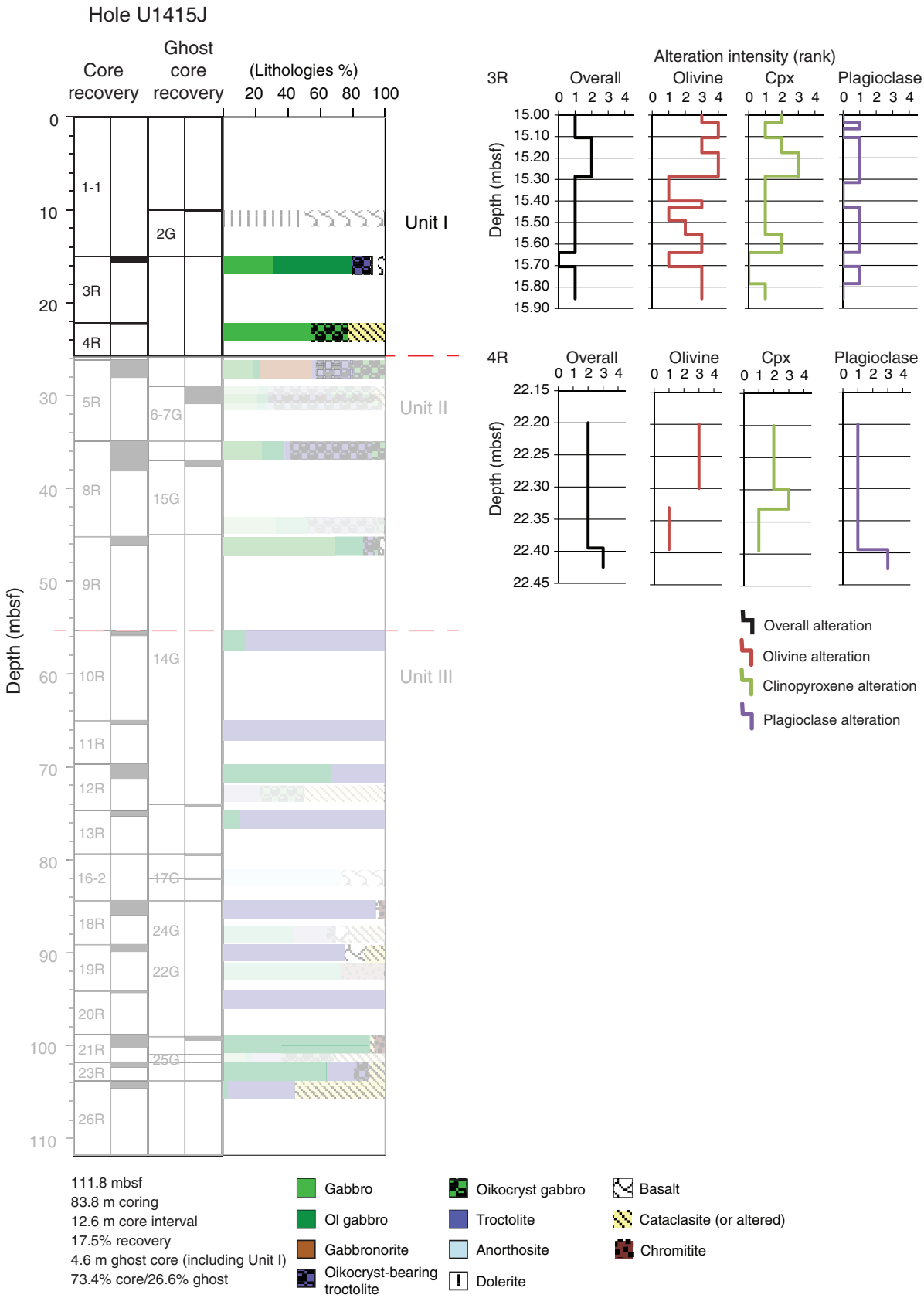

Figure F35. Downhole variation in alteration intensity of igneous minerals, Unit II. Cpx = clinopyroxene, Ol = olivine.

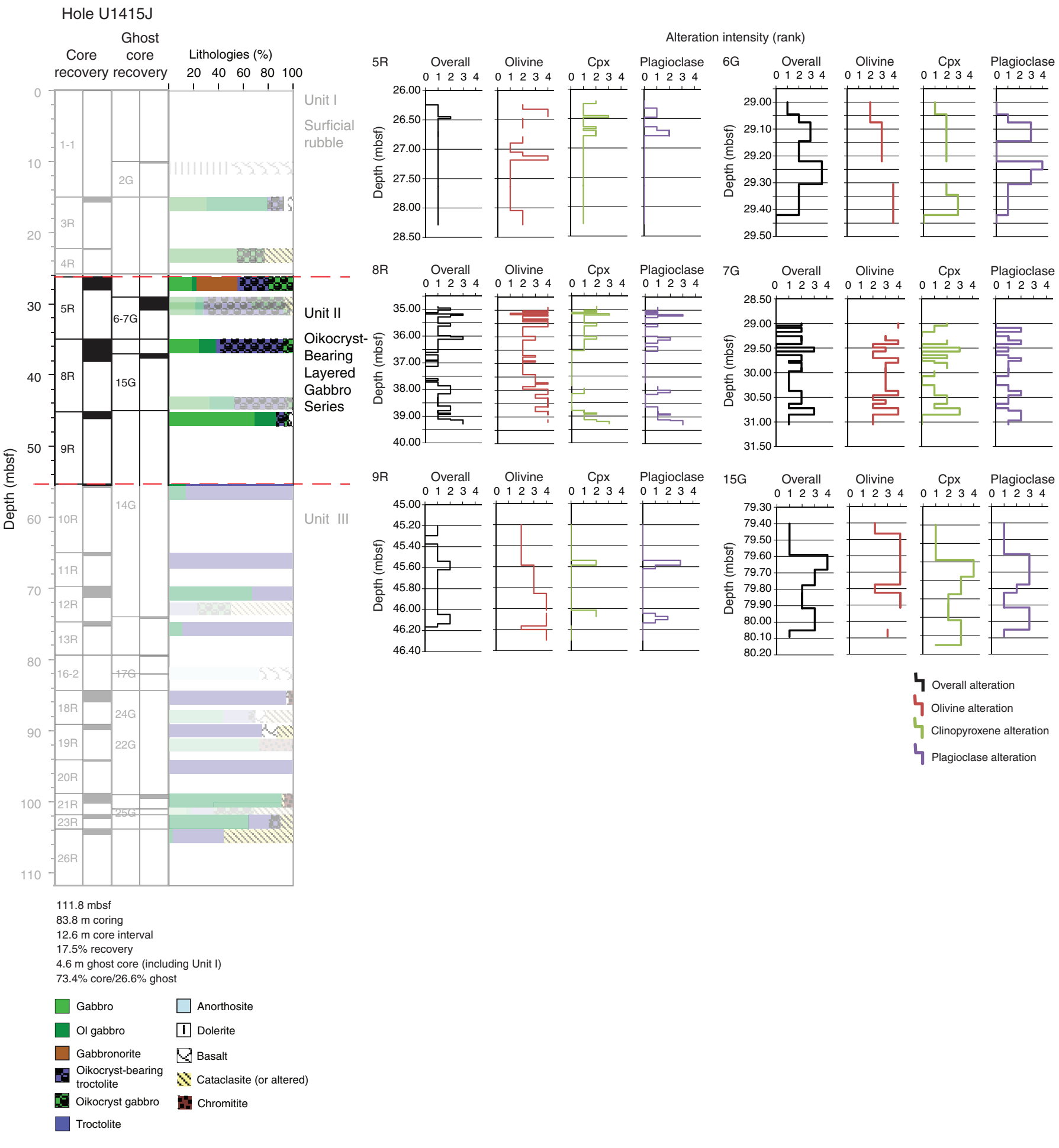

Figure F36. A. Downhole variation in alteration intensity of igneous minerals, Unit III. Cpx = clinopyroxene, Ol = olivine. (Continued on next page.)

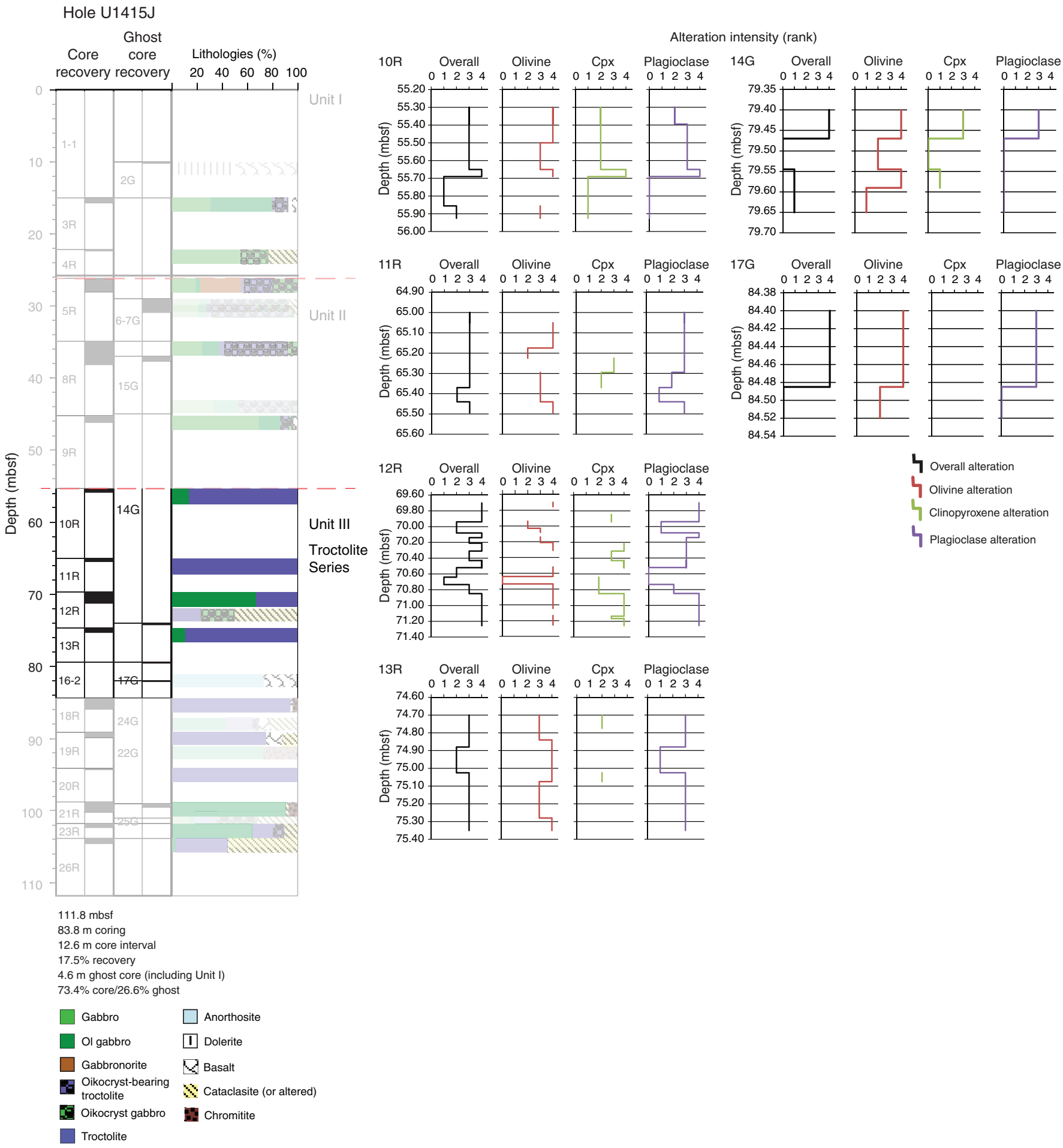

Figure F36 (continued). B. Downhole variation in alteration intensity of igneous minerals, Unit III. Cpx = clinopyroxene, Ol = olivine.

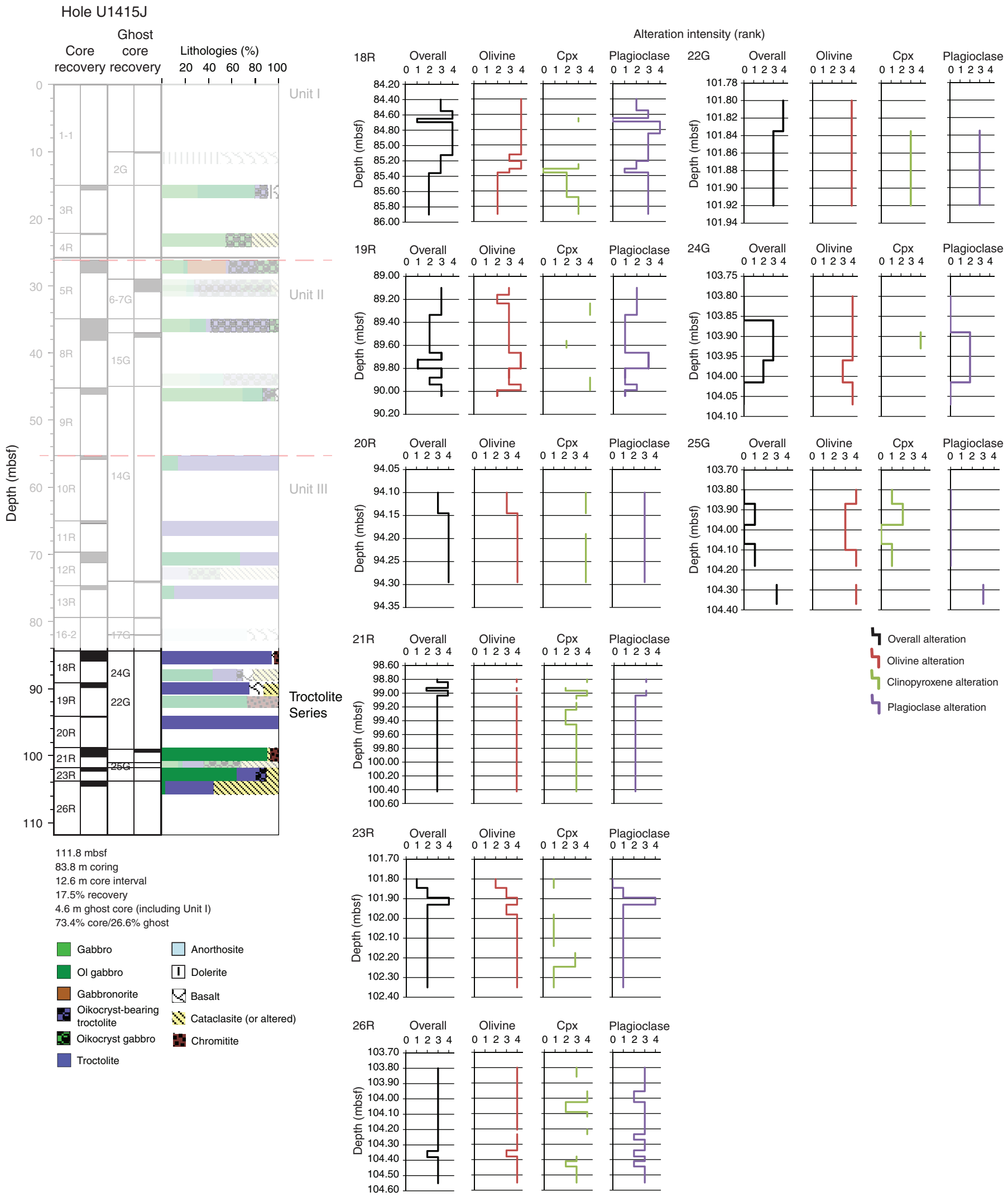

Figure F37. Typical alteration assemblage texture in Unit II showing serpentine (Srp) veins in olivine (Ol) and cracks in plagioclase (Pl) that tend to be subparallel with magmatic foliation in clinopyroxene oikocryst-bearing troctolite. Clay minerals are abundant near densely fractured plagioclase (Thin Section 37; Sample 345-U1415J-5R-1, 117–120 cm [Piece 17B]). **A.** Plane-polarized light. **B.** Under crossed polars.

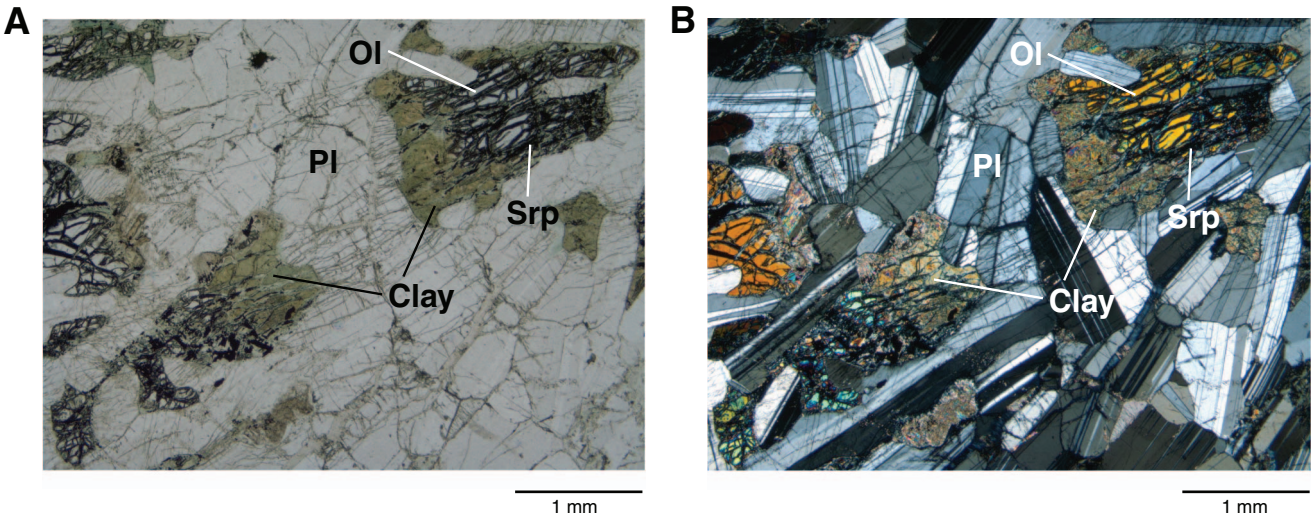

Figure F38. Typical coronitic alteration of olivine, Unit II. **A, B.** Grain edge rimmed by a typical corona, with a rim of cryptocrystalline chlorite (Chl), tremolite (Tr), and talc (Tc) that has formed between plagioclase (Pl) and relict olivine (Ol) in clinopyroxene-bearing olivine gabbro (Thin Section 41; Sample 345-U1415J-7G-1, 35–38 cm [Piece 6]). **C, D.** Olivine with well-developed coronae, surrounded by plagioclase. Note the lack of radial fractures (Thin Section 40; Sample 345-U1415J-7G-1, 28–31 cm [Piece 5]). **E, F.** Clinopyroxene oikocryst-bearing troctolite/gabbronorite in which pseudomorphic replacement of olivine by tremolite and chlorite ± talc (Tc) is concentrated around a chlorite vein that cuts magmatic foliation with a high intersection angle. Amp = amphibole. A, C, and E are under plane-polarized light; B, D, and F are under crossed polars.

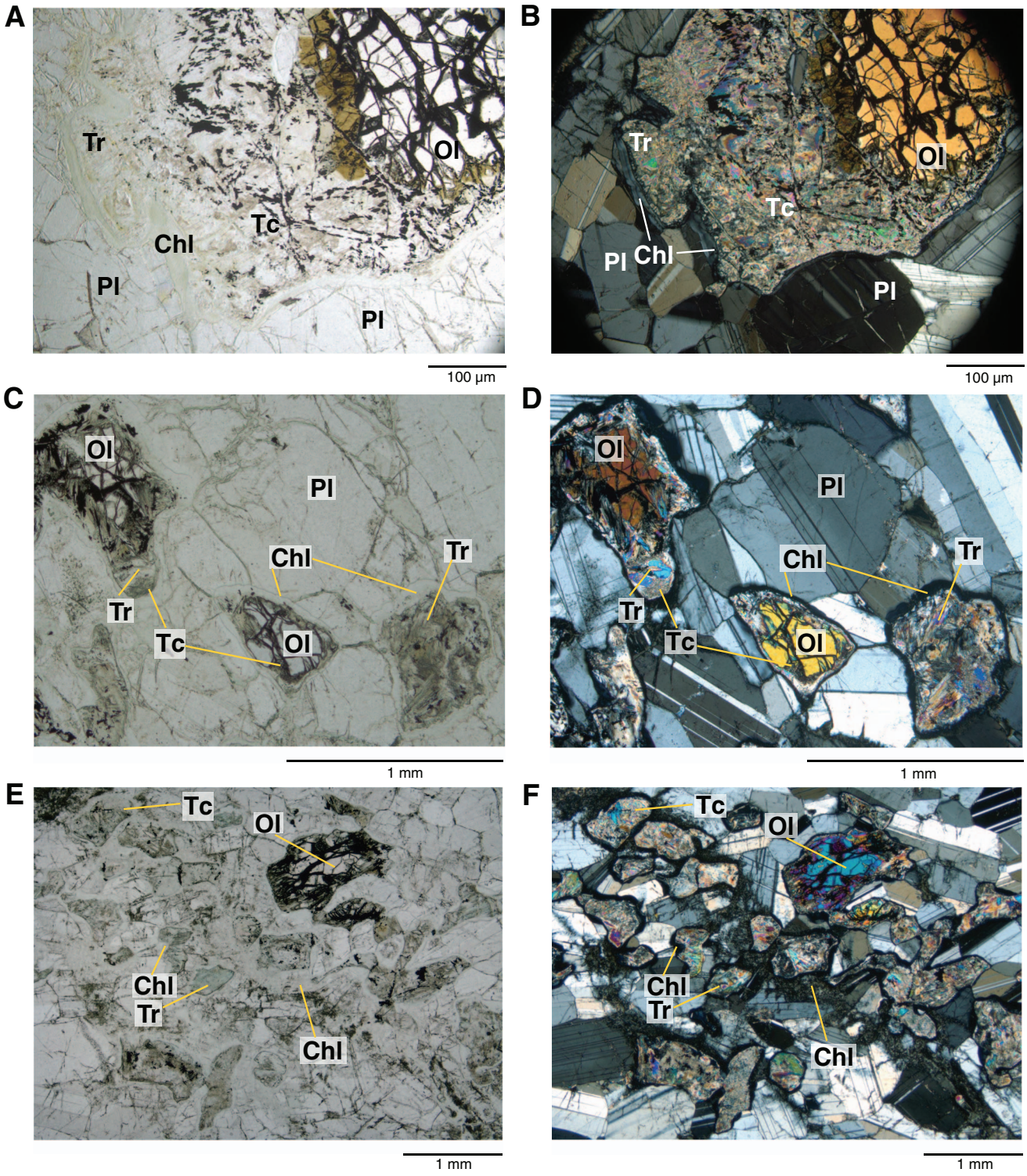

Figure F39. Variation in the percentage of olivine alteration and corona development observed in thin sections, Hole U1415J. Unit III olivine is somewhat more altered and has slightly more corona development than in Units I and II (see also Fig. F37).

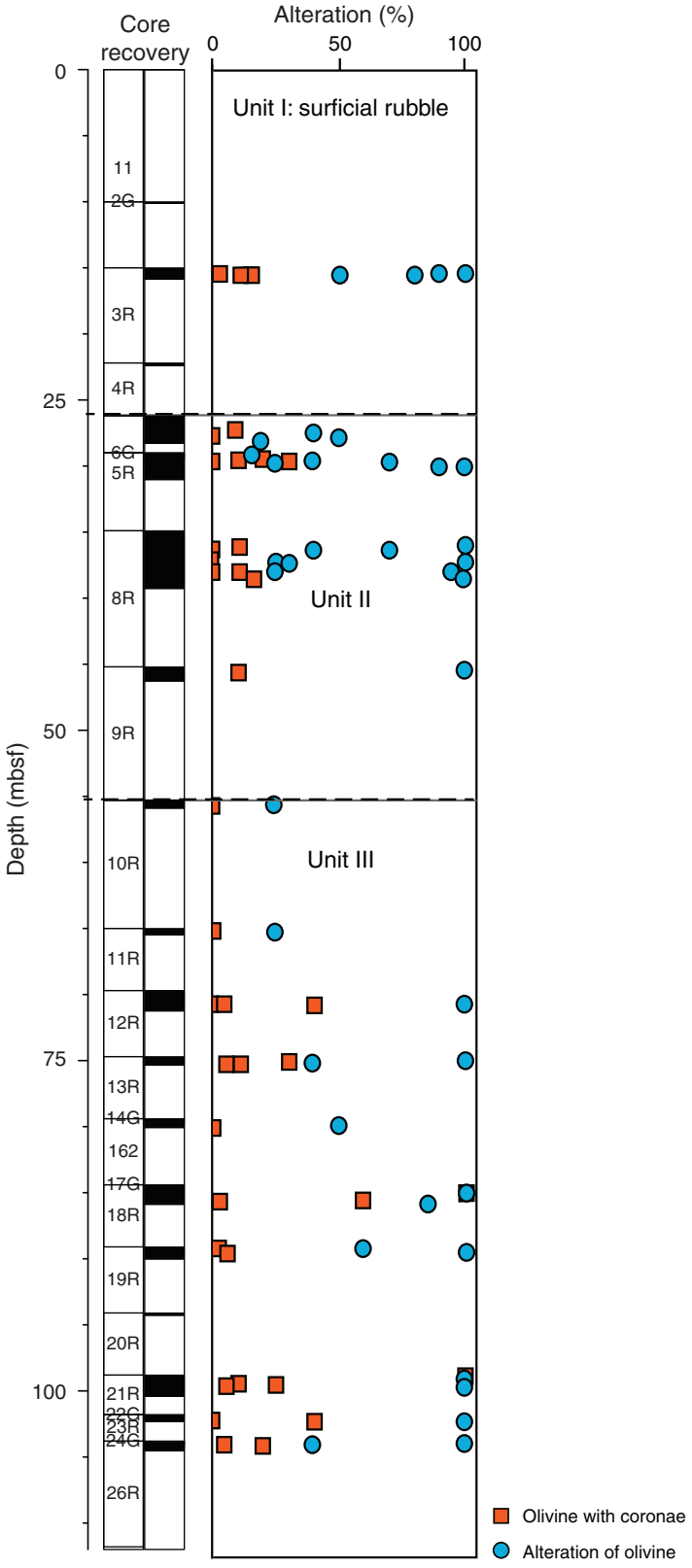

Figure F40. Strongly altered olivine (Ol) gabbro in which green spinel (Spl) completely surrounded by chlorite (Chl) forms a corona texture with pale green amphibole (Am). Clinozoisite (Czo) and prehnite (Prh) pseudomorphically replace plagioclase (Thin Section 67; Sample 345-U1415J-13R-1, 53–56 cm [Piece 7]). **A.** Plane-polarized light. **B.** Under crossed polars.

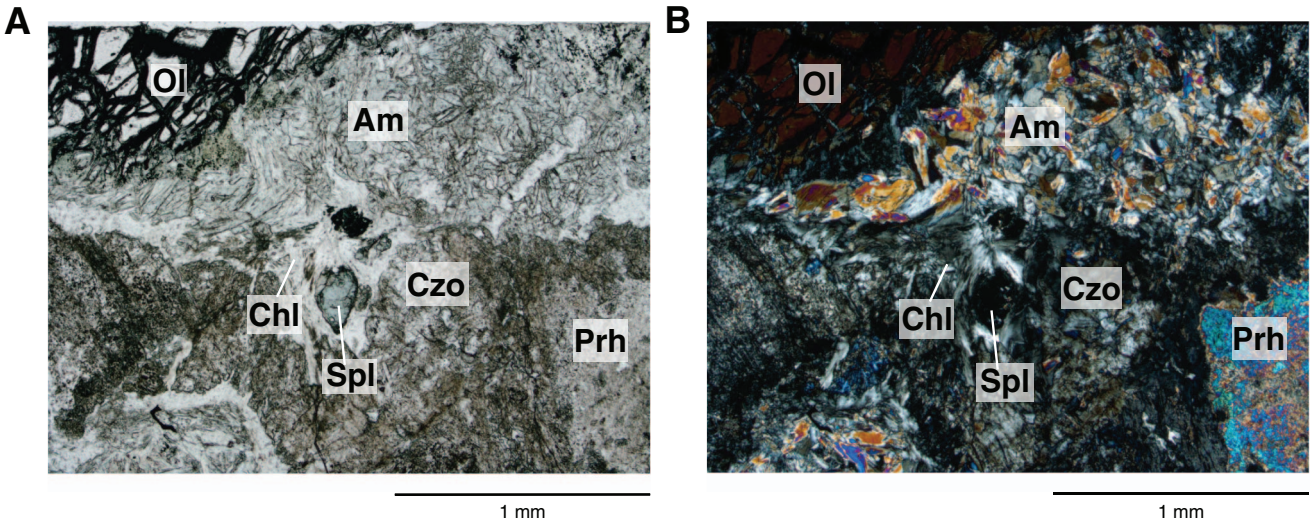

Figure F41. Olivine-bearing gabbro in which clinopyroxene (Cpx) is partially replaced by amphibole (Am) at rims or along cleavage surfaces. Amphibole is colorless to green and bluish green, suggesting variation in chemical composition. Plagioclase (Pl) is partially replaced by chlorite (Chl) (Thin Section 56; Sample 345-U1415J-8R-3, 112–115 cm [Piece 12]). **A.** Plane-polarized light. **B.** Under crossed polars.

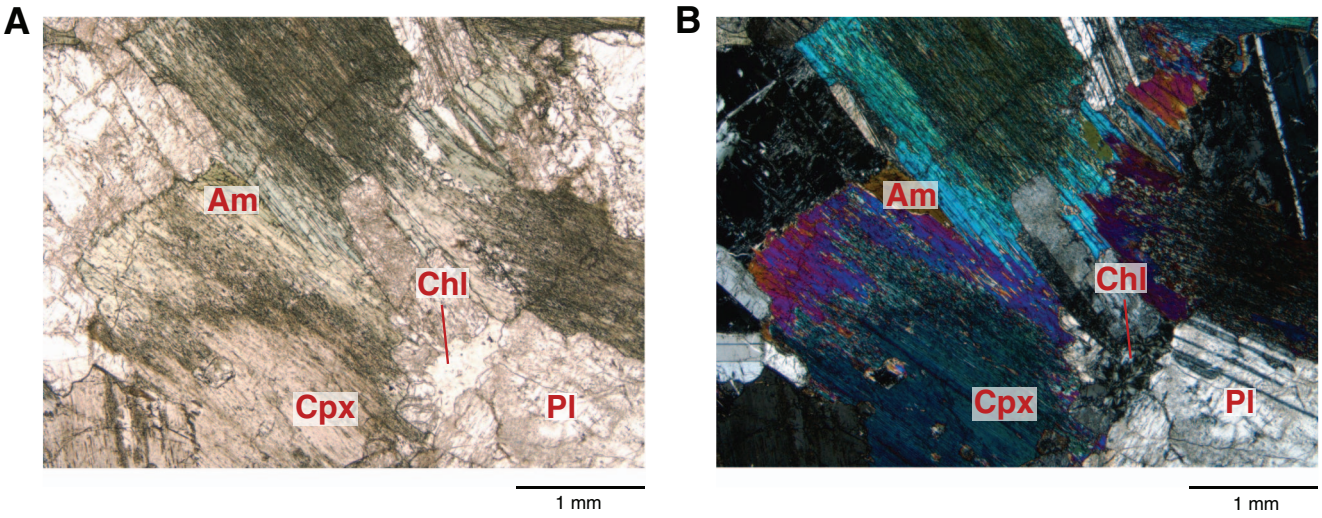

Figure F42. Brown amphibole (Am) intergrown with green amphibole replacing clinopyroxene in olivine gabbro (Thin Section 82; Sample 345-U1415J-23R-1, 39–42 cm [Piece 7]). Pl = plagioclase, Pr = prehnite. **A.** Plane-polarized light. **B.** Under crossed polars.

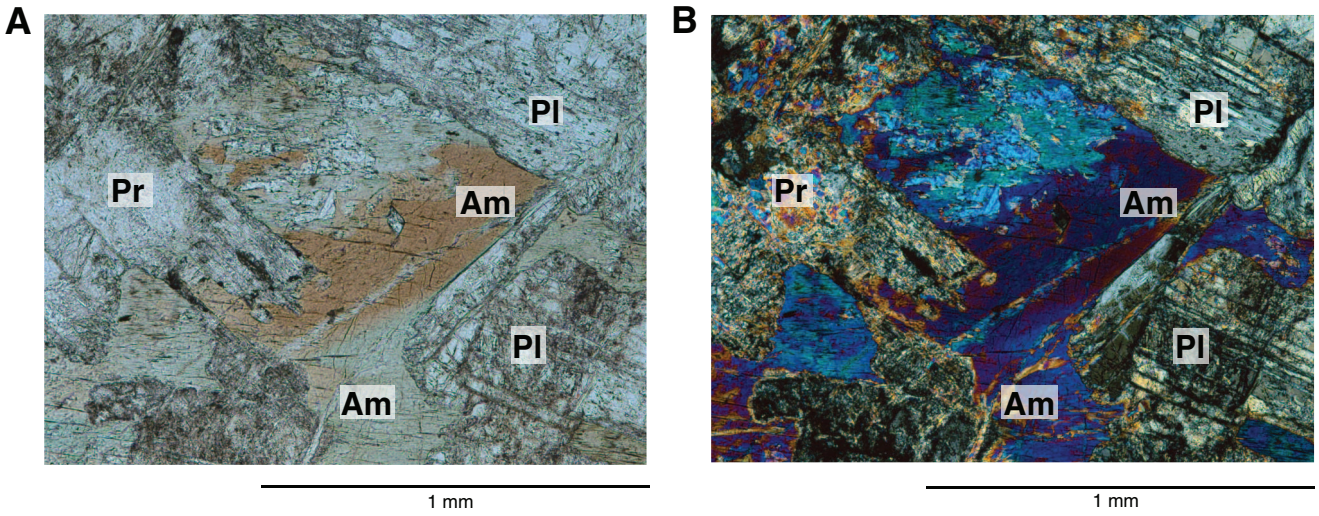

Figure F43. Gabbro in which orthopyroxene (Opx) is replaced by colorless and pale green amphibole (Am) along fractures and cleavage surfaces. Olivine (Ol) is completely replaced by tremolite, talc, serpentine, and clay minerals. Coronitic chlorite (Chl) formed between olivine and plagioclase (Pl) is common but is lacking at the contact with orthopyroxene (Thin Section 29; Sample 345-U1415J-3R-1, 11–13 cm [Piece 4]). **A.** Plane-polarized light. **B.** Under crossed polars.

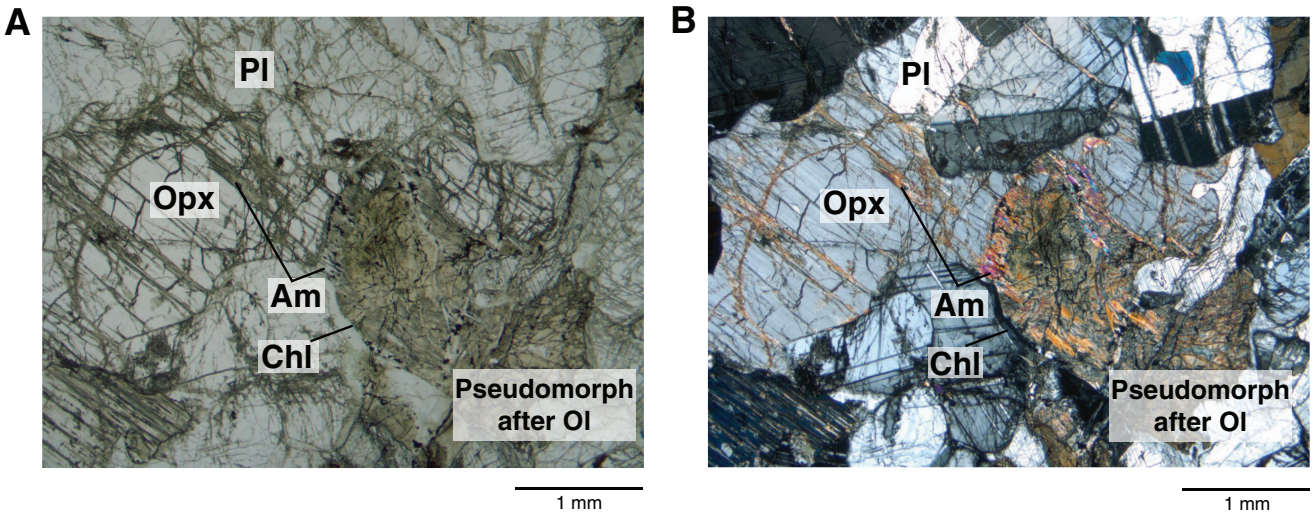

Figure F44. Completely altered chromitite (Thin Section 75; Sample 345-U1415J-21R-1, 9–11 cm [Piece 4]). **A, B.** Chromitite with abundant chlorite (Chl) and magnetite (possibly after chromite). White boxes show locations of C and D. **C, D.** Amphibole (Am) and chlorite with unusual bluish green color in magnetite (Mag) and chlorite-rich rock, which seem to be originally chromitite or chromite-rich troctolite. A and D are under crossed polars; B and C are under plane-polarized light.

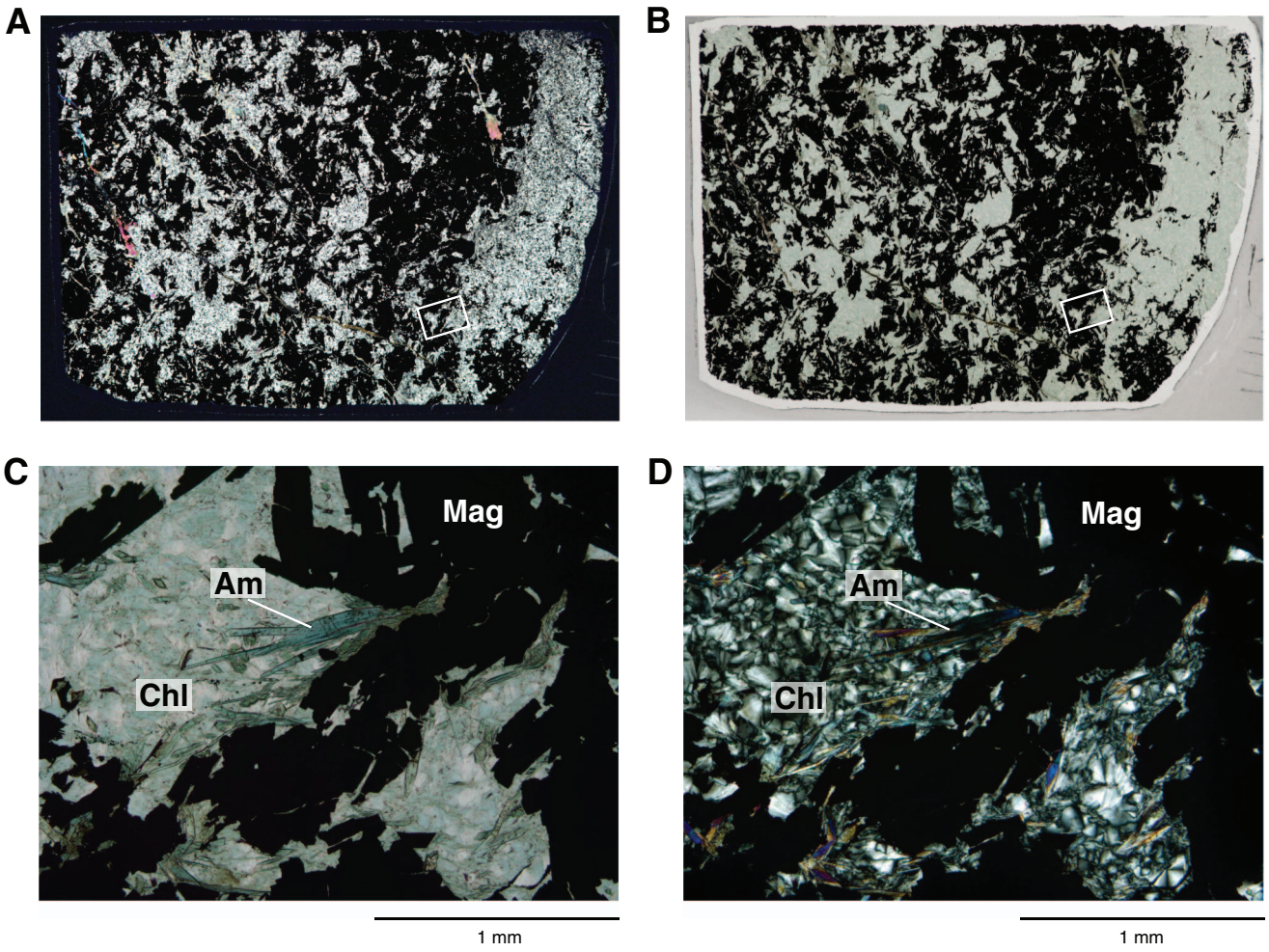

Figure F45. Typical plagioclase (Pl) alteration (under crossed polars). **A.** Simple chlorite (Chl) veins cutting plagioclase adjacent to olivine in gabbro. Chlorite forms a rim around relict olivine that is replaced by clay minerals ± talc and amphibole (Am) (Thin Section 29; Sample 345-U1415J-3R-1, 11–13 cm [Piece 4]). **B.** Diffuse amphibole and chlorite replacement veins in plagioclase. Note high-temperature (hypersolidus) annealed texture of plagioclase in clinopyroxene (Cpx) oikocryst-bearing gabbro (Thin Section 42; Sample 345-U1415J-7G-1, 91–94 cm [Piece 14]). **C, D.** Thin Section 39 (Sample 345-U1415J-5R-2, 60–63 cm [Piece 3]). (C) Irregular patch of chlorite + amphibole after plagioclase at grain boundary. Carbonate (likely calcite [Cal]) is present as a secondary phase, as well as small prehnite (Prh) veins in olivine-bearing gabbro. (D) Fluid inclusion (Fi) trails within plagioclase radiate from a chlorite-carbonate patch and presumably represent healed cracks following fracturing in olivine-bearing gabbro.

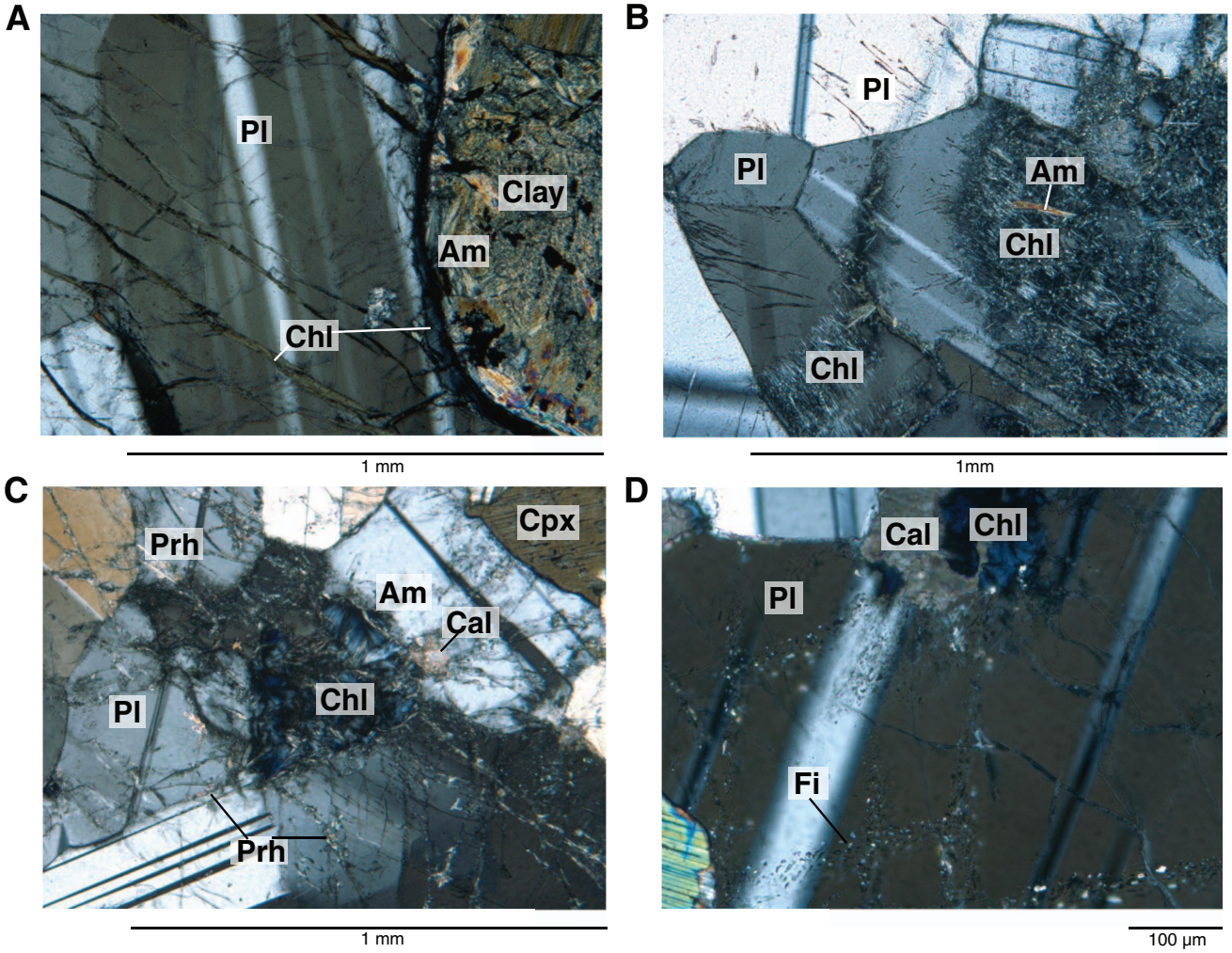

Figure F46. An example of relatively uncommon plagioclase alteration in troctolite (Thin Section 72; Sample 345-U1415J-18R-1, 141–143 cm [Piece 17B]). **A, B.** Replacement of plagioclase by prehnite (Prh), chlorite (Chl), and very fine grained garnet (Grt). Clinopyroxene (Cpx) rim around plagioclase is partially replaced by chlorite. White box in B shows area of enlargement in C. Srp = serpentine, Ol = olivine. **C.** Plagioclase replacement by prehnite and chlorite showing seams of garnet. Chlorite replaces thin clinopyroxene rims. A is under plane-polarized light; B and C are under crossed polars.

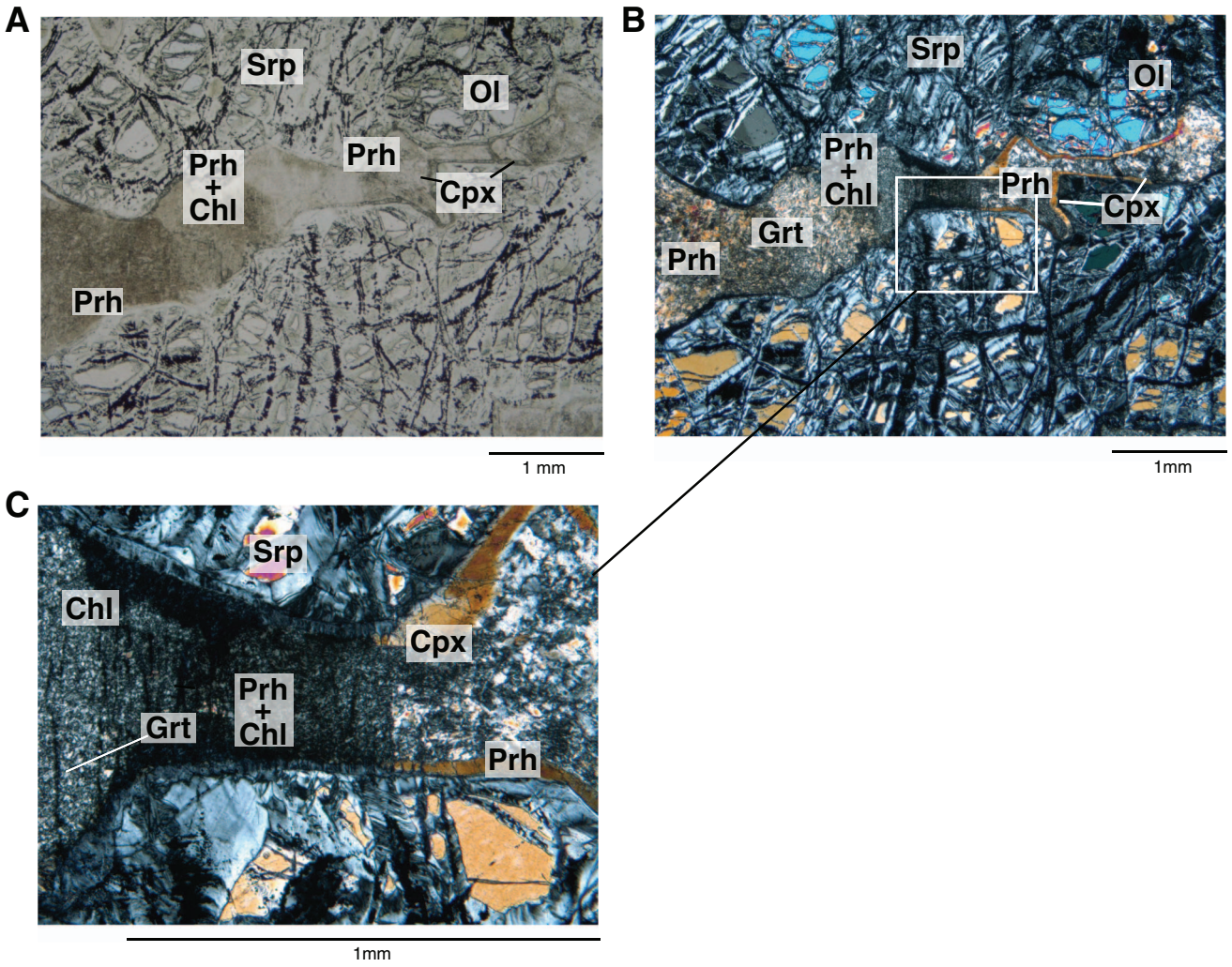

Figure F47. Relatively fresh plagioclase (Pl) with fine-grained prehnite (Prh)- and chlorite (Chl)-filled microcracks in gabbro cut by a perpendicular prehnite and chlorite vein (Thin Section 62; Sample 345-U1415J-12R-1, 86–89 cm [Piece 12]; cross-polarized light). Coarse-grained prehnite veins with chlorite in the center appear to originate in the cataclastic zone.

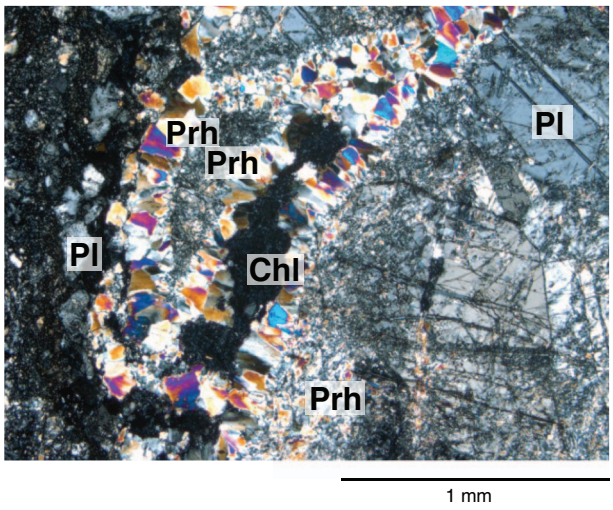

Figure F48. Relative abundance of different vein types in the surficial rubble Unit I, Oikocryst-Bearing Layered Gabbro Series Unit II, and Troctolite Series Unit III, Hole U1415J.

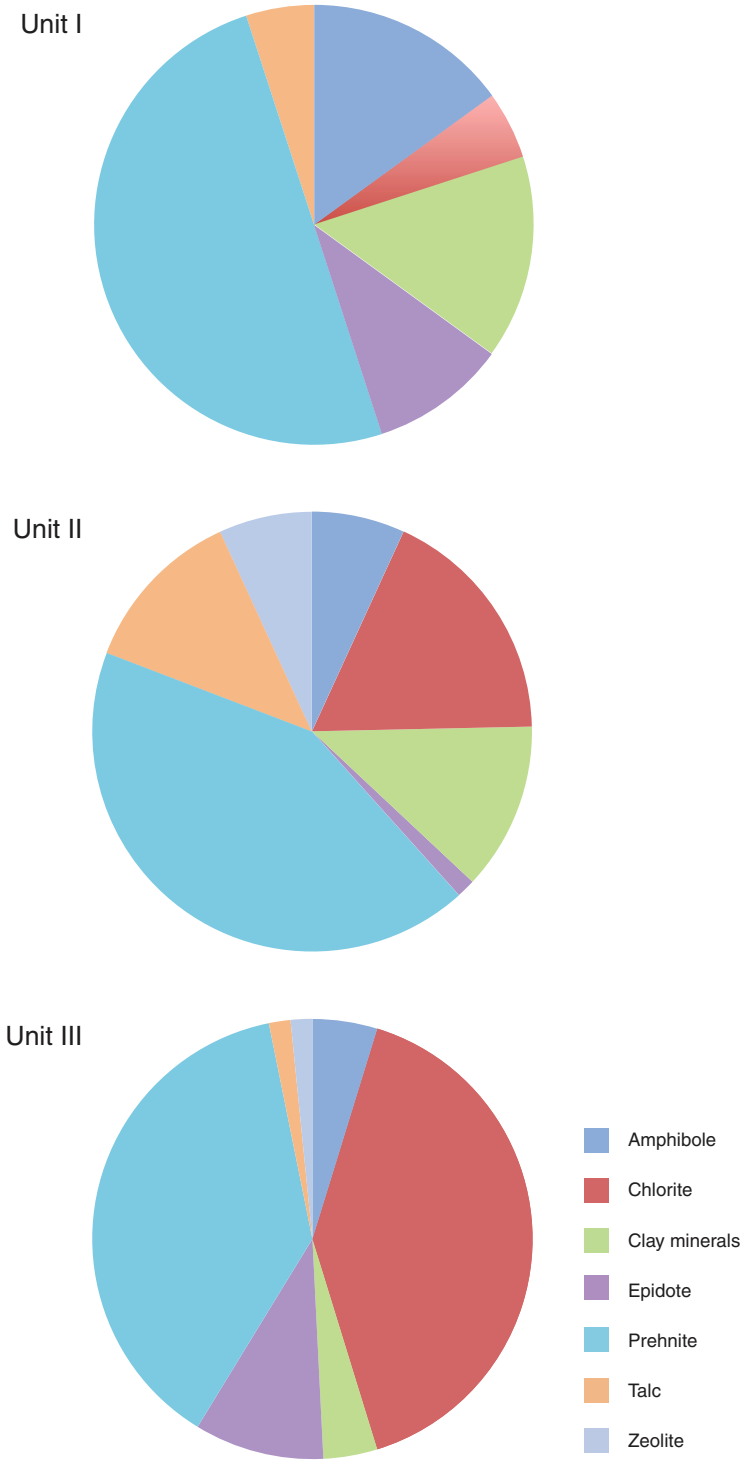

Figure F49. Typical veins. **A.** Prehnite vein with halo in a subcataclastic piece in oikocryst gabbro (interval 345-U1415J-5R-1, 50–59 cm). **B.** Deformed prehnite vein showing boudinage and a network of thin chlorite veins in a cataclastic piece of olivine gabbro (interval 345-U1415J-21R-1, 113–124 cm). **C.** Deformed amphibole vein in olivine gabbro (interval 345-U1415J-13R-1, 50.5–56 cm). **D.** Cataclastic gabbro from the ghost section containing clinozoisite, epidote, and prehnite veins (interval 345-U1415J-14G-1, 0–7 cm [Piece 1]).

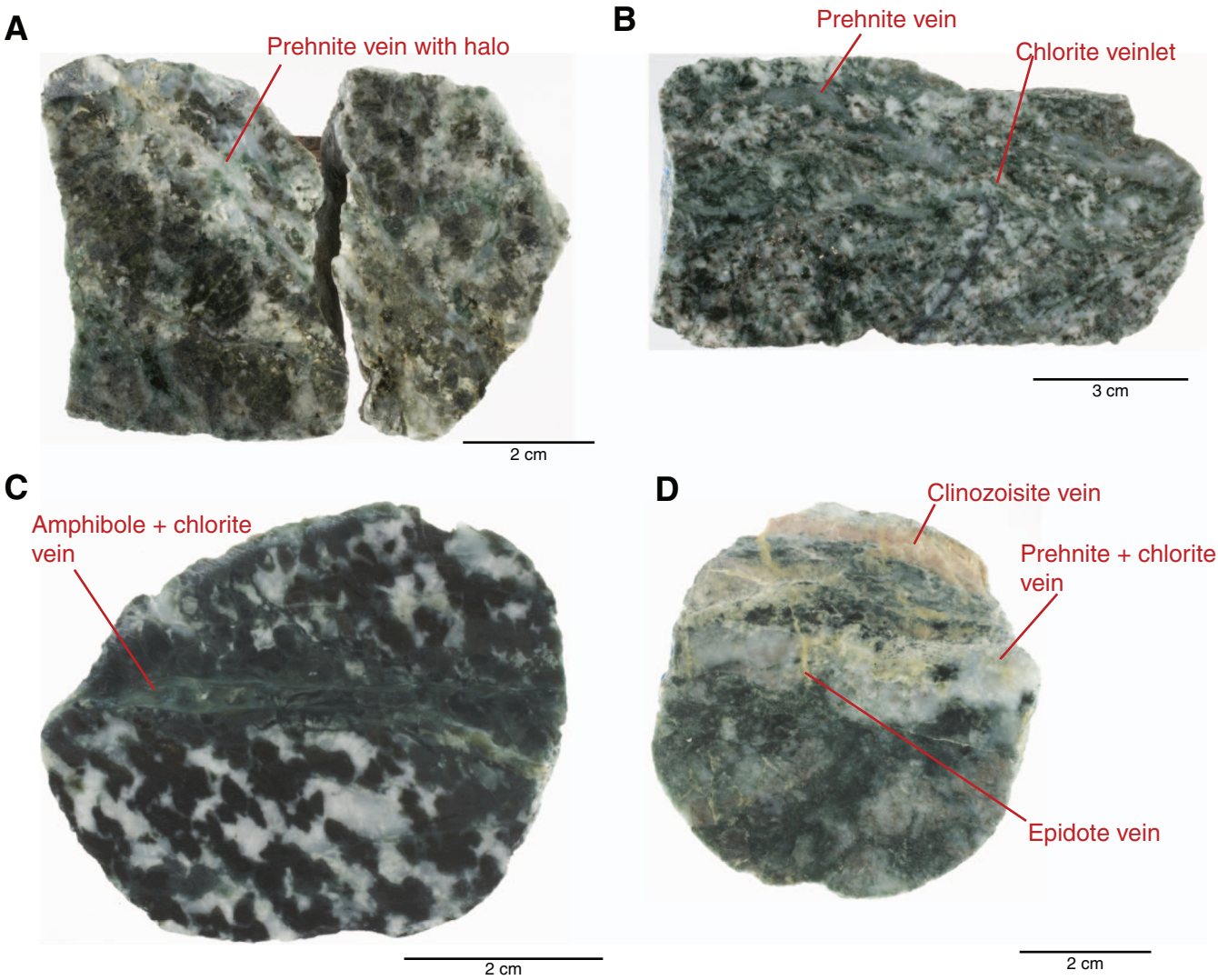

Figure F50. Main vein types. **A.** Chlorite (Chl) vein with cross-fiber texture in clinopyroxene (Cpx) oikocryst-bearing troctolite (Thin Section 46; Sample 345-U1415J-8R-1, 34–37 cm [Piece 7]). **B.** Granular prehnite (Pr) vein with minimal reaction along the vein boundaries in olivine-bearing gabbro (Thin Section 48; Sample 345-U1415J-9R-1, 46–49 cm [Piece 7]). **C, D.** Zeolite (Zeo) vein cutting prehnite veins in olivine gabbro (Thin Section 54; Sample 345-U1415J-8R-3, 35–38 cm [Piece 6]). **E, F.** Zoned chlorite vein cored by carbonate (Car) that is cut by prehnite crystals that form radiating "bloom-like" structures in gabbro (Thin Section 34; Sample 345-U1415J-4R-1, 2–5 cm [Piece 1]). Pl = plagioclase. A, B, D, and F are under cross-polarized light; C and E are under plane-polarized light.

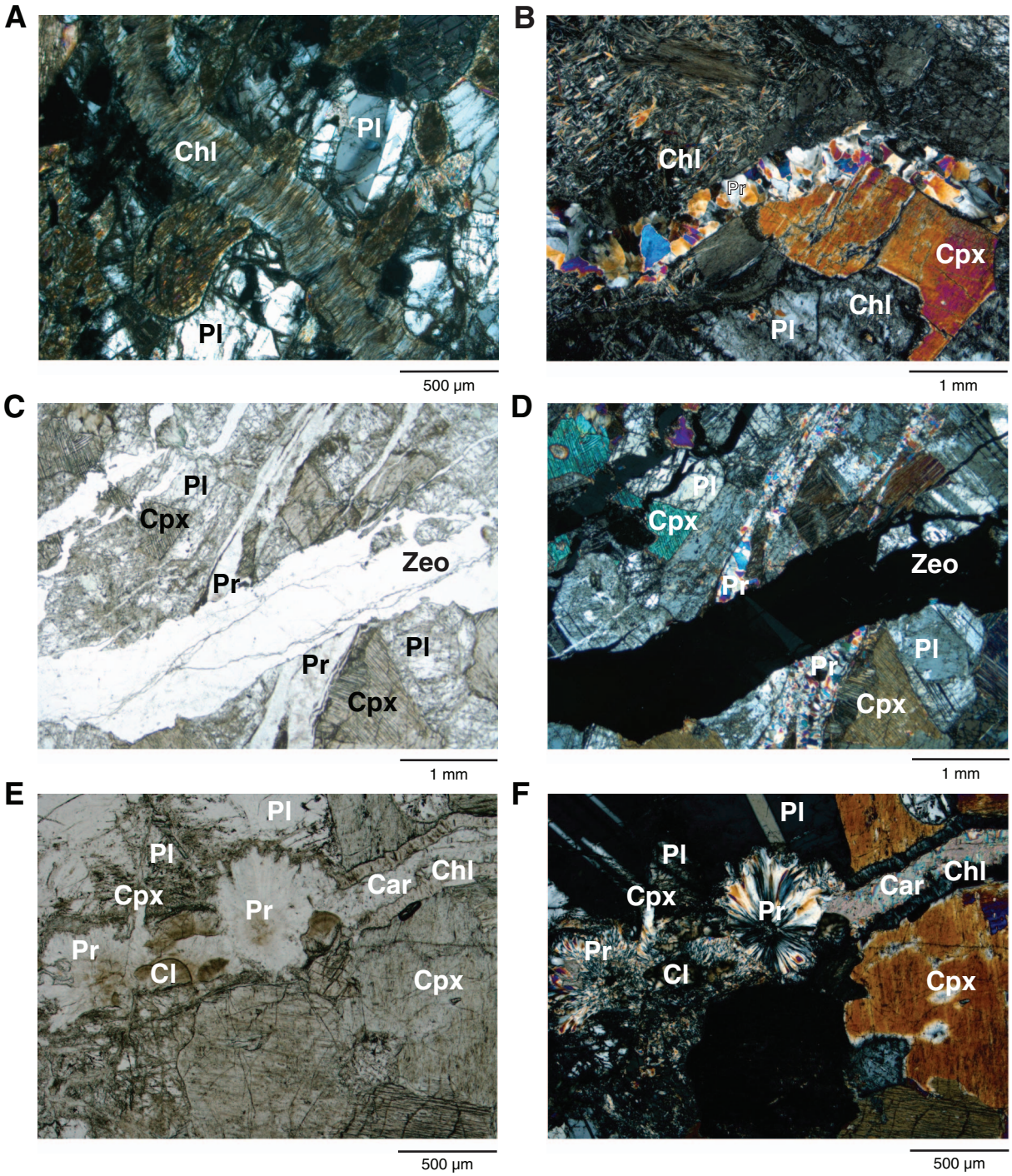

Figure F51. Typical vein morphologies. **A, B.** Several parallel zeolite veins cutting prehnite veins in gabbro (Thin Section 34; Sample 345-U1415J-4R-1, 2–5 cm [Piece 1]). **C, D.** Prehnite and zeolite veins on the margin of a cataclastic zone hosted in gabbro (Thin Section 35; Sample 345-U1415J-5R-1, 55–58 cm [Piece 11B]). **E, F.** Relationships between clinozoisite, prehnite, and chlorite veins in completely altered cataclastic gabbro (Thin Section 68; Sample 345-U1415J-14G-1, 0–4 cm [Piece 1]). **G, H.** Relationships between prehnite, epidote, and clinozoisite veins in cataclasite (Thin Section 81; Sample 345-U1415J-23R-1, 10–12 cm [Piece 3]). A, C, E, and G are under plane-polarized light; B, D, F, and H are under crossed polars.

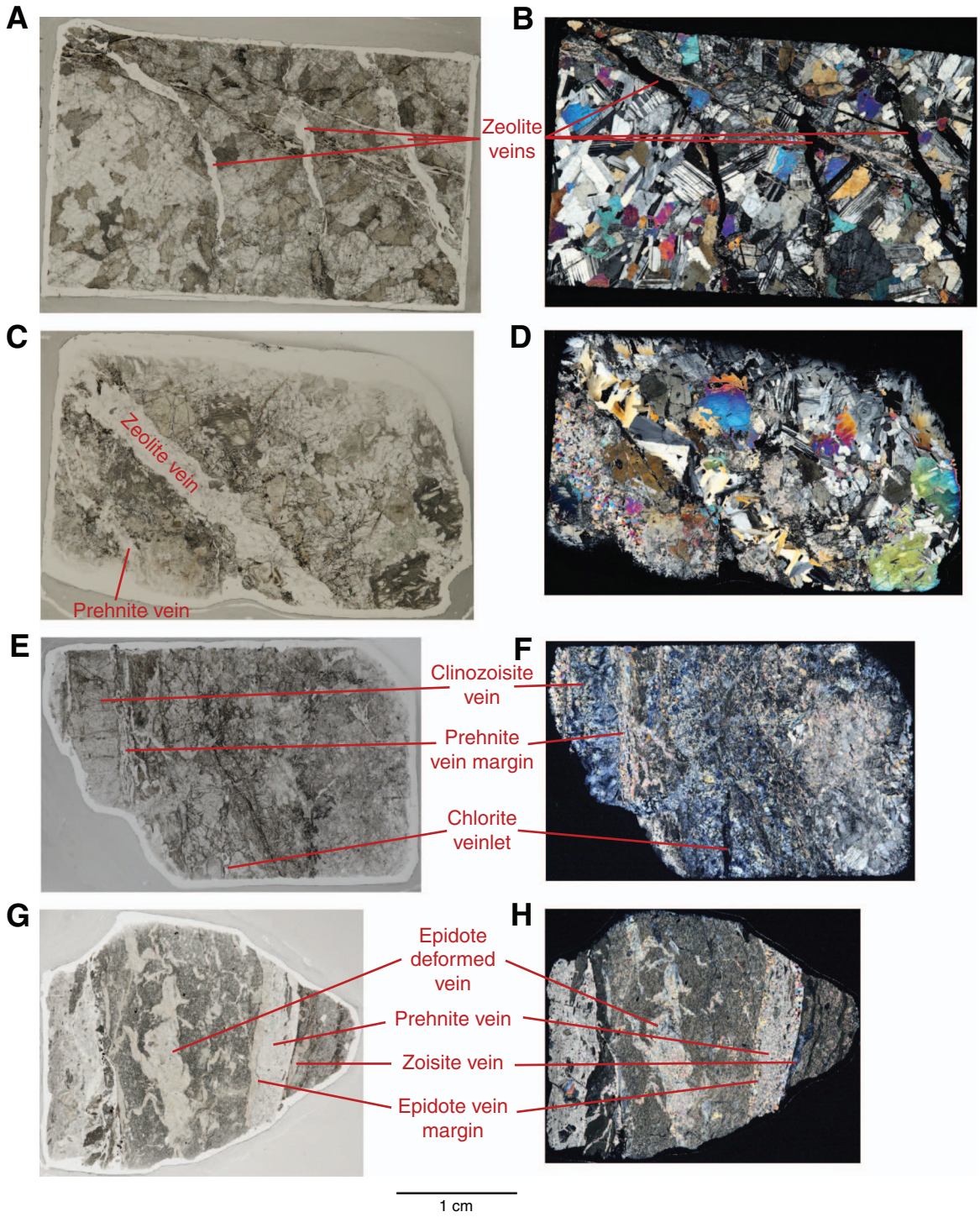

Figure F52. Cataclasite (under crossed polars). **A.** Cataclastic gabbro with two domains (Thin Section 64; Sample 345-U1415J-12R-1, 115–117 cm [Piece 15]). Domain 1 (D1) is cataclasite with abundant prehnite clasts, some relatively coarse grained, and Domain 2 (D2) is a chlorite (Chl)-rich shear zone, chlorite after olivine, and extensively prehnitized plagioclase (Pl). Detail for S1 is given in B; for S2, see Figure F59. **B.** Cataclastic sample with chlorite rim developing between serpentine after olivine (Se) and prehnitized plagioclase. Few relics of plagioclase remain. **C.** Chlorite replacing olivine or phases after olivine in cataclasite with basaltic dike rock fragment (Thin Section 74; Sample 345-U1415J-19R-1, 64–67 cm [Piece 10]). **D.** Chlorite replacing plagioclase and pyroxene. Pyroxene is also partially replaced by amphibole (Am). Cpx = clinopyroxene, SPl = secondary plagioclase.

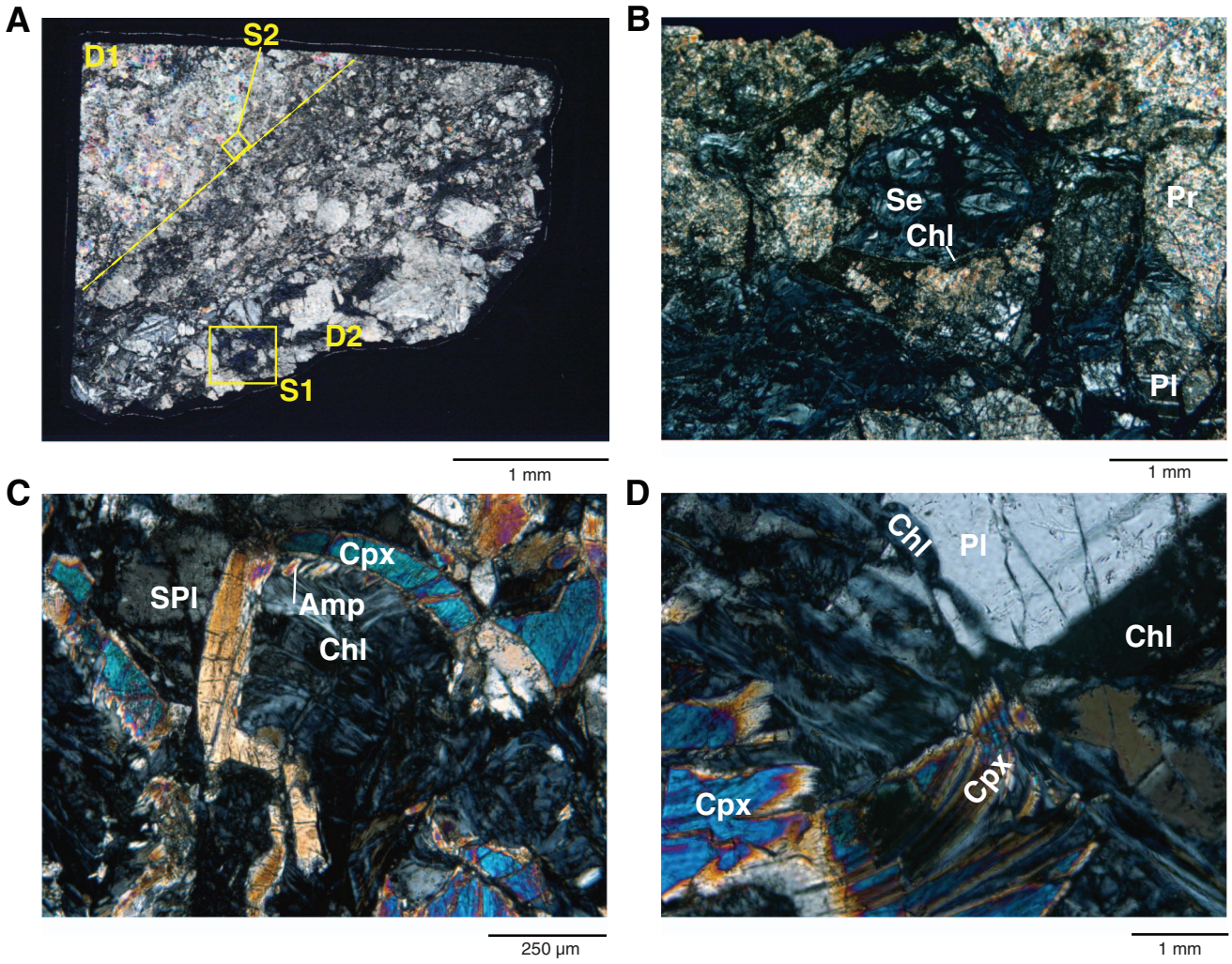

Figure F53. Cataclasite (under crossed polars unless otherwise noted). **A, B.** Cataclasite matrix composed primarily of prehnite (Pr) with chlorite (Chl), clinozoisite (Czo)/epidote (Ep), and dolerite dike rock (Thin Section 81; Sample 345-U1415J-23R-1, 10–12 cm [Piece 3]). A is under plane-polarized light. **C.** Cataclasite in which prehnite, epidote, and chlorite appear metastable (lacking embayment or ragged grain edges) within cataclasite matrix (also Thin Section 81). **D.** Chlorite intergrown with amphibole (amp) with possible former corona textures in a cataclasite zone in gabbro (Thin Section 61; Sample 345-U1415J-12R-1, 11–13 cm [Piece 3]). Tr = tremolite, Cpx = clinopyroxene, CC = cataclasite clast.

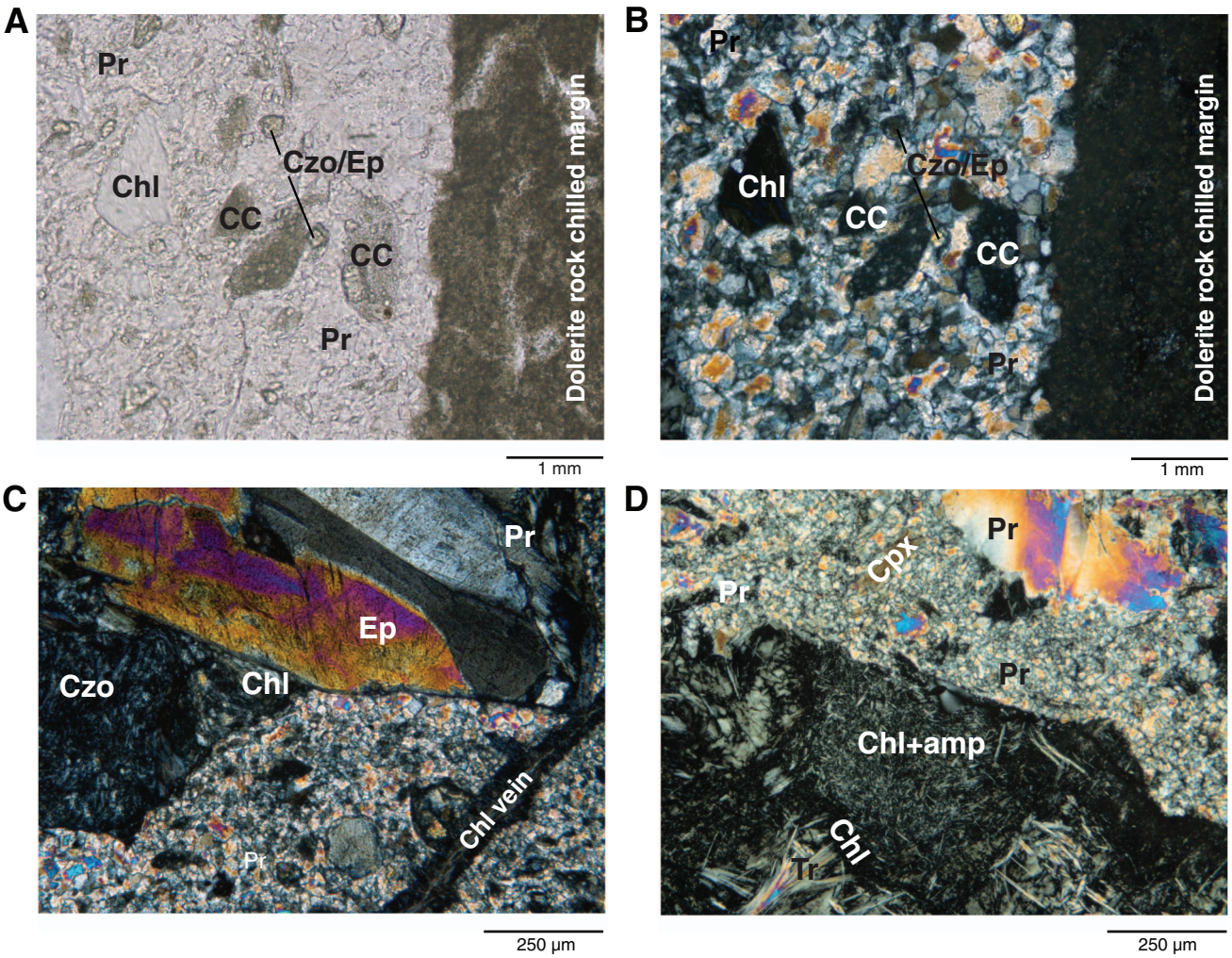

Figure F54. Polydeformed cataclasite (Thin Section 60; Sample 345-U1415J-11R-1, 44–47 cm [Piece 7]). **A.** Cataclastic zones were tentatively assigned relative ages based on crosscutting relationships, with low numbers (e.g., C1) being older. Fragments and shards of clinopyroxene, corona textures of amphibole and chlorite (A+C), and angular and ovoid clasts of polycrystalline prehnite (Pr) suggest that the protolith was olivine-bearing gabbro cut by relatively coarse grained prehnite veins. These clasts occur in a relatively fine grained matrix of prehnite that is locally vuggy (pv; red arrows). Boundaries of truncating bands of cataclasite (red dashed lines) suggest that as many as five generations of microbreccia occur in this rock (see text). C1–C5 = overprinting generations of cataclasite **B.** Large clast of a sixth generation of cataclasite (C3A). A prehnite vein clast (PVC) is identified, along with several of the many clasts of prehnite cataclasite with textures similar to band C2. **C.** Polydeformed cataclasite shown in A. The width of band C3 is identified by the dashed black line. A is under crossed polars; B and C is under plane-polarized light.

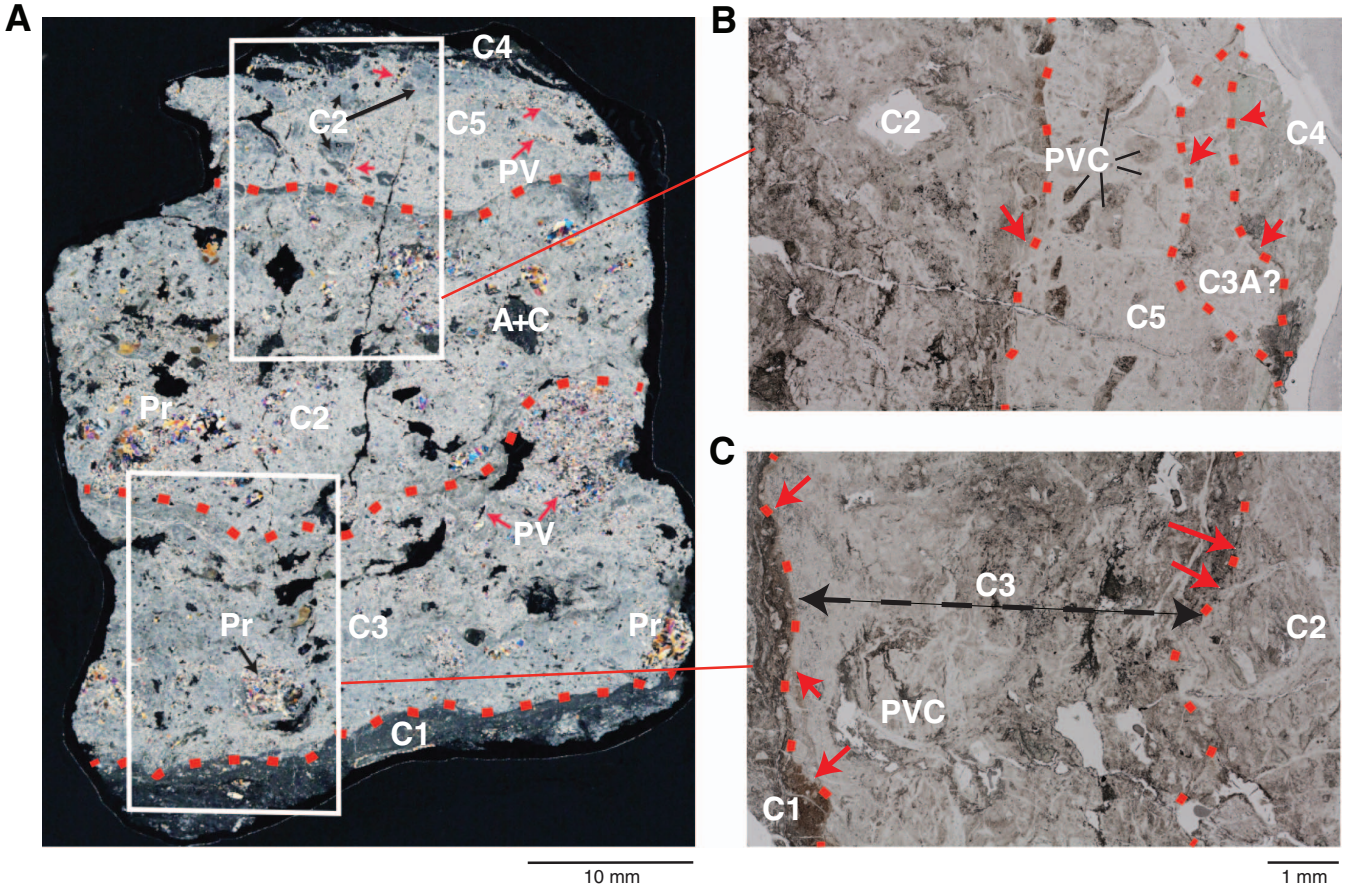

Figure F55. A small fracture in gabbro with incipient cataclasis (Thin Section 33; Sample 345-U1415J-3R-1, 74–82 cm [Piece 10]; under crossed polars). Left lateral slip of ~100 µm has displaced plagioclase (Pl; white arrows). This displacement produced an extensional site in which prehnite (Pr; orange) and both randomly oriented and fibrous chlorite (Chl) have precipitated. Cal = calcite, Cpx = clinopyroxene.

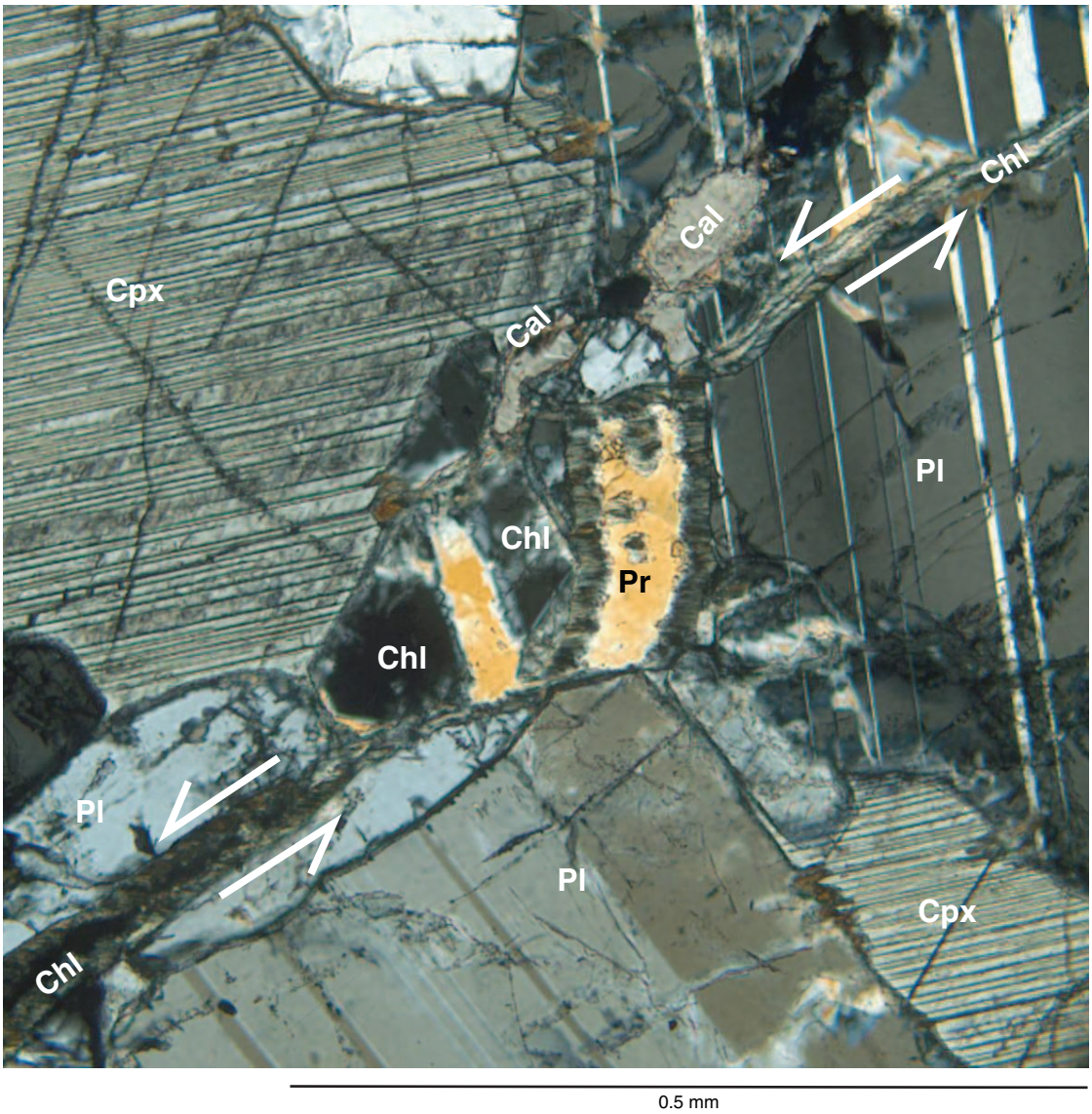

Figure F56. Cataclastic zone in gabbro (between arrows labeled CC [cataclasite]) truncating all earlier structures (Thin Section 29; Sample 345-U1415J-3R-1, 11–13 cm [Piece 4]; under crossed polars). The zone contains broken angular fragments of plagioclase (Pl; pale gray) and clinopyroxene (Cpx; yellow) that apparently do not react with the fine-grained chlorite (Chl) cement. Other fractures break and locally displace grains above and below this zone of microbreccia. Northeast-trending bands of fibrous chlorite (F Chl) crosscut intergrowths of amphibole and chlorite (Am + Chl) that probably replaced magmatic olivine. Also present is amphibole that may have replaced ophitic clinopyroxene at a much higher temperature than the other alterations shown.

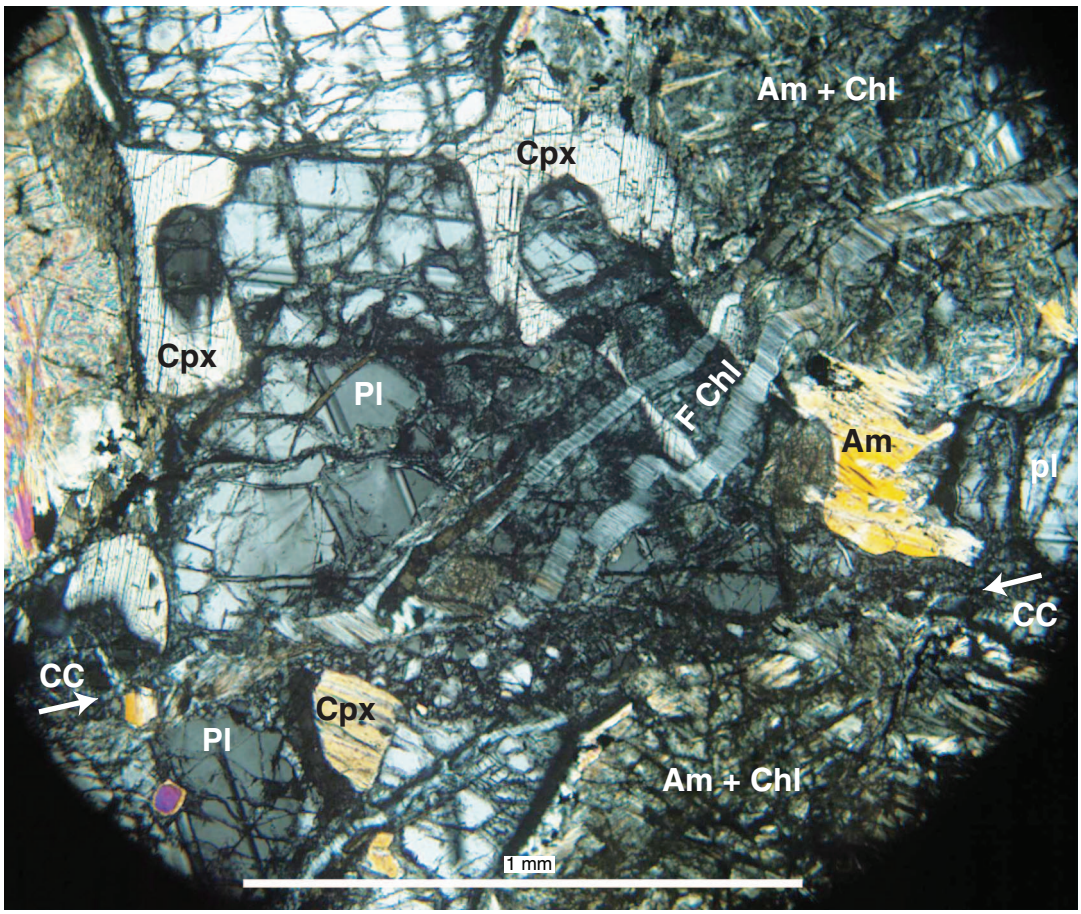

Figure F57. Locally foliated cataclasite after olivine gabbro (Thin Section 79; Sample 345-U1415J-21R-1, 103–107 cm [Piece 14]). Fractured plagioclase (Pl) clasts partially replaced by secondary plagioclase (2Pl) dominate the northwest portion of the image and are set in a cataclastic matrix (CC1). A second cataclasite (southeast quadrant) is dominated by polycrystalline prehnite clasts in a cataclastic matrix (CC2) of prehnite and local chlorite. A band of chlorite trending east-northeast separates the two bands of cataclasite. Near the edges of the image chlorite is in random orientation (Chl-R), whereas the center of the image and along the margins of the cataclasite show strong east-northeast preferred orientation (white arrows), and in the center of the image these chlorite folia are intergrown with small lenses of epidote (Ep). The phyllonitic band (Ph) of chlorite was opened and a small vein of prehnite (Pr; yellow arrows) fills this opening. **A.** Plane-polarized light. **B.** Under crossed polars.

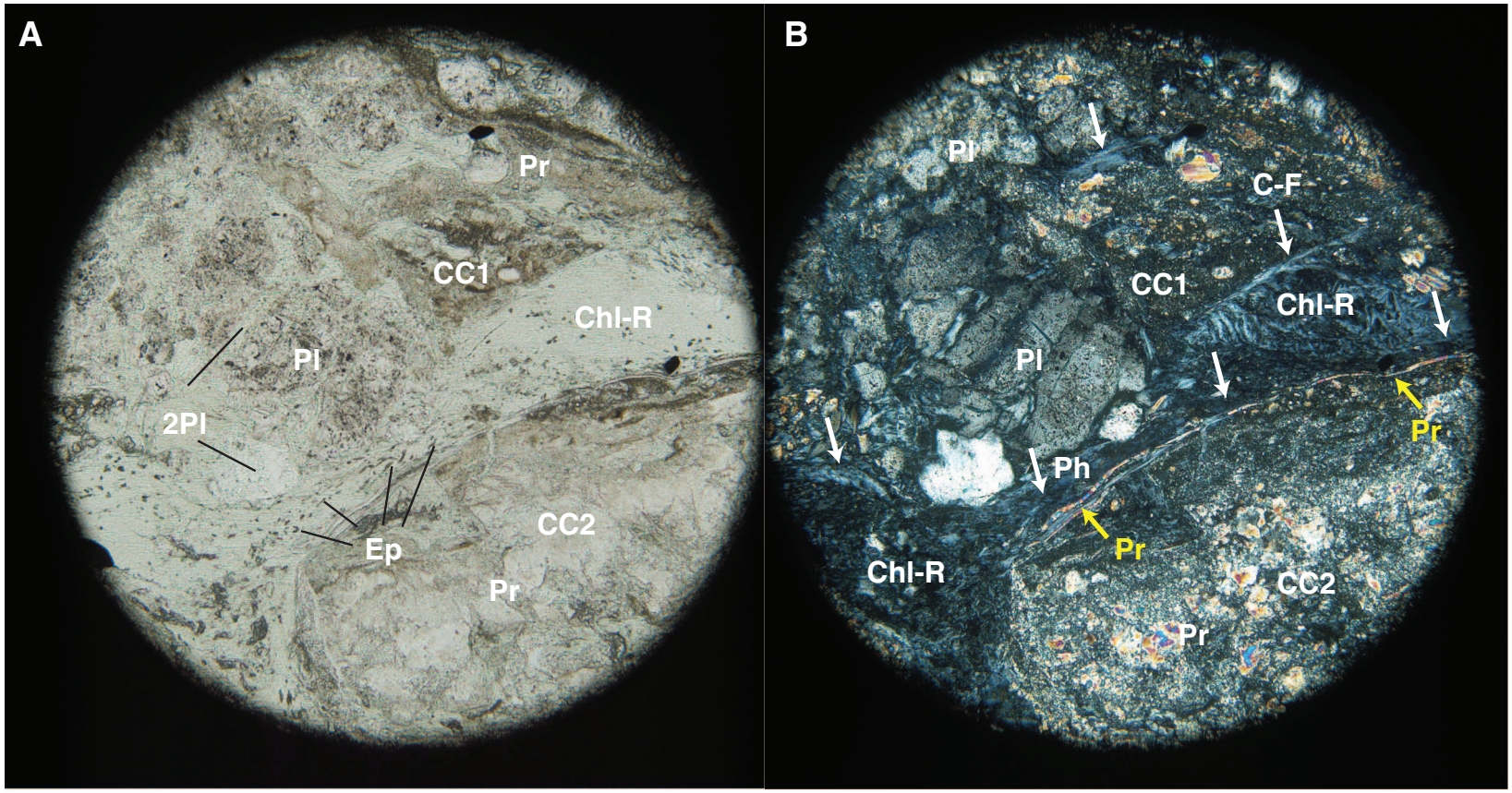

Figure F58. Foliated cataclasite (Thin Section 77; Sample 345-U1415J-21R-1, 17–19 cm [Piece 4]). Plagioclase (Pl) grains become increasingly fractured toward the cataclastic zone (CC) and are highly fractured within the zone. B shows the fragments of plagioclase in the cataclasite are highly embayed and do not fit well together. This suggests that the chlorite surrounding these grains has replaced a substantial amount of plagioclase. Cpx = clinopyroxene, Am = amphibole, Pr = prehnite, Ph = phyllonite. **A.** Under crossed polars. **B.** Plane-polarized light.

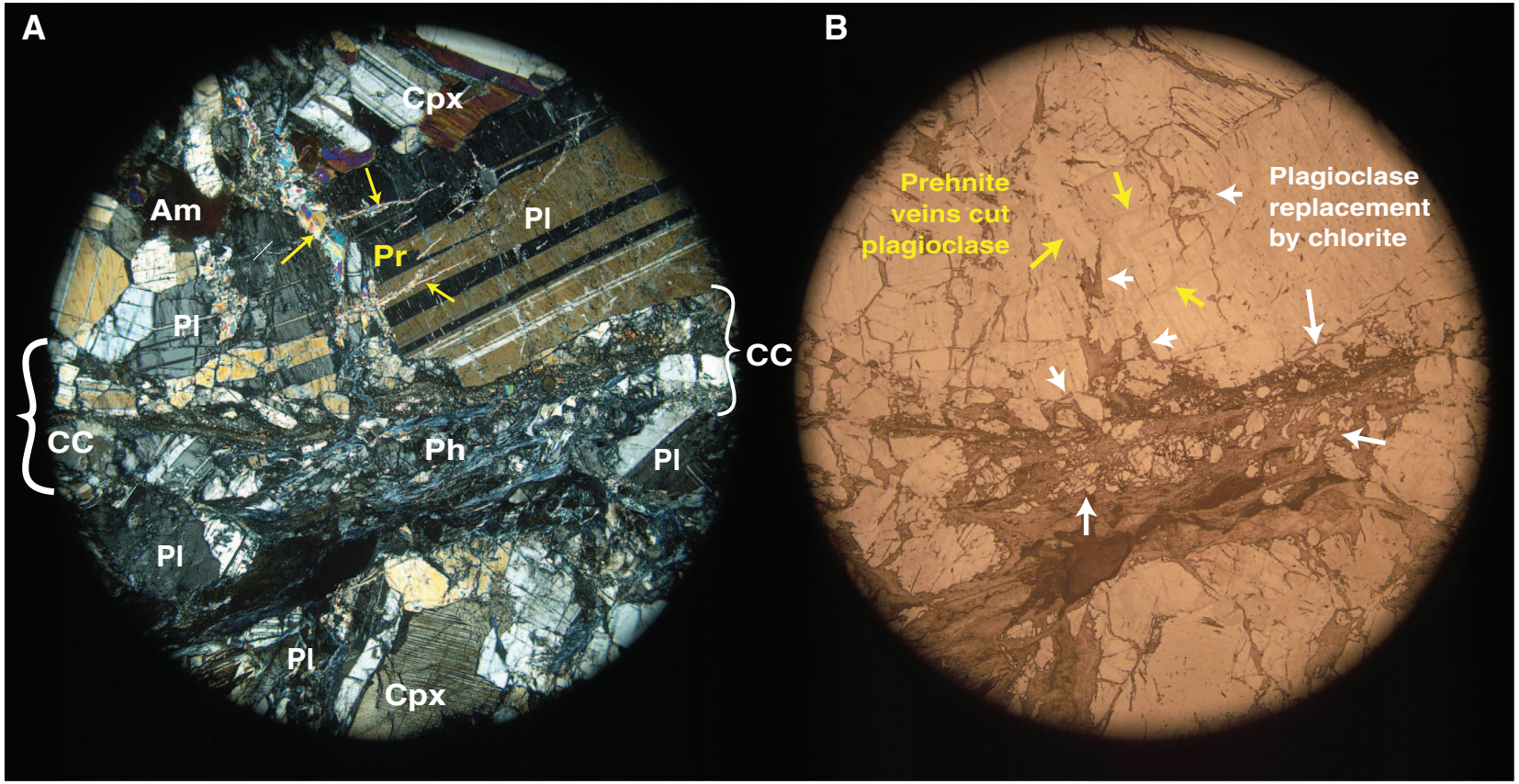

Figure F59. One-wavelength gypsum plate added to a locally foliated cataclasite (Thin Section 77; Sample 345-U1415J-21R-1, 17–19 cm [Piece 4]). Polycrystalline prehnite clasts (CC1) in a cataclastic matrix (CC2) of prehnite (Pr) and chlorite are separated by chlorite-rich foliae. Matrix chlorite generally defines a preferred orientation producing an anastomosing network of northeast-trending foliae (C-F). These are cut by a set of north-northeast–trending chlorite veins also defining a preferred orientation (violet area in B) to produce phyllonitic bands (Ph). These phyllonitic shear zones are in turn cut by a prehnite vein. **A.** Plane-polarized light. **B.** Under crossed polars.

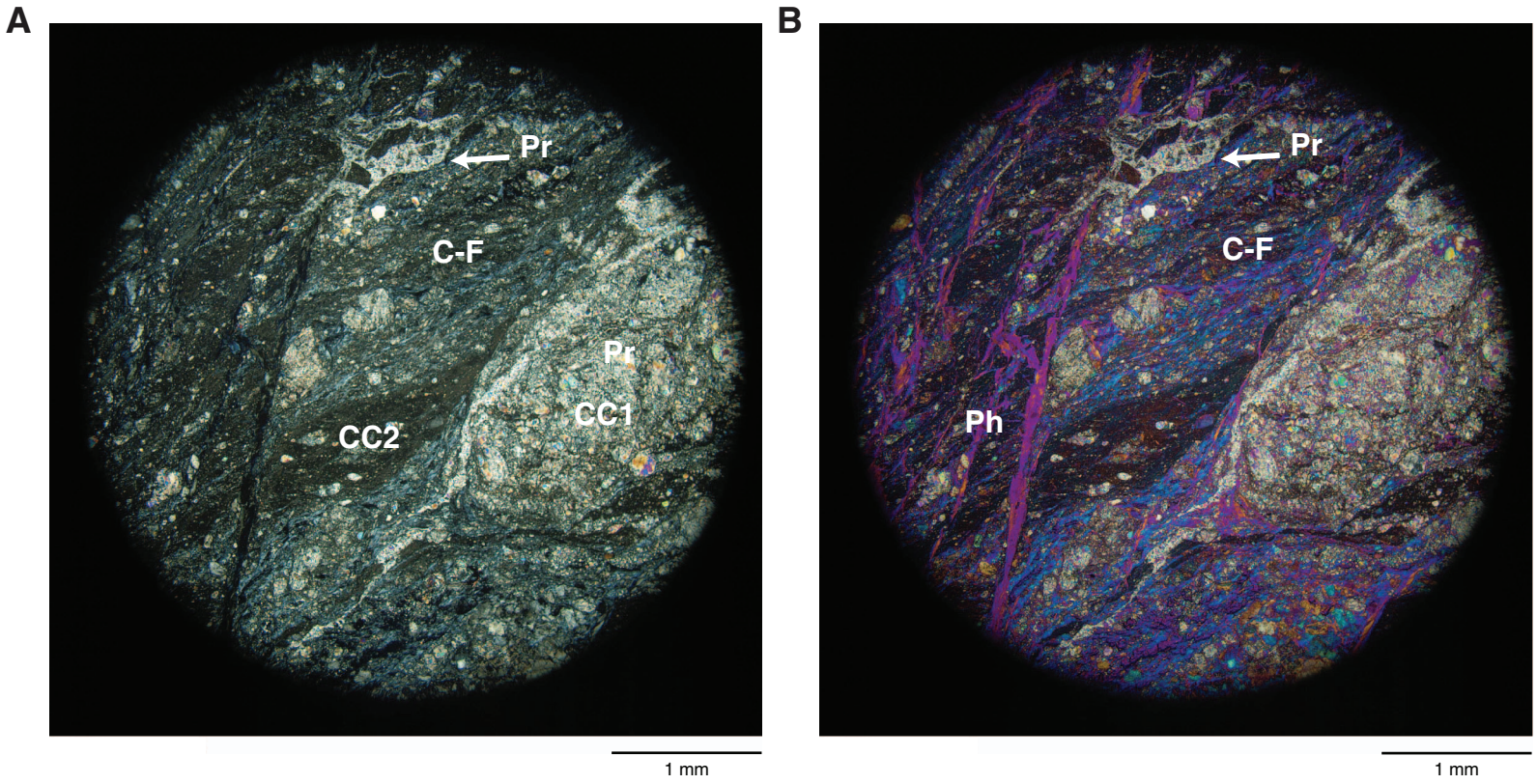

Figure F60. Core recovery in Holes U1415I and U1415J with location of magmatic layering, measured dip of magmatic foliation, location of the three lithologic units in Hole U1415J, and correlation of the upper part of Unit II with Hole U1415I. sd = standard deviation.

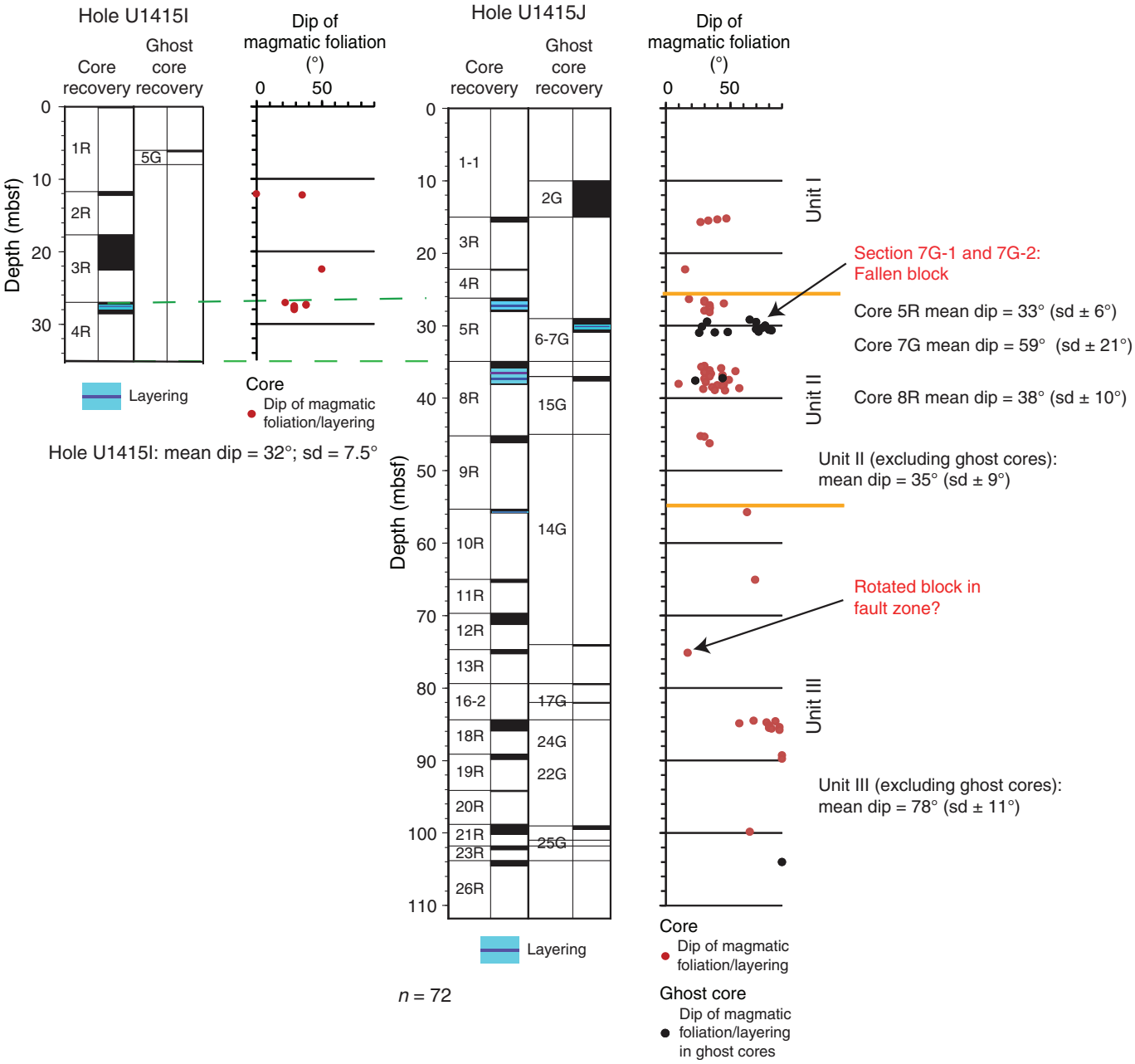

Figure F61. Styles of magmatic layering and foliation, Unit II. **A.** Centimeter-scale modal layering with an olivine-bearing gabbronorite layer (Interval 30; 2.5–6.5 cm) between a troctolite layer (Interval 29; 0.5–2.5 cm) at the top and a second thin troctolite layer (Interval 31; 6.5–9 cm) in turn overlying an olivine-bearing gabbro layer (Interval 32;, 9–63 cm) at the bottom (Sample 345-U1415J-5R-2A, 2.0–17.5 cm [Piece 1]). Also shown is olivine-plagioclase magmatic foliation. **B.** Centimeter-scale modal layering consisting of a 2 cm thick olivine-bearing gabbro layer (Interval 42; 111–116 cm) within a clinopyroxene oikocryst-bearing troctolite layer (interval 345-U1415J-8R-2, 105.5–121.0 cm [Piece 9]). Also shown is olivine-plagioclase magmatic foliation. **C.** Olivine-plagioclase magmatic foliation anastomosing around large (up to 2 cm diameter) clinopyroxene oikocrysts in an oikocryst-bearing troctolite (interval 345-U1415J-8R-3, 76.0–91.5 cm [Piece 9]).

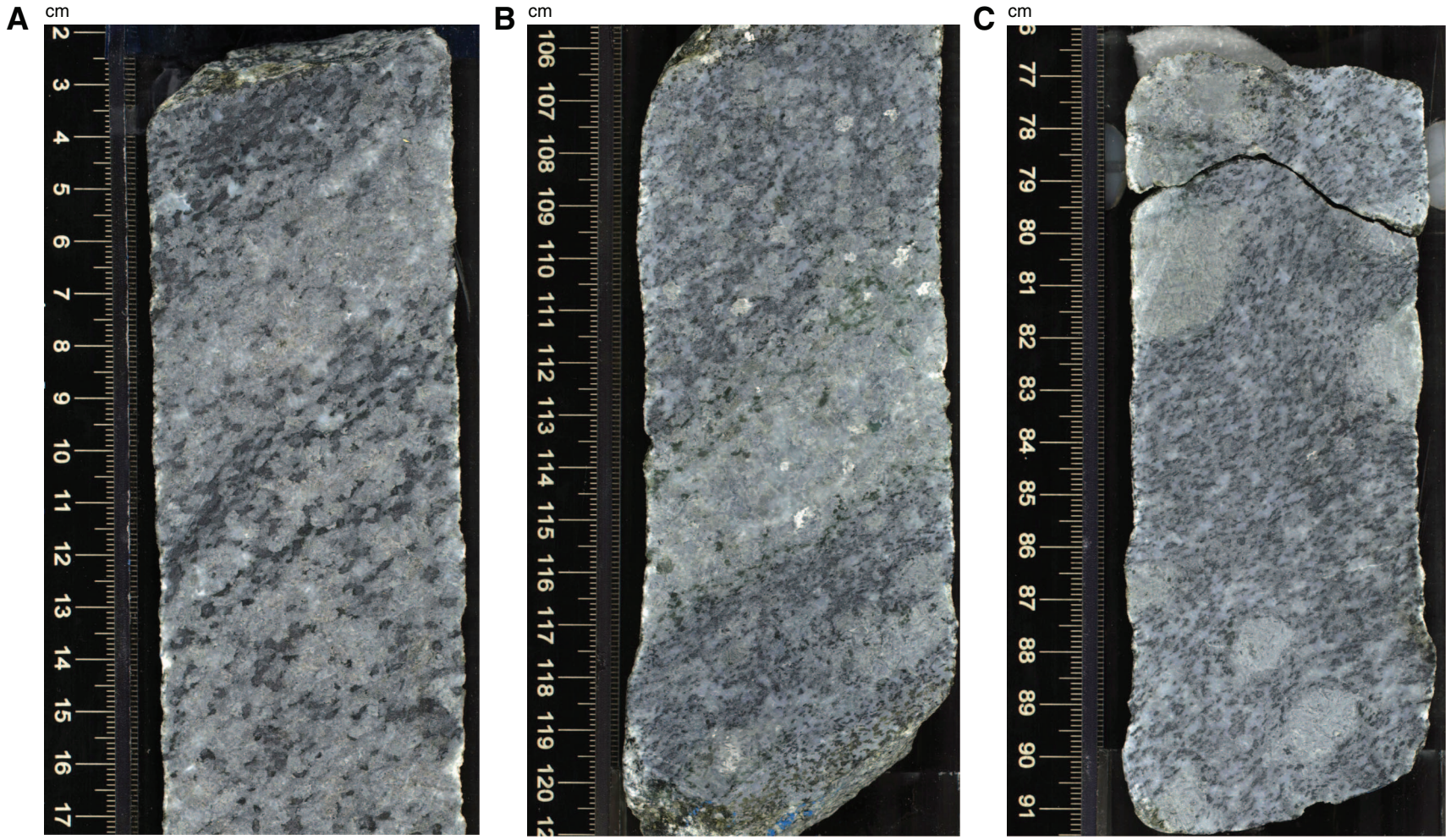

Figure F62. Magmatic foliation strength expressed as percentage of core length for entire core (0–104.55 mbsf), Units II (Sections 345-U1415J-5R-1 to 9R-1; 26.20–55.30 mbsf) and III (Sections 10R-1 to 26R-1; 55.30–104.55 mbsf).

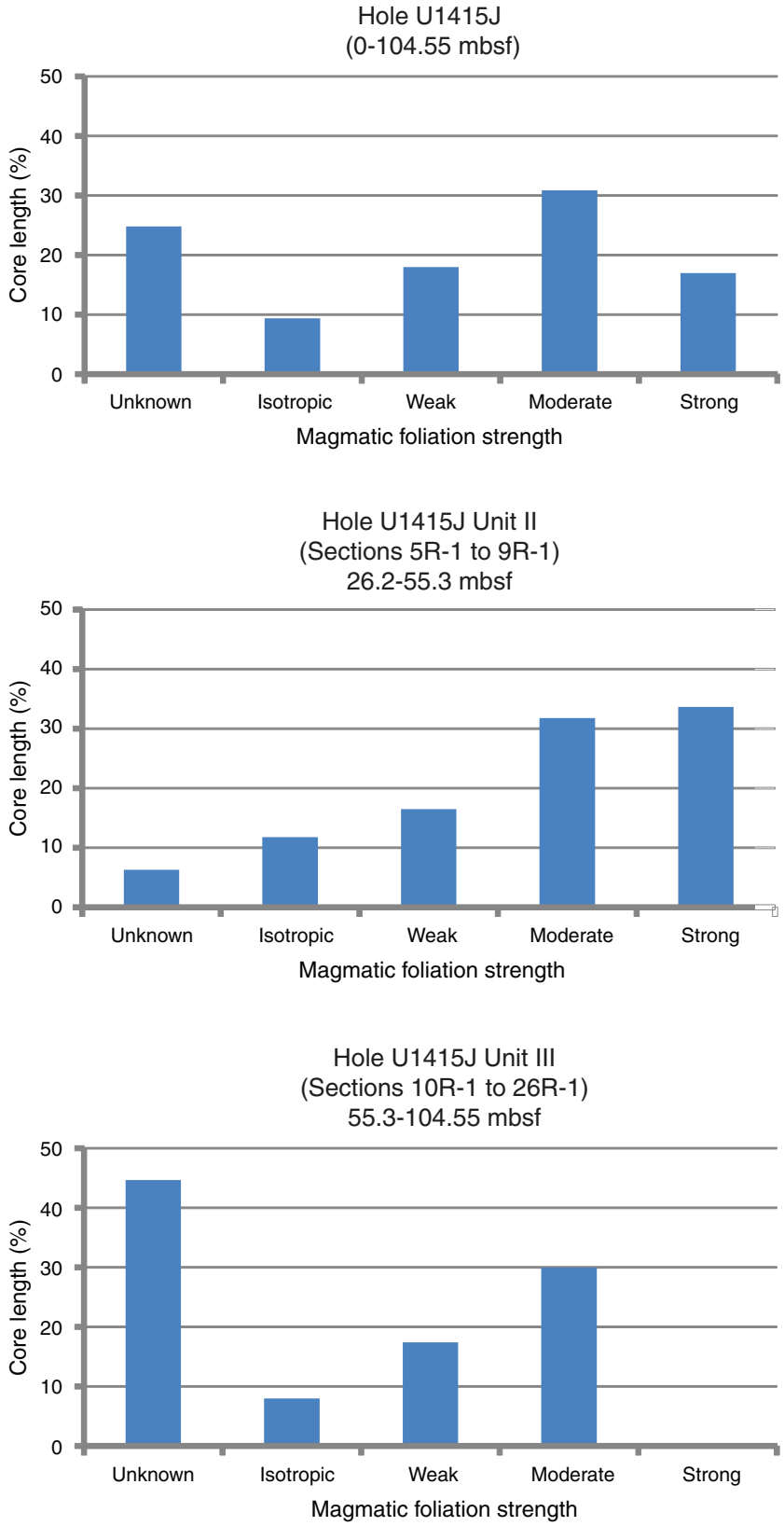

Figure F63. Magmatic foliation strength of dominant rock types in the core expressed as percentage of core length. Histograms are given for gabbro, olivine gabbro, and troctolite in Unit II (Sections 345-U1415J-5R-1 to 9R-1; 26.2–55.3 mbsf) and for troctolite in Unit III (Sections 10R-1 to 26R-1; 55.30–104.55 mbsf).

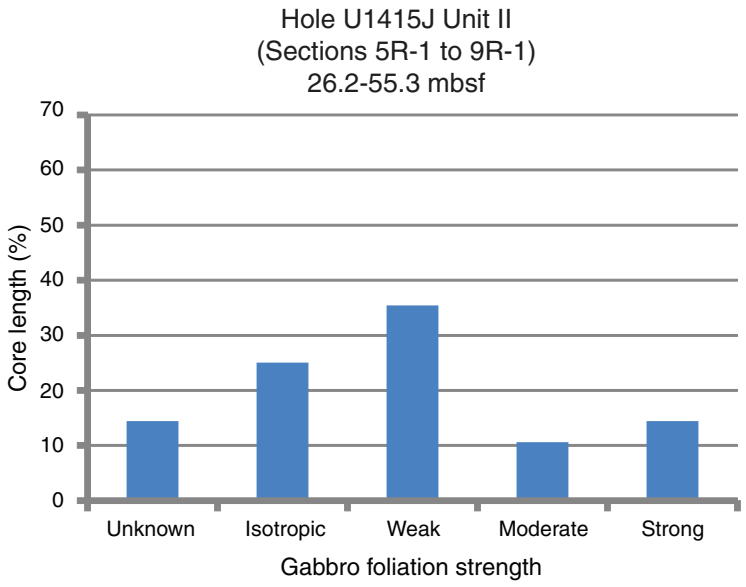

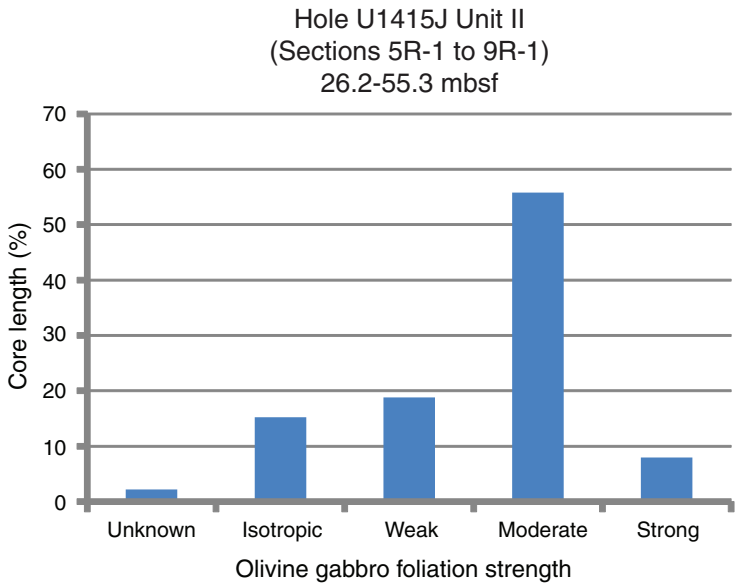

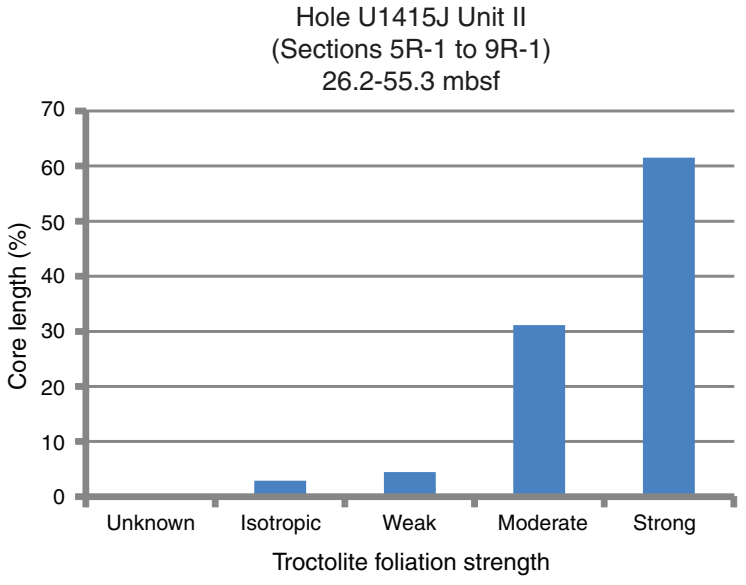

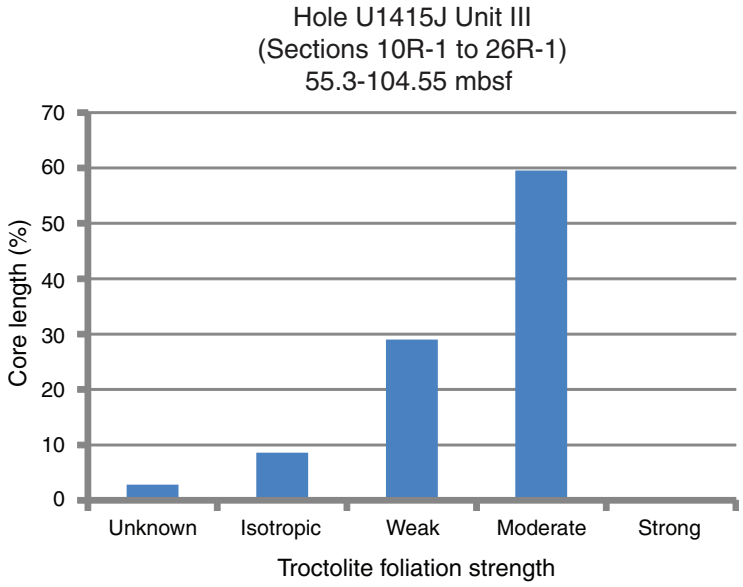

Figure F64. A. Steeply dipping boundary between medium-grained troctolite (Interval 58; 0–50 cm) on the left and coarse-grained olivine gabbro (Unit 59; 50–56 cm) on the right. The olivine-plagioclase magmatic foliation is clearly parallel to the boundary (interval 345-U1415J-10R-1A, 47–55 cm [Piece 6B]; wet image). Red box (tick mark shows upward direction) indicates location and orientation of image in C. **B.** Gradational, vertical boundary defined by modal variation in olivine and plagioclase within troctolite (Interval 73; interval 345-U1415J-18R-1A, 129–142 cm [Piece 17]; dry image). The vertical olivine-plagioclase magmatic foliation parallels the boundary. **C.** Steeply dipping boundary between medium-grained troctolite on the left and coarse-grained olivine gabbro on the right (under crossed polars). Magmatic foliation and orange birefringent clinopyroxene oikocryst extend across the boundary. Red boxes indicate the location and orientation of images in Figures F11A and F11D. Red arrow indicates foliation orientation.

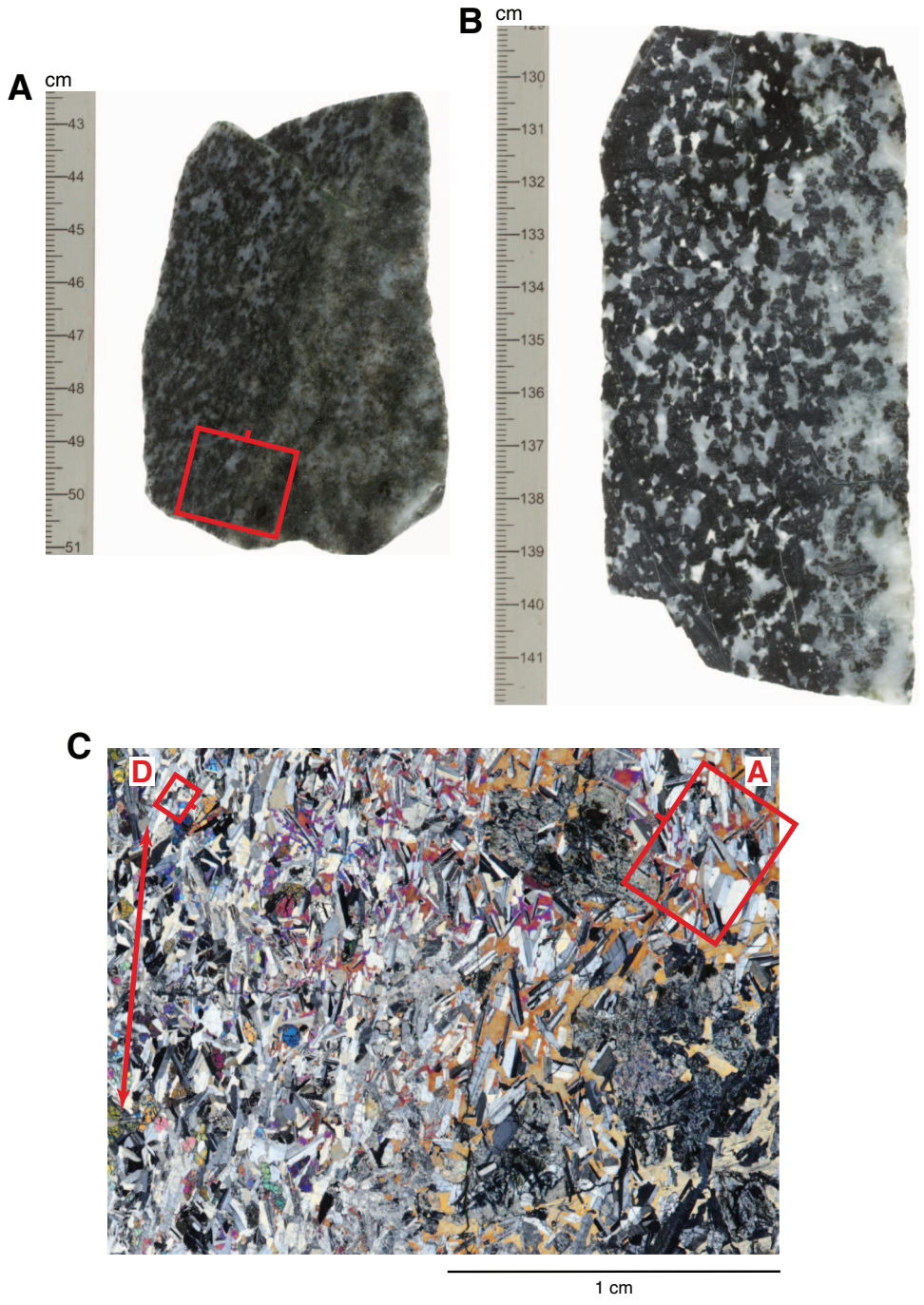

Figure F65. Gabbro and olivine gabbro (under crossed polars). **A, B.** Olivine gabbro (Sample 345-U1415J-3R-1, 22–24 cm [Piece 6]). A. Whole thin section image showing large (as long as 8 mm), high–aspect ratio (10:1) twinned clinopyroxene crystals that define very strong lineation (red arrow) within weak plagioclase foliation and more numerous smaller, equant clinopyroxene crystals. Red box (tick mark shows upward direction) indicates location of image in B. B. Margin of one of the large, elongate clinopyroxene crystals showing a seriate grain boundary with the adjacent annealed plagioclase crystals. **C, D.** Gabbro (Sample 345-U1415J-3R-1, 79–82 cm [Piece 16]). C. Large plagioclase crystals with significant deformation twinning and bending but weakly developed grain boundary annealing. D. Relatively coarse plagioclase grain size (2–5 mm) and moderate plagioclase foliation (red arrow). Red box indicates location and orientation of image in C.

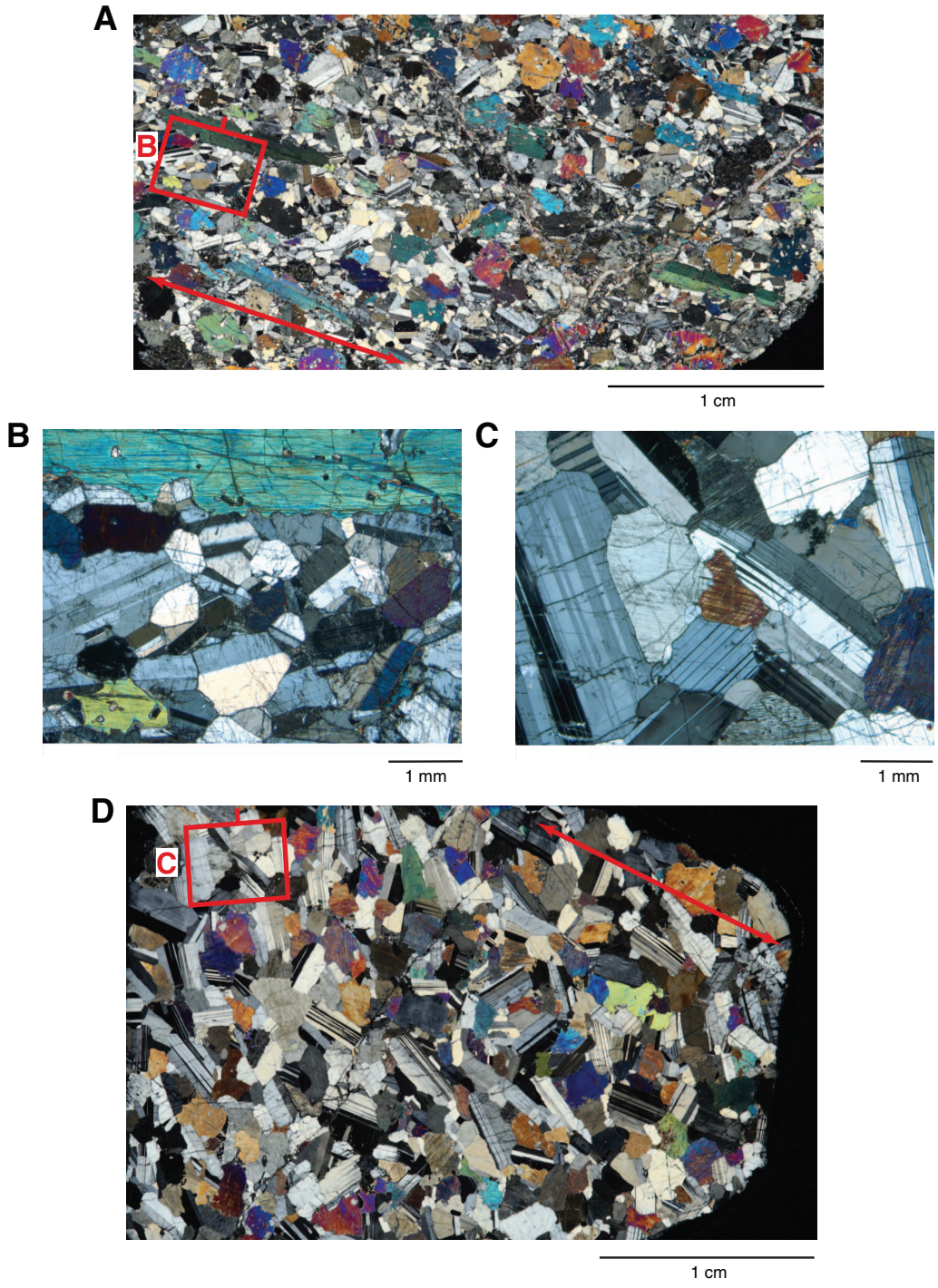

Figure F66. Clinopyroxene oikocrysts (under crossed polars). **A.** Clinopyroxene oikocryst-bearing troctolite (Sample 345-U1415J-5R-1, 117–121 cm [Piece 7B]). Strong olivine-plagioclase magmatic foliation (red arrow) within the relatively fine grained (1–3 mm) troctolitic portion of the rock wraps around the right side and bottom of the oikocryst. Red box (tick mark shows upward direction) indicates location and orientation of E. **B.** Clinopyroxene oikocryst developed in olivine gabbro at troctolite margin (Sample 345-U1415J-7G-1, 28–31 cm [Piece 5]). Strong olivine-plagioclase magmatic foliation (red arrow) within the relatively fine grained (1–3 mm) troctolitic portion of the rock wraps around the bottom of the oikocryst. Red box indicates location and orientation of D. **C.** Large clinopyroxene oikocryst margins, just outside the field of view in A, clearly showing two bent elongate plagioclase crystals within the oikocryst. **D.** Relatively unstrained, large 2–3 mm long plagioclase crystal almost perpendicular to the olivine-plagioclase magmatic foliation. **E.** Large (7 mm long), elongate plagioclase crystal within the olivine-plagioclase foliation showing sigmoidal bending, deformation twins, and subgrains. **F.** Area just outside the field of view in B with a large (6 mm long) plagioclase crystal with deformation twins. Also seen are small (<1 mm) plagioclase crystals immediately adjacent to and within the margins of the large bent plagioclase crystal, illustrating how parts of the plagioclase network of crystals are commonly annealed and strain free.

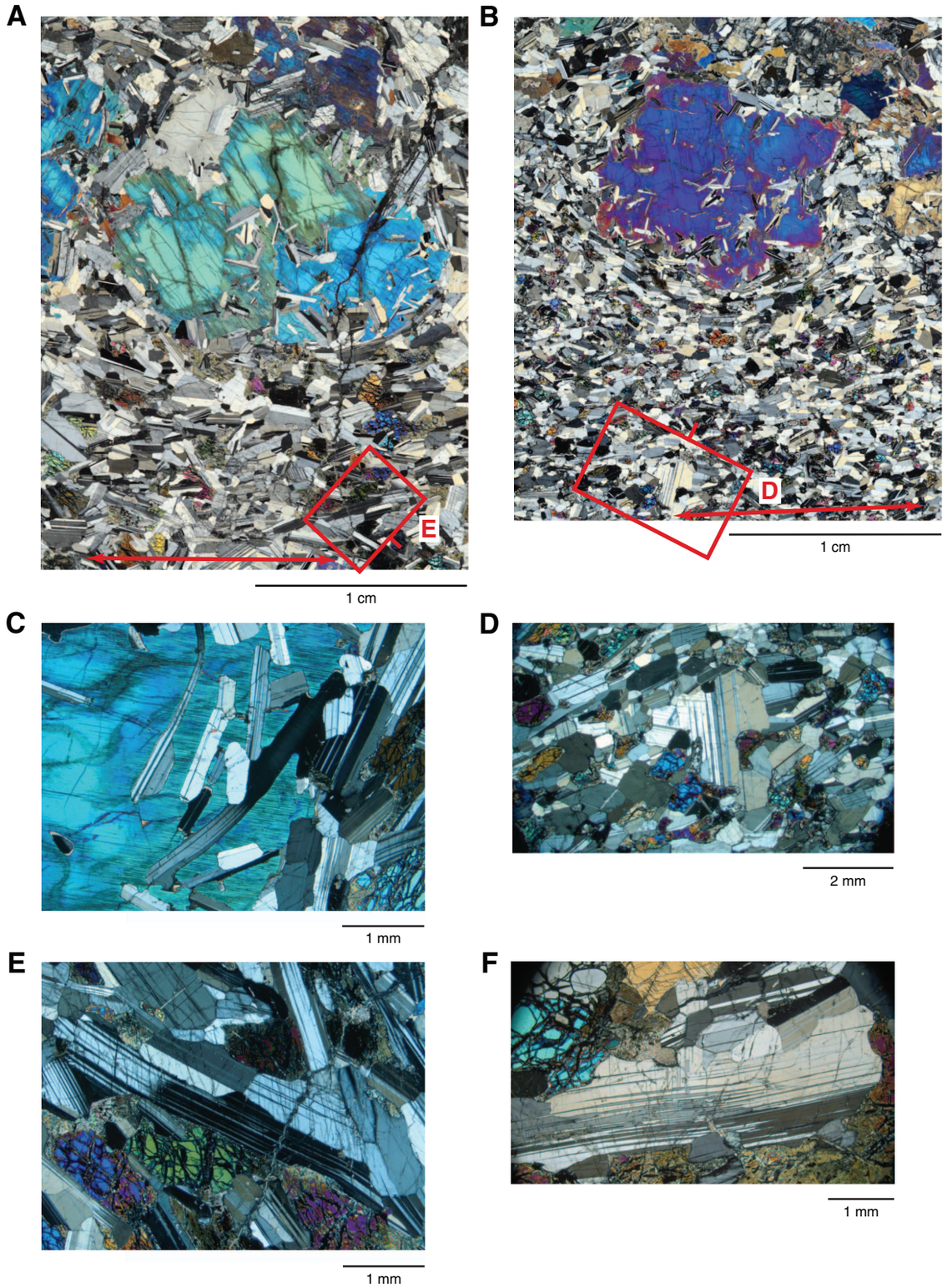

Figure F67. Clinopyroxene oikocrysts (under crossed polars). **A.** Elongate clinopyroxene oikocrysts in olivine gabbro (Sample 345-U1415J-5R-1, 62–64 cm [Piece 12]). Moderate olivine-plagioclase magmatic foliation wraps around the top of the oikocrysts. Red box (tick mark shows upward direction) indicates location and orientation of B. Red arrow indicates foliation orientation. **B.** Relatively large (2–3 mm long) plagioclase crystals partially enclosed by a clinopyroxene oikocryst. The plagioclase crystals are aligned with the dominant foliation, indicating that the pyroxene margins continued to grow after/during foliation development. **C.** Clinopyroxene oikocryst-bearing troctolite with northeast–southwest imbricated or tiled plagioclase crystals within a foliation running approximately horizontally in the figure. Imbrication suggests that a component of shear was involved during foliation development (Sample 345-U1415J-7G-1, 55–56 cm [Piece 8]). **D.** Clinopyroxene oikocryst-bearing troctolite (Sample 345-U1415J-8R-1, 79–82 cm [Piece 13]). Strong olivine-plagioclase magmatic foliation wraps around the top of the oikocrysts. Red boxes indicate location and orientation of E and F. Red arrow indicates foliation orientation. **E.** Strong magmatic foliation defined by annealed plagioclase and tabular olivine crystals. **F.** Deformed clinopyroxene oikocryst exhibiting subgrain development.

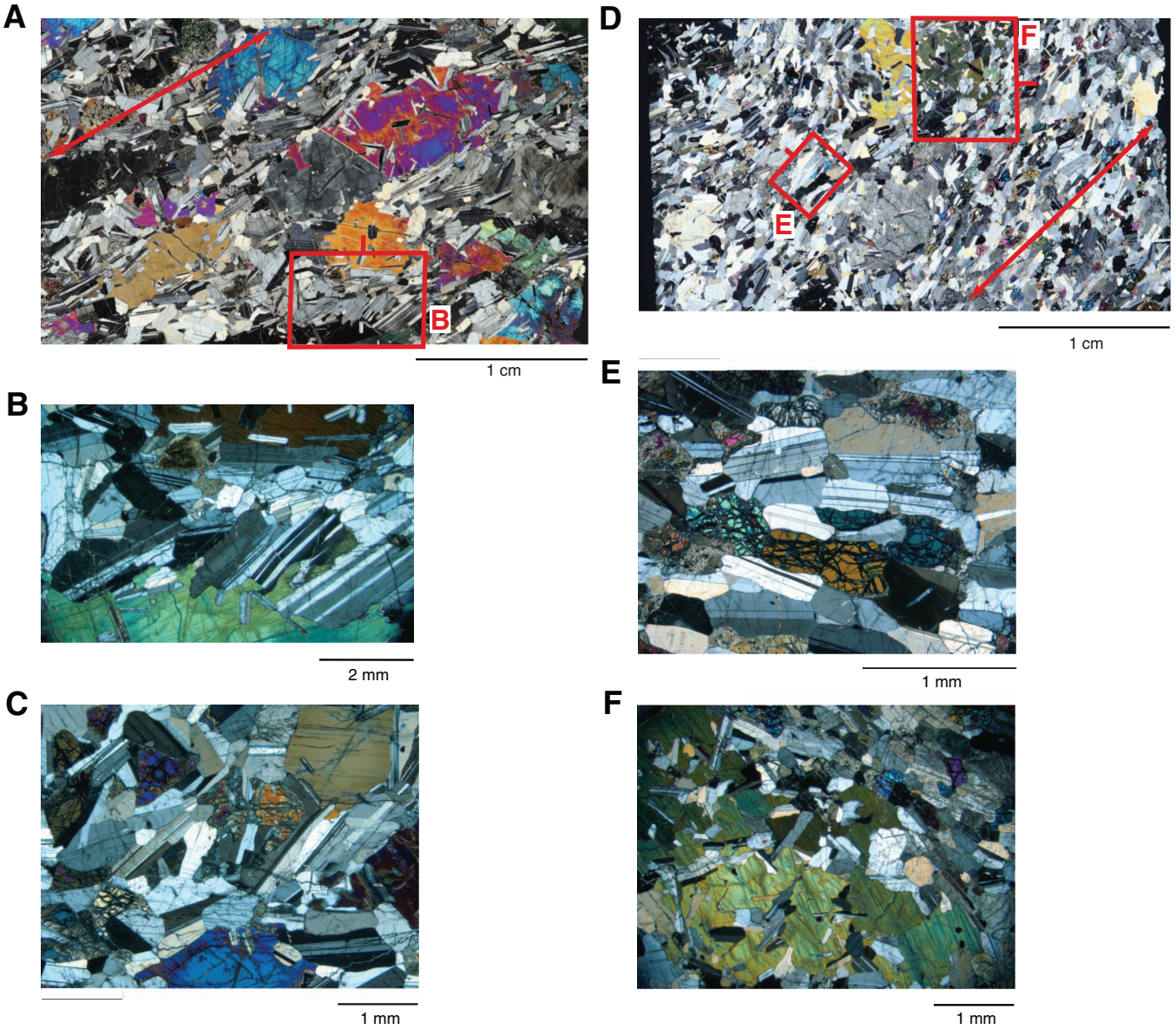

Figure F68. Foliation (under crossed polars). **A–D.** Sample 345-U1415J-10R-1A, 53–55 cm (Piece 6B). Red arrows show foliation orientation. See Figure F23C for the whole thin section image. Images B and C are from outside the field of view. (A) Moderate-strength plagioclase foliation within a clinopyroxene oikocryst in olivine gabbro. (B) Strong magmatic foliation defined by tabular plagioclase and sometimes lobate olivine crystals. (C) Very skeletal olivine crystal with annealing of grain boundaries but no crystal-plastic deformation. (D) Small plagioclase crystals (<0.5 mm) with typical annealing with gently curved grain boundaries and 120° triple junctions. **E.** Relatively weakly altered troctolite with isotropic magmatic foliation (Sample 345-U1415J-11R-1, 22–24 cm [Piece 4]). Large (up to 1 cm diameter) partially serpentinized skeletal olivine shows some undulose extinction and subgrain development but no kinking.

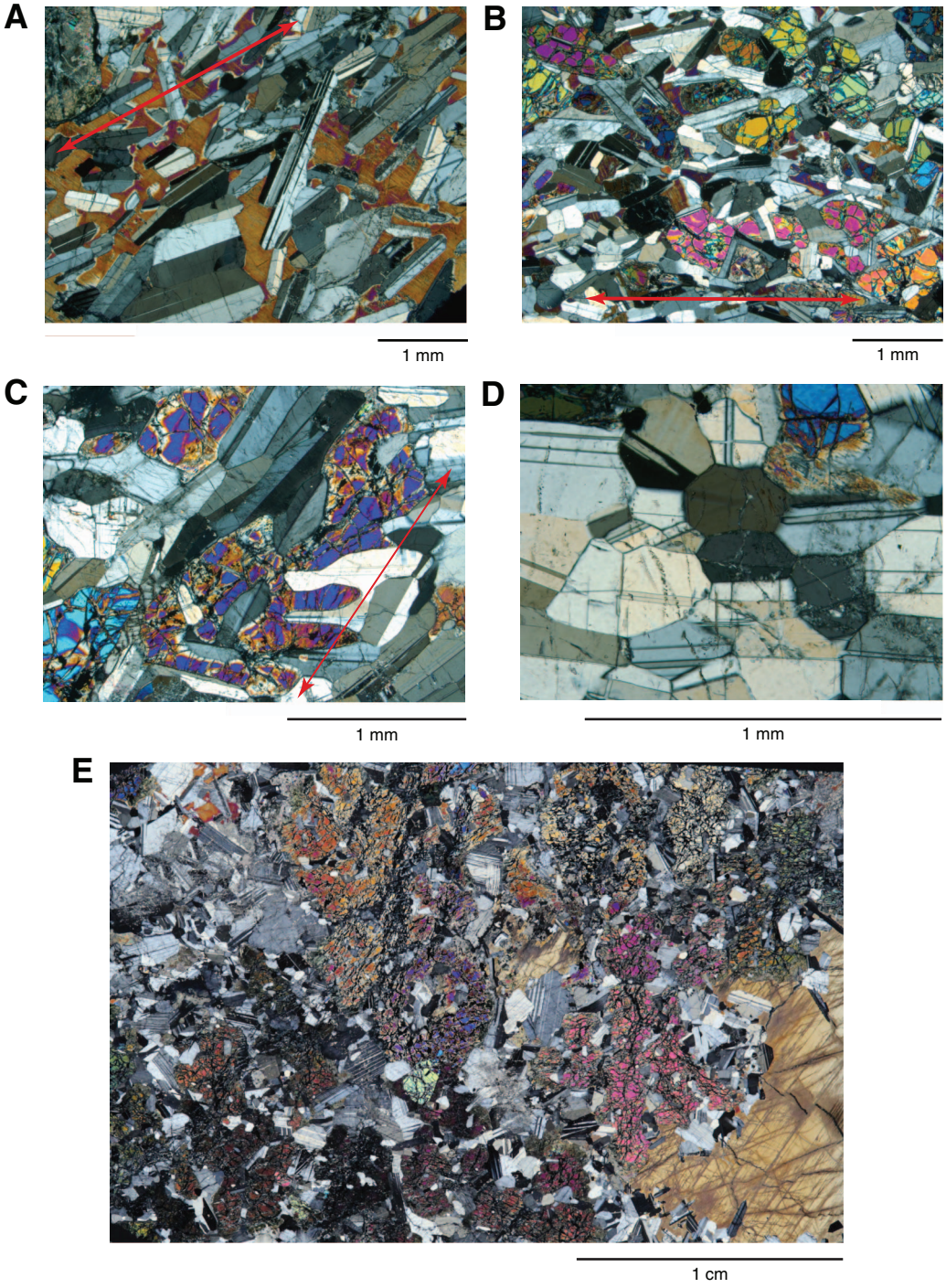

Figure F69. Olivine gabbro (Sample 345-U1415J-25G-1, 11–15 cm [Piece 2]; under crossed polars). **A.** Dramatic range in grain size with large (1–3 cm diameter) clinopyroxene oikocrysts, 0.5–1 cm diameter skeletal olivine crystals, and 0.5–5 mm long plagioclase crystals. Clinopyroxene oikocrysts contain chains of small plagioclase chadacrysts outlining areas of chadacryst-free clinopyroxene. Red boxes (tick marks show upward direction) indicate location and orientation of B–E. **B.** Large (1–5 mm) plagioclase crystals with deformation twinning. **C.** Fine-grained (<1 mm) annealed plagioclase crystals with gently curving grain boundaries. **D.** Narrow zone (0.5–2 mm wide) of submillimeter plagioclase and clinopyroxene crystals between two large clinopyroxene oikocrysts. Here, the grain boundaries are not annealed, and the tiny (<0.5 mm) fragments of clinopyroxene suggest this zone might be a recrystallized high-temperature near-solidus deformation zone between two clinopyroxene oikocrysts. **E.** Chains of small plagioclase chadacrysts outlining areas of chadacryst-free clinopyroxene.

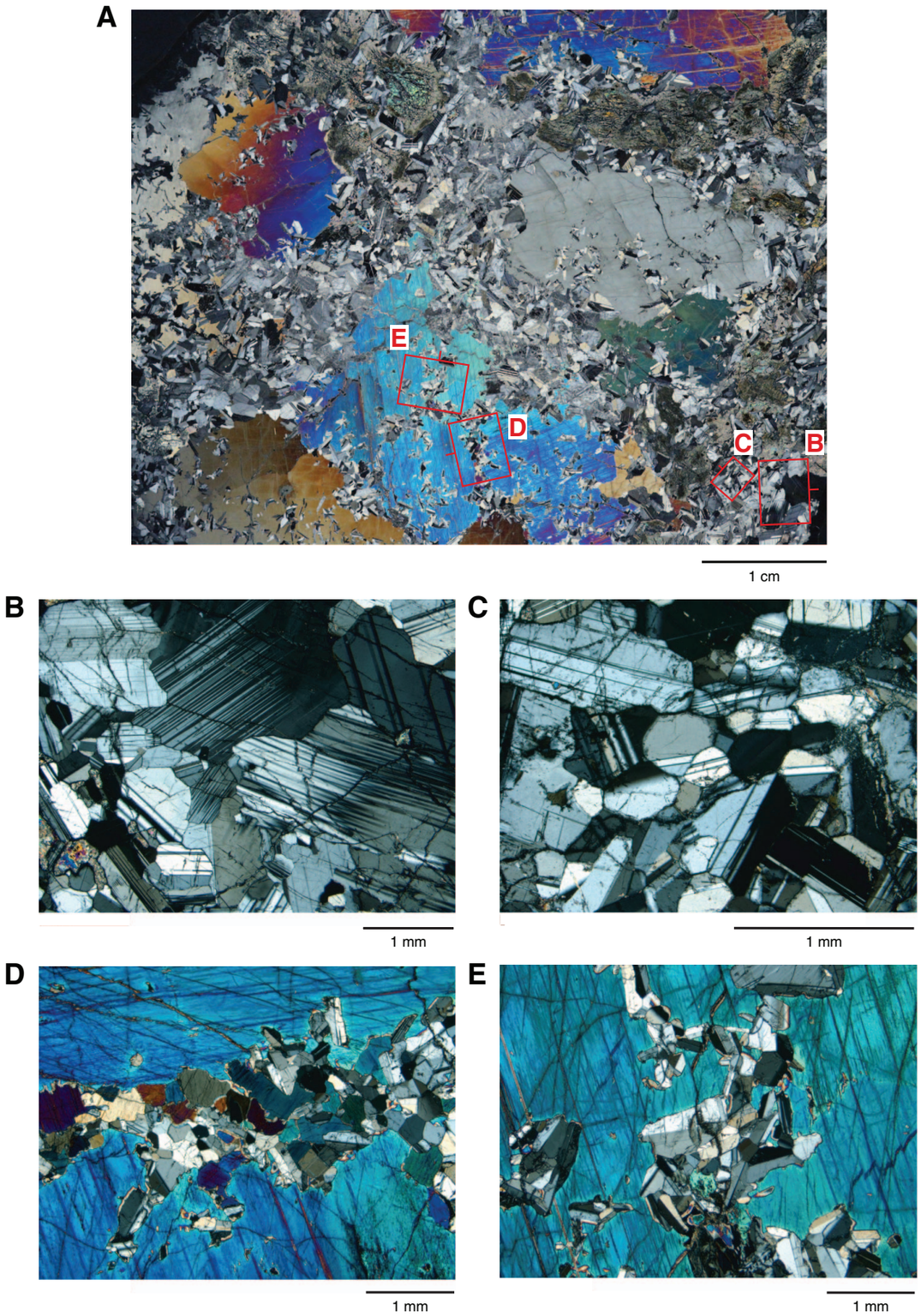

Figure F70. Cataclastic foliation, Sample 345-U1415J-21R-1, 17–19 cm (Piece 4). **A.** Macroscopic rotation of cataclastic foliation into fine-grained zones, microfaulting, and asymmetric prehnite porphyroclasts. **B.** Microstructure of well-developed cataclastic foliation defined by anastomosing ultrafine-grained dark to light brown layers (clay?) separated by lenses hosting porphyroclasts of plagioclase, prehnite, epidote, clinozoisite/zoisite, and carbonate. Red box indicates location of C. **C.** Asymmetric prehnite porphyroclasts ("fish") showing undulose extinction and subgrain formation, hosted in a sheared chlorite matrix. Although sense-of-shear indicators are recognized in thin section, none of the recovered pieces hosting these microstructures are oriented; therefore, no shear sense was determined. Under crossed polars.

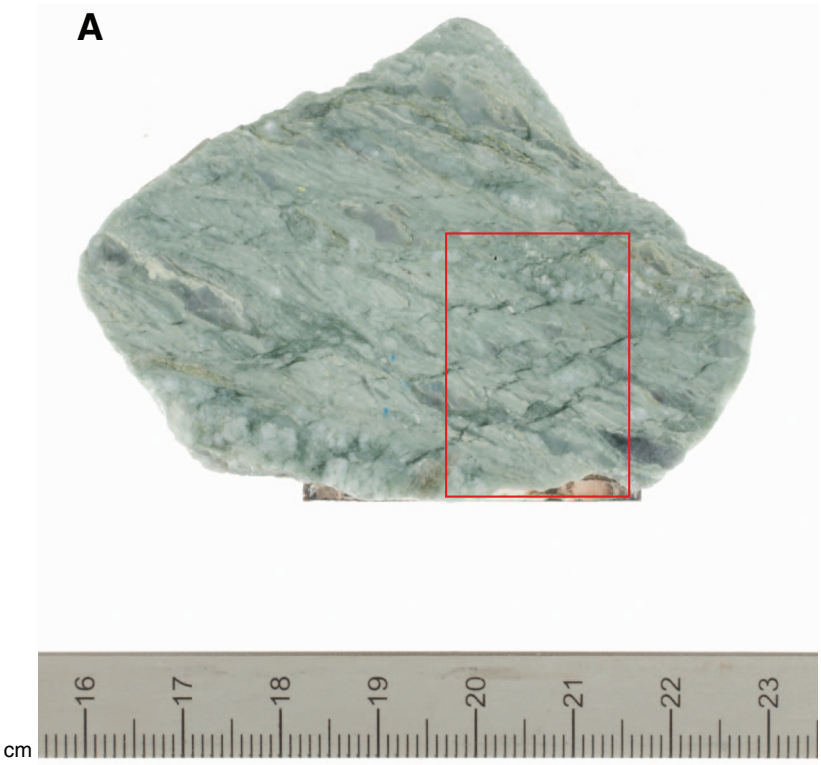

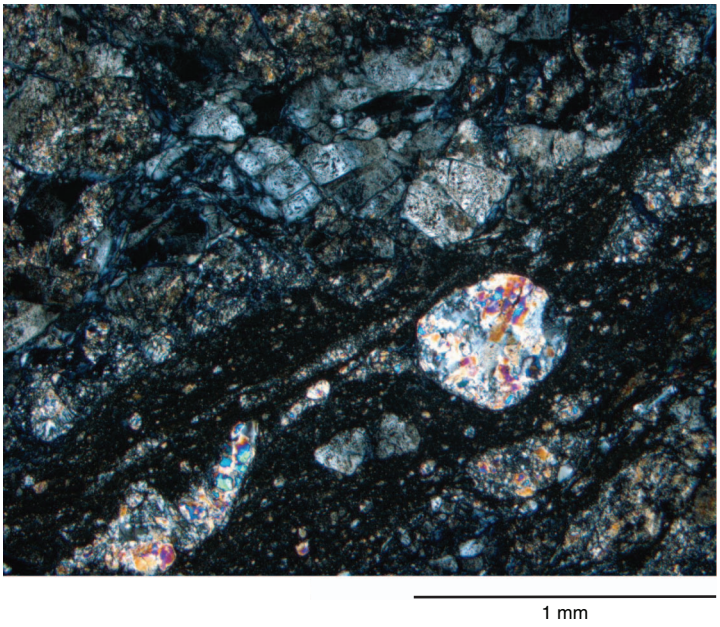

Figure F71. Brittle deformation intensity (Ranks 0–5), Hole U1415J. **A.** Cored intervals. (Continued on next page.)

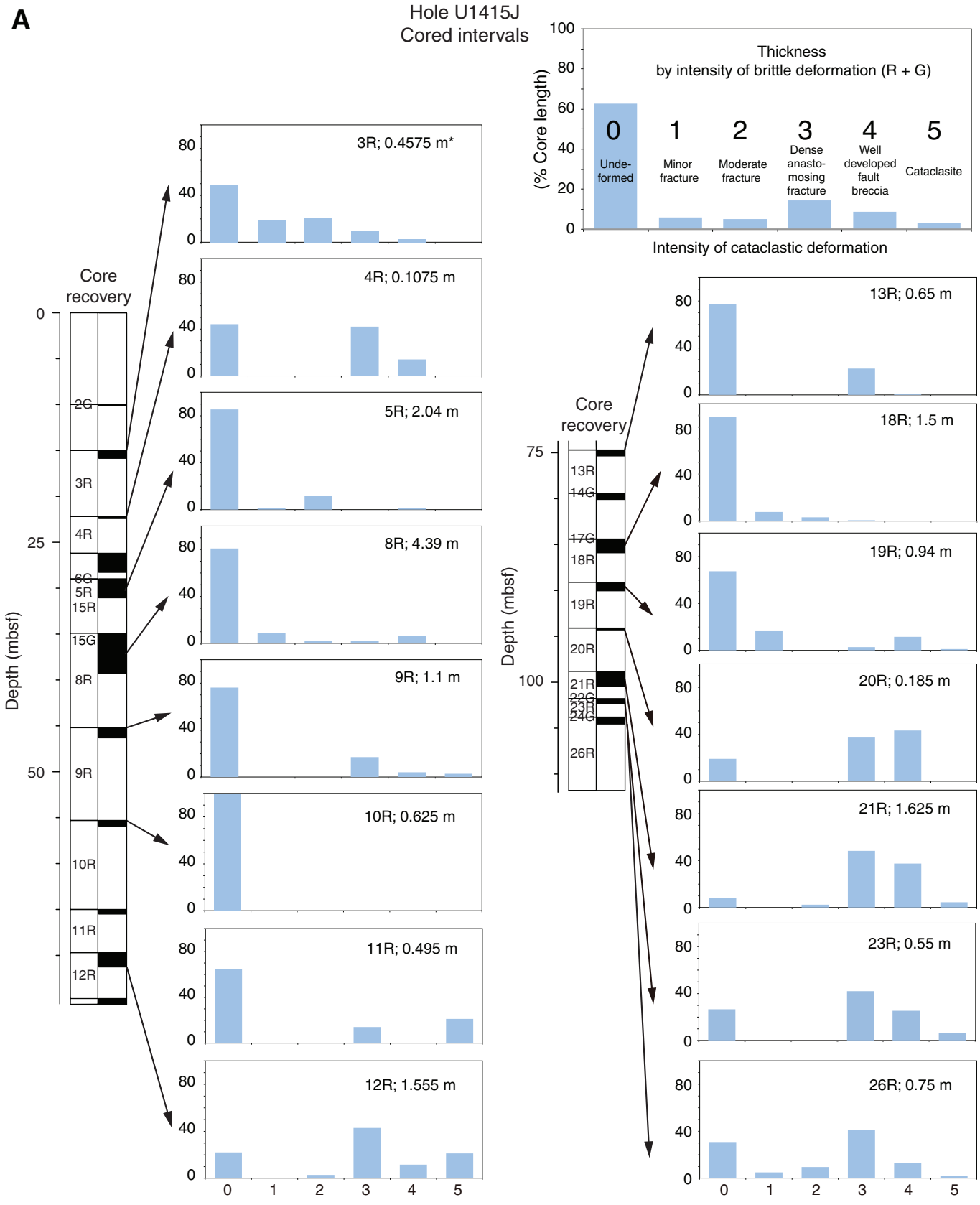

Figure F71 (continued). B. Ghost intervals.

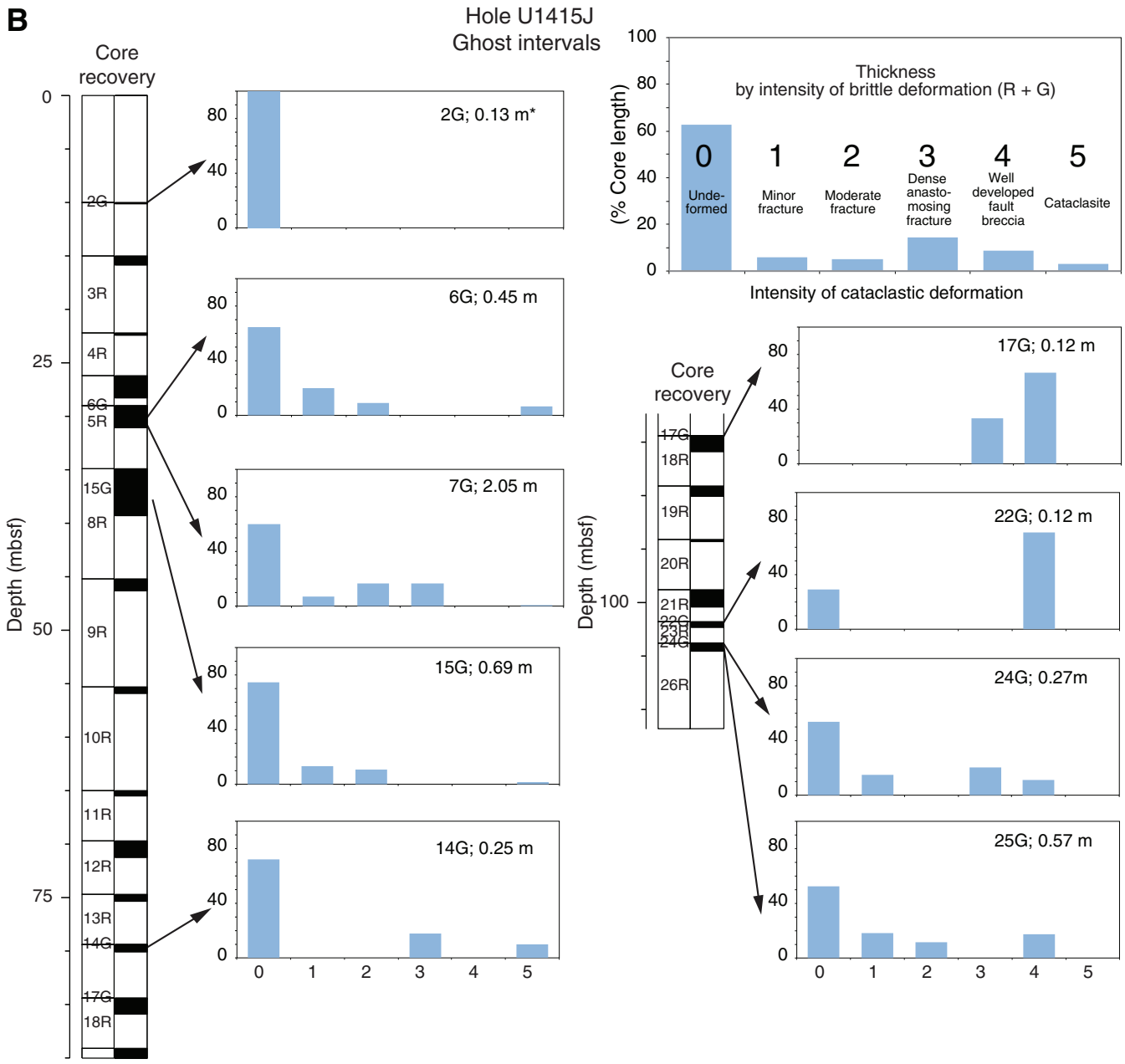

Figure F72. Brittle deformation intensity (Ranks 0–5), Cores 345-U1415J-12R, 13R, 20R, and 21R.

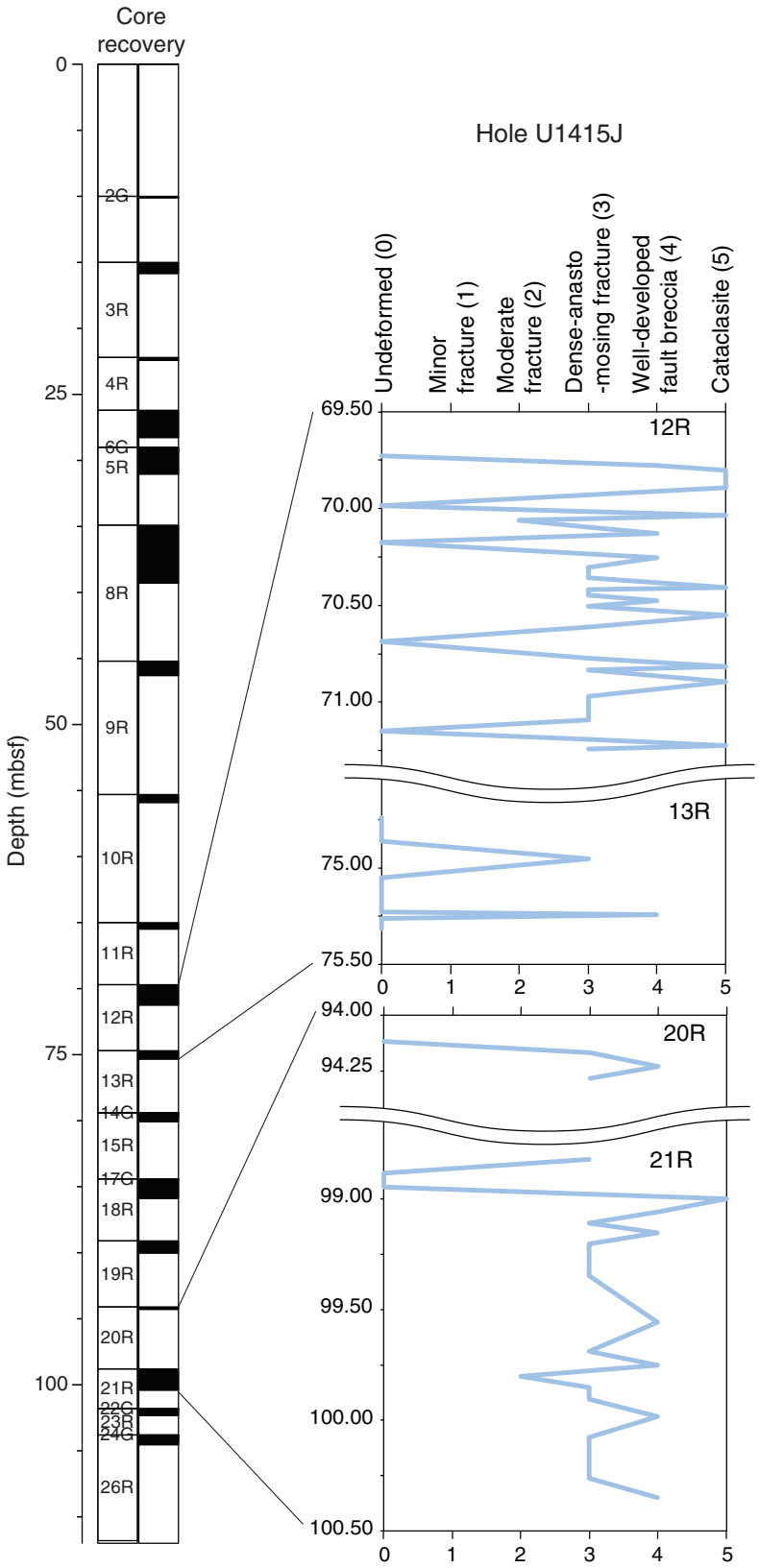

Figure F73. Brittle macro- and microstructures. **A, B.** Rank 3 brittle deformation (dense-anastomosing fracturing) and well-developed brecciation (Rank 4). A. Sample 345-U1415J-12R-1, 82–93 cm (Piece 12). B. Sample 345-U1415J-12R-1, 73–81 cm (Piece 11). **C.** Cataclasite (Sample 345-U1415J-12R-1, 11–14 cm [Piece 3]). **D, F.** Thin Section 61; Sample 345-U1415J-12R-1, 11–13 cm (Piece 3). D. Cataclasite cut by an epidote vein (plane-polarized light). F. Crosscutting relationship between cataclasite and epidote vein (under crossed polars). **E, G.** Thin Section 62; Sample 345-U1415J-12R-1, 86–89 cm (Piece 12); under crossed polars. E. Cataclasite. G. Chlorite-filled space in fractured plagioclase and clinopyroxene.

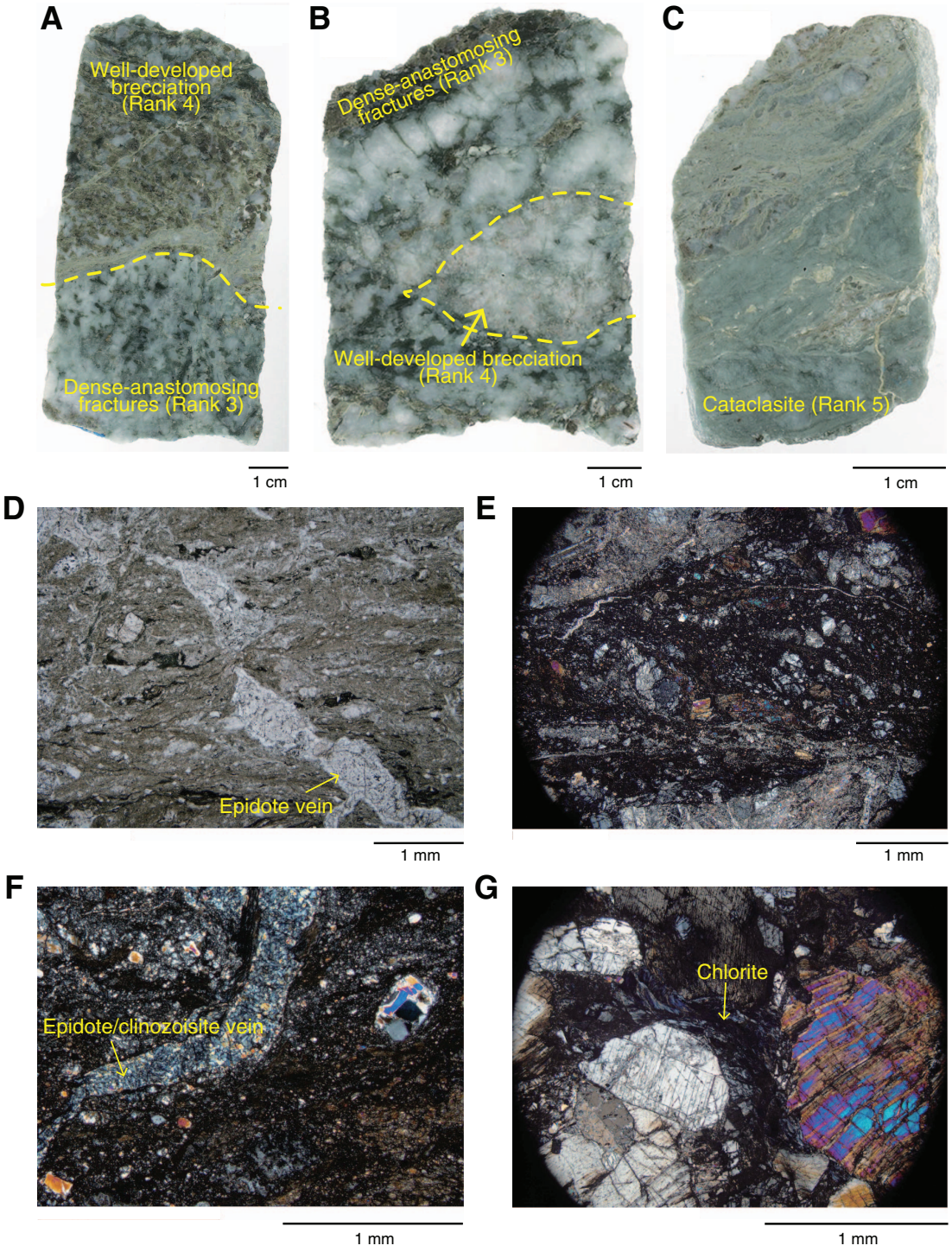

Figure F74. Brittle structures. **A.** Dense anastomosing fracturing (Rank 3; Sample 345-U1415J-21R-1, 0–13 cm [Piece 1]). **B.** Well-developed brecciation (Rank 4; Sample 345-U1415J-21R-1, 113–124 cm [Piece 16]). **C.** Cataclasite (Rank 5) with strong cataclastic foliation (Sample 345-U1415J-21R-1, 16–23 cm [Piece 4]). **D.** Fine-grained prehnite vein (center) and chlorite vein (right) developed along subvertical-oriented cataclasite zone (Thin Section 79; Sample 345-U1415J-21R-1, 103–107 cm [Piece 14]). **E.** Cataclasite (Thin Section 77; Sample 345-U1415J-21R-1, 17–19 cm [Piece 4]). **F.** Crosscutting relationship between cataclasite zone and chlorite vein (also Thin Section 77). **G.** Chlorite filled space in fractured plagioclase (Thin Section 80; Sample 345-U1415J-21R-1, 118–121 cm [Piece 16]). D–G are under crossed polars.

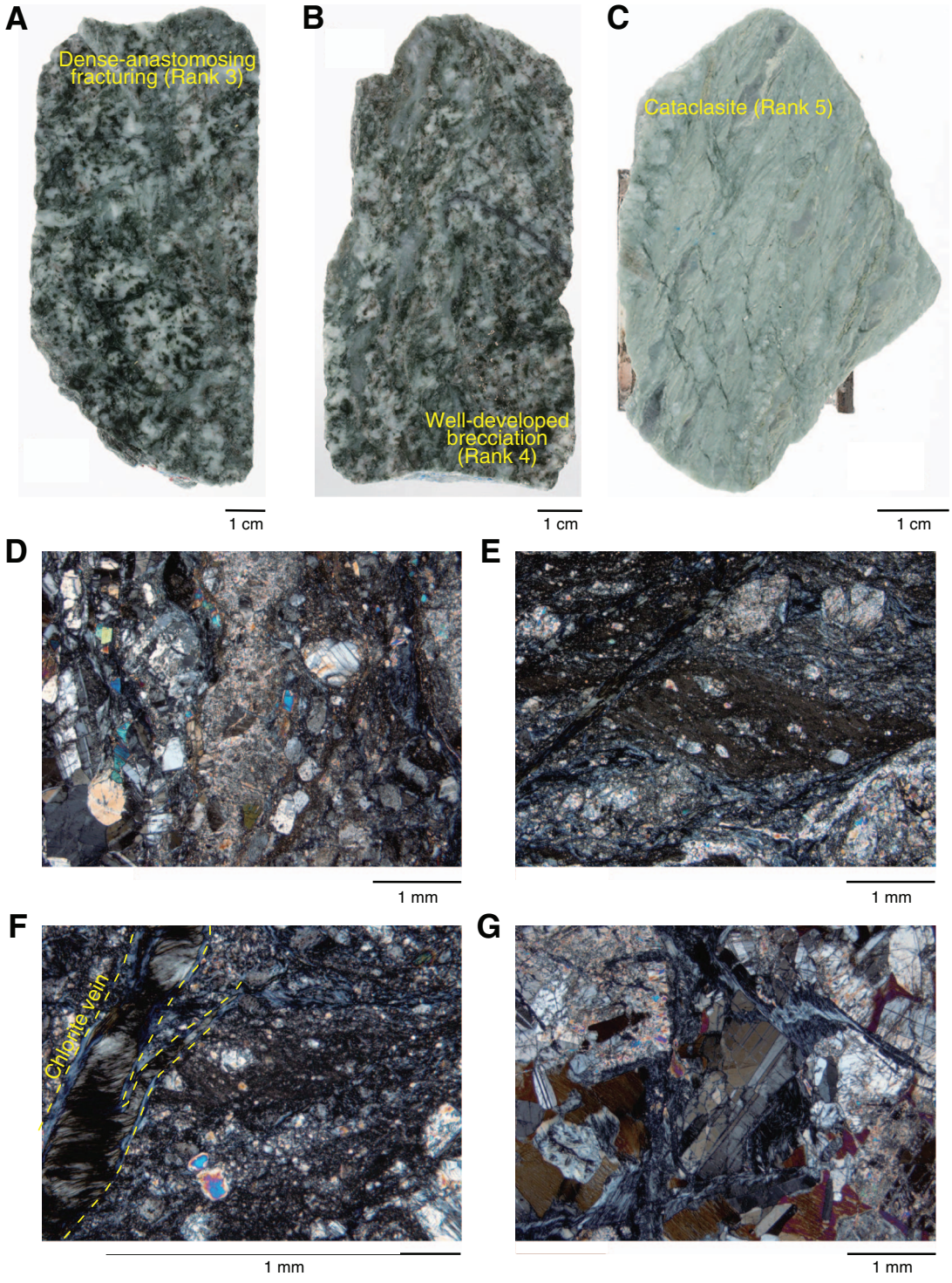

Figure F75. Dips from oriented zones of brittle deformation, Hole U1415J.

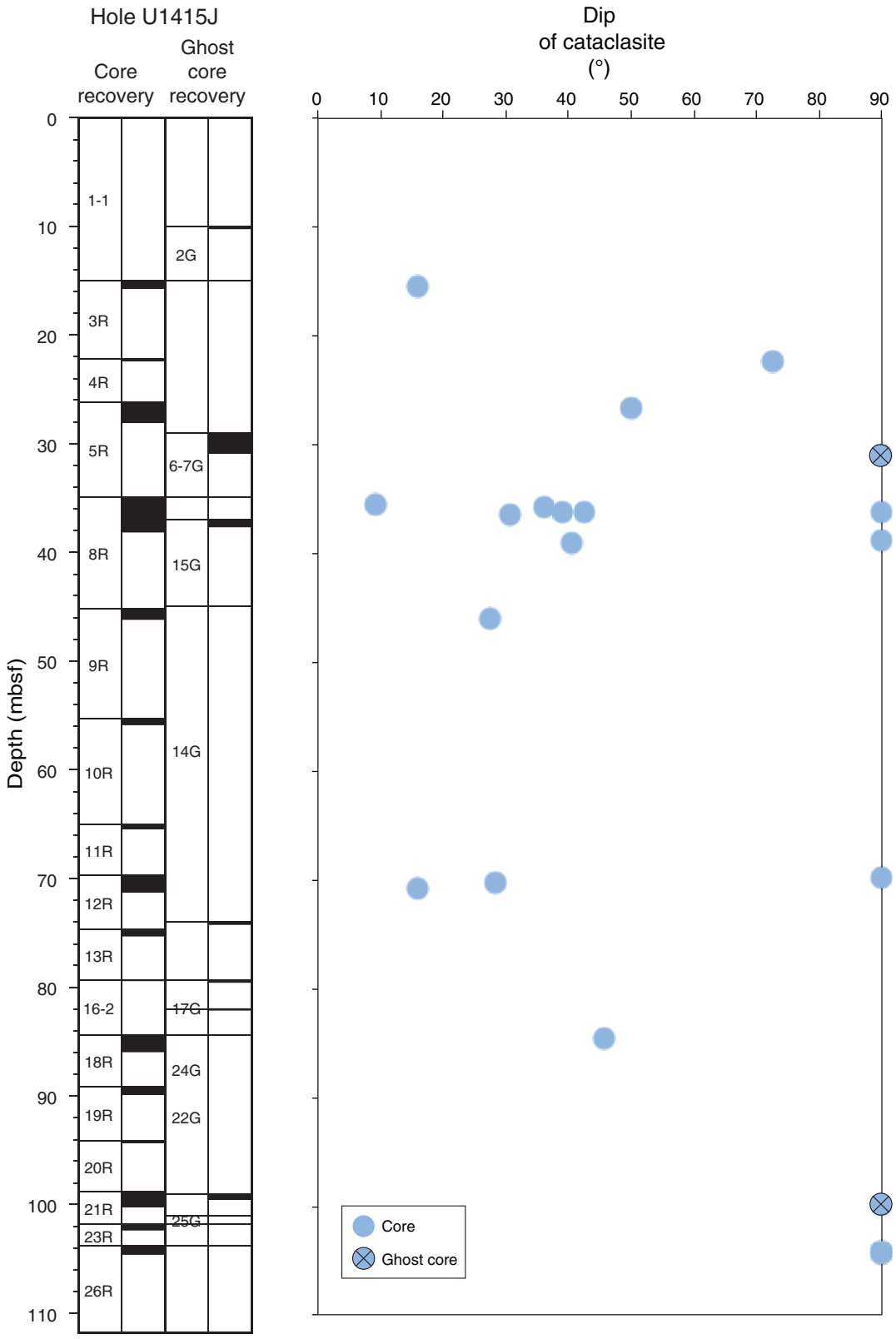

Figure F76. Fractured anorthosite. **A.** Zone of localized strain with subvertical orientation (Sample 345-U1415J-13R-1, 18.5–32.0 cm [Piece 4]). **B–D.** Thin Section 65; Sample 345-U1415J-13R-1, 26–29 cm [Piece 4B]; under crossed polars. (B) Fractured anorthosite. (C) Fractured texture filled by chlorite. (D) Fractured texture filled by fine-grained prehnite.

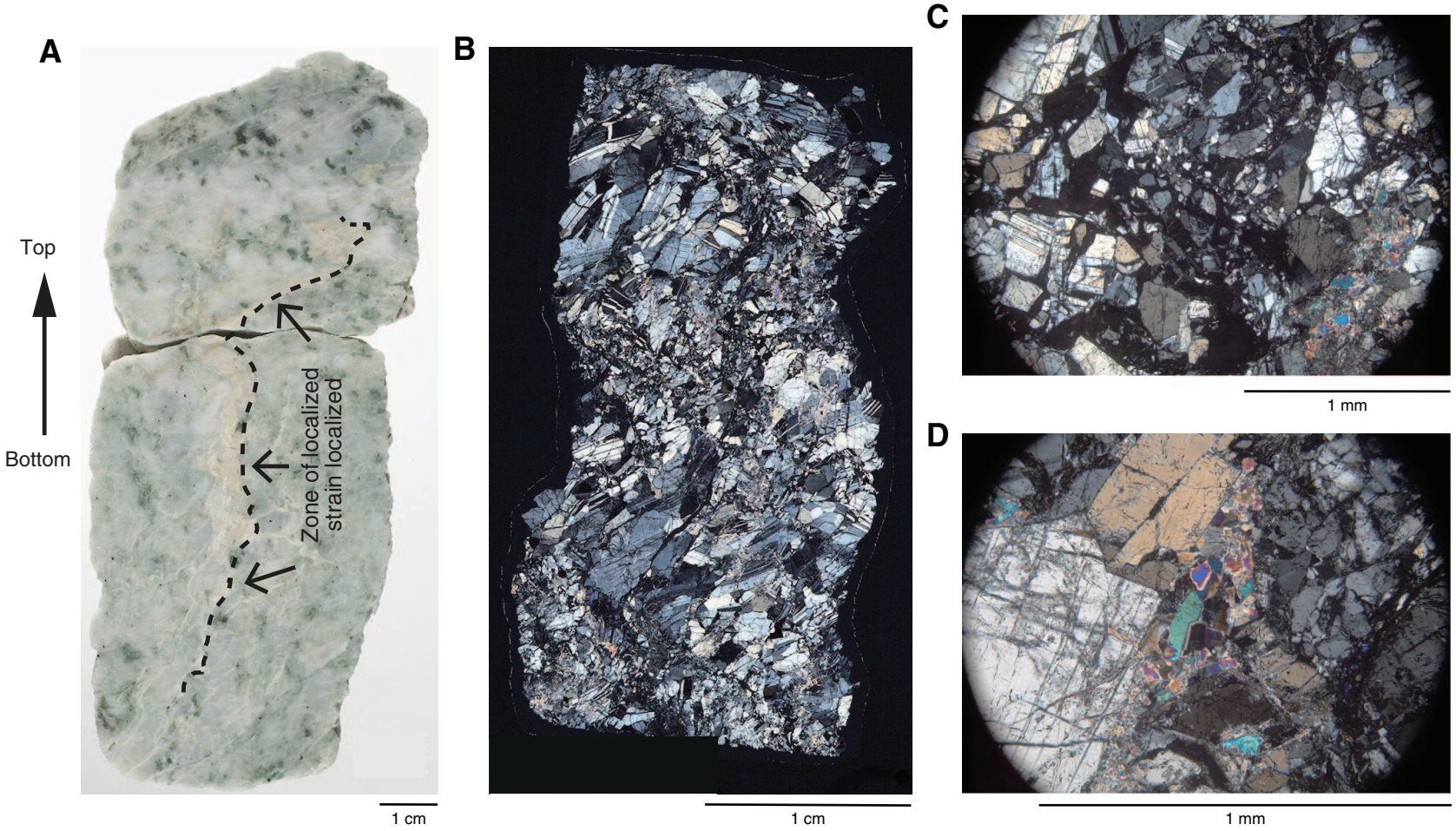

Figure F77. Intrusive relations between basaltic dike and cataclastic deformation (Sample 345-U1415J-19R-1, 63.5–70.0 cm [Piece 10]). **A.** Core close-up. Yellow box shows area in B. **B.** Thin Section 74; Sample 345-U1415J-19R-1, 64–67 cm (Piece 10). Yellow boxes (tick marks show upward direction) indicate locations of C–F (under crossed polars unless otherwise noted). **C.** Cataclasis hosting a deformed prehnite aggregate. **D.** Dike zone with narrow cataclastic deformation. **E.** Contact between cataclasite and dike, with epidote veins that cut the contact (plane-polarized light). **F.** Cataclastic deformation at the contact zone. Two thin zones of cataclasite derived from each zone develop at the contact zone.

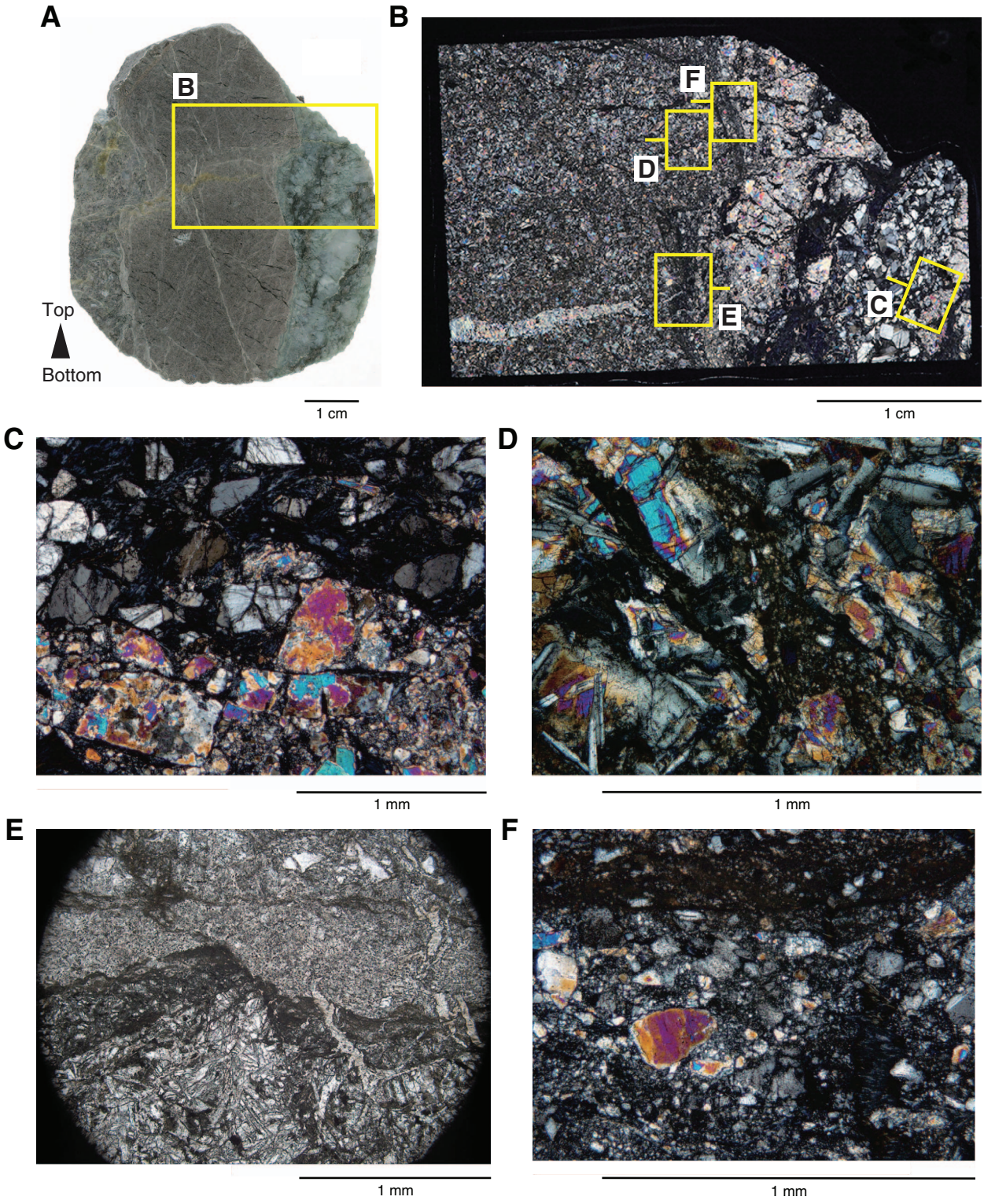

Figure F78. Microstructural relations between dolerite and cataclasite (under crossed polars unless otherwise noted). **A.** Thin Section 81; Sample 345-U1415J-23R-1, 10–12 cm (Piece 3). Yellow boxes (tick marks show upward direction) indicate locations of B–E. **B.** Altered clast in cataclasite zone (plane-polarized light). **C.** Epidote clasts surrounded by chlorite in cataclasite zone. **D.** Boundary between clinozoisite and prehnite veins. **E.** Boundary between cataclasite and dolerite chilled margin.

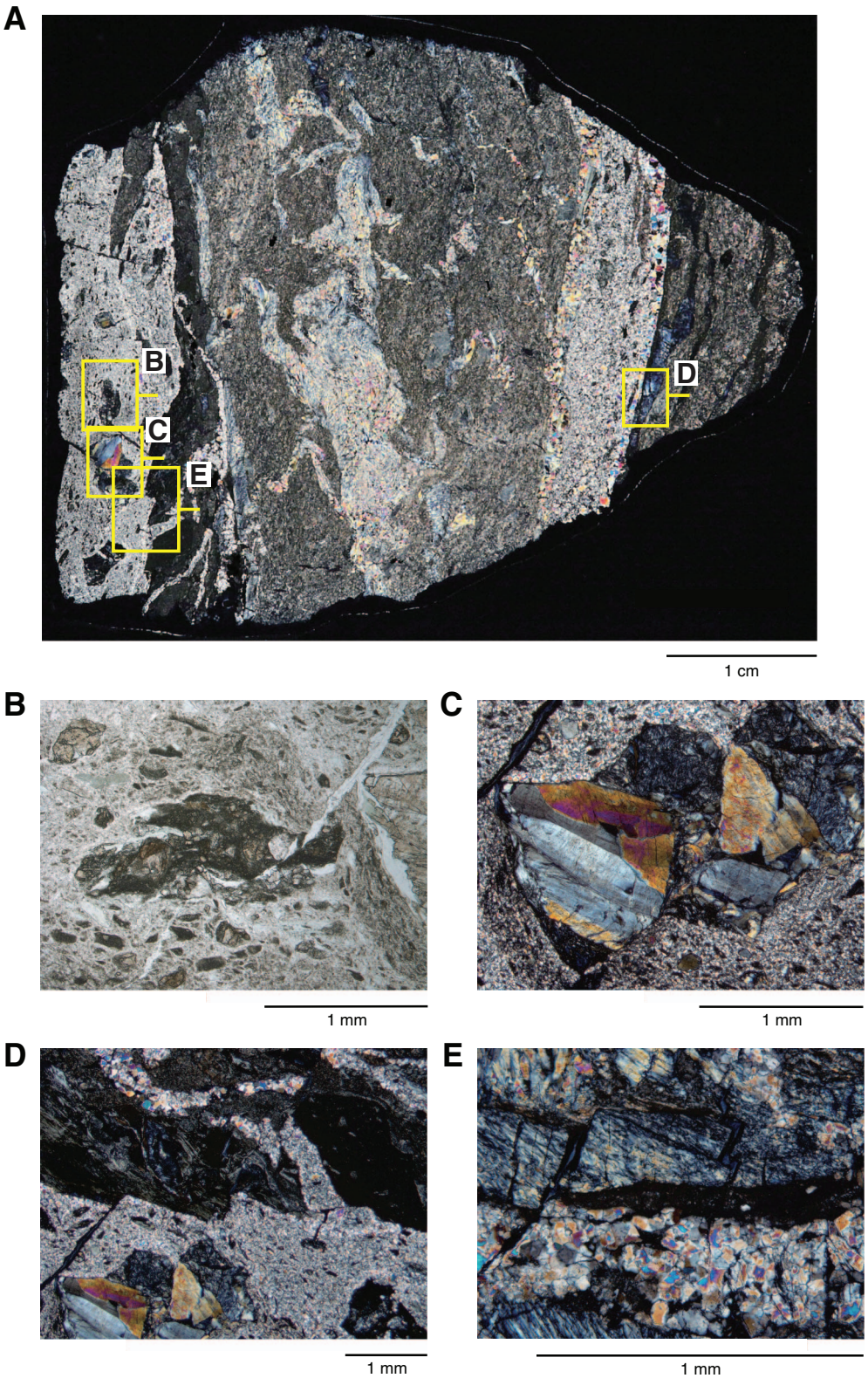

Figure F79. Microstructures in cataclasite (Thin Section 86; Sample 345-U1415J-26R-1, 23–25 cm [Piece 4]; under crossed polars). **A.** Whole thin section image. Yellow boxes (tick mark shows upward direction) indicate locations of B and C. **B.** Cataclasite. Prehnite grains replace plagioclase. **C.** Fractured plagioclase filled by chlorite.

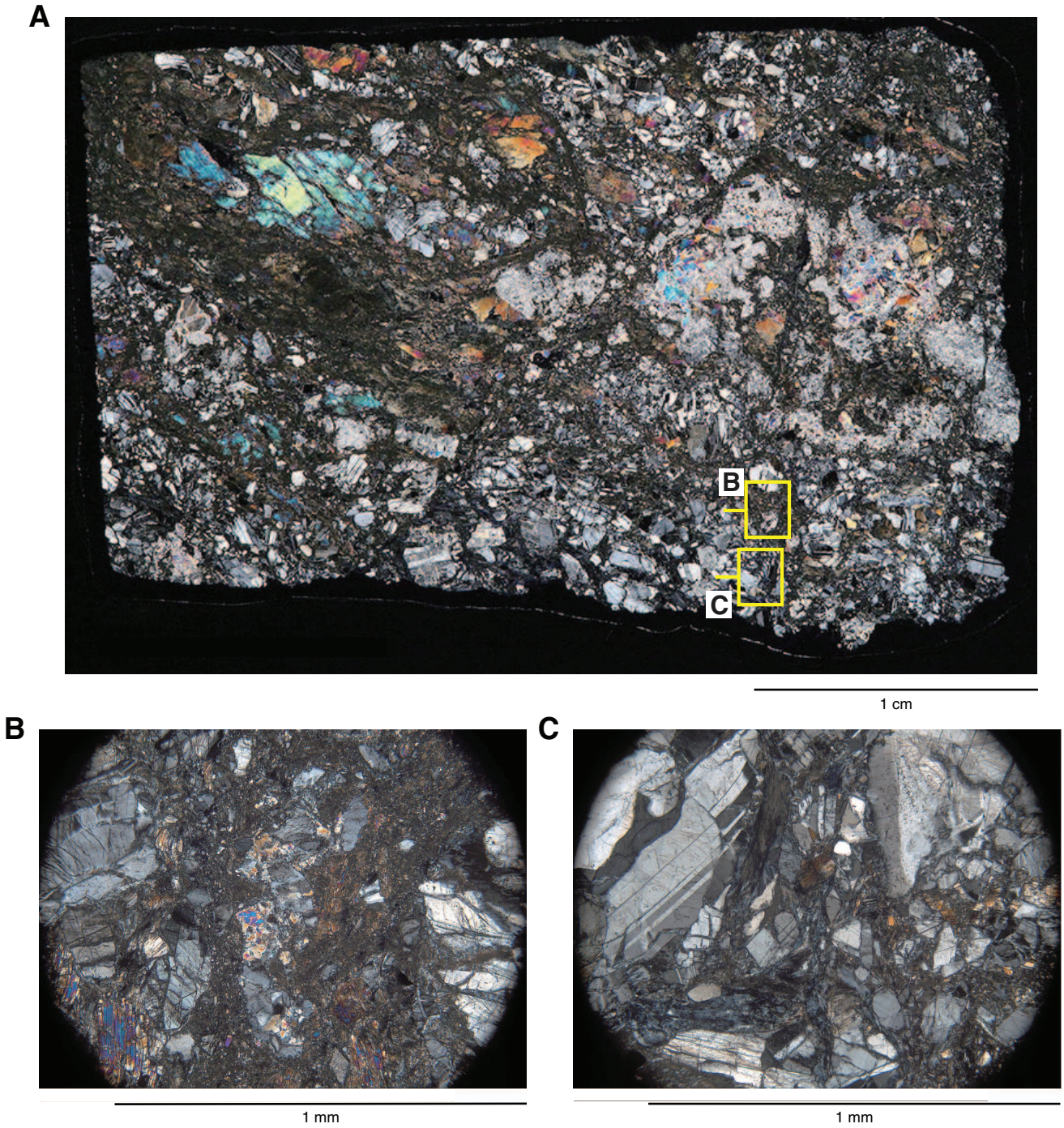

Figure F80. Macroscopic character of veins, Hole U1415J. **A.** Irregular prehnite vein (red arrow) perpendicular to magmatic foliation typical of the upper half of Hole U1415J in Units I and II (Sample 345-U1415J-8R-1A, 88.5–106 cm [Piece 14]). **B.** Set of parallel chlorite (greenish) veins perpendicular to the vertical magmatic foliation and set of parallel prehnite (white) veinlets (red arrows) parallel to the vertical magmatic foliation. Note branching of some vertical prehnite veins into horizontal chlorite veins (Sample 345-U1415J-18R-1A, 137.5–147 cm [Piece 17]).

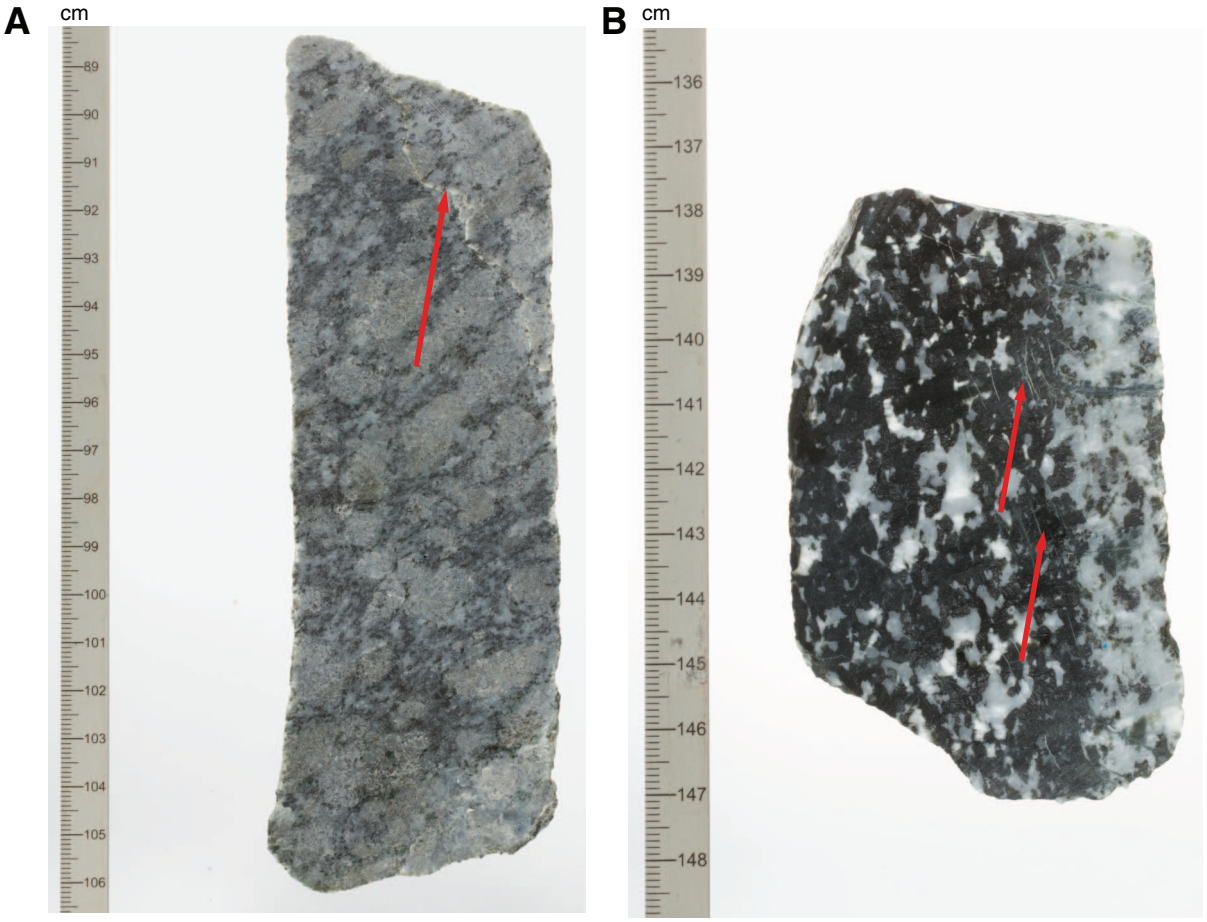

Figure F81. Microscopic character of veins (under crossed polars). **A.** Set of undeformed veins injected into serpentine (Sample 345-U1415J-19R-1, 18–19 cm [Piece 9]). V1 is filled with chlorite. Fibers grew normal to the vein wall (open crack). V2 is filled with prehnite, and V3 is filled with both chlorite and serpentine. **B.** Chlorite vein injected into weakly altered gabbro (Sample 345-U1415J-5R-1, 138–141 cm [Piece 18]). Fibers are perpendicular to the vein walls, but their slightly sigmoidal shape shows moderate shearing during or after crack opening and chlorite crystallization. **C.** Chlorite vein injected into altered troctolite (Sample 345-U1415J-18R-1, 141–143 cm [Piece 17B]). Fibers initially formed perpendicular to vein walls and were eventually sheared along the vein walls. Shear movement caused bending and displacement of the first filling material together with grain size reduction. **D.** Chlorite vein injected into moderately altered troctolite (Sample 345-U1415J-21R-1, 58–59 cm [Piece 9]). Fibers oblique to the vein walls and sigmoidal shape show that the crack opened and chlorite crystallized during shearing. **E.** Strongly sheared chlorite vein associated with cataclasite (Sample 345-U1415J-21R-1, 17–19 cm [Piece 4]). **F.** Chlorite-filled tension gashes filled with chlorite perpendicular to cataclastic foliation (Sample 345-U1415J-23R-1, 10–12 cm [Piece 3]).

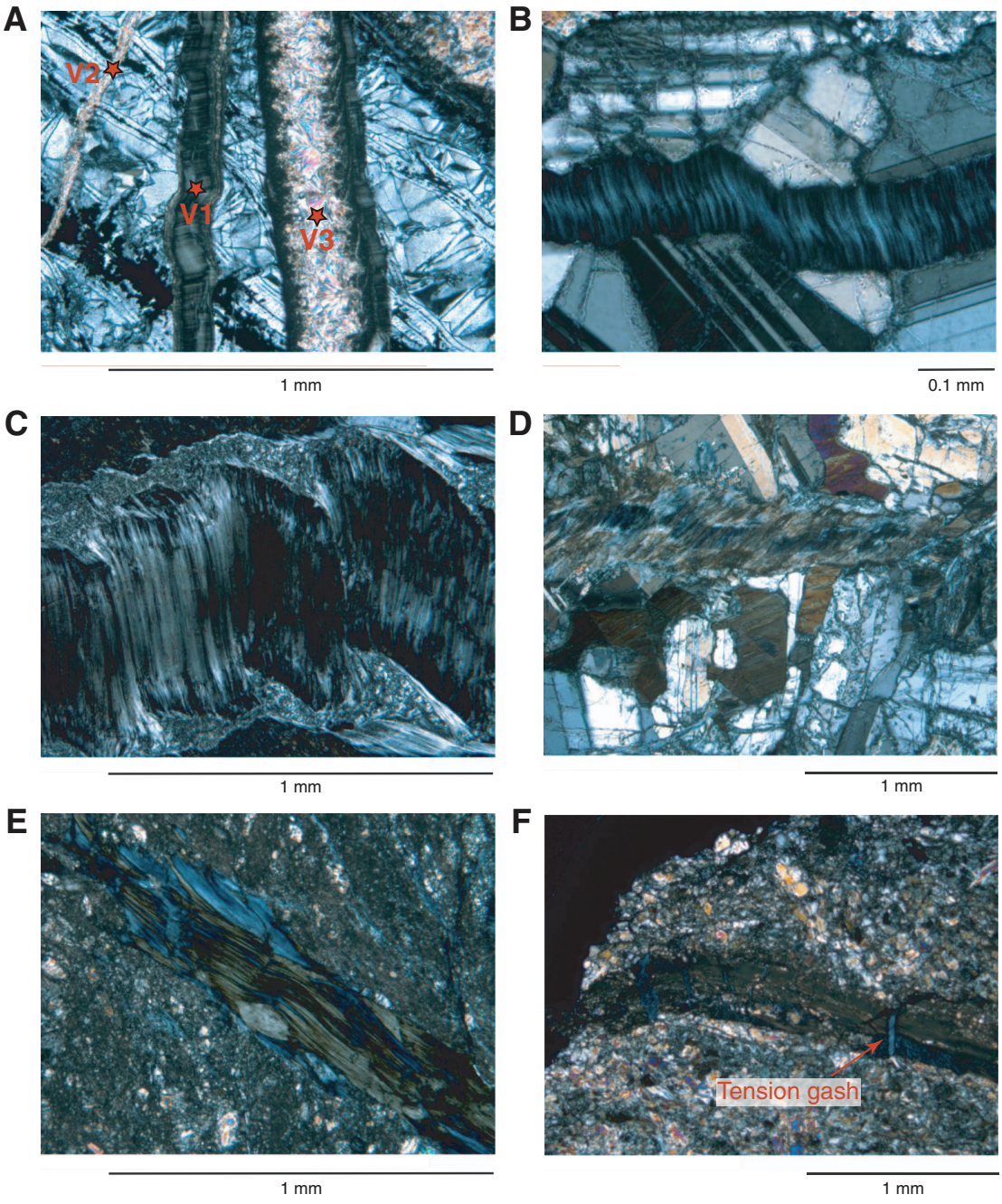

Figure F82. Vein density expressed as percentage of core length for (**A**) the entire core (0–104.55 mbsf), (**B**) Unit II (Sections 345-U1415J-5R-1 to 9R-1; 26.2–55.3 mbsf), and (**C**) Unit III (Sections 345-U1415J-10R-1 to 26R-1; 55.30–104.55 mbsf).

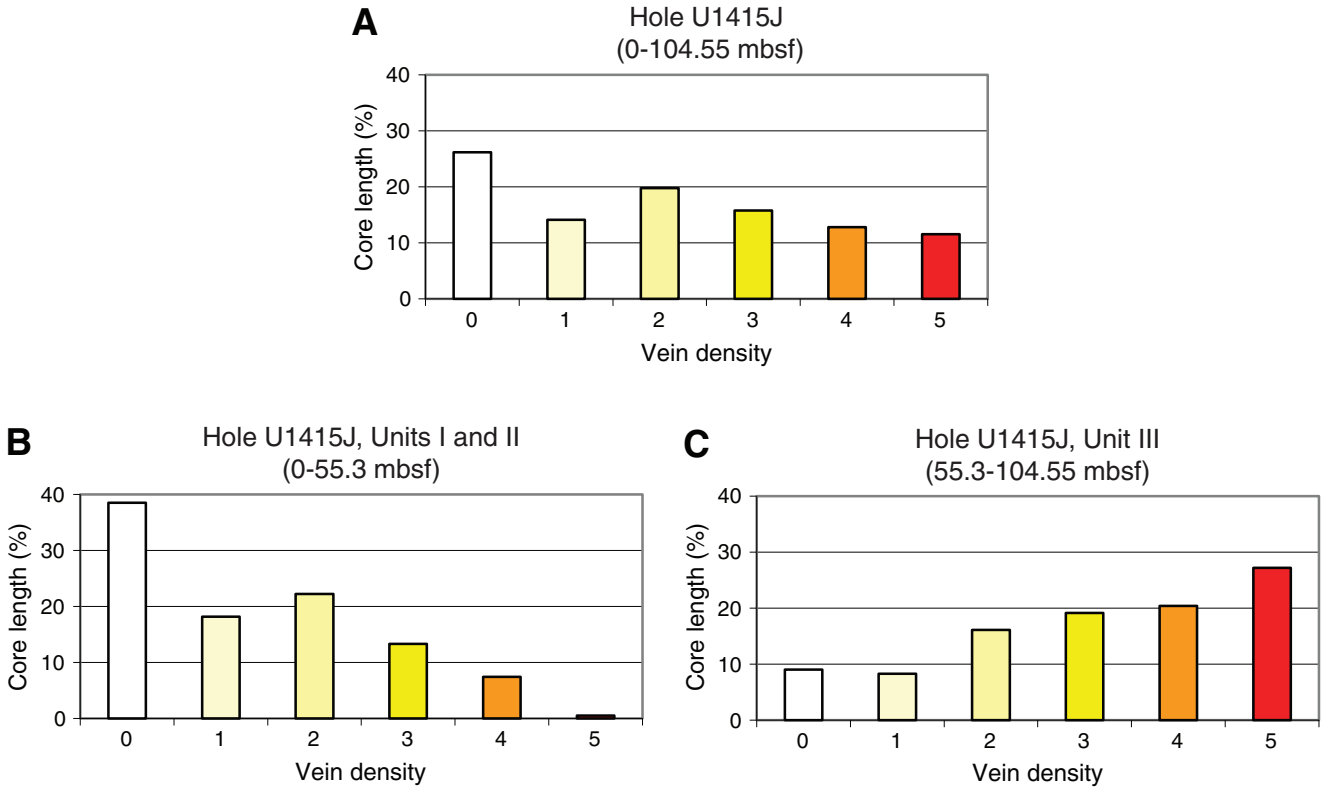

Figure F83. Vein density expressed as percentage of core length (*y*-axis), Hole U1415J.

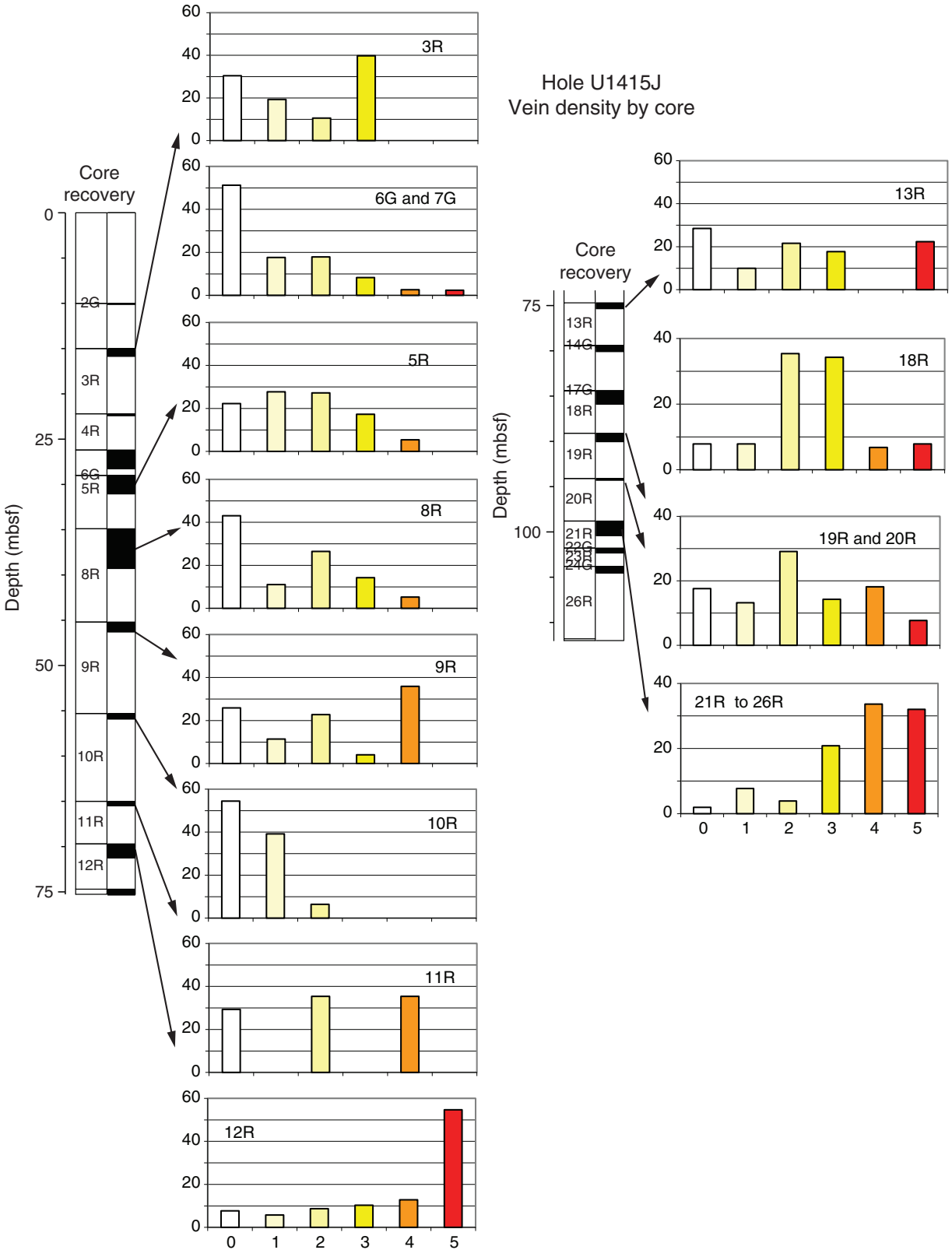

Figure F84. Core recovery and location and measured vein dip, Hole U1415J.

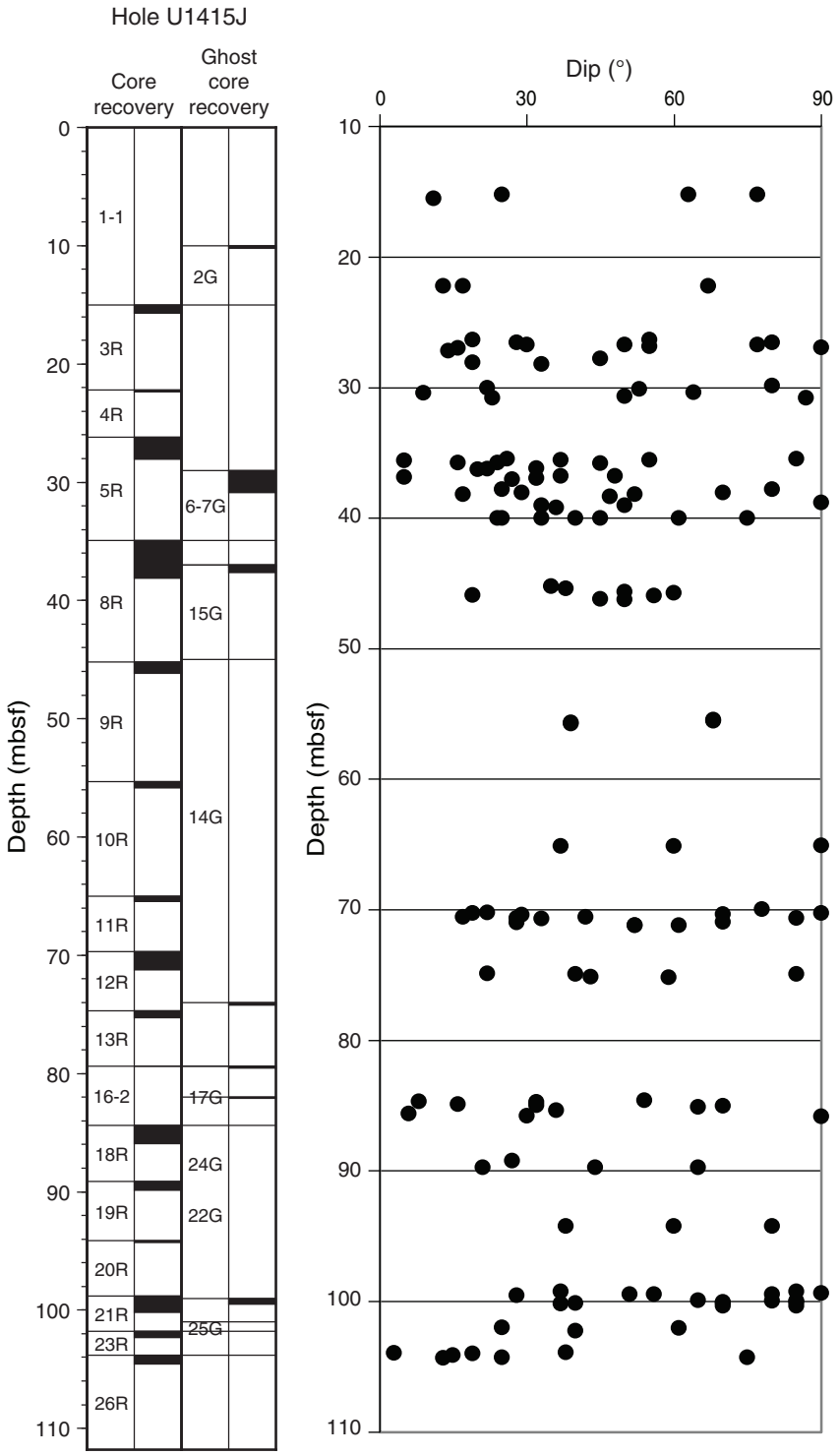

Figure F85. Core recovery and measured vein dip for (**A**) entire hole, (**B**) Units I and II, and (**C**) Unit III, Hole U1415J.

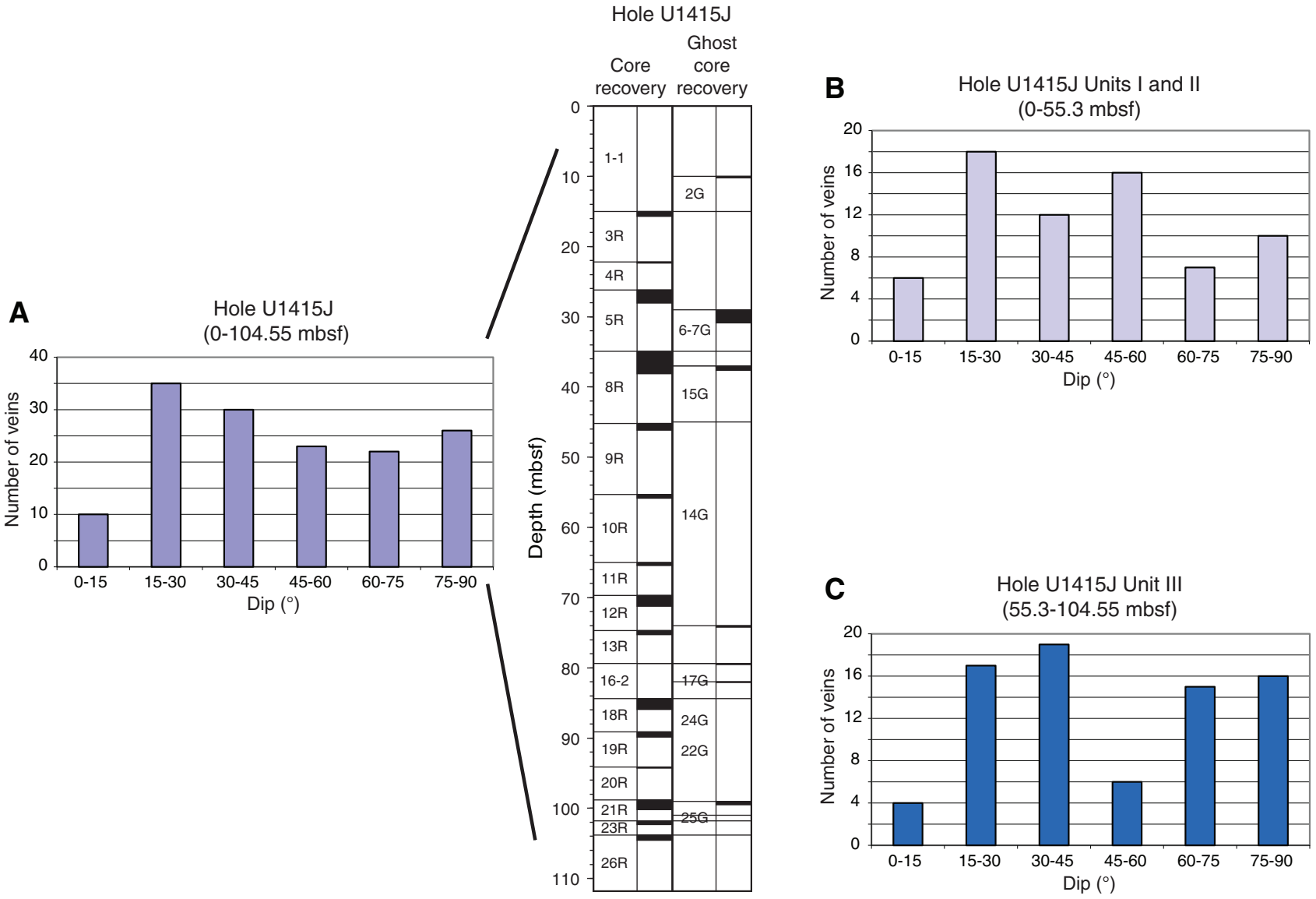

Figure F86. Vein type, location, and measured dip, Hole U1415J.

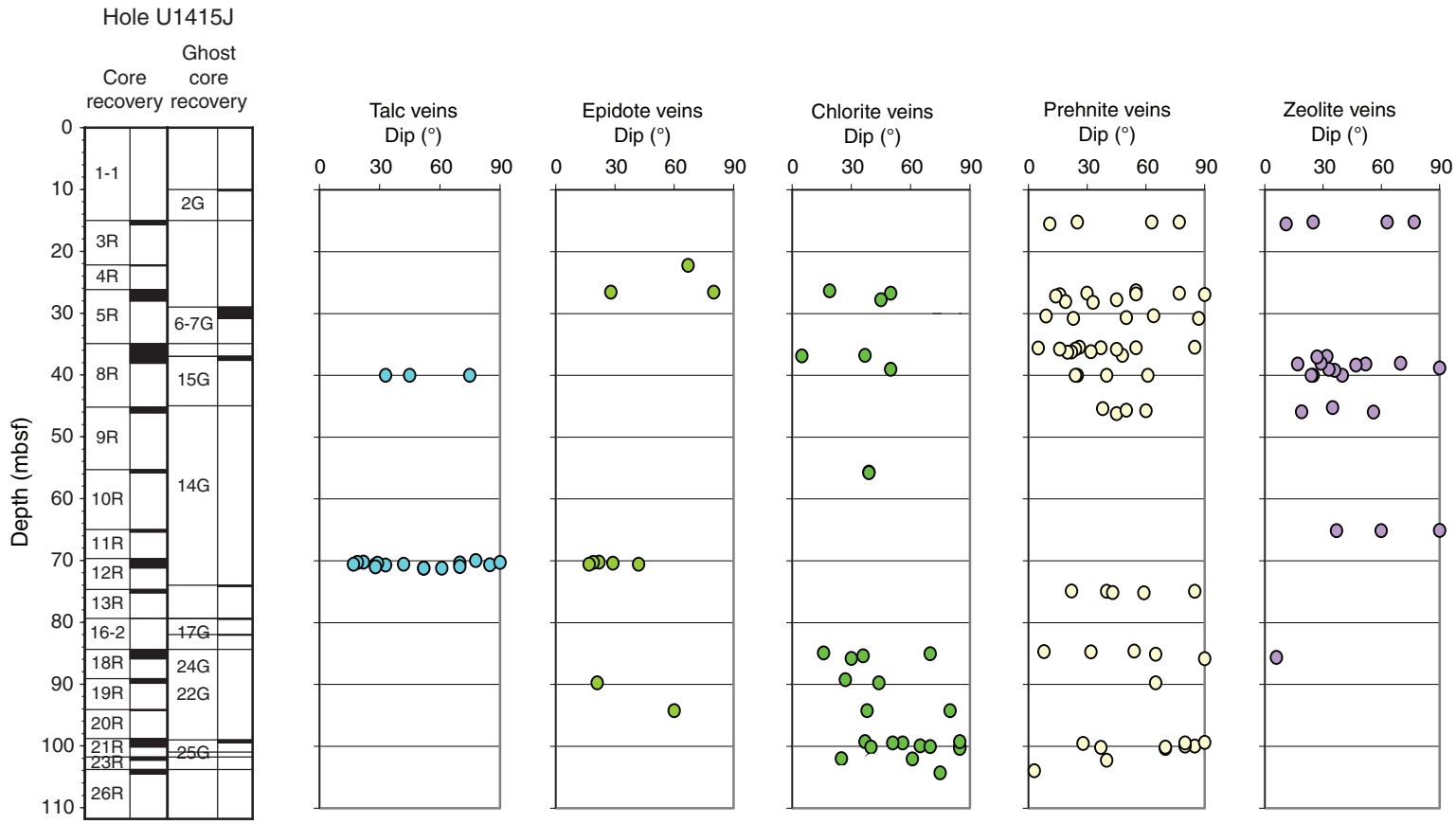

Figure F87. Natural remanent magnetization (NRM) intensity for gabbroic and troctolitic rocks in Hole U1415J based on archive-half core remanence measurements.

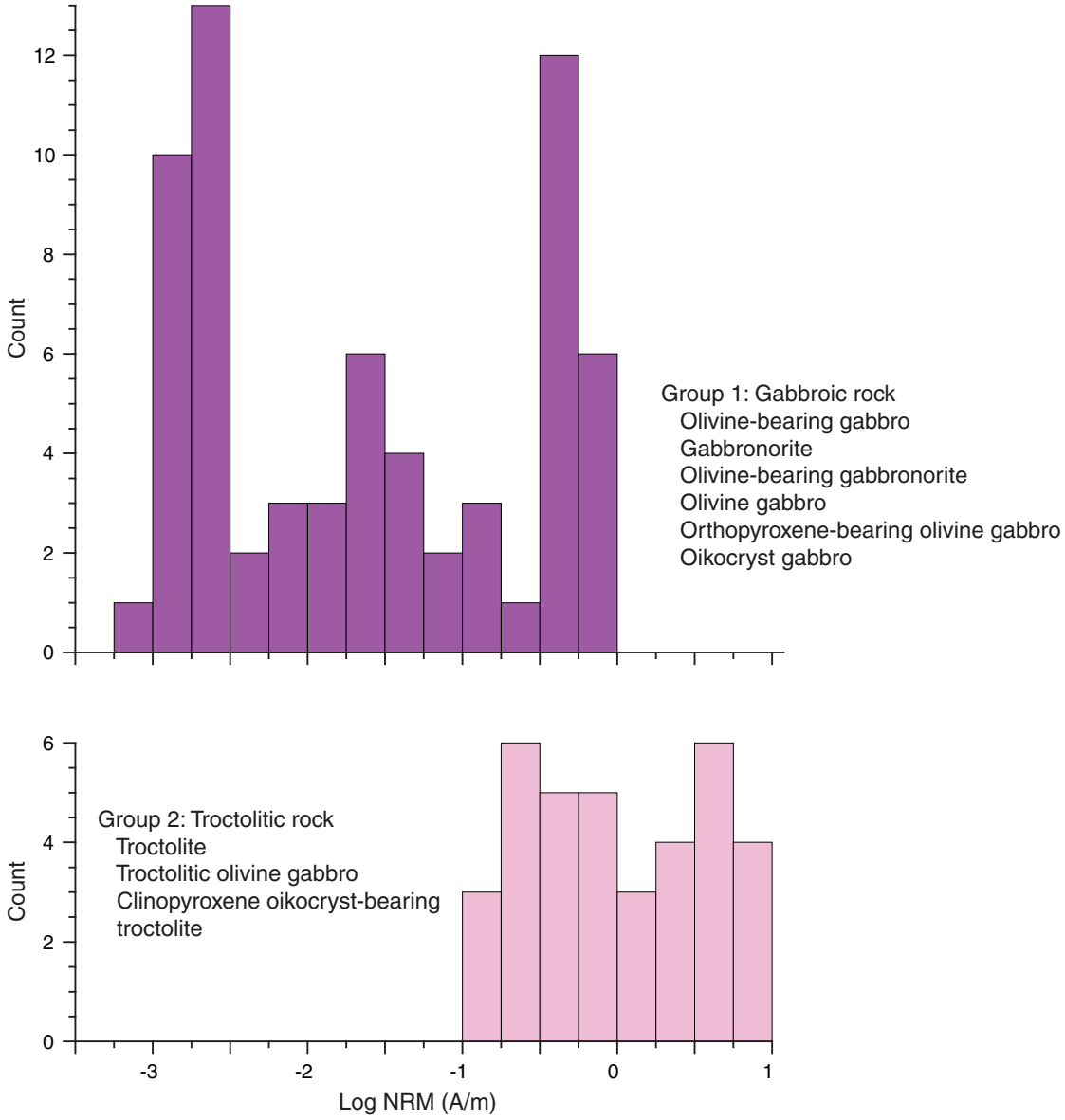

Figure F88. A–I. Representative examples of alternating field demagnetization of archive-half core pieces recovered from Hole U1415J. Solid circles = projection onto the horizontal plane, open circles = projection onto the vertical X–Z plane. NRM = natural remanent magnetization, Cpx = clinopyroxene.

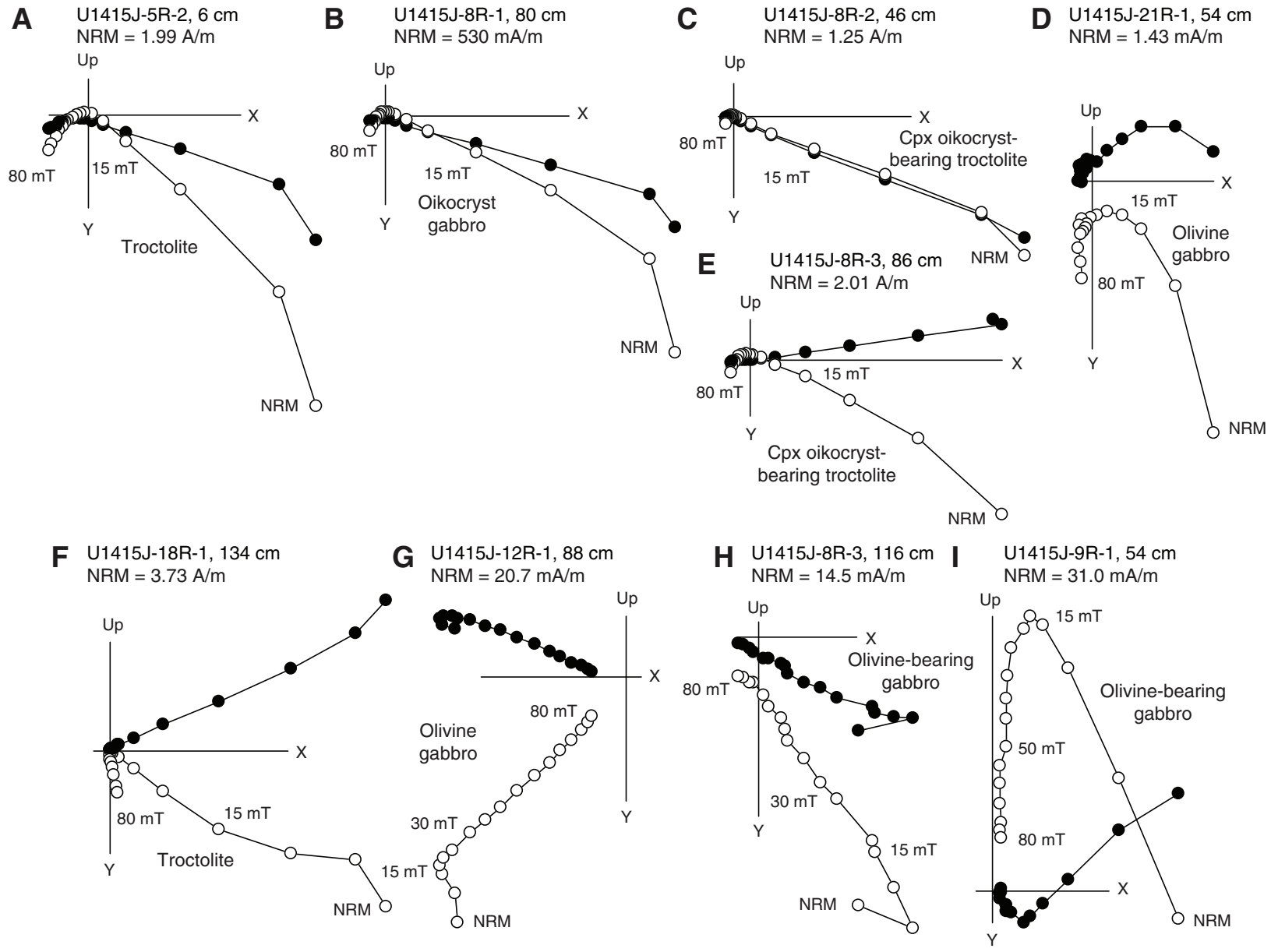

Figure F89. Summary of archive-half core magnetic measurements, Hole U1415J. For inclination and intensity, open circles are natural remanent magnetization data and solid circles are principal component analysis picks. Point magnetic susceptibility was measured on the Section Half Multisensor Logger. Remanence and susceptibility data from within 4.5 cm of piece ends have been excluded.

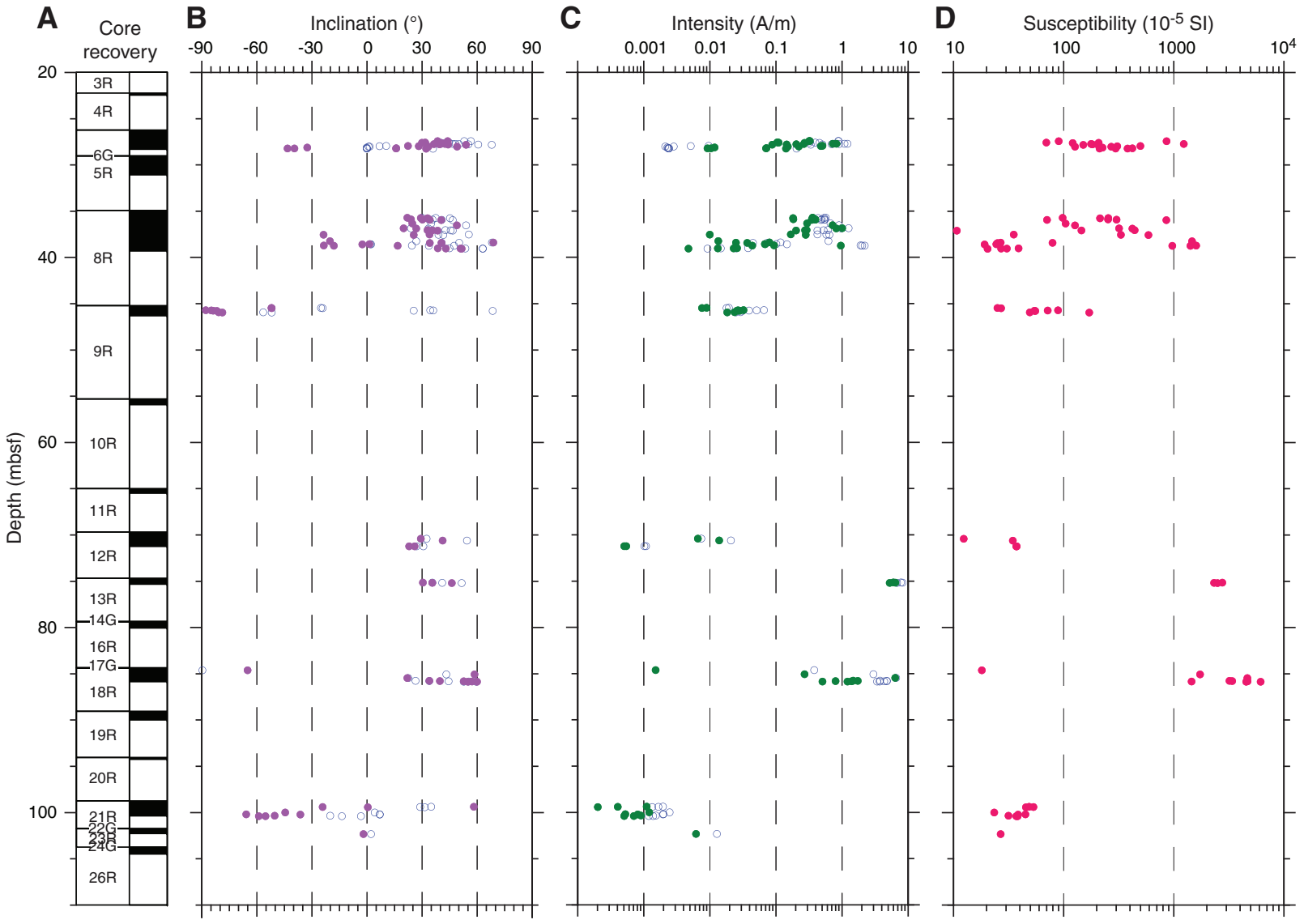

Figure F90. Demagnetization data from adjacent discrete samples containing oikocrysts, Section 345-U1415J-8R-1. Solid circles = projection onto the horizontal plane, open circles = projection onto the vertical X–Z plane. Insets are normalized intensity plots (black line = intensity decay path, red line = vector difference sum). NRM = natural remanent magnetization, LTD1 = first low-temperature demagnetization treatment.

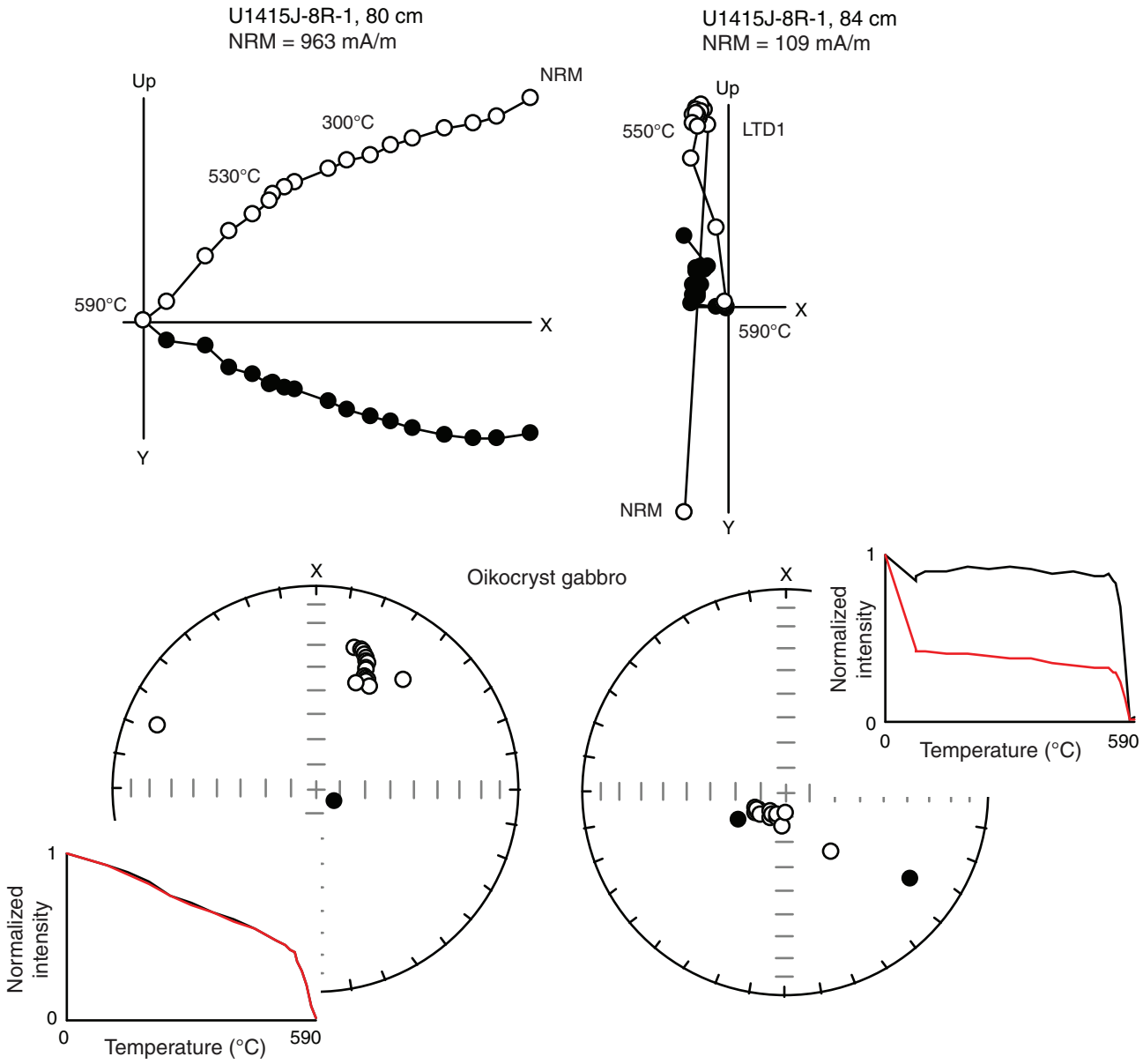

Figure F91. Typical examples of demagnetization behavior in discrete samples in Hole U1415J that have high unblocking temperature single components of magnetization. Solid circles = projection onto the horizontal plane, open circles = projection onto either the vertical X–Z or Y–Z planes. NRM = natural remanent magnetization, LTD1 = first low-temperature demagnetization treatment.

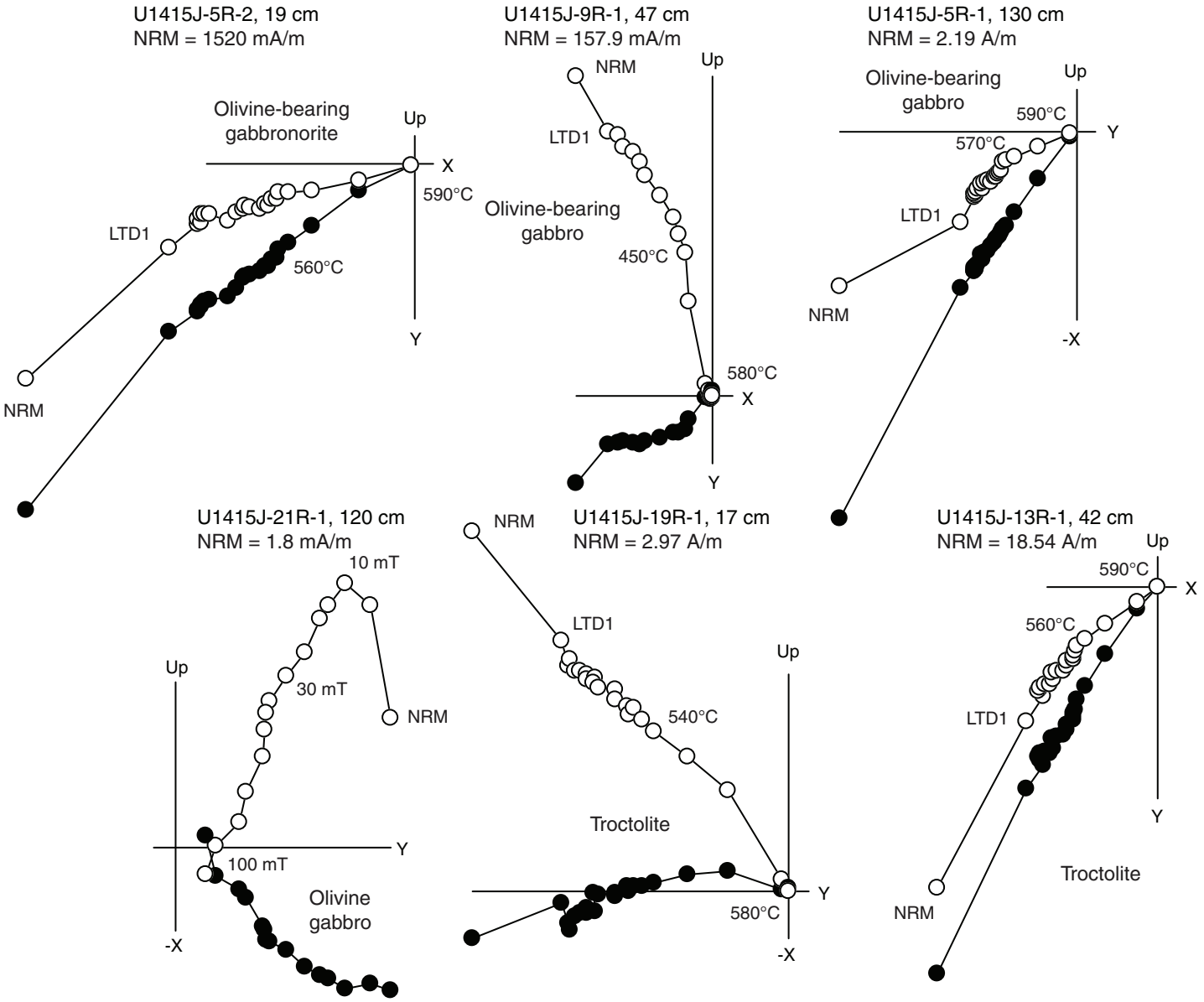

Figure F92. Normalized thermal demagnetization intensity decay curves for selected samples in Hole U1415J that have high unblocking temperature single components of magnetization.

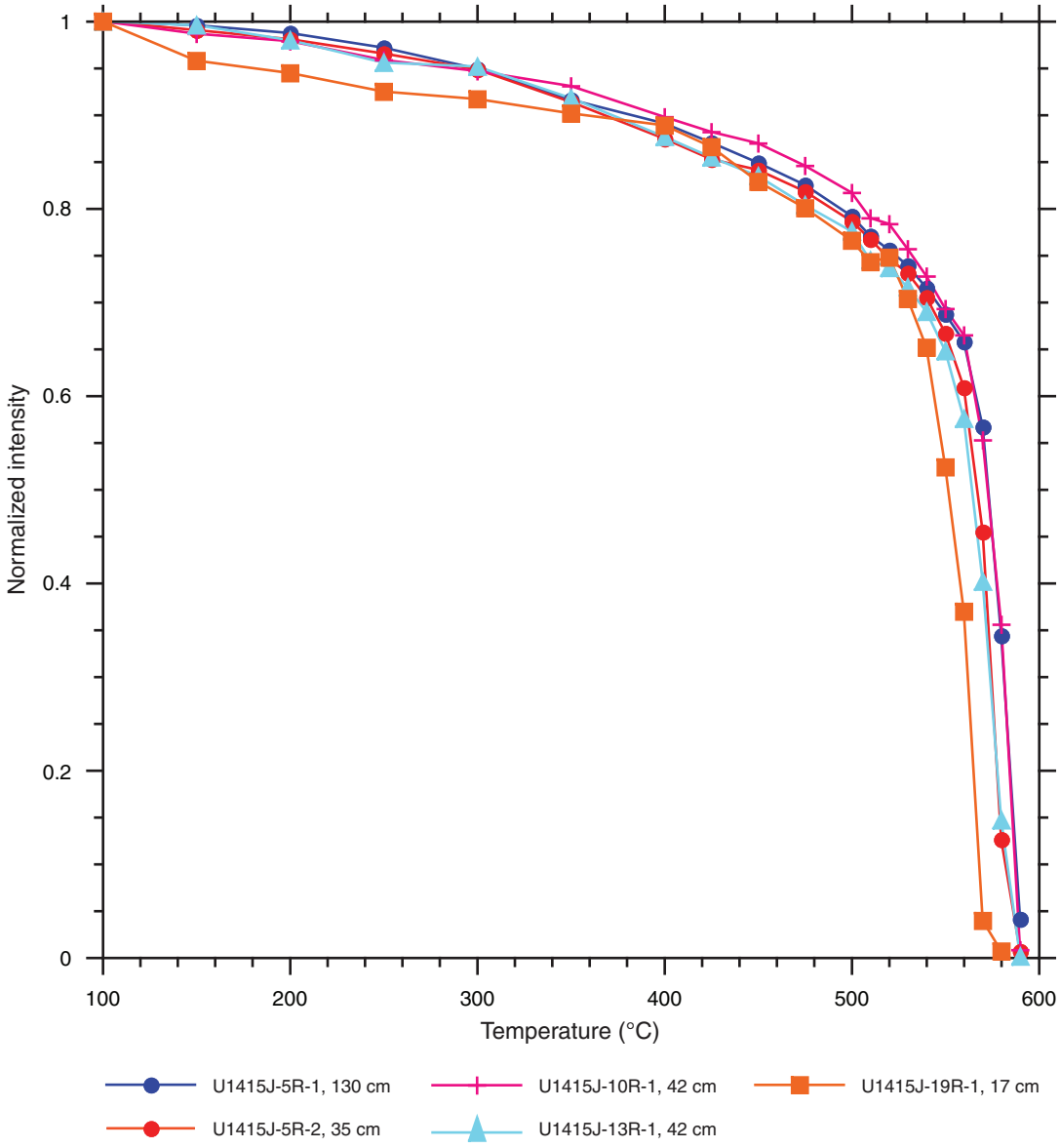

Figure F93. Demagnetization behavior in discrete samples in Hole U1415J that display near-antipodal components of remanence. Solid circles = projection onto the horizontal plane, open circles = projection onto the vertical Y–Z plane. NRM = natural remanent magnetization, Dec. = declination, Inc. = inclination.

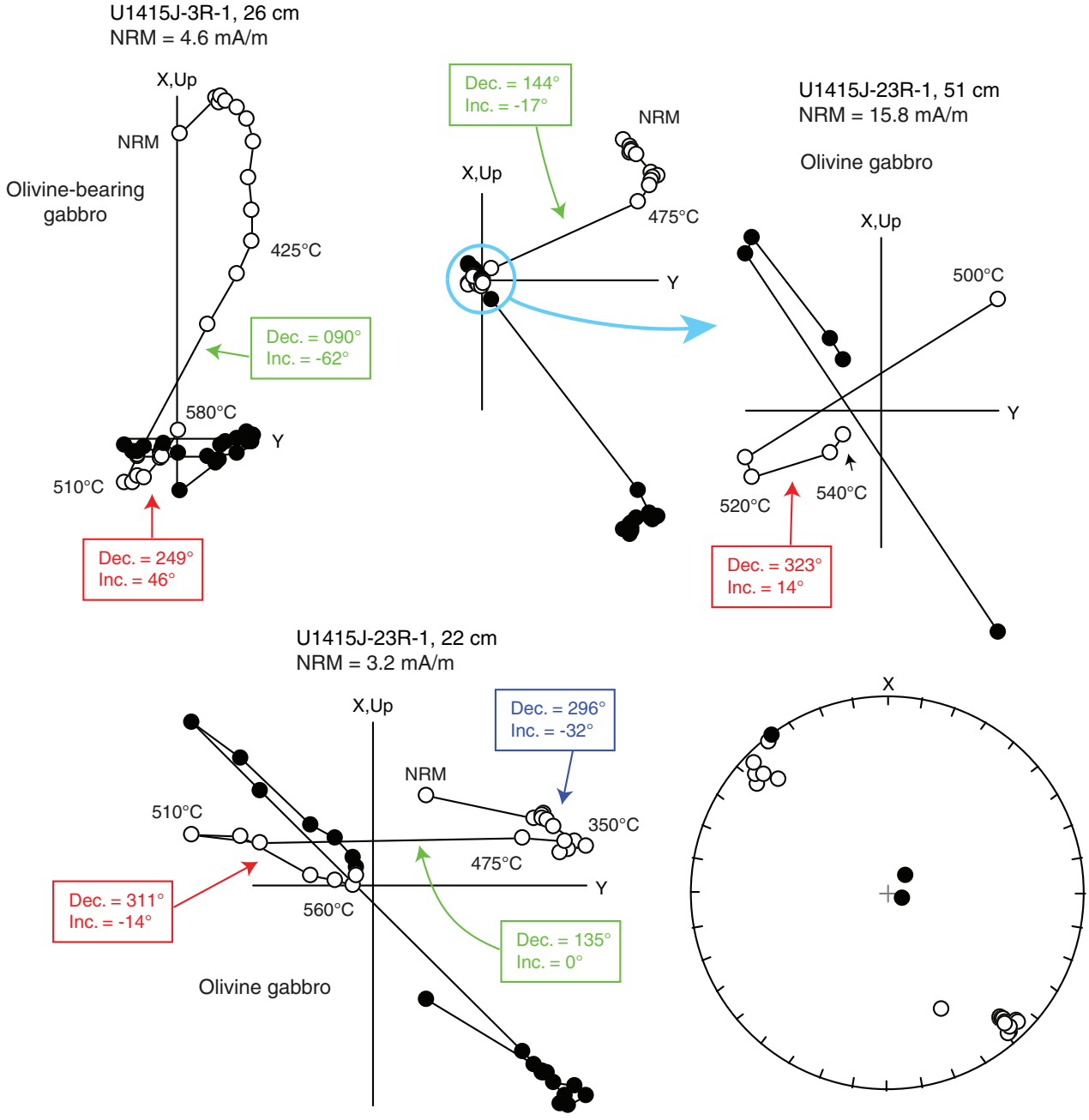

Figure F94. Demagnetization data from thermally demagnetized discrete samples and alternating field demagnetization data from equivalent measuring points in archive-half core samples, Hole U1415J. Solid circles = projection onto the horizontal plane, open circles = projection onto the vertical X–Z plane. Red stars indicate the directions of highest unblocking temperature components from discrete samples for comparison with archive-half core demagnetization paths (solid/open stars = lower/upper hemisphere projections, respectively). NRM = natural remanent magnetization, LTD1 = first low-temperature demagnetization treatment, Cpx = clinopyroxene.

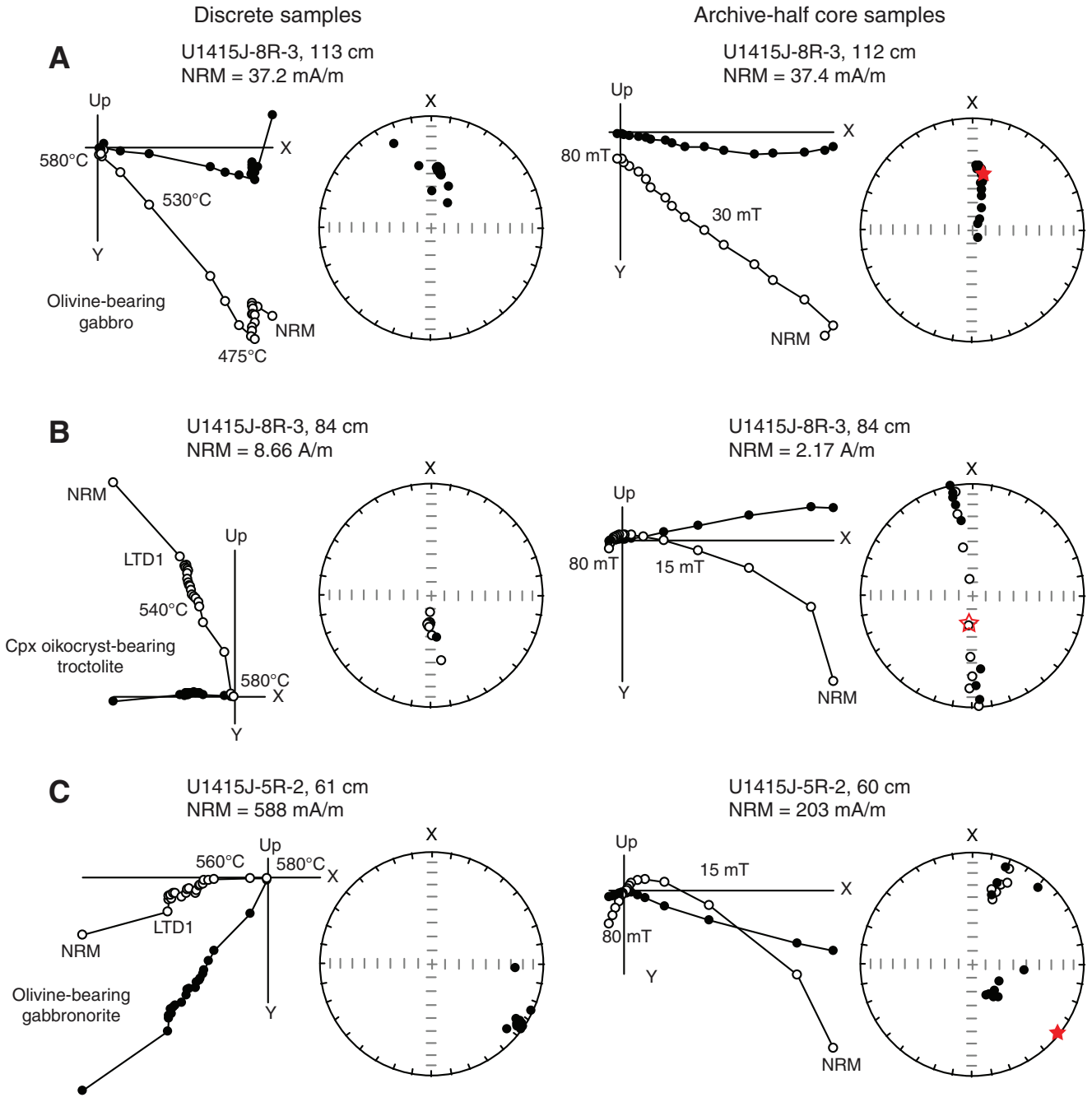

Figure F95. Demagnetization data from thermally demagnetized discrete samples and alternating field demagnetization data from equivalent measuring points in archive-half core samples, Hole U1415J. Solid circles = projection onto the horizontal plane, open circles = projection onto the vertical X–Z plane. Red stars indicate the directions of highest unblocking temperature components from discrete samples for comparison with archive-half core demagnetization paths (solid/open stars = lower/upper hemisphere projections, respectively). NRM = natural remanent magnetization. LTD1 = first low-temperature demagnetization treatment, LDT2 = second low-temperature demagnetization treatment.

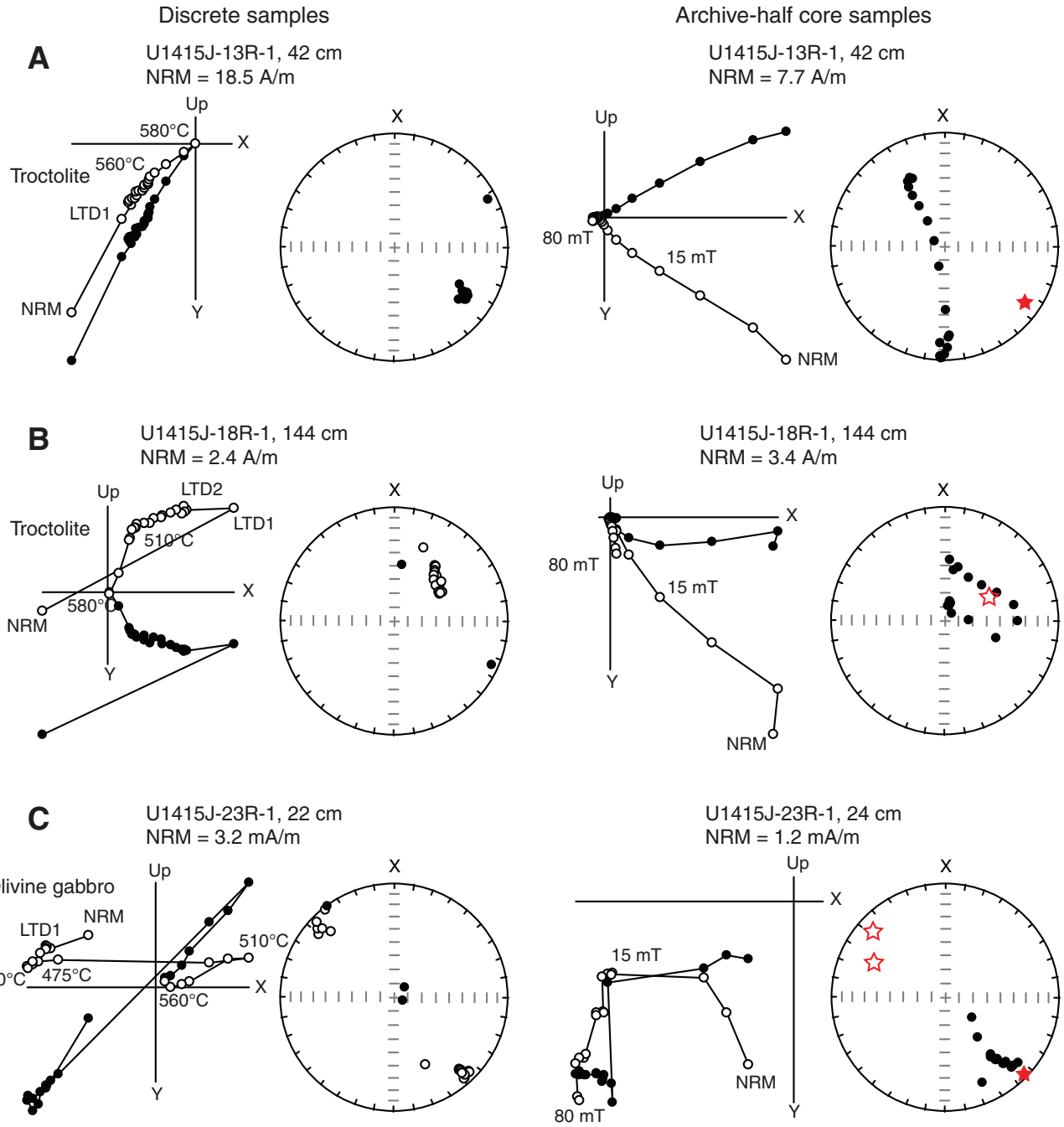

Figure F96. A. Downward-directed linear components picked from alternating field demagnetization data from archive-half core samples measured on the superconducting rock magnetometer. **B.** High unblocking temperature components from discrete samples cut from the working-half core at the same depth (measured on the JR6A spinner magnetometer). Solid/open symbols = lower/upper hemisphere directions, respectively.

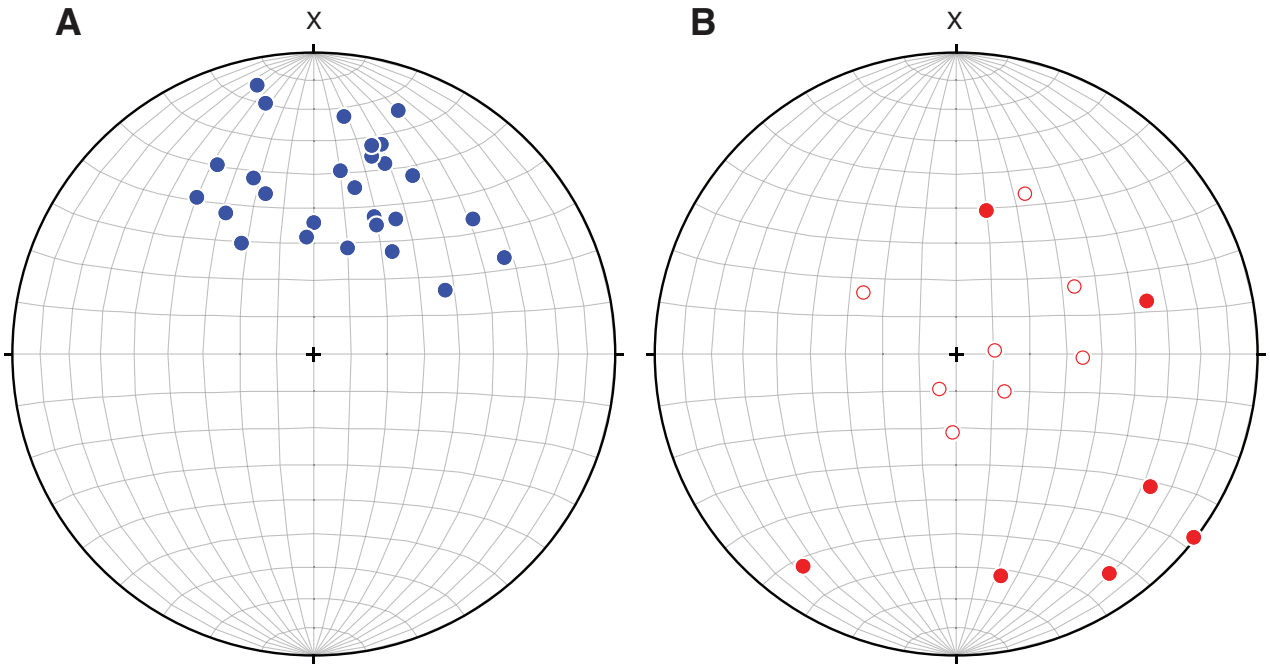

Figure F97. Variation with depth of the inclination of high unblocking temperature components in discrete samples in Hole U1415J, indicating sampling of at least two blocks with independent rotation histories. See text for details. MAD = maximum angular deviation.

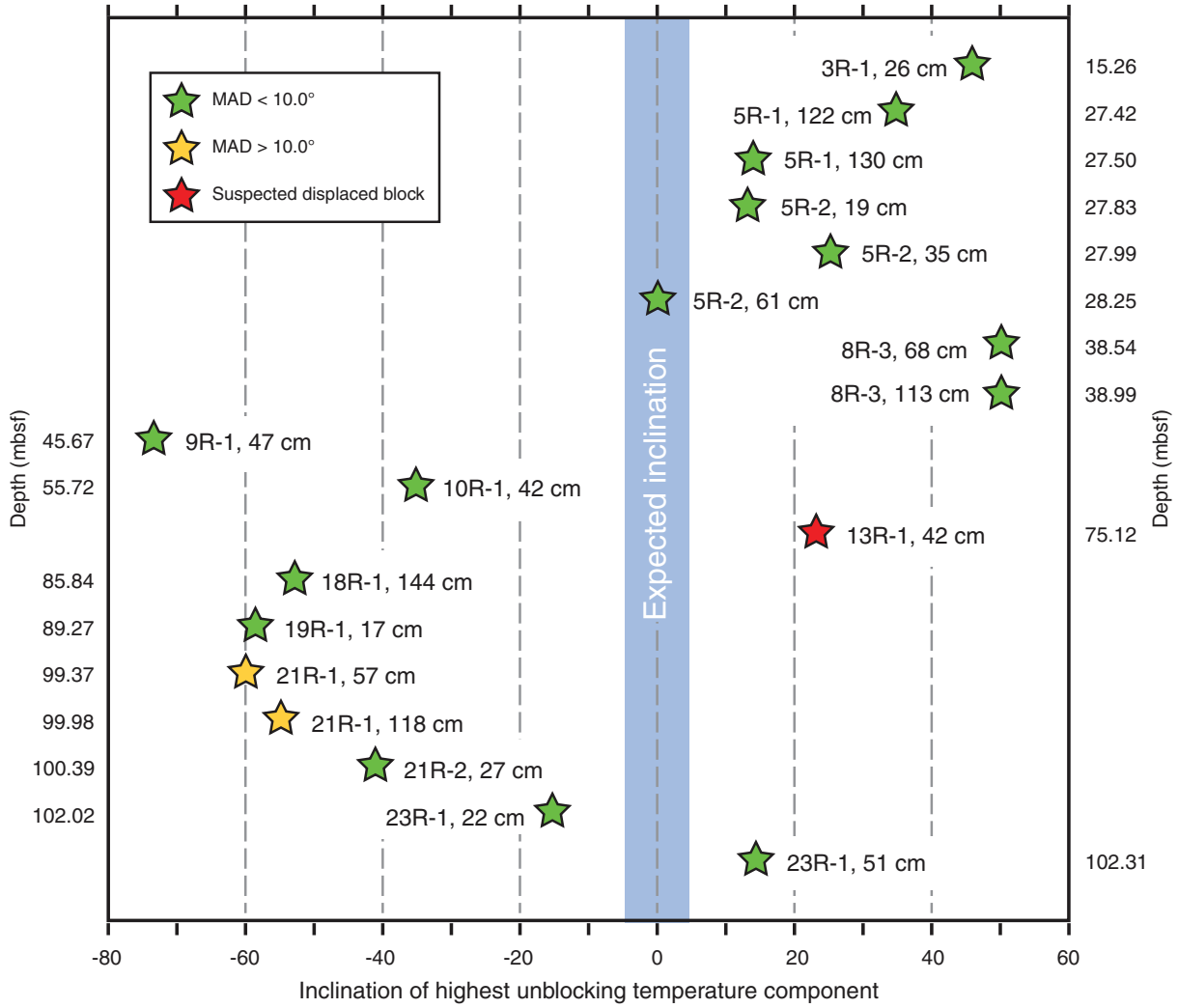

Figure F98. Natural remanent magnetization (NRM) intensity vs. low-field magnetic susceptibility of discrete and archive-half core samples, Hole U1415J. The distribution of values compared to lines of constant *Q* (Königsberger ratio of remanent to induced magnetization; calculated for 25 A/m field) shows that remanence is substantially greater than induced magnetization in most samples.

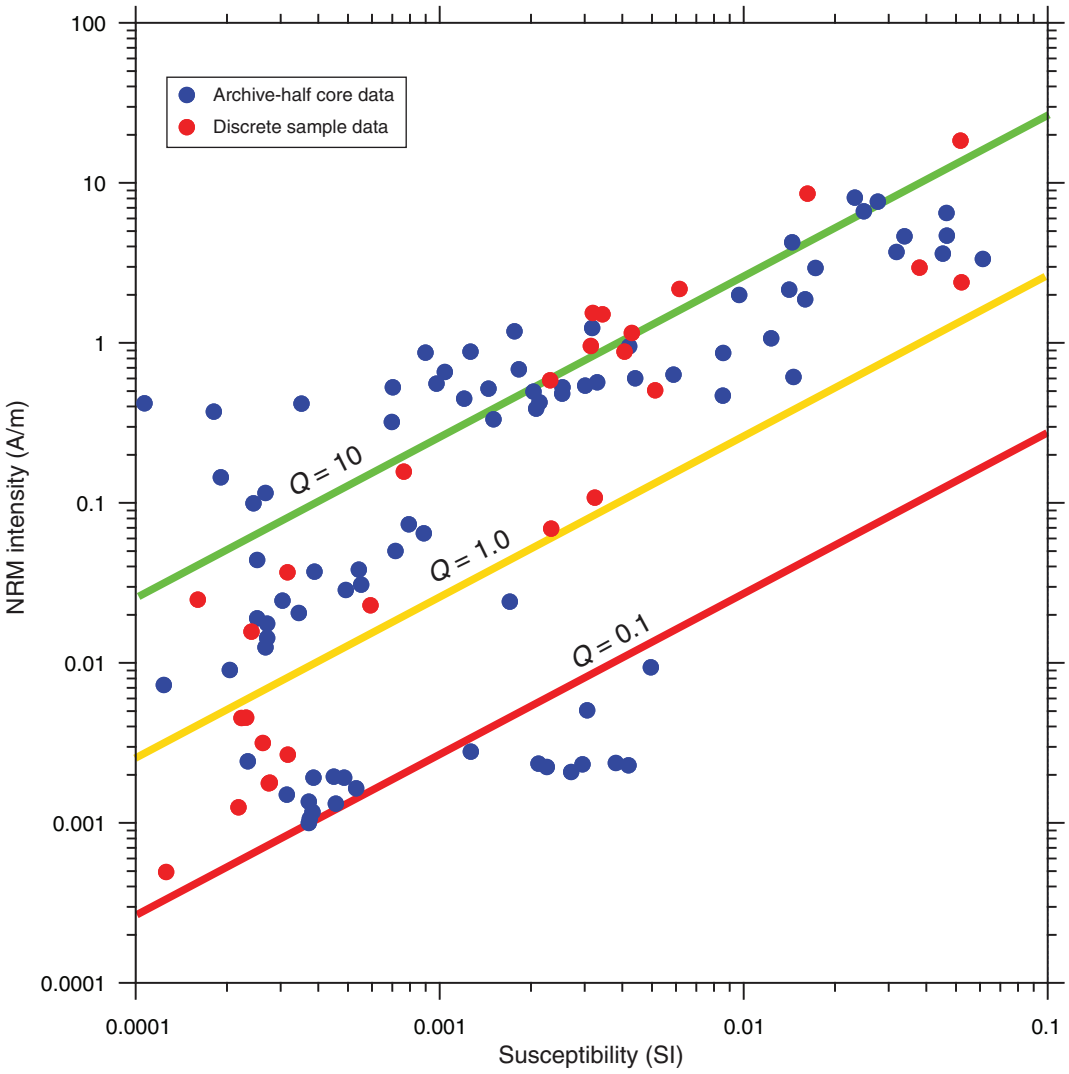

Figure F99. Anisotropy of low-field magnetic susceptibility (AMS) data from 21 of 27 discrete samples, Hole U1415J. Bootstrapped mean eigenvectors averaged from three separate measurements of each discrete sample are shown with 95% confidence ellipses associated with the maximum, intermediate, and minimum eigenvectors. **A.** Consistency in the orientation of magnetic fabric and observed magmatic foliations in these core sections, showing an eastward-dipping fabric within the core reference frame. **B.** A wider range of AMS eigenvectors is evident from samples below 40 mbsf. *C*. Shape factor vs. corrected anisotropy degree shows predominantly oblate AMS ellipsoid shapes (positive *T*), although some samples with triaxial and prolate shapes are also observed.

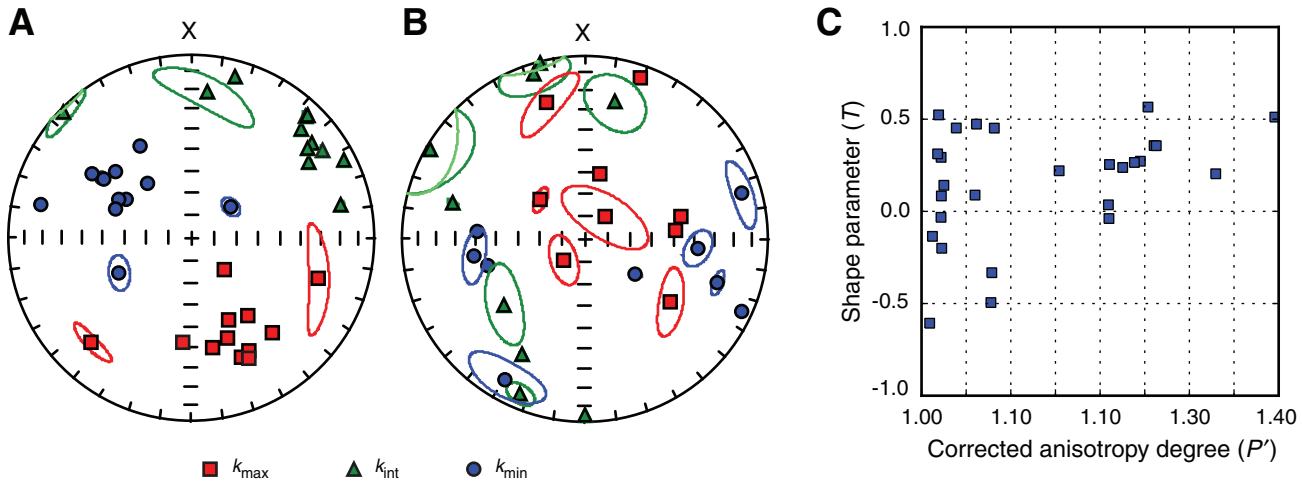

Figure F100. (**A**) H_2O and (**B**) CO_2 contents vs. loss on ignition (LOI) for the different rock types recovered from Hole U1415J. Compositions of samples recovered from Holes U1415E, U1415H, and U1415I are shown for comparison. Cpx = clinopyroxene.

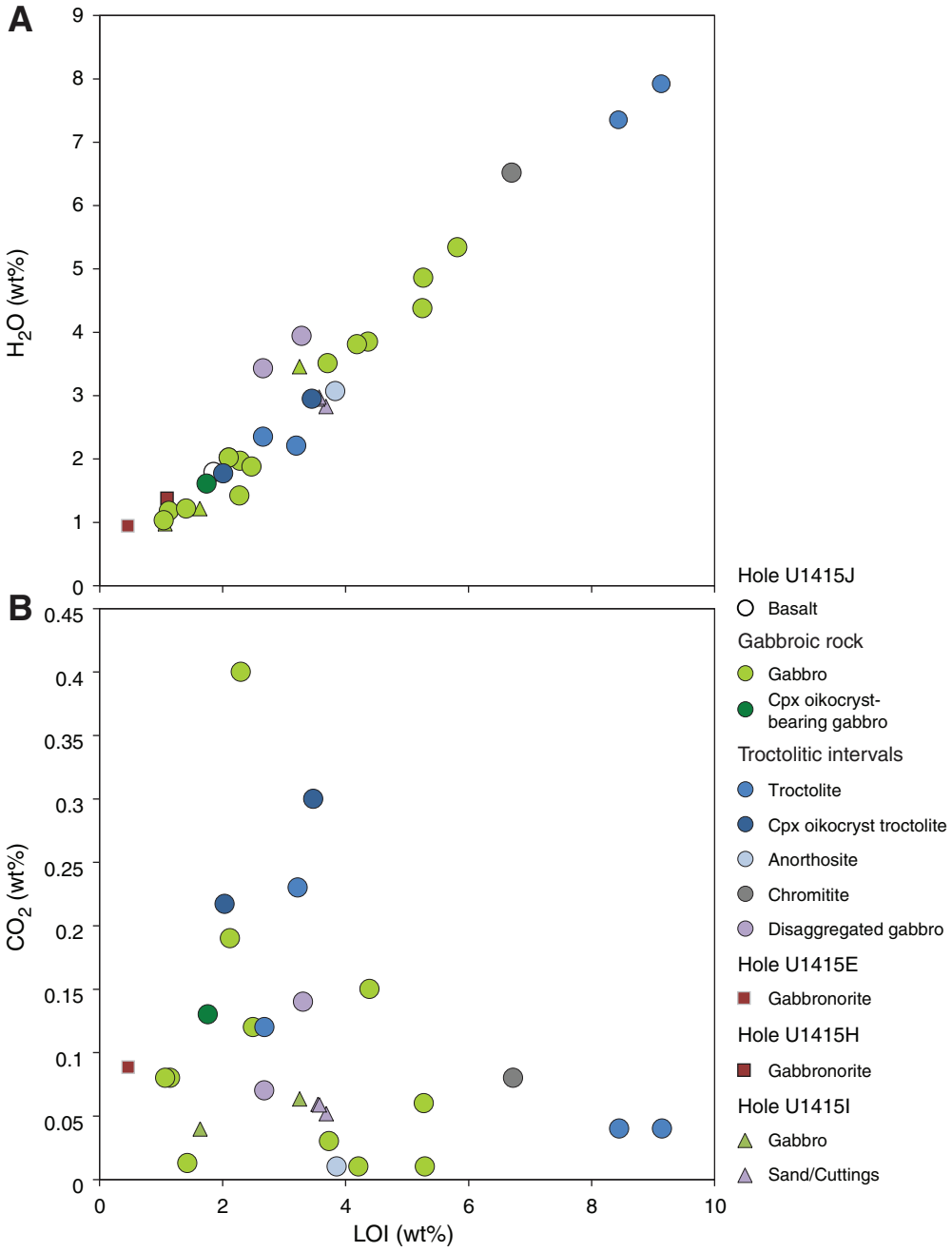

Figure F101. Element concentrations, Hole U1415J. Mg# = 100 × cationic Mg/(Mg + Fe) with all Fe recalculated as Fe^{2+}, Ca# = 100 × cationic Ca/(Ca + Na). G = sampled from ghost core obtained during hole cleaning operations in previously drilled intervals, Cpx = clinopyroxene.

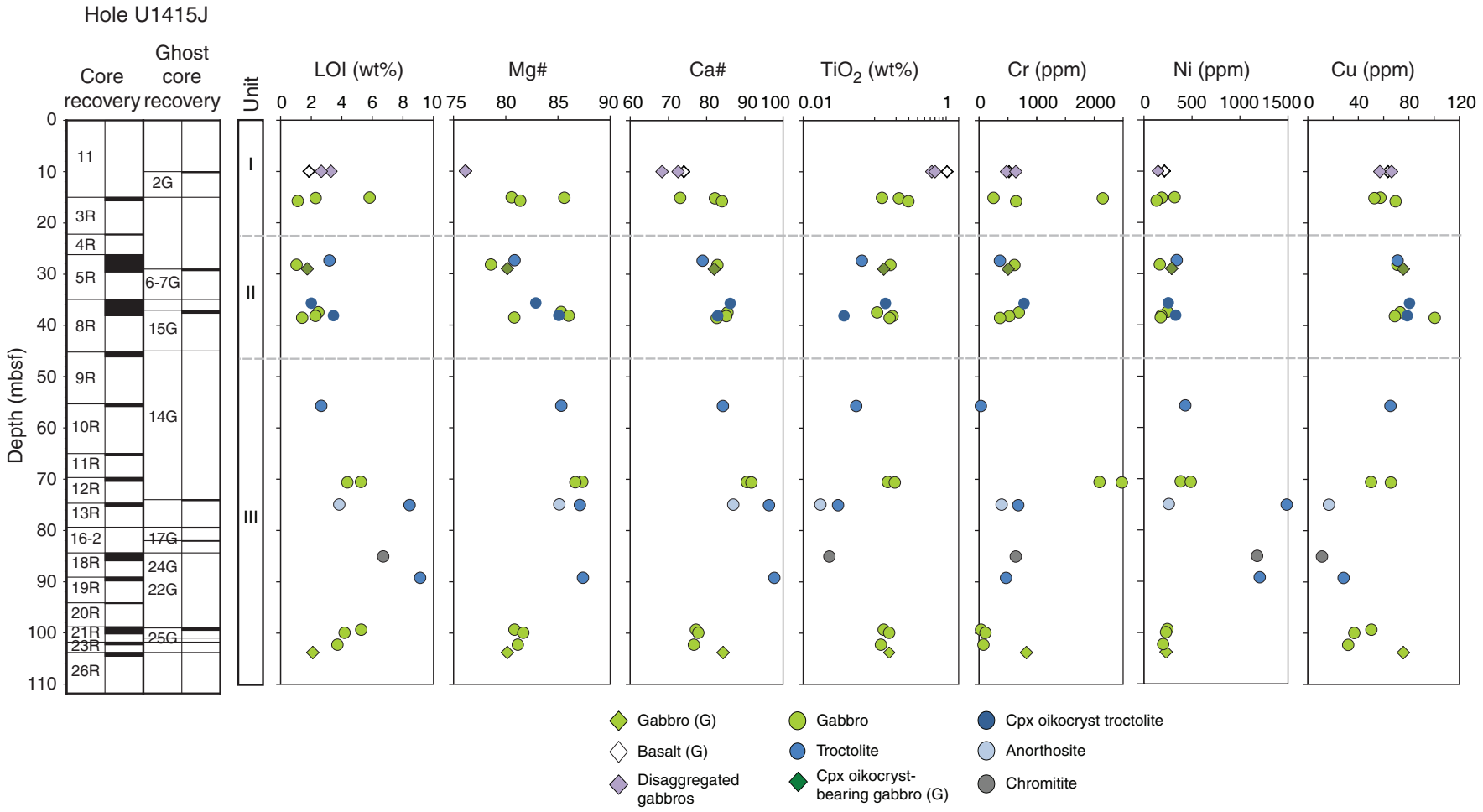

Figure F102. A–F. Compositions of different rock types recovered from Hole U1415J vs. Mg# (100 × Mg/[Mg + Fe] with all Fe recalculated as Fe^{2+}). For comparison, a compilation of the plutonic rock sampled along the East Pacific Rise (EPR) at Hess Deep (Hékinian et al., 1993; Shipboard Scientific Party, 1993; Miller et al., 1996; Natland and Dick, 2009; Pedersen et al., 1996; Hanna, 2004; Kirchner and Gillis, 2012), Pito Deep (Perk et al., 2007), and other locations (Saunders et al., 1982) is shown. Plutonic rock sampled in Holes U1415E, U1415H, and U1415I are also shown for comparison. Cpx = clinopyroxene.

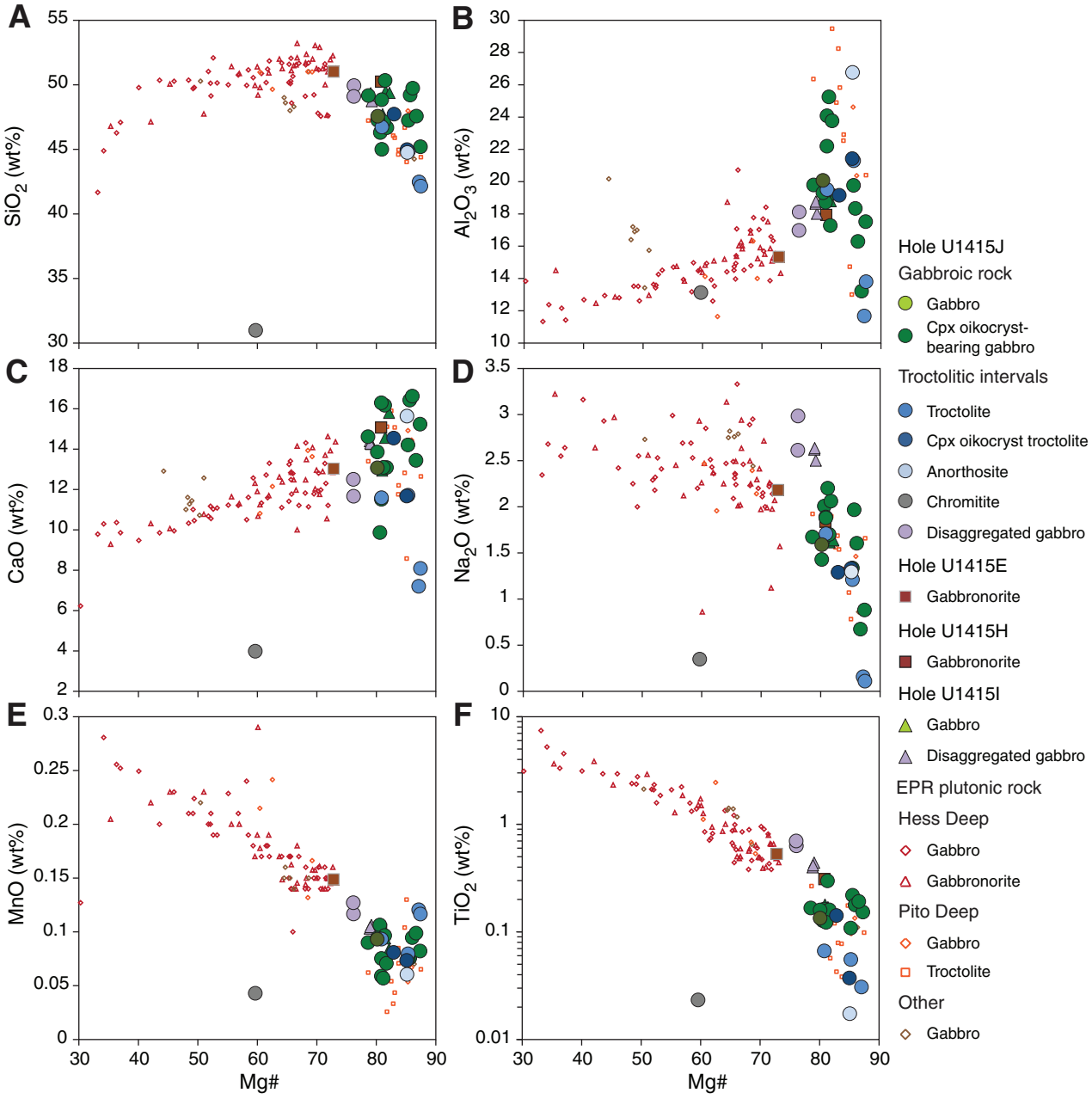

Figure F103. A–C. Compositions of different rock types recovered from Hole U1415J vs. TiO_2. For comparison, a compilation of plutonic rocks sampled along the East Pacific Rise (EPR) at Hess Deep (Hékinian et al., 1993; Shipboard Scientific Party, 1993; Miller et al., 1996; Natland and Dick, 2009; Pedersen et al., 1996; Hanna, 2004; Kirchner and Gillis, 2012), Pito Deep (Perk et al., 2007), and other locations (Saunders et al., 1982) is shown. Plutonic rock sampled in Holes U1415E, U1415H, and U1415I are also shown for comparison. Cpx = clinopyroxene.

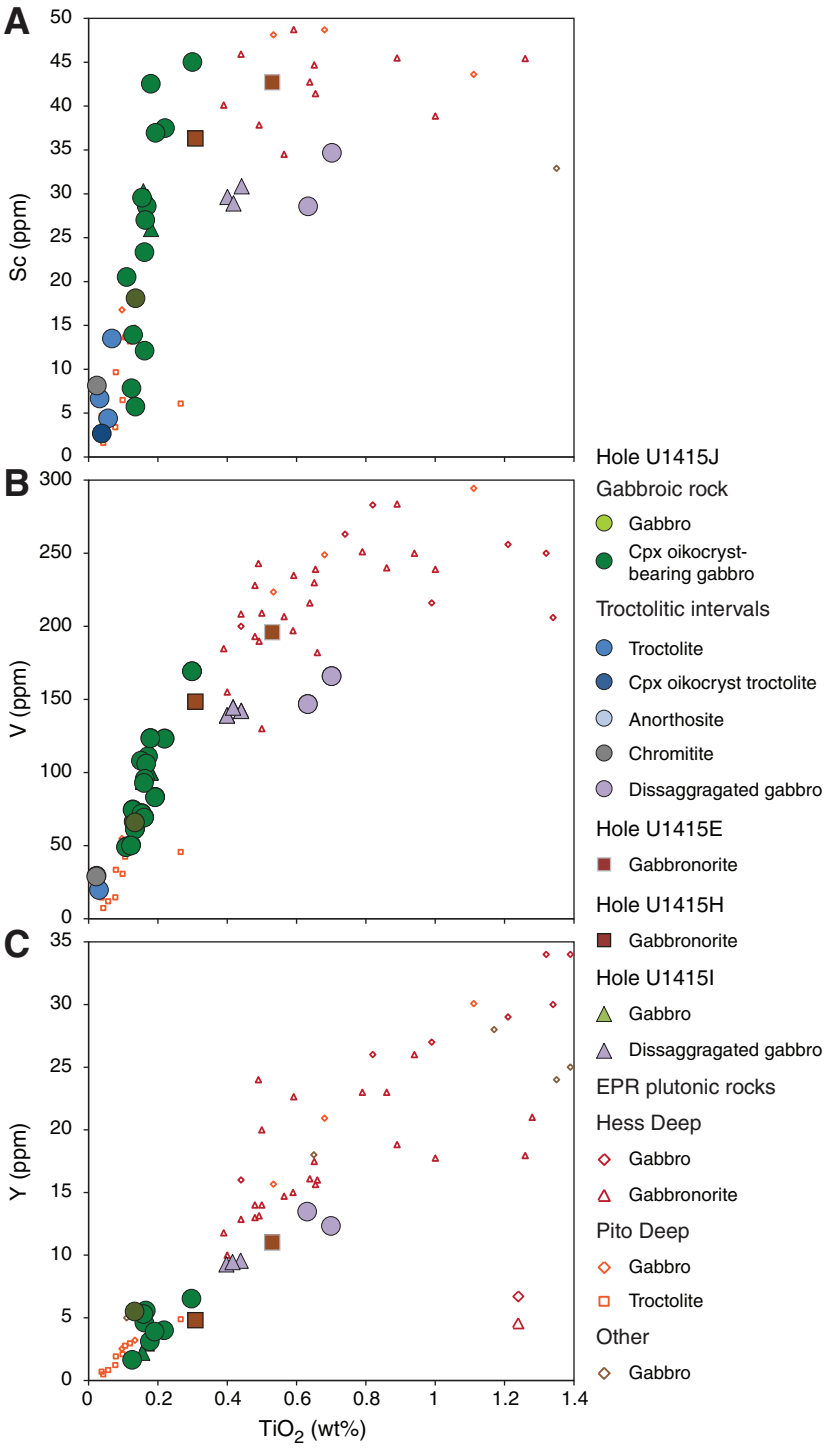

Figure F104. Summary of physical property measurements, Hole U1415J. Data from ghost cores are not shown. Plotted gamma ray attenuation (GRA) density, Whole-Round Multisensor Logger (WRMSL), and Section Half Multisensor Logger (SHMSL) data are filtered (see **"Physical properties"** in the "Methods" chapter [Gillis et al., 2014d]). NGR = natural gamma radiation, MS = magnetic susceptibility.

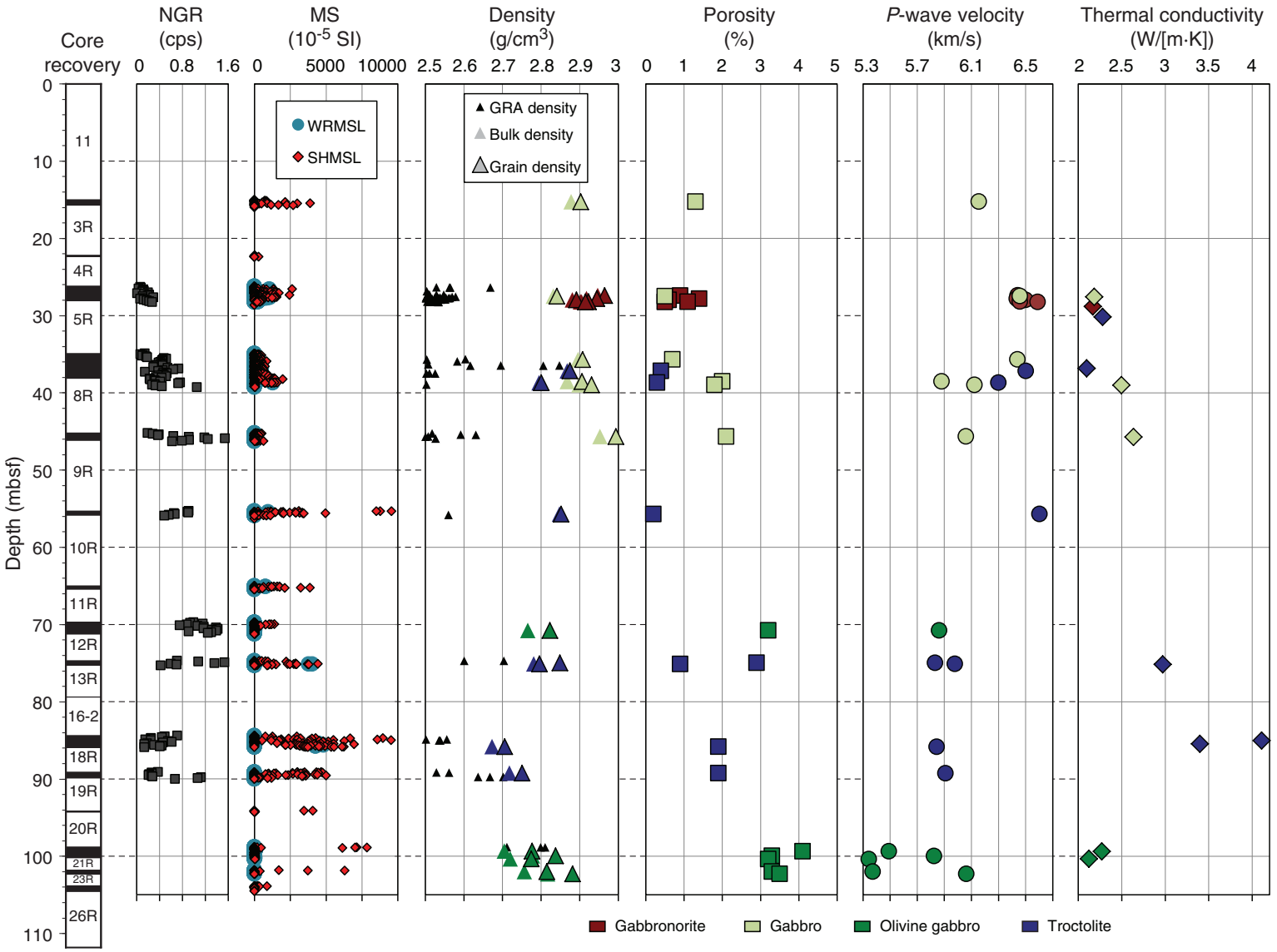

Figure F105. *P*-wave velocity (V_P) vs. grain density at Site U1415 compared with previous data from gabbroic rock from Hess Deep at Ocean Drilling Program (ODP) Leg 147 Site 894 and from slow-spreading crust in ODP Legs 118 and 176 Hole 735B on the Southwest Indian Ridge, in the Mid-Atlantic Ridge at Kane area, at the Mid-Atlantic Ridge in the 15°N area, and at IODP Expedition 304/305 Site U1309 (Atlantis Massif) on the Mid-Atlantic Ridge at 30°N (Shipboard Scientific Party, 1989, 1993, 1999, 2004; Cannat, Karson, Miller, et al., 1995; Expedition 304/305 Scientists, 2006). The locations of slow-spreading crust hole, site, or leg numbers on the plot indicate average values.

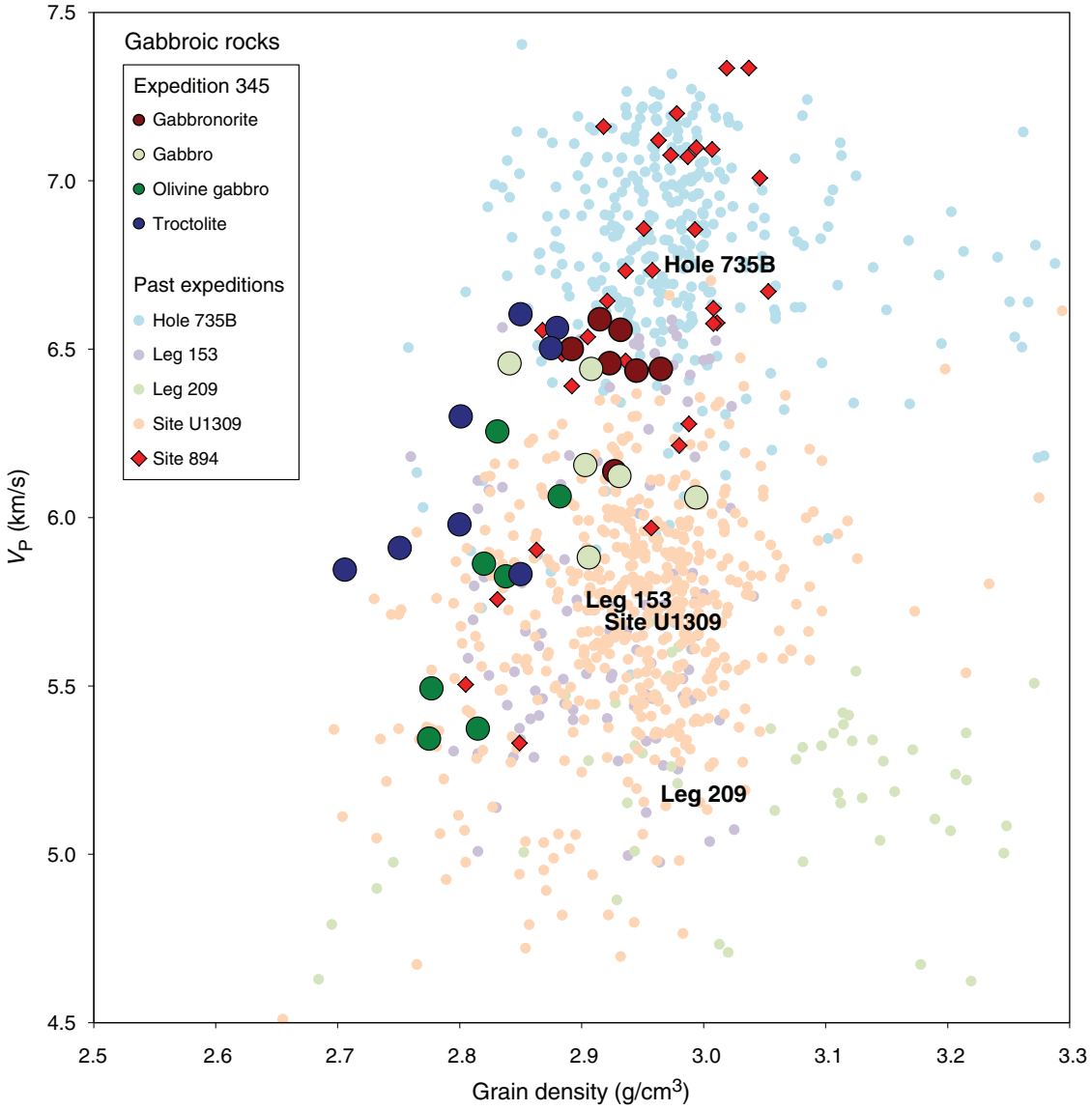

Figure F106. Inverse correlation of grain density with (**A**) background alteration and (**B**) olivine contents, Hole U1415J. Alteration and olivine modes were characterized macroscopically on section halves.

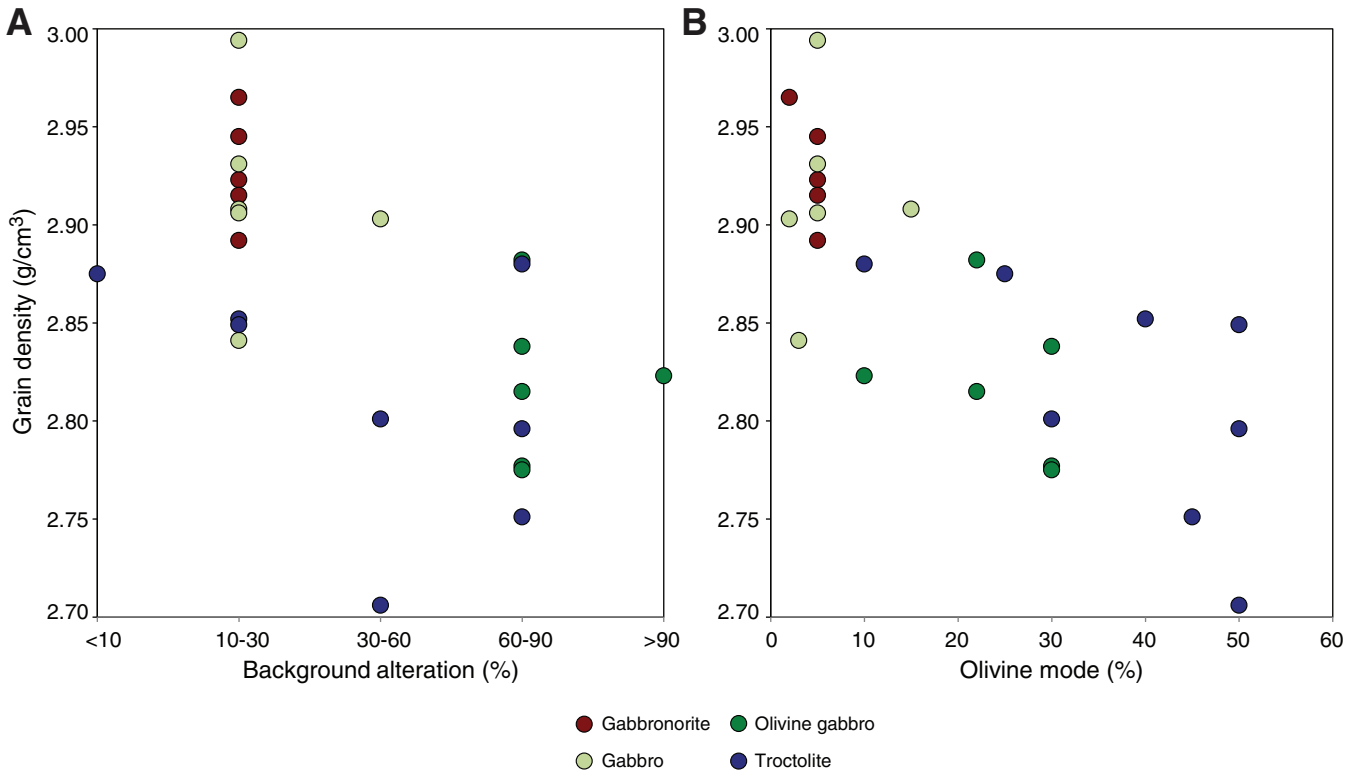

Figure F107. Inverse correlation of *P*-wave velocity (V_P) with porosity, Hole U1415J.

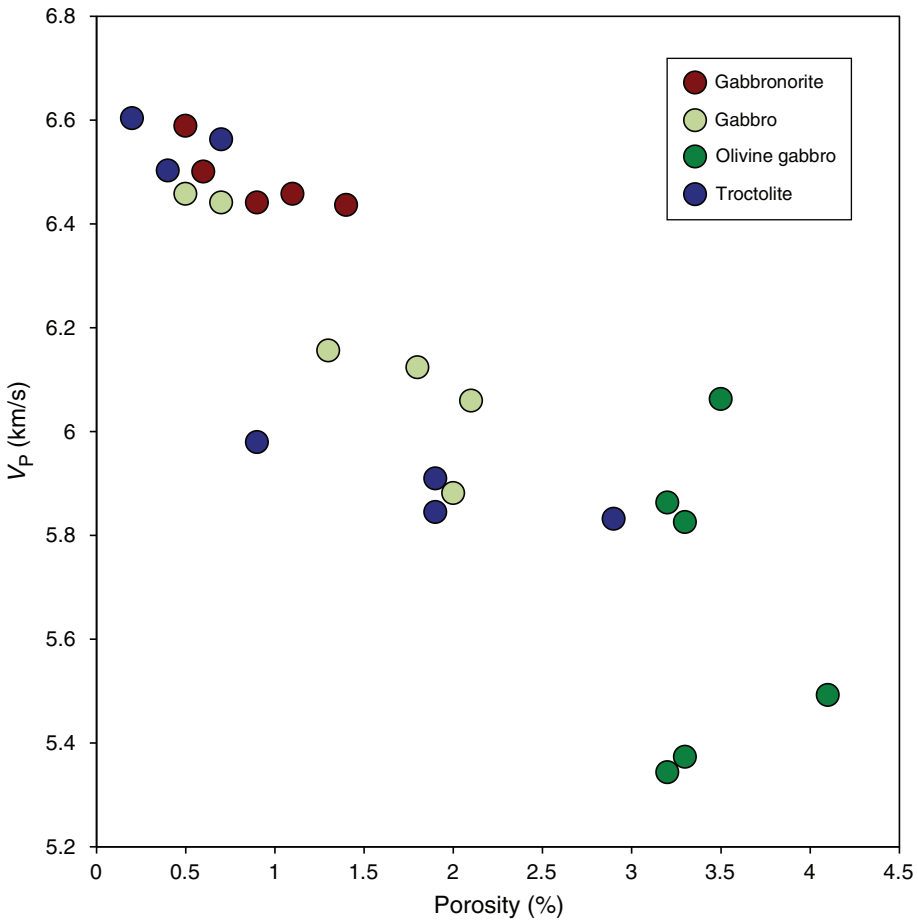

Figure F108. Inverse correlation of intensity of cataclastic deformation with (**A**) *P*-wave velocity (V_P) and (**B**) porosity, Hole U1415J. Cataclastic deformation was characterized macroscopically on section halves (see Fig. F15 in the "Methods" chapter [Gillis et al., 2014d]).

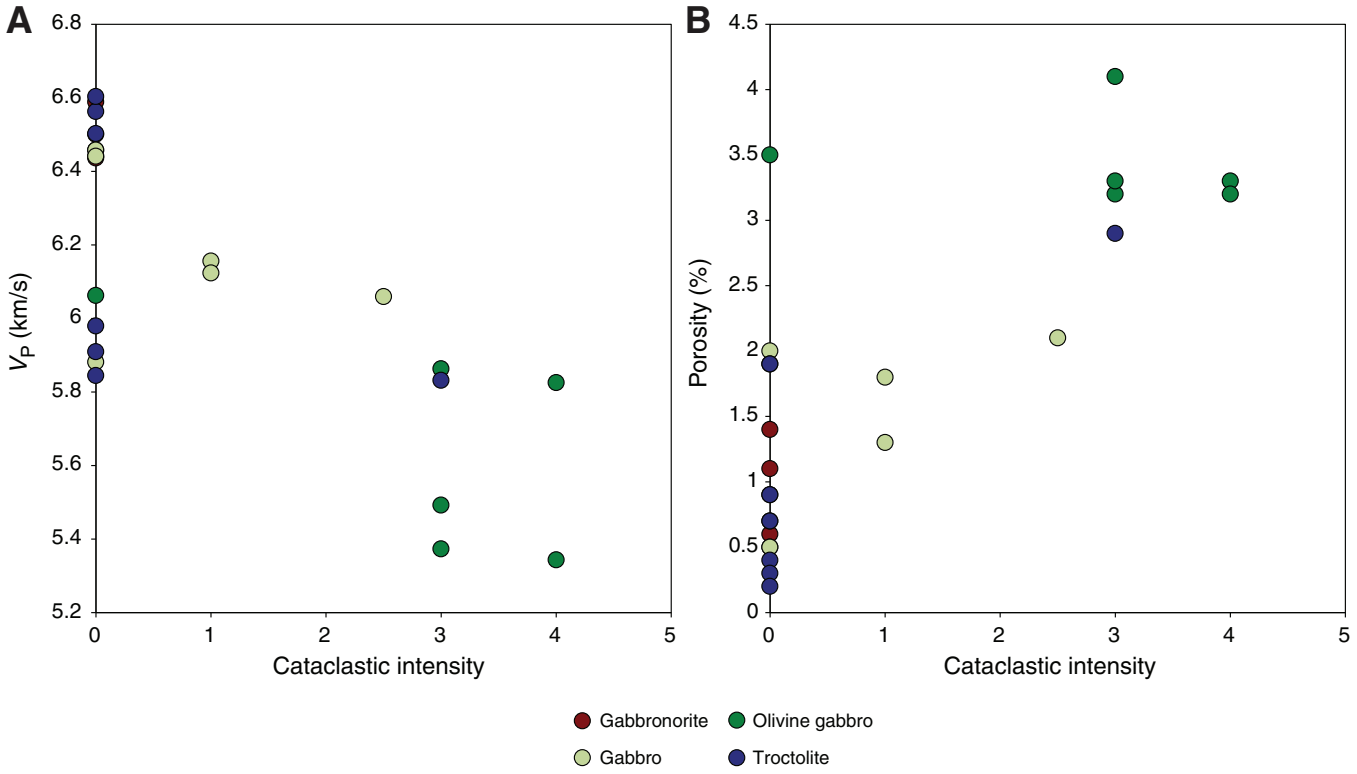

Table T1. Operations summary, Hole U1415J.

Hole U1415J (install seafloor structure and casing; RCB coring):
Latitude: 2°15.1604′N
Longitude: 101°32.6622′W
Time at site (h): 383 (16 days) (0230 h, 31 December 2012–0130 h, 16 January)
Seafloor (drill pipe measurement below rig floor, m DRF): 4850.0
Distance between rig floor and sea level (m): 11.2
Water depth (drill pipe measurement from sea level, mbsl): 4838.8
Total penetration (drilling depth below seafloor, m DSF): 111.8
Total depth (drill pipe measurement from rig floor, m DRF): 4961.8
Total length of cored section (m): 91.8
Total core recovered (m): 14.35
Core recovery (%): 16
Drilled interval (m): 2
Total number of cores: 15 RCB, 9 ghost

Core	Depth (mbsf) Top of cored interval	Depth (mbsf) Bottom of cored interval	Interval cored (m)	Core recovered (m)	Curated length (m)	Recovery (%)	Date (2013)	Time UTC (h)
345-U1415J-								
11	0.0	15.0		****Drilled from 0.0 to 15.0 mbsf****				
2G	10.0	15.0	—	0.20	0.13	—	3 Jan	1745
3R	15.0	22.2	7.2	0.68	0.86	9	4 Jan	0115
4R	22.2	26.2	4.0	0.18	0.22	5	4 Jan	0415
5R	26.2	34.9	8.7	1.88	2.08	22	4 Jan	1350
6G	29.0	34.9	—	0.33	0.45	—	4 Jan	2000
7G	29.0	34.9	—	1.54	2.05	—	5 Jan	0900
8R	34.9	45.2	10.3	3.22	4.39	31	5 Jan	1505
9R	45.2	55.3	10.1	0.94	1.10	9	5 Jan	2055
10R	55.3	65.0	9.7	0.55	0.62	6	6 Jan	0205
11R	65.0	69.7	4.7	0.41	0.50	9	6 Jan	0715
12R	69.7	74.7	5.0	0.74	1.56	15	6 Jan	1230
13R	74.7	79.4	4.7	0.59	0.65	13	6 Jan	1630
14G	37.0	79.4	—	0.15	0.25	—	7 Jan	0150
15G	37.0	45.0	—	0.64	0.69	—	7 Jan	1620
162	79.4	84.4		****Drilled from 79.4 to 84.4 mbsf****				
17G	79.4	84.4	—	0.12	0.12	—	12 Jan	0930
18R	84.4	89.1	4.7	1.50	1.50	32	12 Jan	1325
19R	89.1	94.1	5.0	0.77	0.94	15	12 Jan	1715
20R	94.1	98.8	4.7	0.19	0.20	4	12 Jan	2200
21R	98.8	101.8	3.0	1.39	1.62	46	13 Jan	0400
22G	82.0	101.8	—	0.07	0.12	—	13 Jan	0830
23R	101.8	103.8	2.0	0.53	0.53	27	13 Jan	1530
24G	74.0	101.0	—	0.21	0.27	—	13 Jan	2055
25G	99.0	103.8	—	0.48	0.57	—	15 Jan	0900
26R	103.8	111.8	8.0	0.78	0.75	10	15 Jan	1530
		Total:	91.8	14.35	17.52	16		

Local ship time was UTC – 7 h. Ghost core (G) is not included in totals. DRF = drilling depth below rig floor, DSF = drilling depth below seafloor. R = rotary core barrel (RCB) system, numeric core type = drilled interval. — = not calculated.

Table T2. Summary of lithologic intervals and their classification to units, Hole U1415J. (Continued on next three pages.)

Unit	Description	Core, section, interval (cm)	Depth (mbsf) Top	Depth (mbsf) Bottom	Pieces	Lithologic interval	Contact type	Contact definition	Complete lithology name
		345-U1415J-							
I	Surficial rubble	2G-1A, 0–4	10.000	10.04	1	G1	Not recovered		Aphyric basalt
		2G-1A, 4–8	10.040	10.08	1	G2	Not recovered		Dolerite
		2G-1A, 8–12	10.080	10.12	1	G3	Not recovered		Dolerite
		2G-1A, 12–13	10.120	10.13	1	G4	Not recovered		Basalt
		3R-1A, 0–6	15.000	15.06	1, 2	1	Not recovered		Gabbro
		3R-1A, 7–8	15.070	15.08	3	2	Not recovered		Olivine-bearing dolerite
		3R-1A, 8–9	15.080	15.09	3	3	Not recovered		Aphyric basalt
		3R-1A, 9–10	15.090	15.10	3	4	Not recovered		Doleritic gabbro
		3R-1A, 11–17	15.110	15.17	4	5	Not recovered		Olivine gabbro
		3R-1A, 18–28	15.180	15.28	5, 6	6	Not recovered		Olivine-bearing gabbro
		3R-1A, 29–37	15.290	15.37	7, 8	7	Not recovered		Clinopyroxene oikocryst-bearing troctolite
		3R-1A, 37–40	15.370	15.40	8	8	Not recovered		Olivine gabbro
		3R-1A, 40–42	15.400	15.42	9	9	Modal	Sharp to gradational	Clinopyroxene oikocryst-bearing troctolite
		3R-1A, 43–78	15.430	15.78	10, 11, 12, 13, 14, 15	10	Not recovered		Olivine gabbro
		3R-1A, 79–86	15.790	15.86	16	11	Not recovered		Gabbro
		4R-1A, 13–19	22.330	22.39	1, 2	12	Not recovered		Gabbro
		4R-1A, 20–23	22.400	22.43	3	13	Not recovered		Clinopyroxene oikocryst-bearing olivine gabbro
		4R-1A, 20–23	22.400	22.43	4	14	Not recovered		Alteration vein
II	Oikocryst-Bearing Layered Gabbro Series	5R-1A, 0–4	26.200	26.24	1	15	Not recovered		Gabbro
		5R-1A, 5–12	26.250	26.32	2, 3	16	Not recovered		Olivine gabbro
		5R-1A, 12–24	26.320	26.44	4, 5	17	Not recovered		Orthopyroxene-bearing gabbro
		5R-1A, 25–27	26.450	26.47	6	18	Not recovered		Gabbro
		5R-1A, 28–44	26.480	26.64	7, 8	19	Not recovered		Clinopyroxene oikocryst-bearing troctolite
		5R-1A, 44–59	26.640	26.79	9, 10, 11	20	Not recovered		Oikocryst gabbro
		5R-1A, 59–80	26.790	27.00	12, 13	21	Not recovered		Clinopyroxene oikocryst-bearing olivine gabbro
		5R-1A, 81–85	27.010	27.05	14	22	Not recovered		Clinopyroxene oikocryst-bearing olivine gabbro
		5R-1A, 86–98	27.060	27.18	15, 16	23	Not recovered		Olivine bearing gabbro
		5R-1A, 99–121	27.190	27.41	17	24	Not recovered		Clinopyroxene oikocryst-bearing troctolite
		5R-1A, 121–125	27.410	27.45	17	25	Modal		Olivine-bearing gabbronorite
		5R-1A, 125–132	27.450	27.52	17, 18	26	Modal and textural		Olivine-bearing gabbro
		5R-1A, 132–136	27.520	27.56	18	27	Modal and textural		Olivine-bearing gabbronorite
		5R-1A, 136–144	27.560	27.64	18	28	Modal and textural		Clinopyroxene oikocryst-bearing troctolite
		5R-2A, 0.5–2.5	27.640	27.66	1	29	Not recovered		Troctolite
		5R-2A, 2.5–6.5	27.660	27.70	1	30	Modal and textural		Olivine-bearing gabbronorite
		5R-2A, 6.5–9	27.700	27.73	1	31	Modal and textural		Troctolite
		5R-2A, 9–63	27.725	28.27	1, 2, 3	32	Modal and textural		Olivine-bearing gabbronorite
		8R-1A, 0–5	34.900	34.95	1	33	Not recovered		Gabbro
		8R-1A, 5–12	34.950	35.02	2	34	Not recovered		Olivine gabbro
		8R-1A, 13–16	35.030	35.06	3	35	Not recovered		Clinopyroxene oikocryst-bearing troctolite
		8R-1A, 17–21	35.070	35.11	4	36	Not recovered		Olivine gabbro
		8R-1A, 22–73	35.120	35.63	5, 6, 7, 8, 9, 10, 11, 12, 13	37	Not recovered		Clinopyroxene oikocryst-bearing troctolite
		8R-1A, 74–108	35.640	35.98	13, 14	38	Color	Sharp to gradational	Oikocryst gabbro
		8R-1A, 109–122	35.990	36.12	15, 16	39	Not recovered		Olivine gabbro
		8R-1A, 123–147	36.130	36.37	17, 18	40	Not recovered		Clinopyroxene oikocryst-bearing troctolite
		8R-2A, 0–111	36.370	37.48	1, 2, 3, 4, 5, 6, 7, 8, 9	41	Not recovered		Clinopyroxene oikocryst-bearing troctolite
		8R-2A, 111–116	37.480	37.53	9	42	Modal and textural	Sharp to gradational	Olivine-bearing gabbro

Table T2 (continued). (Continued on next page.)

Unit	Description	Core, section, interval (cm)	Depth (mbsf) Top	Depth (mbsf) Bottom	Pieces	Lithologic interval	Contact type	Contact definition	Complete lithology name
		8R-2A, 116–143	37.530	37.80	9, 10, 11, 12, 13	43	Modal and textural	Sharp to gradational	Olivine gabbro
		8R-2A, 143–149	37.800	37.86	13	44	Modal and textural	Sharp to gradational	Troctolite
		8R-3A, 0–10	37.860	37.96	1, 2	45	Not recovered		Troctolite
		8R-3A, 11–22	37.970	38.08	3, 4	46	Not recovered		Oikocryst gabbro
		8R-3A, 23–30	38.090	38.16	5	47	Not recovered		Clinopyroxene oikocryst-bearing troctolite
		8R-3A, 31–76	38.170	38.62	6, 7, 8	48	Not recovered		Olivine-bearing gabbro
		8R-3A, 77–93	38.630	38.79	9	49	Not recovered		Clinopyroxene oikocryst-bearing troctolite
		8R-3A, 94–143	38.800	39.29	10, 11, 12, 13, 14, 15	50	Not recovered		Olivine-bearing gabbro
		9R-1A, 0–9	45.200	45.29	1	51	Not recovered		Orthopyroxene-bearing olivine gabbro
		9R-1A, 10–17	45.300	45.37	2	52	Not recovered		Clinopyroxene oikocryst-bearing troctolite
		9R-1A, 18–29	45.380	45.49	3	53	Not recovered		Olivine-bearing gabbro
		9R-1A, 30–34	45.500	45.54	4	54	Not recovered		Oikocryst gabbro
		9R-1A, 35–96	45.550	46.16	5, 6, 7, 8, 9, 10, 11, 12, 13	55	Not recovered		Olivine-bearing gabbro
		9R-1A, 97–100	46.170	46.20	14	56	Not recovered		Aphyric basalt
		9R-1A, 101–110	46.210	46.30	15	57	Not recovered		Orthopyroxene-bearing olivine gabbro
III	Troctolite Series	10R-1A, 0–50	55.300	55.85	1, 2, 3, 4, 5, 6	58	Not recovered		Troctolite
		10R-1A, 50–56	55.750	55.85	6	59	Modal and textural	Sharp to gradational	Olivine gabbro
		10R-1A, 56–63	55.860	55.93	7	60	Not recovered		Troctolite
		11R-1A, 0–50	65.000	65.50	1, 2, 3, 4, 5, 6, 7	61	Not recovered		Troctolite
		12R-1A, 0–51	69.700	70.21	1, 2, 3, 4, 5, 6, 7, 8	62	Not recovered		Troctolite
		12R-1A, 52–147	70.220	71.17	9, 10, 11, 12, 13, 14, 15, 16, 17, 18	63	Not recovered		Olivine gabbro
		12R-2A, 0–9	71.165	71.26	1	64	Not recovered		Olivine gabbro
		13R-1A, 0–7	74.700	74.77	1	65	Not recovered		Olivine gabbro
		13R-1A, 8–65	74.780	75.35	2, 3, 4, 5, 6, 7, 8	66	Not recovered		Troctolite
		18R-1A, 0–25	84.400	84.65	1, 2, 3	67	Not recovered		Troctolite
		18R-1A, 26–29	84.660	84.69	4	68	Not recovered		Olivine-moderately phyric basalt
		18R-1A, 30–66	84.700	85.06	5, 6, 7, 8	69	Not recovered		Troctolite
		18R-1A, 67–72	85.070	85.12	9	70	Not recovered		Completely altered chromitite
		18R-1A, 73–128	85.130	85.68	10, 11, 12, 13, 14, 15, 16	71	Not recovered		Troctolite
		18R-1A, 129–150	85.690	85.90	17	72	Modal		Troctolite
		19R-1A, 0–56	89.100	89.66	1, 2, 3, 4, 5, 6, 7, 8,	73	Not recovered		Troctolite
		19R-1A, 57–70	89.670	89.80	9, 10	74	Not recovered		Cataclasite
		19R-1A, 71–94	89.810	90.04	11, 12, 13, 14	75	Not recovered		Troctolite
		20R-1A, 0–20	94.100	94.30	1, 2, 3	75	Not recovered		Troctolite
		21R-1A, 0–4	98.800	98.84	1	76	Not recovered		Cataclastic basalt
		21R-1A, 5–16	98.850	98.96	2, 3	77	Not recovered		Completely altered chromitite
		21R-1A, 17–132	98.970	100.12	4, 5, 6, 7, 8, 9, 10, 11, 12, 13, 14, 15, 16, 17	78	Not recovered		Olivine gabbro
		21R-2A, 0–31	100.115	100.43	1, 2, 3	78	Not recovered		Olivine gabbro
		23R-1A, 0–4	101.800	101.84	1	79	Not recovered		Troctolite

Table T2 (continued). (Continued on next page.)

Unit	Description	Core, section, interval (cm)	Depth (mbsf) Top	Depth (mbsf) Bottom	Pieces	Lithologic interval	Contact type	Contact definition	Complete lithology name
		23R-1A, 5–9	101.850	101.89	2	80	Not recovered		Troctolite
		23R-1A, 10–13	101.900	101.93	3	81	Not recovered		Cataclastic, chilled margin–bearing basalt
		23R-1A, 14–18	101.940	101.98	4	82	Not recovered		Troctolite
		23R-1A, 19–34	101.990	102.14	5	83	Not recovered		Olivine gabbro
		23R-1A, 35–37	102.150	102.17	6	84	Not recovered		Cataclastic olivine gabbro
		23R-1A, 38–53	102.180	102.33	7, 8	85	Not recovered		Olivine gabbro
		26R-1A, 0–15	103.800	103.95	1, 2	86	Modal	Sharp to gradational	Troctolite
		26R-1A, 16–43	103.960	104.23	3, 4, 5, 6, 7	87	Not recovered		Cataclastic olivine gabbro
		26R-1A, 44–58	104.240	104.38	8, 9, 10, 11	88	Not recovered		Troctolite
		26R-1A, 59–61	104.390	104.41	12	89	Not recovered		Cataclastic olivine gabbro
		26R-1A, 62–64	104.420	104.44	13	90	Not recovered		Olivine gabbro
		26R-1A, 65–75	104.450	104.55	14, 15	91	Not recovered		Cataclastic olivine gabbro
Ghost core Cluster 1	Samples recovered from the ghost core; contains rocks from Units I and II, excludes rocks from Unit III	6G-1A, 0–0.6	29.000	29.05	1	G5	Not recovered		Clinopyroxene oikocryst-bearing olivine gabbro
		6G-1A, 5–8	29.045	29.08	2	G6	Not recovered		Olivine gabbro
		6G-1A, 8–11	29.075	29.11	3	G7	Not recovered		Clinopyroxene oikocryst-bearing troctolite
		6G-1A, 11–15	29.110	29.15	4	G8	Not recovered		Clinopyroxene oikocryst-bearing troctolite
		6G-1A, 15–22	29.145	29.22	5	G9	Not recovered		Clinopyroxene oikocryst-bearing troctolite
		6G-1A, 22–25	29.220	29.25	6	G10	Not recovered		Cataclastic gabbro
		6G-1A, 25–31	29.250	29.31	7	G11	Not recovered		Olivine-bearing gabbro
		6G-1A, 31–35	29.305	29.35	8	G12	Not recovered		Olivine-bearing gabbro
		6G-1A, 35–38	29.345	29.38	9	G13	Not recovered		Clinopyroxene oikocryst-bearing olivine gabbro
		6G-1A, 38–42	29.380	29.42	10	G14	Not recovered		Clinopyroxene oikocryst-bearing olivine gabbro
		6G-1A, 42–45	29.420	29.45	11	G15	Not recovered		Clinopyroxene oikocryst-bearing troctolite
		7G-1A, 0–4.5	29.000	29.05	1	G16	Not recovered		Olivine-bearing gabbro
		7G-1A, 4.5–9	29.045	29.09	2	G17	Not recovered		Olivine-bearing gabbro
		7G-1A, 9–17	29.090	29.17	3	G18	Not recovered		Clinopyroxene oikocryst-bearing troctolite
		7G-1A, 17–26	29.170	29.26	4	G19	Not recovered		Olivine-bearing gabbro
		7G-1A, 26–30	29.260	29.30	5	G20	Not recovered		Olivine-bearing gabbro
		7G-1A, 30–34.5	29.300	29.35	6	G21	Not recovered		Clinopyroxene oikocryst-bearing troctolite
		7G-1A, 34.5–42	29.345	29.42	7	G22	Modal and textural	Sharp	Olivine gabbro
		7G-1A, 42–49	29.420	29.49	8	G23	Not recovered		Olivine gabbro
		7G-1A, 49–57	29.490	29.57	9	G24	Not recovered		Clinopyroxene oikocryst-bearing troctolite
		7G-1A, 57–64.5	29.570	29.65	10	G25	Not recovered		Clinopyroxene oikocryst-bearing troctolite
		7G-1A, 64.5–70.5	29.645	29.71	10	G26	Not recovered		Clinopyroxene oikocryst-bearing troctolite
		7G-1A, 70.5–76	29.705	29.76	11	G27	Not recovered		Cataclastic gabbro
		7G-1A, 76–80	29.760	29.80	12	G28	Not recovered		Olivine-bearing gabbro
		7G-1A, 80–91	29.800	29.91	13	G29	Not recovered		Oikocryst gabbro
		7G-1A, 91–97	29.910	29.97	14	G30	Not recovered		Clinopyroxene oikocryst-bearing troctolite
		7G-1A, 97–107	29.970	30.07	15	G31	Not recovered		Clinopyroxene oikocryst-bearing troctolite
		7G-1A, 107–125	30.070	30.25	16	G32	Not recovered		Clinopyroxene oikocryst-bearing troctolite
		7G-1A, 125–137	30.250	30.25	17	G33	Not recovered		Clinopyroxene oikocryst-bearing troctolite
		7G-1A, 137–146	30.370	30.46	18	G34	Not recovered		Olivine-bearing gabbro
		7G-2, 0–10	30.460	30.56	1	G35	Not recovered		Clinopyroxene oikocryst-bearing troctolite
		7G-2, 10–17	30.555	30.63	2	G36	Not recovered		Clinopyroxene oikocryst-bearing troctolite
		7G-2, 17–26	30.630	30.72	3	G37	Not recovered		Clinopyroxene oikocryst-bearing troctolite
		7G-2, 26–31	30.720	30.77	4	G38	Not recovered		Olivine-bearing gabbro
		7G-2, 31–39	30.770	30.85	5	G39	Not recovered		Clinopyroxene oikocryst-bearing troctolite
		7G-2, 39–51	30.850	30.97	6	G40	Not recovered		Clinopyroxene oikocryst-bearing troctolite
		7G-2, 51–59	30.970	31.05	7	G41	Not recovered		Clinopyroxene oikocryst-bearing troctolite
		15G-1A, 0–6	79.400	79.46	1	G46	Not recovered		Clinopyroxene oikocryst-bearing troctolite

Table T2 (continued).

Unit	Description	Core, section, interval (cm)	Depth (mbsf) Top	Depth (mbsf) Bottom	Pieces	Lithologic interval	Contact type	Contact definition	Complete lithology name
		15G-1A, 7–19	79.470	79.59	2	G47	Not recovered		Clinopyroxene oikocryst-bearing troctolite
		15G-1A, 20–28	79.600	79.68	3	G48	Not recovered		Olivine-bearing gabbro
		15G-1A, 29–37	79.690	79.77	4	G49	Not recovered		Olivine-bearing gabbro
		15G-1A, 38–42	79.780	79.82	5	G50	Not recovered		Olivine-bearing gabbro
		15G-1A, 43–51	79.830	79.91	6	G51	Not recovered		Clinopyroxene oikocryst-bearing troctolite
		15G-1A, 52–57	79.920	79.97	7	G52	Not recovered		Olivine gabbro
		15G-1A, 58–65	79.980	80.05	8	G53	Not recovered		Olivine gabbro
		15G-1A, 66–69	80.060	80.09	9	G54	Not recovered		Oikocryst gabbro
Ghost core Cluster 2	Samples recovered from the ghost core; contains rocks from all three units	14G-1A, 0–7	79.400	79.47	1	G42	Not recovered		Cataclastic olivine gabbro
		14G-1A, 8–14	79.480	79.54	2	G43	Not recovered		Olivine gabbro
		14G-1A, 15–19	79.550	79.59	3	G44	Not recovered		Olivine gabbro
		14G-1A, 20–25	79.600	79.65	4	G45	Not recovered		Troctolite
		17G-1A, 0–8	84.400	84.48	1	G55	Not recovered		Cataclastic olivine gabbro
		17G-1A, 9–12	84.490	84.52	2	G56	Not recovered		Aphyric basalt
		22G-1A, 0–3	101.800	101.83	1	G57	Not recovered		Completely altered chromitite
		22G-1A, 4–12	101.840	101.92	2	G58	Not recovered		Olivine gabbro
		24G-1A, 0–6	103.800	103.86	1	G59	Not recovered		Olivine-moderately phyric basalt
		24G-1A, 7–9	103.870	103.89	2	G60	Not recovered		Cataclastic olivine gabbro
		24G-1A, 10–13	103.900	103.93	3	G61	Not recovered		Cataclastic olivine gabbro
		24G-1A, 14–16	103.940	103.96	4	G62	Not recovered		Troctolite
		24G-1A, 17–21	103.970	104.01	5	G63	Not recovered		Troctolite
		24G-1A, 22–27	104.020	104.07	6	G64	Not recovered		Cataclastic basalt
		25G-1A, 0–7	103.800	103.87	1	G65	Not recovered		Olivine-bearing gabbro
		25G-1A, 8–17	103.880	103.97	2	G66	Not recovered		Olivine gabbro
		25G-1A, 18–27	103.980	104.07	3	G67	Not recovered		Troctolite
		25G-1A, 28–30	104.080	104.10	4	G68	Not recovered		Olivine gabbro
		25G-1A, 31–38	104.110	104.18	5	G69	Modal and textural		Olivine gabbro
		25G-1A, 39–42	104.190	104.22	6	G70	Not recovered		Recovered cement
		25G-1A, 43–47	104.230	104.27	7	G71	Not recovered		Recovered cement
		25G-1A, 48–57	104.280	104.37	8	G72	Not recovered		Cataclastic olivine gabbro

Pieces 1–4 from Section 345-U1415J-23R-1A are regarded as representing rubble from an upper part of the hole that fell into the borehole during cleaning operations.

Table T3. Details and explanations for thin sections with two or three domains, Hole U1415J. (Continued on next page.)

Core, section, interval (cm)	Thin section number	Lithologic interval	Rock name	Rock comment	Nature of domains	Contact	Number of domains	Igneous domain	Domain lithology name
345-U1415J-									
3R-1W, 73–75 (Piece 14)	32 (image)	10	Clinopyroxene oikocryst-bearing olivine gabbro	Contains two different lithologies	Contact between two lithologies	Sutured	2	1	Olivine gabbro
								2	Oikocryst olivine gabbro
5R-1W, 117–120 (Piece 17B)	37 (image)	24	Clinopyroxene oikocryst-bearing troctolite	Oikocryst and matrix were described as two different domains	Oikocrysts/Matrix	Sutured	2	1	Troctolite matrix
								2	Clinopyroxene oikocryst
5R-1W, 138–141 (Piece 18)	38 (image)	27/28	Olivine gabbro/ Orthopyroxene-bearing gabbro	Contact between two lithologic Intervals	Contact between two lithologic intervals	Sutured	2	1	Olivine gabbro
								2	Orthopyroxene-bearing, olivine-bearing gabbro olivine-bearing
7G-1W, 28–31 (Piece 5)	40 (image)	G20	Clinopyroxene oikocryst-bearing troctolite/ Gabbronorite	Contact between troctolite and gabbronorite; clinopyroxene oikocryst-bearing			3	1	Troctolite
								2	Clinopyroxene oikocryst-bearing troctolite
								3	Gabbronorite
7G-1W, 35–38 (Piece 6)	41 (image)	G22	Clinopyroxene oikocryst-bearing olivine gabbro	Contains a 2 cm elongated clinopyroxene oikocryst	Oikocrysts/Matrix	Sutured	2	1	Olivine gabbro
								2	Clinopyroxene oikocryst
7G-1W, 91–94 (Piece 14)	42 (image)	G30	Troctolite/Clinopyroxene oikocryst-bearing gabbro	Contains two different lithologies	Contact between two lithologies	Sutured	2	1	Troctolite
								2	Clinopyroxene oikocryst-bearing gabbro
7G-1W, 55–56 (Piece 8)	45 (image)	G24	Clinopyroxene oikocryst-bearing olivine gabbro	Oikocryst and matrix were described as two different domains	Oikocrysts/Matrix		2	1	Troctolite
								2	Clinopyroxene oikocryst
8R-1W, 34–37 (Piece 7)	46 (image)	37	Clinopyroxene oikocryst-bearing troctolite	Oikocryst and matrix were described as two different domains	Oikocrysts/Matrix	Sutured	2	1	Troctolite
								2	Clinopyroxene oikocryst
8R-1W, 73–76 (Piece 13)	47 (image)	38	Clinopyroxene oikocryst-bearing troctolite	Oikocryst and matrix were described as two different domains	Oikocrysts /Matrix	Sutured	2	1	Troctolite
								2	Clinopyroxene oikocryst
8R-2W, 79–82 (Piece 8)	51 (image)	41	Clinopyroxene oikocryst-bearing olivine gabbro,	Oikocryst and matrix were described as two different domains	Oikocrysts/Matrix	Sutured	2	1	Olivine gabbro
								2	Clinopyroxene oikocryst
8R-2W, 112–115 (Piece 9)	52 (image)	42/43	Olivine-bearing gabbro/ Olivine gabbro	Contact between two lithological intervals	Contact between two lithologic intervals	Sutured	2	1	Olivine-bearing gabbro
								2	Olivine gabbro
8R-3W, 26–29 (Piece 5)	53 (image)	47	Clinopyroxene oikocryst-bearing troctolite	Oikocryst and matrix were described as two different domains	Oikocrysts/Matrix	Sutured	2	1	Troctolite
								2	Clinopyroxene oikocryst
10R-1W, 53–55 (Piece 6B)	58 (image)	58	Contact between troctolite and gabbro	Rock contains two different lithologies; moderately altered	Two lithologies	Gradational	2	1	Troctolite
								2	Gabbro
15G-1W, 46–49 (Piece 6)	69 (image)	G51	Clinopyroxene oikocryst-bearing troctolite	Oikocryst and matrix were described as two different domains	Oikocrysts/Matrix	Sutured	2	1	Troctolite
								2	Clinopyroxene oikocryst
18R-1W, 67–69 (Piece 9)	71 (image)	71	Completely altered chromitite	Protolith was probably chomitite/dunite/ troctolite association; some grains of chromian spinel preserved	Two lithologies	Sutured	2	1	Heavily altered chromitite
								2	Heavily altered troctolite
18R-1W, 141–143 (Piece 17B)	72 (image)	73	Troctolite	Contains a layer richer in plagioclase	Modal and grain size	Sutured	2	1	Troctolite
								2	Plagioclase-rich troctolite

Table T3 (continued).

Core, section, interval (cm)	Thin section number	Lithologic interval	Rock name	Rock comment	Nature of domains	Contact	Number of domains	Igneous domain	Domain lithology name
19R-1W, 64–67 (Piece 10)	74 (image)	75	Cataclasite with basaltic fragment	Eventually tectonized gabbro/dike contact	Two or more lithologies	Tectonic	2	1	Basalt
								2	Cataclasite
21R-1W, 103–107 (Piece 14)	79 (image)	79	Cataclasite mainly consisting of olivine gabbro	With basaltic fragment	Two lithologies	Tectonic	2	1	Olivine gabbro
								2	Basalt
23R-1W, 52–53 (Piece 8)	83 (image)	86	Cataclasite with fragments of gabbro	Primary mode estimation not possible			3	1	Cataclasite
								2	Cataclasite
								3	Cataclasite
25G-1W, 11–15 (Piece 2)	84 (image)	G66	Oikocryst gabbro	Oikocryst and matrix were described as two different domains	Oikocrysts/Matrix	Sutured	2	1	Troctolite
								2	Clinopyroxene oikocryst
25G-1W, 32–35 (Piece 5)	85 (image)	G69	Olivine gabbro	With a domain poor in olivine	Two or more lithologies	Sutured	2	1	Olivine gabbro
								2	Olivine-bearing gabbro

Table T4. Summary of igneous contacts of rocks based on macroscopic and thin section description, Hole U1415J.

Unit	Core, section, interval (cm)	Thin section number	Lithologic interval	Contact lithology	Contact type	Contact definition
	345-U1415J-					
II	5R-1, 129–143 (Piece 18)	38	27/28	Olivine- and orthopyroxene-bearing gabbro/Troctolite	Modal and grain size	Sutured/Sharp
Ghost 1	7G-1, 26–34 (Piece 5)	40	G20/G21	Clinopyroxene oikocryst-bearing troctolite/Gabbronorite	Modal and grain size	Sutured/Sharp
	7G-1, 91–94 (Piece 14)	42	G30	Oikocryst-bearing troctolite/Troctolite	Modal and grain size	Sutured/Sharp
II	8R-2, 105–122 (Piece 9)	52	42/43	Olivine gabbro/Olivine-bearing gabbro	Modal and grain size	Sutured/Sharp
	8R-3, 31–41 (Piece 7)	54	48	Gabbro/Olivine gabbro	Modal and grain size	Sutured/Sharp
III	10R-1, 39–55 (Piece 6B)	58	58/59	Troctolite/Olivine gabbro	Modal and grain size	Sutured/Gradational
	18R-1, 141–146 (Piece 17B)	72	72	Olivine-rich troctolite/Troctolite	Modal and grain size	Sutured/Sharp
Ghost 2	25G-1, 30–38 (Piece 5)	85	G69	Olivine-bearing gabbro/Gabbro	Modal	Sutured/Sharp

Table T5. Background alteration modes observed in thin section.

Olivine alteration relative proportions

Unit	Number of samples	Igneous mode	Alteration (%)	Serpentine (%)	Clay minerals (%)	Amphibole (%)	Talc (%)	Chlorite (%)	Other (%)
I background	7	8	80	11	22	30	19	15	4
II background	29	14	64	26	17	13	21	18	4
I/II cataclastic	3	13	100	54	22	9	12	—	4
III background	17	37	68	42	17	25	9	4	2
III cataclastic	23	11	99	18	11	16	3	50	2

Clinopyroxene alteration relative proportions

Unit	Number of samples	Igneous mode	Alteration (%)	Pale amphibole (%)	Clay minerals (%)	Green amphibole (%)	Secondary clinopyroxene (%)	Chlorite (%)	Other (%)
I background	7	30	20	22	—	71	—	8	—
II background	29	28	30	68	1	22	<1	8	1
I/II cataclastic	3	22	37	74	—	26	—	—	—
III background	17	20	50	58	23	17	—	0	2
III cataclastic	23	24	64	35	2	34	<1	24	4

Orthopyroxene alteration relative proportions

Unit	Number of samples	Igneous mode	Alteration (%)	Pale and green amphibole (%)	Talc (%)	Chlorite (%)	Serpentine (%)	Clay minerals (%)	Other (%)
I background	7	5	40	40	20	—	8	24	8
II background	29	6	28	73	8	17	1	—	—
I/II cataclastic	3	10	90	20	—	20	20	40	—
III background	17	1	0	—	—	—	—	—	—
III cataclastic	23	—	—	—	—	—	—	—	—

Plagioclase alteration relative proportions

Unit	Number of samples	Igneous mode	Alteration (%)	Amphibole	Epidote/ clinozoisite (%)	Chlorite (%)	Clay	Prehnite (%)	Garnet	Secondary plagioclase (%)	Zeolite (%)	Carbonate (%)
I background	7	60	10	2	5	37	—	18	—	36	3	—
II background	29	61	16	<1	<1	33	3	48	2	9	5	1
I/II cataclastic	3	65	32	—	—	29	—	39	—	6	26	—
III background	17	45	48	3	3	38	—	49	<1	4	3	<1
III cataclastic	23	70	69	<1	8	20	4	57	<1	6	4	<1

Overall alteration and relative proportions of alteration minerals

Unit	Number of samples	Alteration (%)	Amphibole (%)	Chlorite (%)	Prehnite (%)	Secondary plagioclase (%)	Serpentine (%)	Talc (%)	Clay minerals (%)	Zeolite (%)	Carbonate (%)
I background	7	19	42	18	5	11	4	8	10	1	—
II background	29	29	35	21	17	3	9	7	7	2	<1
I/II cataclastic	3	50	22	16	16	2	17	3	13	11	—
III background	17	55	26	17	19	2	19	4	12	1	<1
III cataclastic	23	70	18	27	40	4	3	0	5	3	<1

Table T6. Metamorphic domains described in thin section, Hole U1415J.

Core, section, interval (cm)	Thin section number	Depth (mbsf) Top	Depth (mbsf) Bottom	Rock name	Number of domains	Alteration domain	Domain relative abundance (%)	Alteration domain or feature
345-U1415J-								
3R-1W, 11–13 (Piece 4)	29	15.11	15.13	Orthopyroxene bearing olivine gabbro	2	1	70	Little deformed olivine gabbro
						2	30	Cataclastic olivine gabbro
7G-1W, 28–31 (Piece 5)	40 (image)	29.28	29.31	Clinopyroxene oikocryst-bearing gabbronorite	2	1	40	Background
				Troctolite		2	60	Background
7G-1W, 91–94 (Piece 14)	42 (image)	29.91	29.94	Metatroctolite	2	2	70	Background
				Troctolite		1	30	Background
8R-1W, 73–76 (Piece 13)	47 (image)	35.63	35.66	Clinopyroxene oikocryst-bearing olivine gabbro	2	1	50	Background
				Olivine gabbro		2	50	Halo
8R-2W, 112–115 (Piece 9)	52 (image)	37.49	37.52	Olivine gabbro	2	1	60	Background: olivine-bearing gabbro
						2	40	Background: olivine gabbro
8R-2W, 71–74 (Piece 7C)	50 (image)	37.08	37.11	Troctolitic gabbro	2	1	50	Background
						2	50	Halo
10R-1W, 53–55 (Piece 6B)	58 (image)	55.83	55.85	Clinopyroxene oikocryst gabbro	2	1	60	Troctolite Background
						2	35	Clinopyroxene oikocryst
12R-1W, 115–117 (Piece 15)	64 (image)	70.85	70.87	Cataclased gabbro	2	1	30	Background
						2	70	Background
14G-1W, 0–4 (Piece 1)	68 (image)	37.00	37.04	Metagabbro	2	1	35	Background
						2	65	Halo
15G-1W, 46–49 (Piece 6)	69 (image)	37.92	37.95	Olivine gabbro	2	1	75	Background
						2	25	Vein halo
18R-1W, 141–143 (Piece 17B)	72 (image)	85.81	85.83	Metatroctolite	2	1	50	Background
						2	50	Halo?
19R-1W, 64–67 (Piece 10)	74 (image)	89.74	89.77	Anorthositic olivine gabbro	2	2	40	Background
				Dike rock in altered gabbro		1	60	Background
23R-1W, 10–12 (Piece 3)	81 (image)	101.90	101.92	Cataclastic gabbro	2	1	10	Background
				Sheared dolerite		2	90	Background
23R-1W, 39–42 (Piece 7)	82 (image)	102.19	102.22	Cataclastic metagabbro	2	2	30	Cataclastic zone
				Metagabbro		1	70	Background
23R-1W, 52–53 (Piece 8)	83 (image)	102.32	102.33	Cataclastic gabbroic rock	2	1	50	Fractured less deformed than Domain 2
						2	50	Zone of more localized deformation
8R-3W, 26–29 (Piece 5)	53 (image)	38.12	38.15	Clinopyroxene oikocryst-bearing troctolite	3	1	75	Background
						2	5	Band close to clinopyroxene oikocryst
						3	20	Clinopyroxene oikocryst
11R-1W, 44–47 (Piece 7)	60 (image)	65.44	65.47	Dark highly altered cataclastic gabbro	3	2	75	Background
				Little altered cataclastic gabbro		1	10	Cataclasite
				Pale highly altered cataclastic gabbro		3	15	Background

Table T7. Results from X-ray diffraction of rubble, cataclasites, and vein-filling material, Hole U1415J.

Core, section, interval (cm)	Sample ID	ASMAN ID (file)			Timestamp (UTC)	Comments	Primary phases	Secondary phases
		PDF	Raw	UXD				
345-U1415J-								
2G-1W, 0.0–13.0	OTHR4565271	20859891	20859921	20859871	35:04	1–4 cm rubble	Na-anorthite	Quartz
4R-1W, 20.0–22.0	OTHR4567151	20859901	20859911	20859881	35:04	Pink vein-filling material	Clinozoisite	
11R-1W, 44.0–49.0	OTHR4571571	20906201	20906221	20906181	40:29	Cataclasite matrix	Prehnite, chlorite	
12R-1W, 11.0–14.0	OTHR4571581	20906191	20906211	20906171	40:27	Cataclasite matrix	Prehnite, chlorite, epidote	Chamosite, Na-anorthite
13R-1W, 26.0–28.0	OTHR4571591	20906241	20906251	20906231	40:33	White cataclasite rock	Albite, chlorite, prehnite	
18R-1W, 37.0–38.0	OTHR4575371	20930991	20931021	20930981	03:19	Vein-filling material	Actinolite	Tremolite (?), nimite (?), corrensite (?)
21R-1A, 17.0–22.0	OTHR4575361	20931001	20931011	20930971	03:19	Cataclasite matrix	Prehnite, corrensite	Clinochlor

Table T8. Distribution of olivine coronae in thin section, Hole U1415J.

Core, section, interval (cm)	Thin section number	Depth (mbsf) Top	Depth (mbsf) Bottom	Lithology	Corona (%)	Total olivine alteration (%)
345-U1415J-						
3R-1W, 11–13 (Piece 4)	29	15.11	15.13	Olivine gabbro	15	90
3R-1W, 22–24 (Piece 6)	30	15.22	15.24	Olivine gabbro	2	100
3R-1W, 45–48 (Piece 10)	31	15.45	15.48	Gabbro	15	50
3R-1W, 73–75 (Piece 14)	32	15.73	15.75	Olivine gabbro	10	80
5R-1W, 62–64 (Piece 12)	36	26.82	26.84	Clinopyroxene oikocryst-bearing olivine gabbro	8	40
5R-1W, 117–120 (Piece 17B)	37	27.37	27.4	Clinopyroxene oikocryst-bearing olivine gabbro	0	50
5R-1W, 138–141 (Piece 18)	38	27.58	27.61	Olivine gabbro	0	20
5R-2W, 60–63 (Piece 3)	39	28.235	28.265	Olivine-bearing gabbronorite	0	15
7G-1W, 28–31 (Piece 5)	40	29.28	29.31	Clinopyroxene oikocryst-bearing troctolite	20	40
7G-1W, 35–38 (Piece 6)	41	29.35	29.38		10	70
7G-1W, 55–56 (Piece 8)	45	29.55	29.56	Clinopyroxene oikocryst-bearing olivine gabbro	0	25
7G-1W, 84–87 (Piece 13)	43	29.84	29.87	Oikocryst-bearing gabbro	10	100
7G-1W, 91–94 (Piece 14)	42	29.91	29.94	Oikocryst-bearing gabbro	30	90
8R-1W, 34–37 (Piece 7)	46	35.24	35.27	Clinopyroxene oikocryst troctolite	10	100
8R-1W, 73–76 (Piece 13)	47	35.63	35.66	Oikocryst gabbro	0	70
8R-1W, 79–82 (Piece 13)	49	35.69	35.72	Oikocryst gabbro	0	40
8R-2W, 71–74 (Piece 7C)	50	37.08	37.11	Clinopyroxene oikocryst troctolite	0	100
8R-2W, 79–82 (Piece 8)	51	37.16	37.19	Clinopyroxene oikocryst troctolite	0	25
8R-2W, 112–115 (Piece 9)	52	37.49	37.52	Clinopyroxene oikocryst troctolite	0	30
8R-3W, 26–29 (Piece 5)	53	38.12	38.15	Clinopyroxene oikocryst troctolite	0	25
8R-3W, 35–38 (Piece 6)	54	38.21	38.24	Olivine gabbro	10	95
8R-3W, 83–86 (Piece 9B)	55	38.69	38.72	Olivine gabbro	0	25
8R-3W, 129–132 (Piece 14A)	57	39.15	39.18	Olivine gabbro	15	100
9R-1W, 46–49 (Piece 7)	48	45.66	45.69	Olivine-bearing gabbro	10	100
10R-1W, 53–55 (Piece 6B)	58	55.83	55.85	Troctolite	0	25
11R-1W, 22–24 (Piece 4)	59	65.22	65.24	Troctolite	0	25
12R-1W, 86–89 (Piece 12)	62	70.56	70.59	Olivine gabbro	0	100
12R-1W, 94–96 (Piece 13)	63	70.64	70.66	Olivine gabbro	5	100
12R-1W, 115–117 (Piece 15)	64	70.85	70.87	Olivine gabbro	40	100
13R-1W, 26–29 (Piece 4B)	65	74.96	74.99	Troctolite	30	100
13R-1W, 39–41 (Piece 6)	66	75.09	75.11	Troctolite	5	40
13R-1W, 53–56 (Piece 7)	67	75.23	75.26	Troctolite	10	100
15G-1W, 46–49 (Piece 6)	69	80.32	80.35	Troctolite	0	50
18R-1W, 49–52 (Piece 7)	70	84.89	84.92	Troctolite	60	100
18R-1W, 67–69 (Piece 9)	71	85.07	85.09	Chromitite	100	100
18R-1W, 141–143 (Piece 17B)	72	85.81	85.83	Troctolite	2	85
19R-1W, 18–19 (Piece 3)	73	89.28	89.29	Troctolite	2	60
19R-1W, 64–67 (Piece 10)	74	89.74	89.77	Cataclasite	5	100
21R-1W, 13–15 (Piece 3)	76	98.93	98.95	Chromitite	100	100
21R-1W, 58–59 (Piece 9)	78	99.38	99.39	Olivine gabbro	10	100
21R-1W, 103–107 (Piece 14)	79	99.83	99.87	Olivine gabbro	25	100
21R-1W, 118–121 (Piece 16)	80	99.98	100.01	Olivine gabbro	5	100
23R-1W, 39–42 (Piece 7)	82	102.19	102.22	Olivine gabbro	40	100
23R-1W, 52–53 (Piece 8)	83	102.32	102.33	Olivine gabbro	0	100
25G-1W, 11–15 (Piece 2)	84	103.91	103.95	Oikocryst gabbro	5	100
25G-1W, 32–35 (Piece 5)	85	104.12	104.15	Clinopyroxene oikocryst gabbro	20	40

Table T9. Modal proportions for grain mounts, Hole U1415J.

Mineral	345-U1415J-2G-Sand, TS 27		345-U1415J-2G-Sand, TS 28		
	Modal (%)	Reconstructed igneous mode	Modal (%)	Reconstructed igneous mode	Mean mode
Plagioclase	23.8	57.1	27.6	63.1	25.7
Pyroxene	13.0	31.6	10.3	25.1	11.7
Amphibole after pyroxene	14.7		10.1		12.4
Polycrystalline amphibole	3.5		3.1		3.3
Secondary plagioclase	8.7		7.8		8.2
Zeolite (including veins and plagioclase replacement)	2.9		3.7		3.3
Cataclasite	8.5		11.1		9.8
Bruised grain of plagioclase or pyroxene	0.0		0.2		0.1
Prehnite vein/Prehnite replacing cataclasite	1.7		1.7		1.7
Prehnite replacing plagioclase	2.9		2.3		2.6
Chlorite	8.7		9.3		9.0
Olivine	0.2	11.3	0.6	11.8	0.4
Clay	5.4		5.2		5.3
Epidote	1.7		1.2		1.4
Carbonate	0.2		0.2		0.2
Serpentine	0.0		0.4		0.2
Volcanic clasts	4.1		5.2		4.7
					0.0
Cataclastic (excluding volcanics, including prehnite replacing cataclasite)	10.6		13.7		12.2
Altered phases	52.5		47.5		50.0
Prehnite	4.6		4.1		4.3

Igneous mode is estimated according to the following formula: plagioclase = plagioclase + secondary plagioclase + zeolite + prehnite + (cataclasite + bruised grains) × 0.7 + chlorite × 0.8 + epidote + carbonate; pyroxene (includes some orthopyroxene) = pyroxene + amphibole after pyroxene + (cataclasite + bruised grains) × 0.3; olivine = olivine + clay minerals + serpentine + polycrystalline amphibole + chlorite × 0.2. TS = thin section.

Table T10. Discrete sample remanence data, Hole U1415J.

Core, section, interval (cm)	Depth (mbsf)	Lithology	NRM			Principal component analysis								
			Declination (°)	Inclination (°)	Intensity (A/m)	Treatment	Low	High	*n* points	Origin model	MAD (°)	Declination (°)	Inclination (°)	Intensity (A/m)
345-U1415J-														
3R-1, 26	15.26	Olivine-bearing gabbro	175.7	–80.1	4.59E–03	LTD/Th	250	425	5	F	3.4	351.3	–84.1	1.80E–03
							425	510	5	F	2.9	90	–62	4.00E–03
							520	560	5	A	6.4	248.9	46.2	6.00E–04
5R-1, 122	27.42	Olivine-bearing gabbronorite	281.9	–13.4	2.31E–02	LTD/Th	350	510	7	F	13.6	299.7	–36.1	1.06E–02
							530	570	5	F	5.9	74.3	34.6	5.30E–03
5R-1, 130	27.50	Olivine-bearing gabbro	211.4	18.9	2.19E+00	LTD/Th	LTD2	550	17	F	5.6	215.6	29.7	2.77E–01
							550	590	5	F	0.8	215.7	14.3	5.45E–01
5R-2, 19	27.83	Olivine-bearing gabbronorite	138.2	22.5	1.52E+00	LTD/Th	LTD2	590	21	F	3.9	145	12.1	7.22E–01
5R-2, 35	27.99	Olivine-bearing gabbronorite	172	18.7	1.55E+00	LTD/Th	LTD1	590	22	F	4.6	168.5	26	1.11E+00
5R-2, 58	28.22	Olivine-bearing gabbronorite	78.1	–44.6	6.94E–02	AF	15	35	5	F	5	83.9	–79.5	4.18E–02
5R-2, 61	28.25	Olivine-bearing gabbronorite	130.9	11.6	5.88E–01	LTD/Th	LTD2	550	17	F	7.1	128.5	14.4	1.47E–01
							550	580	4	F	3.8	127.6	0.6	2.03E–01
8R-1, 80	35.70	Oikocryst gabbro	16	–28.9	9.63E–01	Th	150	530	10	F	2.7	16.2	–19.1	4.59E–01
							530	580	6	F	4.9	23.2	–41.7	3.29E–01
8R-1, 84	35.74	Oikocryst gabbro	238.7	68.5	1.09E–01	LTD/Th	520	580	7	F	4.2	206.3	–79.5	9.56E–02
8R-2, 81	37.18	Clinopyroxene oikocryst-bearing troctolite	249.8	–16.8	8.85E–01	LTD/Th	LTD2	450	10	F	7.2	240	–12	9.98E–02
							450	580	11	F	4.5	251.1	–41.8	4.11E–01
8R-3, 68	38.54	Olivine-bearing gabbro	235.4	45.9	2.50E–02	LTD/Th	LTD1	300	7	F	4.6	235	50.3	1.85E–02
8R-3, 84	38.70	Clinopyroxene oikocryst-bearing troctolite	177.5	–60.4	8.66E+00	LTD/Th	LTD1	580	21	F	3.4	182.8	–68.9	5.30E+00
8R-3, 113	38.99	Olivine-bearing gabbro	349.6	43.4	3.72E–02	LTD/Th	LTD2	475	11	F	9.8	268.3	–69	5.80E–03
							475	580	10	F	2	11.8	49.9	3.66E–02
9R-1, 47	45.67	Olivine-bearing gabbro	147	–63.2	1.58E–01	LTD/Th	100	450	9	F	4	168.4	–59.2	6.05E–02
							450	510	4	F	2.3	127.5	–73.5	6.41E–02
10R-1, 42	55.72	Troctolite	51.7	–30.2	1.16E+00	LTD/Th	LTD1	590	22	F	5.1	32.3	–36.2	7.19E–01
12R-1, 108	70.78	Olivine gabbro	0	55.6	1.26E–03	LTD/Th	No pick							
13R-1, 28	74.98	Highly altered troctolite	94	26.8	4.96E–04	LTD/Th	No pick							
13R-1, 42	75.12	Troctolite	119.5	34.2	1.85E+01	LTD/Th	LTD1	540	17	F	6.9	124.4	34.9	4.06E+00
							540	590	6	F	2.2	124.3	23	5.54E+00
15G1, 15	37.15	Clinopyroxene oikocryst-bearing troctolite	221.9	62.9	5.10E–01	LTD/Th	LTD1	550	17	F	12.1	203.2	77.9	2.03E–01
							550	580	4	F	3.4	224.8	55.3	3.06E–01
18R-1, 144	85.84	Troctolite	114.4	7.1	2.41E+00	LTD/Th	LTD2	510	13	F	8.3	16.4	–17.1	8.19E–01
							510	580	8	F	2.5	60.4	–52.7	1.33E+00
19R-1, 17	89.27	Troctolite	261.3	–48.4	2.97E+00	LTD/Th	400	560	11	F	4.4	259.2	–38.2	1.08E+00
							560	580	3	F	1.7	287.8	–58.5	7.39E–01
21R-1, 57	99.37	Olivine gabbro	306.7	–52	2.69E–03	LTD/Th	LTD1	540	17	F	16.8	303.6	–59.6	1.30E–03
21R-1, 118	99.98	Olivine gabbro	250.2	–79	1.78E–03	LTD/Th	100	450	9	F	12	91.5	–55.5	8.00E–04
21R-1, 120	100.00	Olivine gabbro	123.7	–26.4	1.80E–03	AF	10	80	12	F	4.6	133.3	–58.3	1.94E–03
21R-2, 27	100.39	Olivine gabbro	264.4	–35.6	4.56E–03	LTD/Th	LTD2	350	7	F	11.8	219.3	–36.7	9.00E–04
							350	560	12	A	7.4	290.7	–40.4	2.20E–03
23R-1, 22	102.02	Olivine gabbro	154.8	–35.1	3.19E–03	LTD/Th	100	350	6	F	6.4	296.4	–31.5	1.20E–03
							450	510	4	F	0.8	134.9	0.4	1.09E–02
							510	560	6	F	4.8	311.1	–13.9	4.60E–03
23R-1, 51	102.31	Olivine gabbro	150.2	–25.9	1.58E–02	LTD/Th	NRM	450	12	F	12.7	244	–50.3	2.70E–03
							450	520	5	F	1.4	143.5	–17.1	1.60E–02
							520	540	3	F	3.8	323.1	13.9	7.00E–04

NRM = natural remanent magnetization, LTD = low-temperature demagnetization, Th = thermal demagnetization, AF = alternating field demagnetization. F = free, A = anchored. MAD = maximum angular deviation.

Table T11. Anisotropy of magnetic susceptibility data, Hole U1415J.

Core, section, interval (cm)	Depth (mbsf)	Lithology	Susceptibility (SI)	Maximum			Intermediate			Minimum			Corrected anisotropy degree	Shape parameter
				Eigenvalue	Declination (°)	Inclination (°)	Eigenvalue	Declination (°)	Inclination (°)	Eigenvalue	Declination (°)	Inclination (°)		
345-U1415J-														
3R-1, 26	15.26	Olivine-bearing gabbro	2.30E–04	0.3386	300.3	36.9	0.3352	205.9	5.9	0.3263	108.1	52.5	1.04	0.452
5R-1, 122	27.42	Olivine-bearing gabbronorite	5.89E–04	0.3441	223.3	22	0.3370	314.6	3.2	0.3190	52.3	67.7	1.08	0.452
5R-1, 130	27.50	Olivine-bearing gabbro	6.14E–03	0.3772	157.4	29.6	0.3488	63.4	7.1	0.2740	321.2	59.4	1.40	0.511
5R-2, 19	27.83	Olivine-bearing gabbronorite	3.42E–03	0.3645	169	38.6	0.3375	57.4	24.7	0.2980	303.5	41.3	1.23	0.238
5R-2, 35	27.99	Olivine-bearing gabbronorite	3.18E–03	0.3778	155.4	48.8	0.3375	45.4	16.7	0.2847	302.7	36.4	1.33	0.204
5R-2, 58	28.22	Olivine-bearing gabbronorite	2.32E–03	0.3667	143.8	46	0.3409	43.2	10	0.2923	304	42.3	1.26	0.357
5R-2, 61	28.25	Olivine-bearing gabbronorite	2.31E–03	0.3670	160.1	41.4	0.3410	56.4	15	0.2920	311	44.7	1.26	0.356
8R-1, 80	35.70	Oikocryst gabbro	3.14E–03	0.3624	139.3	32	0.3377	43.7	8.9	0.2999	300	56.5	1.21	0.254
8R-1, 84	35.74	Oikocryst gabbro	3.23E–03	0.3650	152.9	31.2	0.3331	52.1	17.3	0.3019	297.3	53.4	1.21	0.035
8R-2, 81	37.18	Clinopyroxene oikocryst-bearing troctolite	4.05E–03	0.3664	184.3	42	0.3386	77.8	17.5	0.2950	330.8	42.8	1.25	0.272
8R-3, 68	38.54	Olivine-bearing gabbro	1.59E–04	0.3366	40.1	38.4	0.3340	286.1	27.1	0.3294	171.1	39.6	1.02	0.293
8R-3, 84	38.70	Clinopyroxene oikocryst-bearing troctolite	1.62E–02	0.3660	154.5	27.5	0.3315	52.8	21.2	0.3025	290.5	54.1	1.21	–0.039
8R-3, 113	38.99	Olivine-bearing gabbro	3.15E–04	0.3414	108	27.6	0.3363	6.3	21.3	0.3223	243.9	54	1.06	0.473
9R-1, 47	45.67	Olivine-bearing gabbro	7.59E–04	0.3428	311.4	63.7	0.3338	202.5	9.1	0.3234	108.3	24.5	1.06	0.088
10R-1, 42	55.72	Troctolite	4.27E–03	0.3472	13.7	60.1	0.3304	208.4	29.1	0.3223	114.8	6.3	1.08	–0.333
12R-1, 108	70.78	Olivine gabbro	2.17E–04	0.3354	80.3	6.7	0.3331	171.6	10.5	0.3314	318.3	77.5	1.01	–0.136
13R-1, 28	74.98	Highly altered troctolite	1.26E–04	0.3350	107.9	63.1	0.3328	11.2	3.4	0.3322	279.5	26.7	1.01	–0.607
13R-1, 42	75.12	Troctolite	5.15E–02	0.3622	77.4	45.4	0.3457	345.9	1.4	0.2922	254.5	44.6	1.25	0.566
15G1, 15	37.15	Clinopyroxene oikocryst-bearing troctolite	5.10E–03	0.3656	133.7	69.4	0.3384	15.3	10.1	0.2960	282.1	17.7	1.24	0.265
18R-1, 144	85.84	Troctolite	5.19E–02	0.3474	19.3	8.1	0.3292	285.3	26.2	0.3233	125.1	62.4	1.08	–0.495
19R-1, 17	89.27	Troctolite	3.78E–02	0.3554	84.8	48.7	0.3363	179.8	4.4	0.3083	273.5	41	1.15	0.220
21R-1, 57	99.37	Olivine gabbro	3.16E–04	0.3358	89.7	62	0.3344	346.6	6.9	0.3298	253	27	1.02	0.523
21R-1, 118	99.98	Olivine gabbro	2.73E–04	0.3370	224.7	76.7	0.3332	342.8	6.4	0.3298	74.1	11.6	1.02	–0.032
21R-1, 120	100.00	Olivine gabbro	2.76E–04	0.3373	159.6	73	0.3328	299.1	13.1	0.3299	31.6	10.7	1.02	–0.200
21R-2, 27	100.39	Olivine gabbro	2.22E–04	0.3369	43.1	76.6	0.3335	300.1	3.1	0.3296	209.3	13	1.02	0.084
23R-1, 22	102.02	Olivine gabbro	2.61E–04	0.3360	344.6	23.9	0.3339	230.7	42.4	0.3301	94.9	38.1	1.02	0.312
23R-1, 51	102.31	Olivine gabbro	2.40E–04	0.3372	126.4	41.2	0.3337	12.7	24.6	0.3291	261.1	38.8	1.03	0.142

Table T12. *P*-wave velocity, density, and porosity measurements, Hole U1415J.

Core, section, interval (cm)	Depth (mbsf)	*P*-wave velocity											Bulk density (g/cm³)	Grain density (g/cm³)	Porosity (vol%)	Primary lithology	Background alteration (%)
		Mean (km/s)			Standard deviation (km/s)			Standard deviation (%)			Mean (km/s)	Apparent anisotropy (%)					
		x	*y*	*z*	*x*	*y*	*z*	*x*	*y*	*z*							
345-U1415J-																	
3R-1W, 25–27	15.25	6.21	6.22	6.03	0.0025	0.0033	0.0266	0.04	0.05	0.44	6.16	3.2	2.88	2.90	1.3	Olivine-bearing gabbro	30–60
5R-1W, 121–123	27.41	6.52	6.37	6.44	0.0025	0.0052	0.0322	0.04	0.08	0.50	6.44	2.3	2.95	2.97	0.9	Olivine-bearing gabbronorite	10–30
5R-1W, 129–131	27.49	6.40	6.55	6.42	0.0006	0.0010	0.0030	0.01	0.02	0.05	6.46	2.2	2.83	2.84	0.5	Olivine-bearing gabbro	10–30
5R-2W, 18–20	27.815	6.36	6.51	6.44	0.0013	0.0030	0.0052	0.02	0.05	0.08	6.44	2.4	2.92	2.95	1.4	Olivine-bearing gabbronorite	10–30
5R-2W, 34–36	27.975	6.42	6.56	6.52	0.0076	0.0012	0.0106	0.12	0.02	0.16	6.50	2.2	2.88	2.89	0.6	Olivine-bearing gabbronorite	10–30
5R-2W, 57–29	28.205	6.33	6.53	6.52	0.0008	0.0130	0.0084	0.01	0.20	0.13	6.46	3.2	2.90	2.92	1.1	Olivine-bearing gabbronorite	10–30
5R-2W, 60–62	28.235	6.65	6.49	6.62	0.0029	0.0015	0.0049	0.04	0.02	0.07	6.59	2.4	2.91	2.92	0.5	Olivine-bearing gabbronorite	10–30
7G-1W, 52–54	29.52	6.60	6.65	6.44	0.0042	0.0015	0.0096	0.06	0.02	0.15	6.56	3.2	2.87	2.88	0.7	Clinopyroxene oikocryst-bearing troctolite	60–90
8R-1W, 79–81	35.69	6.31	6.51	6.50	0.0032	0.0008	0.0005	0.05	0.01	0.01	6.44	3.1	2.90	2.91	0.7	Oikocryst gabbro	10–30
8R-2W, 80–82	37.17	6.53	6.44	6.54	0.0036	0.0035	0.0014	0.06	0.05	0.02	6.50	1.6	2.87	2.88	0.4	Clinopyroxene oikocryst-bearing troctolite	<10
8R-3W, 67–69	38.53	5.84	6.06	5.74	0.0024	0.0012	0.0008	0.04	0.02	0.01	5.88	5.4	2.87	2.91	2.0	Olivine-bearing gabbro	10–30
8R-3W, 83–85	38.69	6.13	6.30	6.47	0.0012	0.0029	0.0014	0.02	0.05	0.02	6.30	5.5	2.80	2.80	0.3	Cpx-oikocryst bearing troctolite	30–60
8R-3W, 112–114	38.98	6.23	5.98	6.16	0.0020	0.0061	0.0024	0.03	0.10	0.04	6.12	4.1	2.90	2.93	1.8	Olivine-bearing gabbro	10–30
9R-1W, 46–48	45.66	6.03	6.10	6.05	0.0039	0.0046	0.0031	0.06	0.08	0.05	6.06	1.0	2.95	2.99	2.1	Olivine-bearing gabbro	10–30
10R-1W, 41–43	55.71	6.62	6.70	6.49	0.0154	0.0027	0.0031	0.23	0.04	0.05	6.60	3.3	2.85	2.85	0.2	Troctolite	10–30
12R-1W, 107–109	70.77	5.89	5.91	5.78	0.0012	0.0072	0.0023	0.02	0.12	0.04	5.86	2.2	2.77	2.82	3.2	Olivine gabbro	>90
13R-1W, 27–29	74.97	5.71	5.85	5.94	0.0163	0.0012	0.0021	0.29	0.02	0.04	5.83	4.0	2.80	2.85	2.9	Troctolite (cataclastic)	10–30
13R-1W, 41–43	75.11	5.96	6.02	5.96	0.0027	0.0005	0.0005	0.04	0.01	0.01	5.98	1.1	2.78	2.80	0.9	Troctolite	60–90
18R-1W, 143–145	85.83	5.84	5.82	5.88	0.0079	0.0054	0.0017	0.14	0.09	0.03	5.84	1.1	2.67	2.71	1.9	Troctolite	30–60
19R-1W, 16–18	89.26	5.88	5.92	5.93	0.0019	0.0055	0.0017	0.03	0.09	0.03	5.91	0.8	2.72	2.75	1.9	Troctolite	60–90
21R-1W, 56–58	99.36	5.55	5.45	5.48	0.0008	0.0021	0.0052	0.01	0.04	0.09	5.49	1.7	2.71	2.78	4.1	Olivine gabbro	60–90
21R-1W, 117–119	99.97	5.79	5.72	5.96	0.0043	0.0068	0.0008	0.07	0.12	0.01	5.83	4.1	2.78	2.84	3.3	Olivine gabbro	60–90
21R-2W, 26–28	100.375	5.29	5.32	5.42	0.0021	0.0014	0.0008	0.04	0.03	0.02	5.34	2.5	2.72	2.78	3.2	Olivine gabbro	60–90
23R-1W, 21–23	102.01	5.47	5.23	5.42	0.0010	0.0068	0.0012	0.02	0.13	0.02	5.37	4.3	2.76	2.82	3.3	Olivine gabbro	30–60
23R-1W, 50–52	102.3	6.01	6.20	5.98	0.0034	0.0053	0.0109	0.06	0.09	0.18	6.06	3.7	2.82	2.88	3.5	Olivine gabbro	30–60
										Mean:	6.12	2.83	2.83	2.86	1.71	
										Standard deviation:	0.38	1.29	0.08	0.07	1.20	
										Maximum:	6.60	5.51	2.95	2.99	4.10	
										Minimum:	5.34	0.84	2.67	2.71	0.20	

Table T13. Thermal conductivity measurements, Hole U1415J.

Core, section	Depth (mbsf)	Number of measurements	Thermal conductivity (W/[m·K])	Standard deviation (W/[m·K])	Standard deviation (%)	Apparent anisotropy (%)	Lithology	Comment
345-U1415J-								
5R-1A (Piece 18)	27.56	10	2.183	0.009	0.43		Olivine-bearing gabbro/gabbronorite	Large probe
5R-2A (Piece 2)	28.82	10	2.167	0.010	0.47		Olivine-bearing gabbronorite	Large probe
7G-1A (Piece 16)	30.18	10	2.279	0.022	0.95		Clinopyroxene-bearing troctolite	Large probe
8R-2A (Piece 5)	36.83	9	2.096	0.007	0.34		Clinopyroxene oikocryst-bearing troctolite	Large probe
8R-3A (Piece 12)	39.01	9	2.497	0.070	2.80		Olivine-bearing gabbro	Large probe
9R-1A (Piece 7A)	45.71	10	2.634	0.016	0.63		Olivine-bearing gabbro	Large probe
13R-1A (Piece 6)	75.15	10	2.972	0.015	0.51		Troctolite	Large probe
18R-1A (Piece 8)	85.03	20	4.109	0.021	0.51		Troctolite	Large probe
18R-1A (Piece 14)	85.44	10	3.399	0.046	1.37		Troctolite	Large probe
21R-1A (Piece 9)	99.38	10	2.270	0.020	0.87		Olivine gabbro	Large probe
21R-2A (Piece 3)	100.345	6	2.122	0.021	0.99		Olivine gabbro	Large probe
		Mean:	2.612	0.023	0.90			Large probe
		Standard deviation:	0.642	0.019	0.70			Large probe
		Maximum:	4.109	0.070	2.80			Large probe
		Minimum:	2.096	0.007	0.34			Large probe
5R-2A (Piece 2)	28.82	8	2.153	0.075	3.50	3.6	Olivine-bearing gabbronorite	Small probe (needle parallel to foliation)
5R-2A (Piece 2)	28.82	7	2.231	0.046	2.04		Olivine-bearing gabbronorite	Small probe (needle perpendicular to foliation)
18R-1A (Piece 14)	85.44	8	3.536	0.121	3.42	0.1	Troctolite	Small probe (needle parallel to foliation)
18R-1A (Piece 14)	85.44	6	3.541	0.109	3.07		Troctolite	Small probe (needle perpendicular to foliation)